Disturbed Interactions between Mitochondria and the Endoplasmic Reticulum: Implications for Human Disease

David Moore (BSc, MRes)

Thesis submitted for the degree of

Doctor of Philosophy

October 2016

Institute of Genetic Medicine

Faculty of Medical Science

Abstract

Inherited optic neuropathies cause significant visual impairment and this group of disorders affect at least 1 in 10,000 people in the United Kingdom. The pathological hallmark of inherited optic neuropathies is the preferential loss of retinal ganglion cells within the inner retina, which leads to optic nerve degeneration and subsequent visual failure. This thesis describes investigations into the underlying disease mechanisms of inherited optic neuropathies, including the potential involvement of mitochondrial dysfunction in the pathophysiology of Wolfram syndrome.

A robustly phenotyped cohort of 30 optic atrophy patients with a likely genetic cause for their visual failure was screened for possible pathogenic mutations in the *WFS1* (4p16.1), *RTN4IP1* (6q21) and *C12orf65* (12q24.31) genes. No pathogenic mutations were identified.

Wolfram syndrome 1 (WFS1) is a rare genetic disease characterised by diabetes insipidus, diabetes mellitus, optic atrophy and deafness, and it is primarily caused by mutations in the *WFS1* gene (4p16.1). A cell culture model consisting of fibroblasts derived from five patients harbouring confirmed recessive or dominant *WFS1* mutations was used to explore the disease mechanisms of Wolfram syndrome. *WFS1* mutations had a deleterious impact on calcium (Ca^{2+}) transfer from the ER to the mitochondria, which was associated with impaired mitochondrial oxidative phosphorylation and differential sensitivity to the ER stressor thapsigargin.

Wolfram syndrome 2 (WFS2) is caused by recessive mutations in the *CISD2* gene (4q24) and shares many of the clinical features of WFS1. In *CISD2*-mutant fibroblasts, mitochondria-ER apposition was increased and there was evidence of disturbed Ca^{2+} homeostasis, including amplified Ca^{2+} transfer from the ER to mitochondria and raised cytosolic Ca^{2+}.

These results indicate that *WFS1* and *CISD2* mutations disturb cellular Ca^{2+} homeostasis and alter mitochondrial function supporting the hypothesis that mitochondrial dysfunction plays an important role in the neuropathology of Wolfram syndrome.

Acknowledgements

First and foremost, I would like to thank my supervisor Dr Patrick Yu-Wai-Man for the opportunity to undertake this PhD project and for the continued support, guidance and encouragement provided over the last four years. I have enjoyed doing my PhD and it has been a pleasure to be a part of the group.

I would also like to thank Dr Florence Burté and Dr Aurora Gomez-Duran for their support and question answering during my PhD. Also thanks are due to everyone who has been part of the mitochondrial research group and has made the lab a great place to work.

I extend my thanks to Dr Alain Lacampagne, Dr Jérémy Fauconnier and Dr Guy Lenaers for the opportunity to undertake a placement in their laboratories in Montpellier. I learned valuable skills that contributed to the outcome of this project. I also would like to thank Dr Cécile Rouzier and Professor Véronique Paquis-Flucklinger for their collaborations on the WFS2 project.

Table of Contents

List of Figures

List of Tables

List of Publications

1. Angebault, C., Guichet, P.O., Talmat-Amar, Y., Charif, M., Gerber, M., Fares-Taie, L., Gueguen, N., Halloy, F., **Moore, D**., Amati-Bonneau, P., Manes, G., Hebrard, M., Bocquet, B., Quiles, M., Piro-Megy, C., Teigell, M., Delettre, C., Rossel, M., Meunier, I., Preising, M., Lorenz, B., Carelli, V., Chinnery, P.F., Yu-Wai-Man, P., Kaplan, J., Roubertie, A., Barakat, A., Bonneau, D., Reynier, P., Rozet, J.M., Bomont, P., Hamel, C.P., Lenaers, G. (2015) 'Recessive Mutations in RTN4IP1 cause isolated and syndromic optic neuropathies', *American Journal of Human Genetics*, 97(5), 754-60.

2. Genin, E.C., Plutino, M., Bannwarth, S., Villa, E., Cisneros-Barroso, E., Roy, M., Ortega-Vila,B., Fragaki, K., Lespinasse, F., Pinero-Martos, E., Auge, G., **Moore, D**., Burte, F., Lacas-Gervais, S., Kageyama, Y., Itoh, K., Yu-Wai-Man, P., Sesaki, H., Ricci, J.E., Vives-Bauza, C., Paquis-Flucklinger, V (2015) 'CHCHD10 mutations promote loss of mitochondrial cristae junctions with impaired mitochondrial genome maintenance and inhibition of apoptosis', *EMBO Mol Med*, 8, 58-72.

3. Bannwarth, S., Ait-El-Mkadem, S., Chaussenot, A., Genin, E., Lacas-Gervais, S., Fragaki, K., Berg-Alonso, L., Kageyama, Y., Serre, V., **Moore, D**., Vershcueren, A., Rouzier, C., Le Ber, I., Auge, G., Cochaud, C., Lespinasse, F., N'Guyen, K., de Septenville, A., Brice, A., Yu-Wai-Man, P., Sesaki, H., Pouget, J., Paquis-Flucklinger, V (2014) 'A mitochondrial origin for frontotemporal dementia and amyotrophic lateral sclerosis through CHCHD10 involvement', *Brain*, 137(8), 2329-45.

4. Pyle, A., Ramesh, V., Bartsakoulia, M., Boczonadi, V., Gomez-Duran, A., Herczegfalvi, A., Blakely, E.L., Smertenko, T., Duff, J., **Moore, D**., Yu-Wai-Man, P., Douroudis, K., Santibanez-Koref, M., Griffin, H., Lochmuller, H., Karcagi, V., Taylor, R.W., Chinnery, P.F and Horvath, R (2014) 'Behr's Syndrome is Typically Associated with Disturbed Mitochondrial Translation and Mutations in the C12orf65 Gene', *Journal of Neuromuscular Diseases*, 1(1), 55-63.

5. Pfeffer, G., Gorman, G.S., Griffin, H., Kurzawa-Akanbi, M., Blakely, E.L., Wilson, I., Sitarz, K., **Moore, D**., Murphy, J.L., Alston, C.L., Pyle, A., Coxhead,

J., Payne, B., Gorrie, G.H., Longman, C., Hadjivassiliou, M., McConville, J., Dick, D., Imam, I., Hilton, D., Norwood, F., Baker, M.R., Jasier, S.R., Yu-Wai-Man, P., Farrel, M., McCarthy, A., Lynch, A., McFarland, R., Schaefer, A.M., Turnbull, D.M., Horvath, R., Taylor, R.W and Chinnery, P.F (2014) 'Mutations in the SPG7 gene cause chronic progressive external opthalmoplegia through disordered mitochondrial DNA maintenance', *Brain*, 137(5), 1323-36.

Abbreviations

~	Approximately
µl	Microlitre
µm	Micrometre
µM	Micromole
2-DG	2-deoxy-D-glucose
2YT	2X Yeast Tryptone
AD	Alzheimer's disease
ADP	Adenosine diphosphate
ALS	Amyotrophic lateral sclerosis
ATF6	Activating transcription factor 6
ATP	Adenosine triphosphate
BAK	Bcl-2 antagonist or killer
BAX	Bcl-2 associated X protein
Bcl-2	B-cell lymphoma 2
Bip	Binding immunoglobulin protein
Bp	Base pair
BSA	Bovine serum albumin
CI	Complex I
CII	Complex II
CI+CII	Complexes I and II
Ca^{2+}	Calcium
CaM	Calmodulin
CAPOS	Cerebellar ataxia, areflexia, pes cavus, optic atrophy and sensorineural hearing loss
CFP	Cyan fluorescent protein

CISD2	CDGSH Iron Sulfur Domain 2
CISD2	CDGSH iron-sulfur domain containing protein 2
CMT-2A	Charcot Marie Tooth disease type 2A
CNS	Central nervous system
CPEO	Chronic progressive external ophthalmoplegia
dbSNP	Single Nucleotide Polymorphism Database
DIDMOAD	Diabetes Insipidus, Diabetes Mellitus, Optic Atropy and Deafness
DMSO	Dimethyl sulfoxide
DNA	Deoxyribonucleic acid
dNTP	Deoxyribonucleotide triphosphate
DOA	Dominant optic atrophy
DRP1	Dynamin-related protein 1
EDTA	Ethylenediaminetetraacetic acid
ER	Endoplasmic reticulum
ERAD	ER associated protein degradation
ERSE	ER stress response element
ETC	Electron transport chain
F	Fluorescence
F_o	Basal fluorescence
$FADH_2$	Flavin adenine dinucleotide
FBS	Fetal bovine serum
FCCP	Carbonylcyanide-p-trifluoromethoxyphenylhydrazone
Fe/S	Iron-sulfur
Fis1	Fission protein 1
FMN	Flavin mononucleotide
FRET	Fluorescence resonance energy transfer

GECI	Genetically-encoded calcium indicator
GGQ	Glycine-glycine-glutamine
GRP75	Glucose regulated protein 75
GRP94	Glucose regulated protein 94 (GRP94)
GTP	Guanosine triphosphate
H_2DCFDA	2', 7'-dichlorodihydrofluorescein diacetate
H_2O	Water
HBSS	Hank’s balanced salt solution
HEK293	Human embryonic kidney 293
HMW	High molecular weight
HPF	Hours post fertilization
HSP	Hereditary spastic paraplegia
IMJ	Inter-mitochondrial junctions
IMM	Inner mitochondrial membrane
INF2	Inverted formin 2
ICDH	Isocitrate dehydrogenase
IP_3	Inositol 1, 4, 5-triposphate
IP_3R	Inositol-1, 4, 5-triphosphate receptor
IRE1α	Inositol requiring enzyme 1α
K^+	Potassium
KDH	α-ketoglutarate dehydrogenase
KiFs	Kinesin superfamily proteins
LDS	Lithium dodecyl sulfate
LHON	Leber’s hereditary optic neuropathy
MAMs	Mitochondria associated membranes
MCU	Mitochondrial Ca^{2+} uniporter

MEM	Minimum essential media
Mid49	Mitochondrial dynamics protein of 49 kDa
Mid51	Mitochondrial dynamics protein of 51 kDa
MFF	Mitochondrial fission factor
MFN1	Mitofusin-1
MFN2	Mitofusin-2
ml	Millilitre
mm	Millimetre
mM	Millimole
MOMP	Mitochondrial outer membrane permeabilization
mPTP	Mitochondrial permeability transition pore
mtDNA	Mitochondrial DNA
MTT	3-[4,5-dimethylthiazol-2-yl]-2,5 diphenyl tetrazolium bromide
Na^+	Sodium
NADH	Nicotinamide adenine dinucleotide
NCBI	National Centre for Biotechnology Information
nl	Nanolitre
nm	Nanometre
nM	Nanomole
O_2	Oxygen
O_2^-	Superoxide
OCT	Optical coherence tomography
OMM	Outer mitochondrial membrane
OPA1	Optic atrophy 1
OXPHOS	Oxidative phosphorylation
PBA	4-phenylbutyric acid

PBS	Phosphate buffered saline
PC	Phosphatidylcholine
PCR	Polymerase chain reaction
PD	Parkinson’s disease
PDH	Pyruvate dehydrogenase
pPDH	Phosphorylated PDH
PE	Phosphatidylethanolamine
PERK	Protein kinase RNA (PKR)-like kinase
Pi	Inorganic phosphate
PMF	Proton motive force
PS	phosphatidylserine
PTPIP51	Protein tyrosine phosphatase interacting protein 51
PVDF	Polyvinylidene difluoride
ROS	Reactive oxygen species
RF-1	Release factor-1
RGCs	Retinal ganglion cells
rRNA	ribosomal RNAs
RTN4	Reticulon 4
RT-qPCR	Real-time quantitative PCR
RyR	Ryanodine receptor
SERCA	Sarco-endoplasmic reticulum Ca^{2+}-ATPase
SNHL	Sensorineural hearing loss
STS	Staurosporine
TAE	Tris-acetate-EDTA
t-BH	tert-Butyl hydroperoxide
TBST	Tris Buffer Saline Tween 20

TCA	Tricarboxylic acid
TEM	Transmission electron microscopy
Tg	Thapsigargin
TMRM	Tetramethylrhodamine, methyl ester
tRNA	transfer RNAs
TUDCA	Tauroursodeoxycholic acid
UPR	Unfolded protein response
V	Voltage
VAPB	Vesicle-associated membrane protein associated protein B
VDAC	Voltage dependent anion channels
v/v	Volume/volume
WFS1	Wolfram syndrome 1
WFS2	Wolfram syndrome 2
w/v	Weight/volume
XBP1	X-box binding protein 1
YFP	Citrine fluorescent protein

Chapter 1. Introduction

1.1 Mitochondria

Mitochondria are subcellular organelles found in all nucleated mammalian cells (Friedman and Nunnari, 2014). They likely originate from an α-proteobacterial progenitor which in an endosymbiotic event was engulfed and subsequently assimilated by an ancestral eukaryotic cell (Margulis, 1971; Gray, 2012). The main function of mitochondria is the production of adenosine triphosphate (ATP) through oxidative phosphorylation (OXPHOS) (Koopman *et al.*, 2013). In addition, mitochondria have a crucial role in numerous other metabolic processes, and in many cellular processes including the regulation of cellular calcium (Ca^{2+}) homeostasis and the propagation of apoptosis (Tuppen *et al.*, 2010; La Rovere *et al.*, 2016). Mitochondria are essential for cellular integrity and mitochondrial dysfunction is increasingly being recognised as a cause of human disease (Friedman and Nunnari, 2014).

1.2 Structure

Mitochondria have a complex and dynamic ultrastructure that changes according to functional demands (Cogliati *et al.*, 2016). They are spherical or tubular shaped organelles bound by two distinct membranes termed the outer mitochondrial membrane (OMM) and inner mitochondrial membrane (IMM), which differ in composition, structure and function (Palade, 1952; Mannella, 2008).

The arrangement of the two membranes creates three separate internal aqueous sub-compartments within mitochondria: (i) the intermembrane space between the two membranes, (ii) the intracristal space and (iii) the central IMM enclosed protein rich matrix (**Figure 1.1**) (Pernas and Scorrano, 2016). These serve to compartmentalise specific enzymes, metabolites and ions to optimise mitochondrial functions. The matrix is the site of multiple metabolic pathways such as the β-oxidation of fatty acids and the tricarboxylic acid (TCA) cycle (Pernas and Scorrano, 2016).

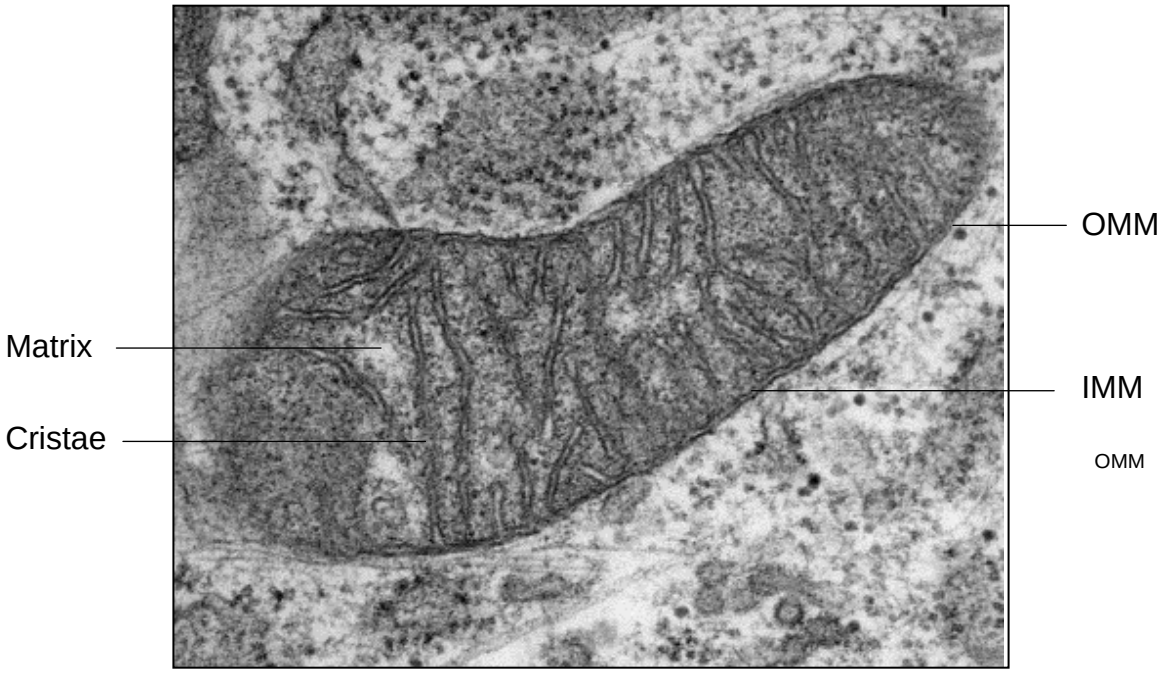

Figure 1.1 The ultrastructure of mitochondria. Transmission electron microscopy (TEM) image of a mitochondrion (Image courtesy of Dr Cécile Rouzier, Nice Sophia-Antipolis University, France).

The OMM encloses the whole organelle; it is lipid rich, relatively smooth and has the smaller surface area of the two membranes. The OMM is highly permeable to ions and small molecules of <5 kDa due to the abundance of pore forming voltage dependent anion channels (VDAC) (Dukanovic and Rapaport, 2011), whereas, mitochondrial proteins are imported through a dedicated protein import machinery (Schmidt *et al.*, 2010). The OMM proteome comprises integral membrane proteins and peripheral membrane associated proteins, which as a group facilitate the interaction between the mitochondria and the cell (Dukanovic and Rapaport, 2011). At least two subdomains of the OMM have been described to mediate interactions with other organelles: (i) the mitochondria associated membranes (MAMs), which mediate interactions with the endoplasmic reticulum (ER) and (ii) inter-mitochondrial junctions (IMJ), which mediate interactions with other mitochondria (Vance, 1990; Picard *et al.*, 2015).

The IMM is composed of two distinct subdomains: the inner boundary membrane and the cristae membrane. These two subdomains are contiguous and are connected by narrow tubular openings of 20 to 50 nm termed cristae junctions (Pernas and Scorrano, 2016). The inner boundary membrane runs parallel to the

OMM; the two membranes are closely apposed and functionally interact in certain pathways. In contrast, the cristae membrane projects into the interior of the mitochondria in tubular or lamellar shaped folds that greatly increase the surface area of the IMM (Mannella *et al.*, 2013). Compared to the OMM, the IMM is particularly protein rich and largely impermeable, a feature that enables the establishment of a transmembrane electrochemical gradient (Vogel *et al.*, 2006). The protein composition of the IMM subdomains is distinct but not exclusive; the inner boundary membrane contains the mitochondrial carriers which transfer metabolites and ions across the IMM, whereas, the cristae membrane is the primary site of the assembled complexes of the OXPHOS system (Vogel *et al.*, 2006; Wilkens *et al.*, 2013).

1.3 Mitochondrial Genetics

Due to their endosymbiotic origin, mitochondria contain their own DNA (mtDNA) (Nass, 1966; van Bruggen *et al.*, 1966; Bogenhagen, 2012). However, mitochondria are not autonomous and rely on the import of over 1000 nuclear-encoded proteins for the mitochondrial proteome (Calvo *et al.*, 2016). The human mtDNA is a circular, double-stranded DNA molecule of 16,569 base pairs (bp) that is packaged into DNA-protein complexes termed nucleoids (Andrews *et al.*, 1999b; Bogenhagen, 2012). Nucleoids are composed of a single copy of mtDNA and a core set of proteins involved in mtDNA maintenance (Kukat *et al.*, 2011; Kopek *et al.*, 2012). Multiple copies of mtDNA are present in each cell and depending upon bioenergetic demand a cell can contain hundreds to thousands of mtDNA molecules (Chinnery and Hudson, 2013).

The human mtDNA is compactly organised and encodes 37 genes: 13 polypeptides, 22 mitochondrial transfer ribonucleic acids (tRNAs) and 2 mitochondrial ribosomal RNAs (rRNAs). The 13 polypeptides are all essential subunits of the multisubunit complexes that compose the OXPHOS system. The RNA products are components of the mitochondrial translation system and are required for the translation of mtDNA-encoded polypeptides (Chinnery and Hudson, 2013). As all mtDNA-encoded genes are required for the OXPHOS system, mutations and deletions in mtDNA can cause mitochondrial dysfunction and are implicated in human disease (Holt *et al.*, 1988; Wallace *et al.*, 1988). Similarly, alterations of mtDNA copy number are also associated with human disease (Spiegel *et al.*, 2016).

1.4 Mitochondrial OXPHOS

The primary function of mitochondria is the production of ATP through OXPHOS. ATP is an energy rich compound used to meet cellular energy demands and to maintain cellular integrity. ATP content is therefore maintained in a strict equilibrium between hydrolysis and synthesis (Koopman *et al.*, 2013). The OXPHOS system is composed of five multisubunit complexes (I-V) embedded in the IMM and two mobile electron carriers: ubiquinone (coenzyme Q_{10}) and cytochrome *c* (Yu-Wai-Man *et al.*, 2011a). The five complexes are divided into two functional groups: (i) the electron transport chain (ETC) comprising complexes I-IV and (ii) complex V which generates ATP (**Figure 1.2**) (Koopman *et al.*, 2013).

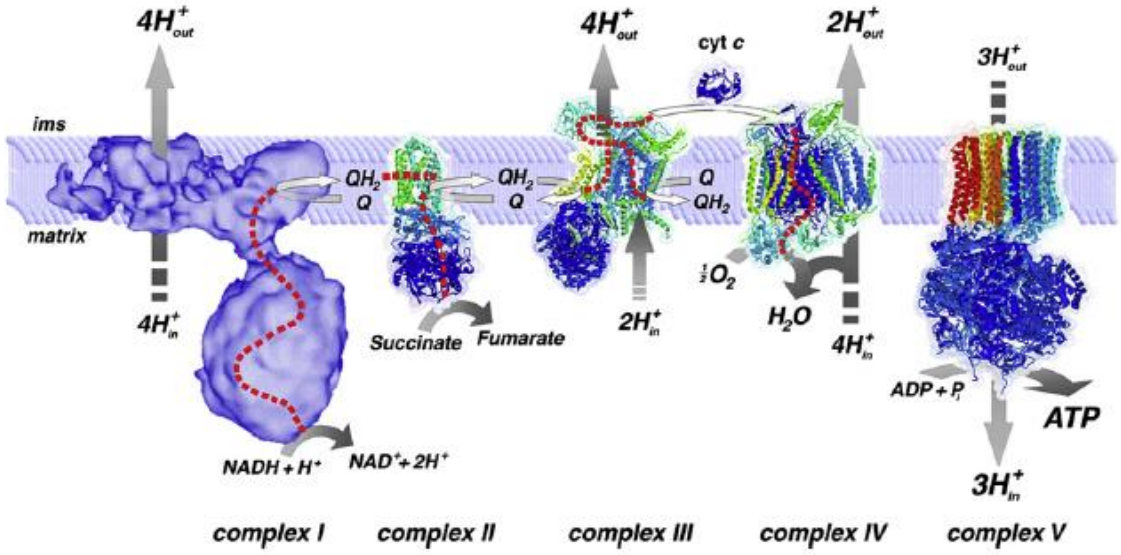

Figure 1.2 The mitochondrial OXPHOS system. (Reproduced from Yu-Wai-Man *et al.*, 2011a).

Electrons extracted from nutrient compounds such as monosaccharides and fatty acids are transferred to form nicotinamide adenine dinucleotide (NADH) and flavin adenine dinucleotide ($FADH_2$) through glycolysis, β-oxidation and the TCA cycle (Fernandez-Vizarra *et al.*, 2009). Electrons from NADH and $FADH_2$ enter the ETC at complexes I and II, respectively. These electrons are sequentially transferred along the ETC and at complex IV are donated to oxygen (O_2), reducing it to form water (H_2O). The energy released as electrons are transferred along the ETC is used to transport protons from the matrix across the IMM into the intermembrane space at complexes I, III and IV (Nsiah-Sefaa and McKenzie, 2016). This establishes a proton

motive force (PMF) across the IMM consisting of a difference in electrical potential (~180 mV, negative inside) and pH gradient (~0.8, alkaline inside). The electrochemical gradient of protons is utilized by complex V to drive the production of ATP from adenosine diphosphate (ADP) and inorganic phosphate (Pi) (Brand and Nicholls, 2011).

1.4.1 Complex I

Complex I (NADH:ubiquinone oxidoreductase) is composed of 45 (44 unique) subunits and 9 redox cofactors: a flavin mononucleotide (FMN) and eight iron-sulfur (Fe/S) clusters (Vinothkumar *et al.*, 2014). Seven complex I subunits are mtDNA-encoded (ND1, 2, 3, 4, 4L, 5 and 6) and the rest are nuclear-encoded. The core of the enzyme is formed by 14 subunits which are surrounded by 31 'accessory' subunits that form a shell around the core (Fiedorczuk *et al.*, 2016). Complex I is L shaped, comprising a hydrophilic peripheral arm which protrudes into the matrix and a lipophilic IMM-embedded arm. The two arms have independent functions; the peripheral arm harbors the cofactors which mediate electron transfer from NADH to ubiquinone, involving the reduction of the FMN cofactor and transfer along a series of Fe/S clusters to the ubiquinone reduction site. In parallel, the membrane arm catalyzes proton translocation across the IMM (Sazanov, 2015). Complex I is thought to translocate four protons for every two electrons transferred, although how electron transfer is coupled to proton translocation is currently unknown (Sazanov, 2015).

1.4.2 Complex II

Complex II (succinate:ubiquinone oxidoreductase) functions in both the TCA cycle and the OXPHOS system. The oxidation of succinate to fumarate in the TCA cycle is coupled to the reduction of ubiquinone (Koopman *et al.*, 2013). Complex II is the only respiratory complex that does not contain mtDNA-encoded subunits or pump protons across the IMM (Sun *et al.*, 2005; Rutter *et al.*, 2010). The complex consists of four nuclear-encoded subunits (SDHA-D); two form the catalytic core and two form an integral membrane domain that anchors the complex to the IMM. The catalytic domain contains a covalently bound flavin adenine dinucleotide (FAD) cofactor and three Fe/S clusters which mediate electron transfer from succinate to ubiquinone. The membrane domain contains a heme *b* moiety, the function of which remains unclear (Sun *et al.*, 2005; Rutter *et al.*, 2010).

1.4.3 Complex III

Complex III (ubiquinol:cytochrome *c* oxidoreductase) is composed of up to 11 subunits, of which only cytochrome *b* is mtDNA-encoded (Benit *et al.*, 2009). Three subunits contain prosthetic groups and form the catalytic core of the complex: cytochrome *b* with two noncovalently bound heme *b* groups, cytochrome c_1 with a covalently bound heme *c* and the Rieske iron-sulfur protein with a [2Fe-2S] cluster (Lange and Hunte, 2002). Complex III couples electron transfer between ubiquinol (QH_2) and cytochrome *c* with proton translocation across the IMM in a mechanism termed the Q cycle. In total, four protons are released into the intermembrane space and two protons are removed from the matrix (Lange and Hunte, 2002).

1.4.4 Complex IV

Complex IV (cytochrome *c* oxidase) is the terminal ETC enzyme and catalyses the transfer of electrons from reduced cytochrome *c* to O_2, the final acceptor (Fernandez-Vizarra *et al.*, 2009). Complex IV consists of 13 subunits; 3 of which are mtDNA-encoded (COX1-3) and form the core of the complex. Together, COX1 and COX2 contain two heme groups (cytochrome *a* and cytochrome a_3) and thee copper ions arranged in two copper centres (Cu_A and Cu_B) which mediate electron transfer. COX3 is thought to facilitate proton pumping (Kadenbach and Huttemann, 2015). In the course of each reaction cycle eight protons are removed from the matrix: four protons are taken up by the reduced O_2 moiety forming H_2O and four protons are pumped across the IMM (Popovic, 2013).

1.4.5 Complex V

Complex V (F_oF_1-Atpase) uses the energy stored in the proton gradient across the IMM to link the flow of protons back into the matrix with the production of ATP by rotary catalysis (Kuhlbrandt, 2015). The complex is composed of 19 subunits, two of which are mtDNA-encoded (ATP6 and ATP8). The subunits assemble into two functional rotary motors: the F_0 module which spans the IMM and contains the proton channel and the catalytic F_1 module located in the matrix which synthesizes ATP from ADP and P_i through a sequence of conformational changes, driven by the rotary movement generated during proton translocation (Jonckheere *et al.*, 2012). Each ATP molecule produced requires the translocation of 2.7 protons (Watt *et al.*, 2010).

1.5 Mitochondrial OXPHOS and ROS

The OXPHOS system is a major source of intracellular reactive oxygen species (ROS), mainly due to electron leak at complexes I and III (Murphy, 2009). At least 10 other mitochondrial enzymes are also thought to contribute to ROS production, including complex II (Quinlan *et al.*, 2013). ROS can be formed by the one-electron reduction of O_2 producing the free radical superoxide (O_2^-), the source of most other cellular ROS (Shadel and Horvath, 2015). In the physiological range, ROS production has a signalling role and regulates several cellular processes such as development, the immune system and maintenance of redox balance (Shadel and Horvath, 2015). However, ROS are highly reactive and elevated ROS levels can cause oxidative damage to nucleic acids, proteins and lipids, which can lead to the activation of cell death processes. The balance between ROS production and their removal by antioxidant enzymes is therefore crucial for cellular integrity (Maresca *et al.*, 2013).

1.6 Apoptosis

Mitochondria have a central role in the regulation and execution of apoptosis, a form of programmed cell death that is important for the development and homeostasis of multicellular organisms (Tait and Green, 2010). Mitochondria are primarily involved in the intrinsic pathway of apoptosis, which is activated in response to cellular stress and regulated by complex interactions between pro- and antiapoptotic proteins belonging to the B-cell lymphoma 2 (Bcl-2) family (Galluzzi *et al.*, 2012). The intrinsic pathway involves the activation of pro-apoptotic effectors Bcl-2 associated X protein (BAX) and Bcl-2 antagonist or killer (BAK), which induce mitochondrial outer membrane permeabilization (MOMP) (Tait and Green, 2010). Loss of mitochondrial integrity results in the release of pro-apoptotic proteins, such as cytochrome *c*, from the mitochondrial intermembrane space into the cytosol, a key event that results in the activation of both caspase-dependent and -independent mechanisms of apoptotic cell death (Orrenius *et al.*, 2015). Caspases (cysteine-aspartic proteases) are proteolytic enzymes that exist as inactive zymogens and require specific proteolysis for their activation. Once activated the proteolytic activity of effector caspases (caspase-3, -6 and -7) results in the cleavage of at least 1000 substrates located throughout the cell to dismantle the cell contents and create an apoptotic body ready to be phagocytosed (Crawford and Wells, 2011).

1.7 Mitochondrial dynamics

Mitochondria are highly dynamic organelles that undergo frequent changes in morphology and subcellular distribution through fusion, fission and transport. These processes are essential for maintaining a functional mitochondrial population and enabling mitochondria to respond the physiological demands of the cell (Mishra and Chan, 2016). Not surprisingly, disturbances in mitochondrial dynamics are associated with cellular dysfunction and numerous disease states including autosomal dominant optic atrophy (DOA), Charcot-Marie-Tooth disease type-2A (CMT-2A) and hereditary spastic paraplegia (HSP) (Mishra and Chan, 2016). Despite intensive research, the molecular mechanisms and physiological roles of mitochondrial dynamics are still not completely understood and the relationship between mitochondrial dynamics and disease is often unclear (Roy *et al.*, 2015).

1.7.1 Fusion

Mitochondrial fusion is a two-step process coordinated by three dynamin-like GTPases: mitofusin-1 (MFN1), mitofusin-2 (MFN2) at the OMM and optic atrophy 1 (OPA1) at the IMM (Olichon *et al.*, 2002; Eura *et al.*, 2003). The mitofusins form homo- and heterotypic oligomers that tether opposing mitochondria and initiate OMM fusion in a guanosine triphosphate (GTP) dependent manner (Chen *et al.*, 2003; Schrepfer and Scorrano, 2016). Following OMM fusion, IMM fusion occurs in an almost simultaneous but distinct event mediated by OPA1 (Liu *et al.*, 2009; Song *et al.*, 2009). OPA1 is regulated by alternative splicing and proteolytic processing to give rise to long and short isoforms (L-OPA1 and S-OPA1) which are thought to coordinate to mediate IMM fusion (Ishihara *et al.*, 2006; Song *et al.*, 2007), although, it has recently been suggested that L-OPA1 is sufficient for IMM fusion and that S-OPA1 is instead associated with IMM fission (Anand *et al.*, 2014).

1.7.2 Fission

Mitochondrial fission is performed by a dynamin-like GTPase termed dynamin-related protein 1 (DRP1). DRP1 is predominantly located in the cytosol and can be recruited to the mitochondria through numerous signalling pathways to induce fission (Chang and Blackstone, 2010). DRP1 lacks a lipid-binding pleckstrin homology domain and interacts with several integral OMM protein adaptors to mediate fission including: mitochondrial fission protein 1 (Fis1), mitochondrial fission factor (MFF) and

mitochondrial dynamics proteins of 49 and 51kDa (MiD49 and MiD51) (Loson *et al.*, 2013). Once present at the OMM, DRP1 self assembles into oligomeric structures that surround mitochondria and conformational changes driven by GTP hydrolysis constrict mitochondria ultimately leading to fission (Mears *et al.*, 2011).

The ER and actin cytoskeleton participate in mitochondrial fission and are thought to act upstream of DRP1 recruitment. Mitochondrial fission predominantly occurs at sites with ER contact; ER tubules are suggested to encircle mitochondria and provide the initial constriction that facilitates subsequent DRP1-mediated fission (**Figure 1.3**) (Friedman *et al.*, 2011). Furthermore, at the mitochondria-ER contact site, ER localised inverted formin 2 (INF2) is activated to polymerise actin, a process which is suggested to enable force generation to assist mitochondrial constriction (Korobova *et al.*, 2013).

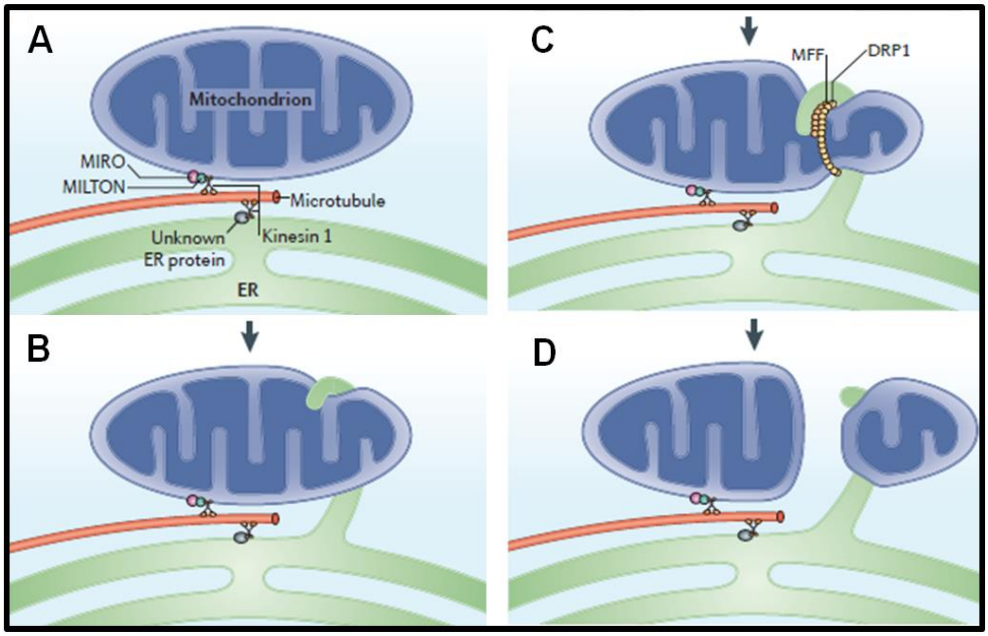

Figure 1.3 ER-mitochondrial contact in mitochondrial dynamics. The ER tubule encircles mitochondria to provide the initial constriction prior to DRP1-dependent mitochondrial fission. (Adapted from Rowland and Voeltz, 2012).

1.7.3 Transport

The long-range transport of mitochondria is largely dependent on microtubule based motor proteins via mechanism which require ATP hydrolysis. Kinesin superfamily proteins (KiFs), particularly the Kinesin-1 family, mediate anterograde transport and

dyneins mediate retrograde transport (Pilling *et al.*, 2006). Mitochondria connect to motor proteins through motor adaptor proteins and mitochondrial receptor proteins. These motor-adaptor-receptor complexes are highly regulated to ensure the selective transport and precise distribution of mitochondria (Lin and Sheng, 2015).

The primary kinesin motor adaptor proteins in mammals are the Milton proteins, Trak1 and Trak2, and these proteins are linked to mitochondria through the OMM located receptor proteins, Miro1 and Miro2 (Fransson *et al.*, 2006; Koutsopoulos *et al.*, 2010). Miro proteins are part of the Rho-GTPase family and contain two Ca^{2+} binding EF hand motifs which coordinate the Ca^{2+}-dependent regulation of mitochondrial transport (Saotome *et al.*, 2008; Macaskill *et al.*, 2009; Wang and Schwarz, 2009). The molecular mechanisms linking dynein motors to mitochondria are not well characterised (Lin and Sheng, 2015). It is suggested that specific binding of kinesin or dynein to Trak1/2 may coordinate the bidirectional transport of mitochondria. This model is based on the observation that Trak1 binds both kinesins and dyneins, whereas, Trak2 predominantly binds dyneins (van Spronsen *et al.*, 2013). In addition to long-range transport, mitochondrial distribution is dependent on short-range transport mediated by myosin motors on actin filaments and the docking of stationary mitochondria, primarily via interactions with the protein syntaphilin (**Figure 1.4**) (Lin and Sheng, 2015).

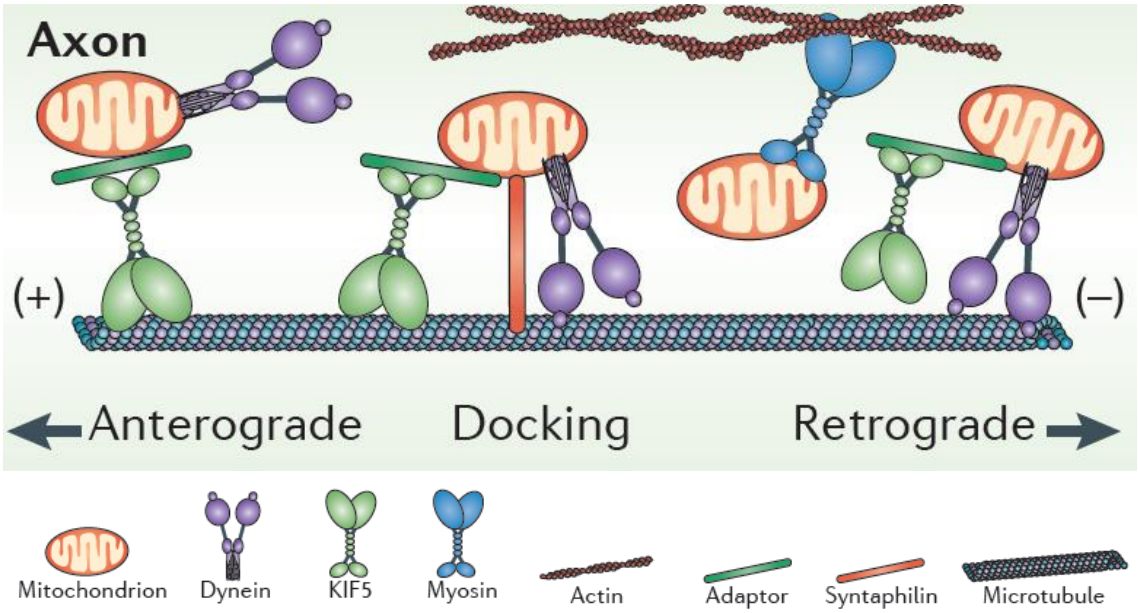

Figure 1.4 The mitochondrial transport machinery. (Reproduced from Sheng and Cai, 2012).

1.7.4 The functions of mitochondrial dynamics

The balance between fusion and fission events maintains mitochondria within a dynamic network. Mitochondrial morphology varies according to the cell type and physiological context, ranging from small distinct organelles to tubular interconnected filaments (Scorrano, 2013). Mitochondrial fusion is required for the exchange of contents between mitochondria, including metabolites, proteins and mtDNA, and the absence of mitochondrial fusion is associated with OXPHOS dysfunction, mtDNA depletion and increased ROS production (Chen *et al.*, 2010; Westermann, 2012). A fused mitochondrial network positively correlates with high OXPHOS activity and a shift towards fusion has been shown to occur in response to cellular energy demand, nutrient availability and cellular stress (Tondera *et al.*, 2009; Gomes *et al.*, 2011; Rambold *et al.*, 2011). Mitochondrial fission is equally important and is required for the segregation of mitochondria into daughter cells during cell division and the elimination of dysfunctional mitochondria via mitophagy (the specific degradation of mitochondria) through fission and selective fusion events (Taguchi *et al.*, 2007; Twig *et al.*, 2008). In addition, mitochondrial fission is associated with the intrinsic pathway of apoptosis and DRP1-dependent fissions is thought to be essential for cristae remodelling and cytochrome *c* release during the early phase of apoptosis (Otera *et al.*, 2016).

Transport mechanisms are required to distribute mitochondria throughout the cell to satisfy the local demand for ATP, Ca^{2+} buffering and other mitochondrial functions. Regulation of mitochondrial transport is particularly important in neurones due to their unique structure and is essential for the function of synapses and maintenance of dendrites and axons (Sheng and Cai, 2012). Two signalling pathways that control mitochondrial transport are sensing ATP and ADP levels and alterations of cytosolic [Ca^{2+}] (Mironov, 2007; Macaskill *et al.*, 2009). Mitochondrial velocity appears to increase in areas with high ATP levels and decrease in areas with local ATP depletion, thus ensuring mitochondria respond to cellular energy demand (Mironov, 2007). Similarly, elevated cytosolic [Ca^{2+}] is suggested to arrest mitochondrial movement, as Ca^{2+} influx largely occurs at sites of high energy demand, such as neuronal synapses, this mechanism ensures mitochondria are positioned to both buffer Ca^{2+} and supply ATP (Macaskill *et al.*, 2009; Wang and Schwarz, 2009).

1.8 The Mitochondria Associated Membrane

Mitochondria interact with the ER at specialised interfaces termed MAMs (Vance, 1990). These contact sites are defined as regions where the two organelles are closely apposed and functionally interact, but remain as distinct organelles (Rowland and Voeltz, 2012). The best characterised functions of the MAM are phospholipid synthesis and the transfer of Ca^{2+} from the ER to mitochondria, which serves to regulate cytosolic Ca^{2+} signalling, mitochondrial bioenergetics and mitochondrial-mediated apoptosis (van Vliet *et al.*, 2014).

1.8.1 The Endoplasmic Reticulum

The ER is a large membrane bound intracellular organelle that is continuous with the nuclear envelope and extends into to the periphery of the cell in a dynamic network of interconnected sheets and tubules (Schwarz and Blower, 2016). The ER has functional subdomains including the nuclear, transitional, rough and smooth ER that together perform the numerous cellular functions of the ER (**Figure 1.5**) (Schwarz and Blower, 2016). Both the smooth and rough ER have been shown to mediate ER interactions with mitochondria at the MAMs, although whether these interactions have distinct functions is unclear (Csordas *et al.*, 2006).

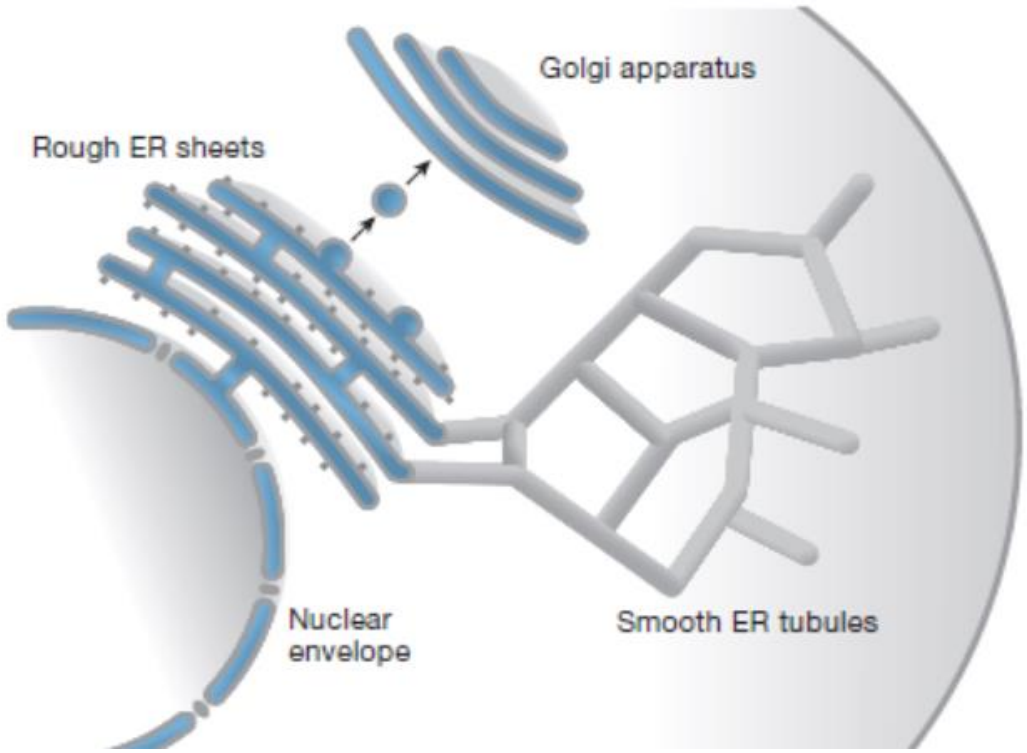

Figure 1.5 Schematic of the ER. The structure and functional subdomains of the ER (Reproduced from Park and Blackstone, 2010)

One function of the ER is the synthesis and maturation of proteins. Protein synthesis occurs at the ribosomes which coat the rough ER and further processing is facilitated by ER-resident protein chaperones (Park and Blackstone, 2010). The ER is also involved in the synthesis of phospholipids, cholesterol and steroids (Schwarz and Blower, 2016). Importantly, the ER is the main intracellular Ca^{2+} store and has a role in cellular Ca^{2+} signalling, a feature that is central to the functional interaction between the ER and mitochondria at the MAM (Kaufman and Malhotra, 2014).

1.8.2 ER Ca^{2+} homeostasis

In the cell, Ca^{2+} ions are utilized as second messengers and a rise in intracellular [Ca^{2+}] regulates numerous physiological functions such as metabolism, gene expression, hormone secretion, synaptic transmission and cell death (Kaufman and Malhotra, 2014). An increase in cytosolic [Ca^{2+}] (~100 nM resting) can be produced through two mechanisms: (i) the entry of Ca^{2+} from the extracellular milieu (~1 mM) or (ii) the release from intracellular Ca^{2+} stores, primarily the ER (total ~1 mM) (Bononi *et al.*, 2012).

The ER Ca^{2+} store is regulated by: (i) Ca^{2+} binding proteins in the ER lumen, (ii) Ca^{2+} uptake through the sarco-endoplasmic reticulum Ca^{2+}-ATPase (SERCA) and (iii) Ca^{2+} release through channels including the inositol-1, 4, 5-triphosphate receptor (IP_3R) and the ryanodine receptor (RyR) (Szabadkai *et al.*, 2006; Zatyka *et al.*, 2015). The ER luminal Ca^{2+} binding proteins have a low affinity but a high capacity for Ca^{2+} buffering and maintain free ER [Ca^{2+}] at ~200 µM (Prins and Michalak, 2011). The SERCA couples ATP hydrolysis to the transport of Ca^{2+} into the ER against the ion gradient, with a stoichiometry of 2:1 Ca^{2+}/ATP. There are three genes encoding SERCAs, with alternate splicing producing additional isoforms and each has a different activity, expression level and tissue distribution (Krebs *et al.*, 2015). The IP_3R is the most ubiquitously expressed ER Ca^{2+} channel and is activated in response to inositol 1, 4, 5-triposphate (IP_3) production. Three genes encode IP_3Rs, with further splice isoforms and these form homo- or heterotetrameric Ca^{2+} channels (Kiviluoto *et al.*, 2013). Regulation of IP_3R activity primarily occurs through: (i) the local environment, (ii) phosphorylation and dephosphorylation by many kinases and phosphatases and (iii) direct interactions with regulatory proteins which can stimulate or inhibit IP_3R activity (Kiviluoto *et al.*, 2013). One role of the IP_3R is the transfer of Ca^{2+} from the ER to mitochondria at the MAM **(Figure 1.6)** (Bononi *et al.*, 2012).

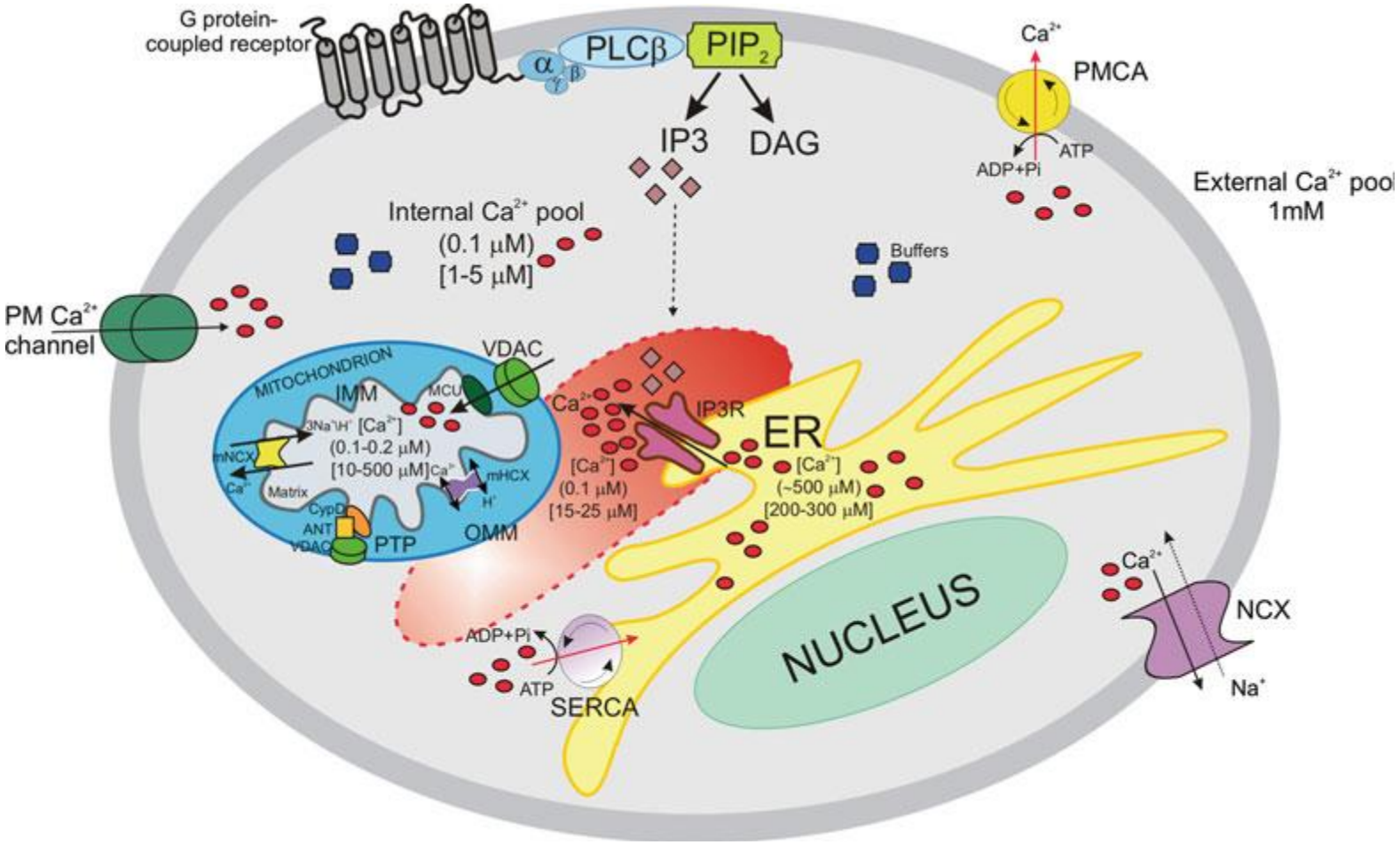

Figure 1.6 Schematic model of intracellular Ca^{2+} homeostasis. Cellular Ca^{2+} signals are tightly regulated by the coordinated action of Ca^{2+} channels, pumps, exchangers and binding proteins mainly located at the plasma membrane, ER and mitochondria. Activation of plasma membrane G protein coupled receptors results in the production of IP_3 which stimulates IP_3R dependent ER Ca^{2+} release. The MAM domain facilitates the efficient transfer of Ca^{2+} from the ER to mitochondria (Reproduced from Bononi *et al.*, 2012).

1.8.3 Structural composition of the MAM

The MAM interface is essential for coordinating the function of the mitochondria and the ER, including processes that involve both organelles (Paillusson *et al.*, 2016). Approximately 1000 proteins are thought to be enriched at the MAM (Zhang *et al.*, 2011; Poston *et al.*, 2013). A core set of proteins comprise the basic MAM proteome to mediate key MAM functions, and the MAM is able to recruit a diverse range of proteins to perform further functions according to cellular demands (Van Vliet *et al*., 2014).

The MAM is highly dynamic and the length and width of organelle apposition are regulated by the cell. In HeLa cells, the total surface of the OMM apposed to the ER was estimated to range from 5 to 20 %, whereas, in mouse liver cells the percentage of OMM in contact with the ER varied from 4.7% to 11.2%, dependent upon the metabolic state of the cell (Rizzuto *et al.*, 1998; Sood *et al.*, 2014). In addition, the width of the MAM is thought to range from ~10 to 30 nm (Csordas *et al.*, 2006). These parameters shape the properties of the MAM and are modulated by the cell to control fundamental MAM functions. However, the mechanisms which mediate formation and regulation of the MAMs are not well characterised (Giacomello and Pellegrini, 2016).

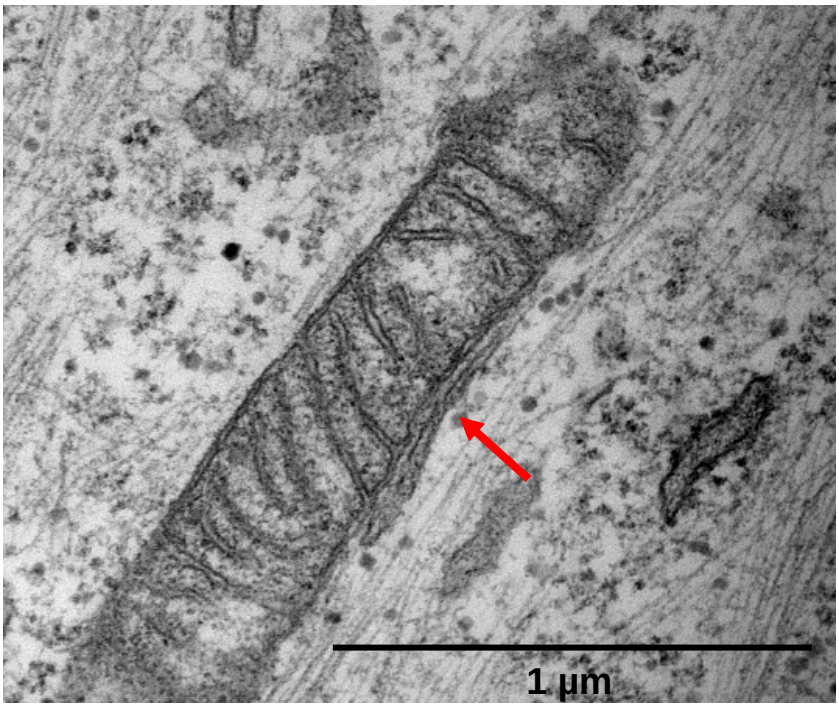

Figure 1.7 The MAM. A TEM image showing the apposition between a mitochondrion and the ER at the MAM (Image courtesy of Dr Cécile Rouzier, Nice Sophia-Antipolis University, France).

1.8.4 Protein tethers at the MAM

Protein complexes that may contribute to ER-mitochondrial tethering at the MAM have been observed by electron tomography. The length of the tethers connecting the OMM and the smooth ER were ~9 to 16 nm, whereas, the tethers connecting the OMM and the rough ER were ~19 to 30 nm in length (Csordas *et al.*, 2006).

One protein tether identified in mammalian cells is a complex formed by the IP_3R on the ER and the VDAC on the OMM which are physically tethered by the chaperone glucose regulated protein 75 (GRP75) (Szabadkai *et al.*, 2006). However, studies describing overexpression of GRP75 or complete loss of the IP_3Rs demonstrate that neither disturbs ER-mitochondrial apposition, indicating that this complex does not represent a structural tether and can instead be considered a functional tether which promotes ER-mitochondrial Ca^{2+} transfer (Csordas *et al.*, 2006; Szabadkai *et al.*, 2006).

Another candidate protein tether at the MAM is homo- or heterocomplexes of MFN2 on the ER with MFN1 or MFN2 on the OMM. Ablation of MFN2 was reported to decrease MAM apposition and disturb MAM functions including ER-mitochondrial Ca^{2+} transfer and amplification of apoptosis (de Brito and Scorrano, 2008). However, recent studies have suggested that MFN2 ablation increases the structural and functional interaction between the ER and mitochondria, indicating that the model regarding MAM tethering by MFN2 needs to be revised (Cosson *et al.*, 2012; Filadi *et al.*, 2015).

A final protein tether at the MAM is an interaction between the ER localised vesicle-associated membrane protein associated protein B (VAPB) and the OMM localised protein tyrosine phosphatase interacting protein 51 (PTPIP51). Overexpression of VAPB and/or PTPIP51 increases ER-mitochondria contact, whereas, siRNA-mediated knockdown of VAPB and/or PTPIP51 reduces organelle contact, suggesting that this tether is required for the structure of the MAM. Notably, dysfunction of the VAPB-PTPIP51 protein tether is implicated in amyotrophic lateral sclerosis (ALS) (De Vos *et al.*, 2012; Stoica *et al.*, 2014).

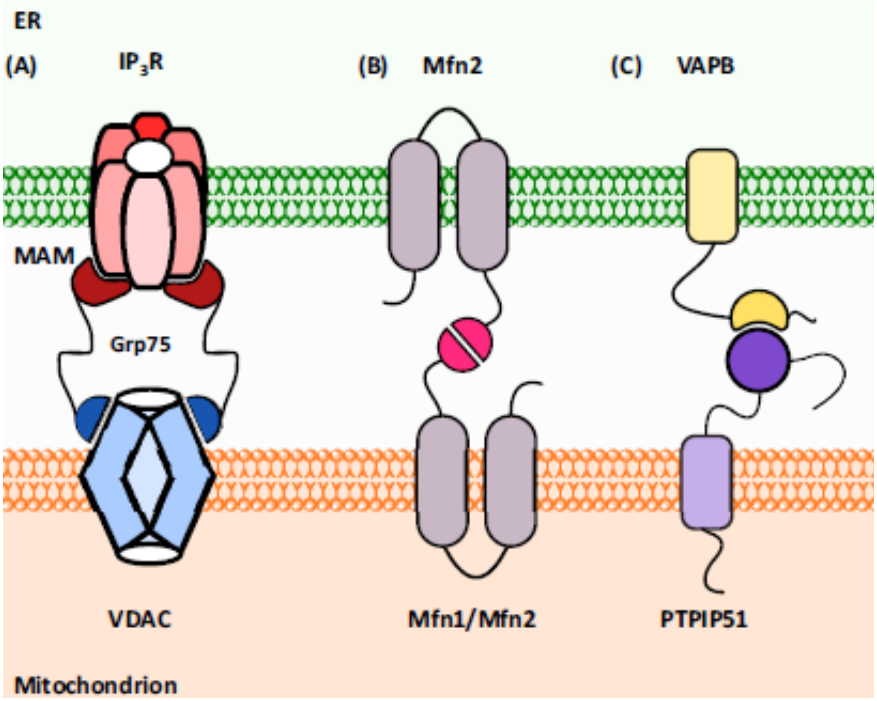

Figure 1.8 The MAM protein tethers. (A) IP_3R interacts with VDAC through GRP75, (B) MFN2 on the ER has been proposed to interact with MFN1 or MFN2 on the OMM, and (C) VAPB interacts with PTPIP51 (Reproduced from Paillusson *et al.*, 2016).

1.8.5 Functions of the MAM

Two fundamental processes occurring at the MAM are phospholipid synthesis and ER-mitochondrial Ca^{2+} transfer (van Vliet *et al.*, 2014).

The MAM is enriched with enzymes associated with phospholipid synthesis allowing the ER and mitochondria to coordinate the biosynthesis of three abundant cellular phospholipids: phosphatidylserine (PS), phosphatidylethanolamine (PE) and phosphatidylcholine (PC) (Stone and Vance, 2000). Phospholipid synthesis is dependent on close apposition between the two organelles. PS is first synthesized on the ER and then translocated to the IMM where decarboxylation of PS produces PE. In turn, PE is translocated back to the ER where it is converted into PC (Osman *et al.*, 2011). An increase or decrease in the MAM interface area is known to correlate with a corresponding increase or decrease in phospholipid synthesis, highlighting how modulation of organelle apposition relates to MAM function (Giacomello and Pellegrini, 2016).

Another function of the MAM is the transfer of Ca^{2+} from the ER to the mitochondria, predominantly occurring through the IP_3R-GRP75-VDAC complex

(Rizzuto *et al.*, 1998; Szabadkai *et al.*, 2006). Once across the OMM, the mitochondrial Ca^{2+} uniporter (MCU) complex (the MCU and regulatory elements) mediates Ca^{2+} uptake across the IMM into the mitochondrial matrix, dependent upon the mitochondrial membrane potential (Baughman *et al.*, 2011; De Stefani *et al.*, 2011). The MCU has a low affinity for Ca^{2+} uptake and the microdomain theory suggests that close apposition between the ER and mitochondria exposes the mitochondria to high cytosolic [Ca^{2+}] domains, 5 to 10 fold greater than the overall cytosol, thus enabling efficient mitochondrial Ca^{2+} uptake (Rizzuto *et al.*, 1998; Giacomello *et al.*, 2010). These Ca^{2+} microdomains are facilitated by: (i) the close apposition of the ER and mitochondria, (ii) the enrichment of Ca^{2+} handling machinery at MAMs and (iii) the tethering of the IP_3R and VDAC by GRP75 (Krols *et al.*, 2016). Consequently, factors which decrease or increase MAM apposition modulate ER-mitochondrial Ca^{2+} flux in parallel (Csordas *et al.*, 2006). Numerous studies support this concept, for example overexpression of presenelin 2 or α-synuclein have been shown to increase ER-mitochondria Ca^{2+} flux dependent on increased ER-mitochondria apposition (Zampese *et al.*, 2011; Cali *et al.*, 2012).

One function of ER-mitochondrial Ca^{2+} transfer is the regulation of OXPHOS. Consistent low level Ca^{2+} transfer to mitochondria via the IP_3R is required to stimulate ATP production under basal conditions and loss of this function compromises mitochondrial bioenergetics (Cardenas *et al.*, 2010). Furthermore, Ca^{2+} dependent OXPHOS stimulation is utilized to upregulate OXPHOS function in response to activity-dependent rises in cellular ATP demand, for example during neuronal activity (Rangaraju *et al.*, 2014). There are several mechanisms by which Ca^{2+} regulates OXPHOS. A rise in mitochondrial matrix Ca^{2+} stimulates the activity of the TCA cycle directly at isocitrate dehydrogenase (ICDH) and α-ketoglutarate dehydrogenase (KDH), and indirectly at pyruvate dehydrogenase (PDH) through a Ca^{2+}-dependent phosphatase, thus increasing the production of NADH and electron entry into the ETC (Denton, 2009). Mitochondrial Ca^{2+} uptake also stimulates the activity of complex V, directly increasing ATP synthesis, through an unknown mechanism that likely involves a post-translational modification of the complex. In addition, complexes III and IV are potentially regulated by mitochondrial Ca^{2+} levels (Glancy and Balaban, 2012), and the activity of several mitochondrial carriers are Ca^{2+}-dependent (**Figure 1.9**) (Llorente-Folch *et al.*, 2015).

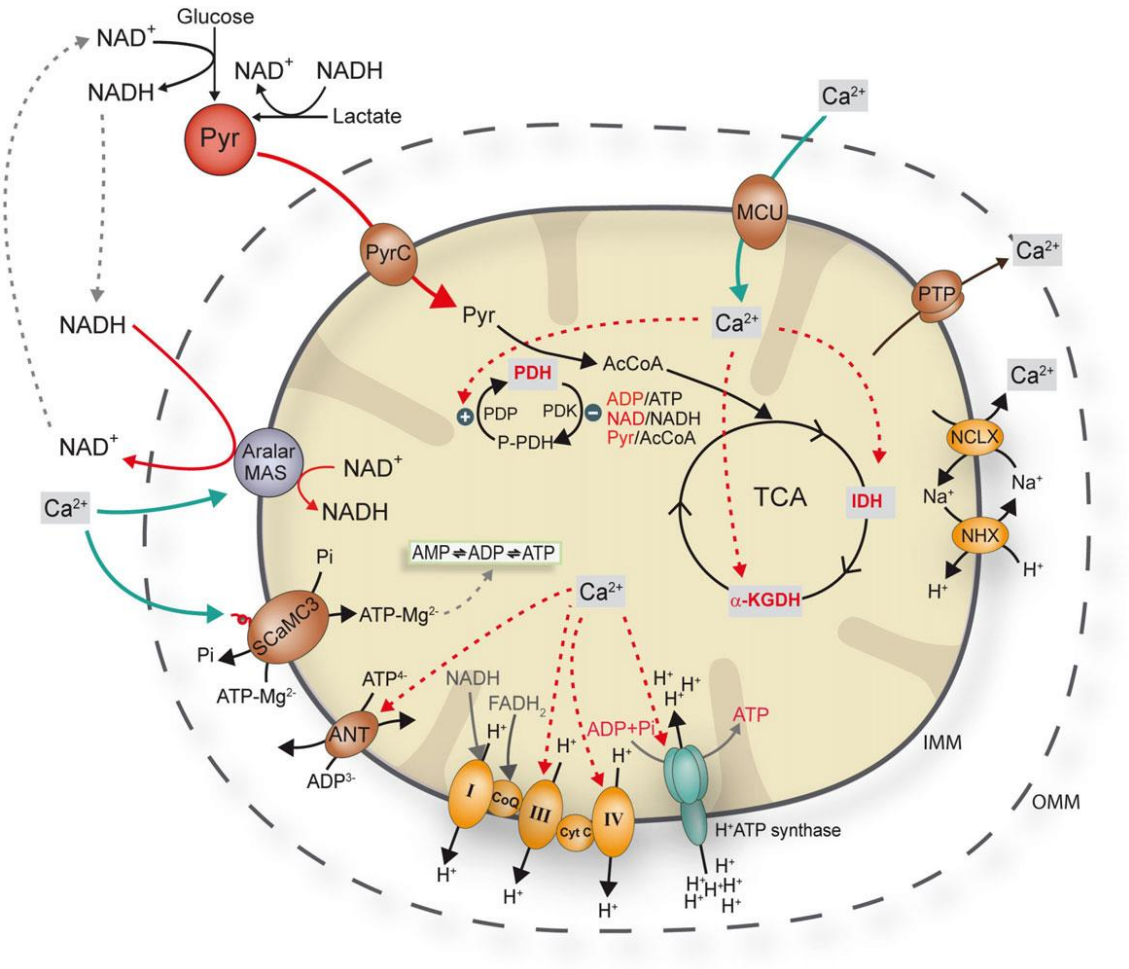

Figure 1.9 A schematic of Ca^{2+} regulation of mitochondrial bioenergetics. Three TCA enzymes and complex V are stimulated by Ca^{2+} uptake to increase OXPHOS. Complexes III and IV and some of the mitochondrial carriers may also be regulated by mitochondrial matrix Ca^{2+} (Reproduced from Llorente-Folch *et al.*, 2015).

On the contrary, excessive ER-mitochondrial Ca^{2+} transfer is associated with the induction of cell death (Mendes *et al.*, 2005). Mitochondrial Ca^{2+} overload provokes opening of the mitochondrial permeability transition pore (mPTP), a high conductance channel at the IMM formed by dimers of the c subunit of complex V (Giorgio *et al.*, 2013). Opening of the mPTP increases the permeability of the IMM to ions and solutes. This results in the loss of membrane potential, osmotic swelling of mitochondria and the rupture of the OMM, leading to the release of pro-apoptotic factors into the cytosol and cell death (Rizzuto *et al.*, 2009). The mechanism by which mitochondrial Ca^{2+} overload provokes opening of the mPTP remains unknown (La Rovere *et al.*, 2016). Nevertheless, many observations support the role of ER-mitochondrial Ca^{2+} flux in the regulation of apoptosis. The antiapoptotic proteins of

the Bcl-2 family are suggested to exert their effect in part by suppressing ER-mitochondrial Ca^{2+} flux, either through depletion of the ER Ca^{2+} store or by inhibition of high-amplitude IP_3R Ca^{2+} transients (Distelhorst and Bootman, 2011). Moreover, factors that promote ER-mitochondrial Ca^{2+} transfer are known to correlate with an increased susceptibility of Ca^{2+}-dependent mPTP activation, including the artificial tightening of the ER-mitochondrial interaction with a synthetic ER-mitochondrial linker or the induction of ER stress through treatment with cellular stressors (Csordas *et al.*, 2006; Chami *et al.*, 2008; Deniaud *et al.*, 2008).

1.8.6 ER stress and the MAM

ER homeostasis is essential for cell function and conditions which compromise ER integrity such as genetic factors, elevated secretary protein synthesis or disturbed Ca^{2+} homeostasis result in ER stress and activation of an adaptive response known as the unfolded protein response (UPR) (Kaufman and Malhotra, 2014). The UPR comprises three overlapping pathways that are initiated by three ER transmembrane receptor proteins: activating transcription factor 6 (ATF6), protein kinase RNA (PKR) like kinase (PERK) and inositol requiring enzyme 1α (α1α). These pathways act in parallel to restore ER homeostasis by increasing ER chaperone synthesis, arresting mRNA translation and degrading accumulated proteins via ER associated protein degradation (ERAD) (Kaufman and Malhotra, 2014). However, if ER stress is prolonged, the UPR induces cell death via both mitochondrial dependent and independent pathways (Bravo-Sagua *et al.*, 2013).

Modulation of the MAM has been linked to the adaptive response to ER stress. At the onset of ER stress contact between the ER and mitochondria increases as a pro-survival response, this redistribution results in increased ER-mitochondrial Ca^{2+} flux and enhanced cellular bioenergetics (Bravo *et al*. 2011). In contrast, in the late stages of ER stress, prolonged ER-mitochondrial contact is associated with increased mitochondrial Ca^{2+} accumulation and apoptosis (Chami *et al.*, 2008).

1.8.7 The MAM and human disease

The MAM is enriched in proteins associated with human disease and MAM dysfunction is currently associated with at least Alzheimer's disease (AD), Parkinson's disease (PD) and ALS (Area-Gomez *et al.*, 2012; De Vos *et al.*, 2012; Guardia-Laguarta *et al.*, 2014).

Evidence suggests that presenilin 1 and presenilin 2 (both mutated in familial AD) and their activities are enriched at the MAM (Area-Gomez *et al.*, 2009). Primary fibroblasts established from both familial and sporadic AD patients showed increased ER-mitochondrial apposition, which correlated with increased MAM function measured by upregulated cholesterol ester and phospholipid synthesis (Area-Gomez *et al.*, 2012). These findings suggest that the altered Ca^{2+} homeostasis and disturbed mitochondrial function observed in previous models of AD are likely related to perturbed ER-mitochondria interactions at the MAM (Area-Gomez and Schon, 2016).

Familial PD is caused by mutations in genes encoding the proteins α-synuclein, Parkin, and protein deglycase DJ-1. Modifying the expression of these proteins has been shown to alter the apposition of the ER and mitochondria (Cali *et al.*, 2013; Ottolini *et al.*, 2013; Guardia-Laguarta *et al.*, 2014). Moreover, ectopic expression of an α-synuclein mutant reduced the overall apposition between the ER and mitochondria, decreased MAM function and caused fragmentation of the mitochondrial network (Guardia-Laguarta *et al.*, 2014).

Numerous genes associated with familial ALS have been found to encode proteins which are enriched at the MAM. The Sigma1R is a chaperone protein localised at the MAM that regulates cellular Ca^{2+} signalling through the IP_3R and has been implicated in a juvenile form of autosomal recessive ALS (Al-Saif *et al.*, 2011). Sigma1R loss of function has been associated with altered ER structure, loss of ER-mitochondrial contacts and disturbed Ca^{2+} homeostasis indicating that MAM dysfunction likely has a role in ALS pathogenesis (Hayashi and Su, 2007; Bernard-Marissal *et al.*, 2015). In addition, a dominant mutation in the gene encoding VAPB has been implicated in ALS; this mutation results in tightening of the VAPB-PTPIP51 MAM protein tether and augmented Ca^{2+} transfer to mitochondria (De Vos *et al.*, 2012). Interestingly, overexpression of the ALS-associated mutant TDP43 has been shown to disrupt the VAPB-PTPIP51 MAM protein tether, thereby decreasing ER-mitochondrial Ca^{2+} flux (Stoica *et al.*, 2014).

Together these findings implicate MAM dysfunction in human disease and emphasize the importance of MAM integrity for cellular function (Paillusson *et al.*, 2016).

1.9 Inherited optic neuropathies

Retinal ganglion cells (RGCs) are specialised neurones located in the inner retina of the eye, whose long axons form the optic nerve and relay visual information gathered by the retina to the visual processing centres in the brain (Yu *et al.*, 2013). Inherited optic neuropathies are a group of disorders characterised by the loss of RGCs, optic nerve atrophy and progressive visual impairment (Yu-Wai-Man *et al.*, 2011a). These disorders collectively affect at least 1 in 10,000 of the population and patients can present with isolated optic atrophy or optic atrophy as part of a complex multi-systemic disorder (Lopez Sanchez *et al.*, 2016).

The most common inherited optic neuropathies are Leber's hereditary optic neuropathy (LHON) and DOA, which share overlapping clinical and pathological features, despite being caused by mutations in different genes. LHON is secondary to point mutations in the mtDNA, whereas, DOA is primarily caused by mutations in the *OPA1* gene (Yu-Wai-Man *et al.*, 2016). The characteristic pathological feature of these two disorders is the preferential loss of RGCs within the papillomacular bundle, a dense collection of small RGCs which subserve central vision, and this pattern of RGC loss results in a visual field defect that extends from the central vision known as a scotoma (Yu-Wai-Man *et al.*, 2016). The loss of RGCs in both LHON and DOA is directly related to mitochondrial dysfunction. For unresolved reasons, RGCs appear to be particularly vulnerable to mitochondrial dysfunction and this disease mechanism underlies RGC loss throughout inherited optic neuropathies. With the exception of *WFS1* and *CISD2*, all the genes associated with inherited optic neuropathies encode proteins that are directly related to mitochondrial function (**Table 1.1**) (Yu-Wai-Man *et al.*, 2016).

Inheritance	Locus	Gene	Phenotype
Dominant	1p36.2	*MFN2*	Hereditary motor and sensory neuropathy type 6
	3q28-q29	*OPA1*	Isolated optic atrophy and syndromic dominant optic atrophy
	4p16.1	*WFS1*	Wolfram syndrome spectrum disorders
	12p11.21	*DRP1*	Optic atrophy and abnormal brain development
	19q13.2-q13.3	*OPA3*	Autosomal dominant optic atrophy and early-onset cataracts
Recessive	3q26.33	*DNAJC19*	DMCA syndrome ± optic atrophy
	4p16.1	*WFS1*	Wolfram syndrome 1
	4q24	*CISD2*	Wolfram syndrome 2
	5q22.1	*SLC25A46*	Optic atrophy ± peripheral neuropathy/cerebellar syndrome
	6q21	*RTN4IP1*	Optic atrophy ± cerebella syndrome/mental retardation/epilepsy
	9q13-q21.1	*FXN*	Friedreich ataxia
	11q14.1-q21	*TMEM126A*	Optic atrophy ± auditory neuropathy
	12q24.31	*C12orf65*	Optic atrophy ± spastic paraplegia/peripheral neuropathy
	16q24.3	*SPG7*	Hereditary spastic paraplegia type 7
	19q13.2-q13.3	*OPA3*	Type III 3-methylglutaconic aciduria
	22q13.2	*ACO2*	Optic atrophy ± cerebellar syndrome/encephalopathy
	Xq22.1	*TIMM8A*	Mohr-Tranebjaerg syndrome ± optic atrophy
Mitochondrial	-	-	Leber's hereditary optic neuropathy and overlapping phenotypes

Table 1.1 Mitochondrial disorders associated with optic atrophy (Reproduced from Yu-Wai-Man *et al.*, 2016).

1.10 Disease mechanisms of inherited optic neuropathies

A number of disease mechanisms have been proposed to explain RGC loss in inherited optic neuropathies including mitochondrial bioenergetic failure, oxidative stress, disturbed Ca^{2+} homeostasis and altered mitochondrial dynamics (Lopez Sanchez *et al.*, 2016). The selective vulnerability of RGCs to mitochondrial dysfunction remains unresolved, although the unique structural properties of RGCs are thought to be relevant (Yu-Wai-Man *et al.*, 2016). The final stage of the neurodegenerative process is suggested to be the inappropriate activation of apoptosis (Maresca *et al.*, 2013).

1.10.1 Anatomy of the optic nerve

RGCs display the typical properties of central nervous system (CNS) neurones, and comprise dendritic and axonal compartments that are connected at the cell body or soma (Lopez Sanchez *et al.*, 2016). The dendrites of RGCs receive visual input from photoreceptor cells (rods and cones) via two different neuronal cells: bipolar and amacrine cells (Yu *et al.*, 2013). The RGC somata are located in the ganglion cell layer of the inner retina and have a non-linear distribution, being particularly concentrated in the central macular region (Carelli *et al.*, 2004). The axons of RGCs are thin (0.5-1 μm) and long (~50 mm); they extend inwards and traverse across the retina towards the optic nerve head, turn, and exit the eye through pores in a collagen structure termed the lamina cribosa. The axons travel via the optic nerve, optic chiasm and optic tract to synapse with the main image forming nuclei including the lateral geniculate nucleus, superior colliculus and pretectal nuclei, which in turn relay information to the higher visual processing centers in the brain (Yu *et al.*, 2013).

1.10.2 Bioenergetic failure

It is well established that RGCs have a high energy demand and rely on mitochondria for ATP production via OXPHOS (Yu *et al.*, 2013). Inherited optic neuropathies are commonly associated with mitochondrial bioenergetic defects, primarily complex I dysfunction, indicating that bioenergetic failure likely contributes to RGC loss (Baracca *et al.*, 2005; Chevrollier *et al.*, 2008; Zanna *et al.*, 2008). However, as other cell types such as photoreceptors or substantia nigra neurones have similar or higher energy demands than RGCs, bioenergetic failure alone cannot explain the vulnerability of RGCs to mitochondrial dysfunction (Yu-Wai-Man *et al.*, 2011a).

1.10.3 Oxidative stress

Another mechanism thought to contribute to RGC loss is oxidative stress, defined as an imbalance between ROS production and the antioxidant system (Hayashi and Cortopassi, 2015). OXPHOS dysfunction is associated with increased ROS production and elevated ROS levels have been described in cell culture, *Drosophila* and mouse models of LHON and DOA (Yarosh *et al.*, 2008; Tang *et al.*, 2009; Lin *et al.*, 2012; Millet *et al.*, 2016). However, the individual contribution of OXPHOS dysfunction or elevated ROS levels to RGC loss remains unclear (Yu-Wai-Man *et al.*, 2016).

1.10.4 Disturbed Ca^{2+} homeostasis

Emerging evidence implicates disturbed cellular Ca^{2+} homeostasis in the pathogenesis of inherited optic neuropathies. Basal mitochondrial Ca^{2+} content was increased in *OPA1* knockdown RGCs, suggesting that mitochondria are dependent on OPA1 for the regulation of Ca^{2+} buffering (Dayanithi *et al.*, 2010). In agreement, *OPA1* knockdown HeLa cells and fibroblasts established from DOA patients harbouring *OPA1* mutations showed enhanced ER-mitochondrial Ca^{2+} flux (Fulop *et al.*, 2011; Fulop *et al.*, 2015). Together these results indicate that OPA1 restrains mitochondrial Ca^{2+} uptake and suggest that *OPA1* loss of function may be associated with mitochondrial Ca^{2+} overload and cell death. However, one study found that *OPA1* knockdown in HeLa cells reduced ER-mitochondrial Ca^{2+} flux, and this was associated with decreased cytosolic Ca^{2+} buffering and an increased sensitivity to glutamate-mediated excitotoxicity in *OPA1* knockdown RGCs (Kushnareva *et al.*, 2013). The relationship between LHON mutations and cellular Ca^{2+} homeostasis is unclear. No defect in agonist or perfusion induced mitochondrial Ca^{2+} uptake was found in an osteosarcoma-derived cybrid model harbouring all three common LHON mutations (Cruz-Bermudez *et al.*, 2016). In contrast, mitochondrial Ca^{2+} buffering was disturbed in a teratoma-derived cybrid harbouring the m.11778G>A LHON mutation (Haroon *et al.*, 2007). Despite differences, the overall picture suggests that dysregulation of cellular Ca^{2+} homeostasis contributes to RGC loss in optic neuropathies and further investigations are required to clarify the mechanisms.

1.10.5 Mitochondrial dynamics

An important mechanism explaining RGC loss in inherited optic neuropathies is disturbed mitochondrial dynamics. The RGC soma is the biogenesis site of all the cells organelles, including mitochondria (Lopez Sanchez *et al.*, 2016). Dynamic mitochondrial processes including fusion, fission and transport are therefore essential for the transport and maintenance of mitochondria throughout RGCs (Mishra and Chan, 2016). Alterations of mitochondrial network morphology have been reported in numerous models of DOA. Fibroblasts established from DOA patients showed normal or highly fragmented mitochondrial networks, dependent upon the *OPA1* mutation (Chevrollier *et al.*, 2008; Zanna *et al.*, 2008). Moreover, mitochondrial structural alterations have been observed in myotubes and skeletal muscle from DOA patients and in mouse models of DOA (Alavi *et al.*, 2007; Davies *et al.*, 2007; Amati-Bonneau *et al.*, 2008; Spinazzi *et al.*, 2008). Importantly, it has been shown that alterations of mitochondrial network morphology induced by *OPA1* deficiency in turn disturb mitochondrial transport in neuronal axons (Bertholet *et al.*, 2013).

The importance of mitochondrial dynamics in RGCs is related to their specific structural and functional properties (Lopez Sanchez *et al.*, 2016). RGC axons only become myelinated beyond the lamina cribosa. The generation and propagation of action potentials in the prelaminar unmyelinated region of the RGC axon therefore requires a high energetic input (Carelli *et al.*, 2004). Correspondingly, mitochondria show an uneven but specific distribution along the RGC axon and are concentrated in the prelaminar region in order to meet cellular energy demands (**Figure 1.10**) (Andrews *et al.*, 1999a; Bristow *et al.*, 2002). Consequently, the transport and distribution of mitochondria along RGC axons is critical for normal function (Yu *et al.*, 2013), and disturbance of this process due to disturbed ATP production, cellular Ca^{2+} homeostasis or mitochondrial morphology could explain the loss of RGCs in inherited optic neuropathies (Yu-Wai-Man *et al.*, 2011a).

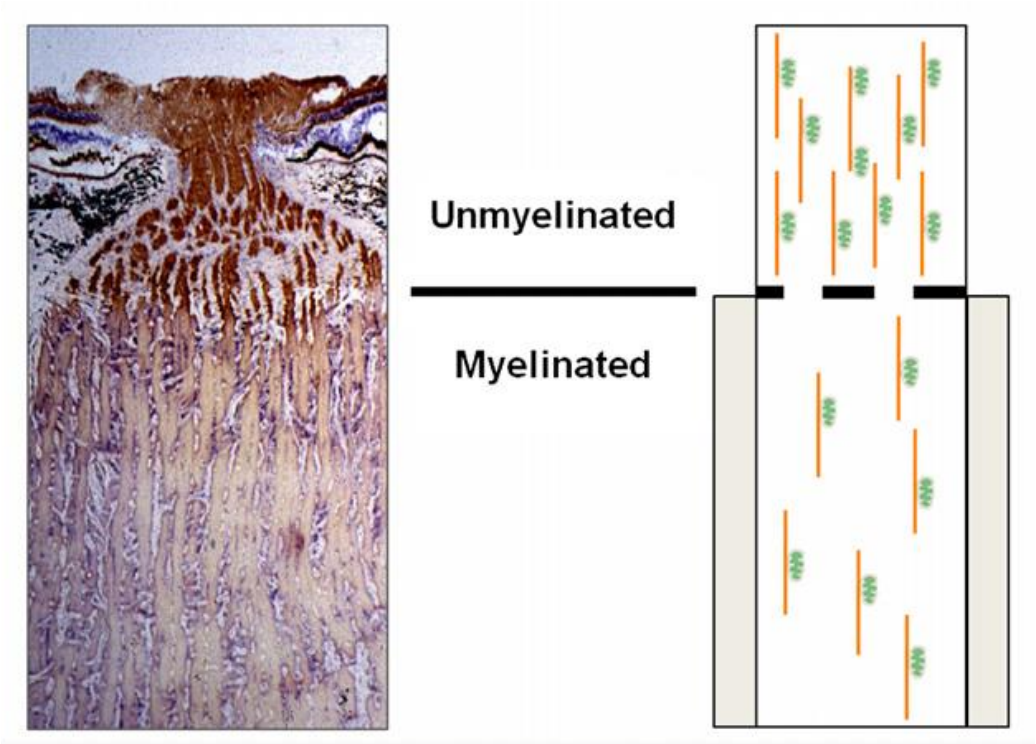

Figure 1.10 The distribution of mitochondria in the optic nerve.
Mitochondria are concentrated in prelaminar unmyelinated region due to higher energy demands for signal conduction. The left panel shows a section of human optic nerve stained for COX/SDH; the darker COX staining in the prelaminar unmyelinated region is consistent with a higher density of mitochondria. The right panel is a schematic illustrating microtubule dependent mitochondrial transport and distribution (Reproduced from Yu-Wai-Man *et al.*, 2011a).

1.11 Wolfram syndrome

Wolfram syndrome is a multisystemic neurodegenerative disease characterised by the association of juvenile-onset diabetes mellitus and optic nerve atrophy, typically with a range of additional clinical features (Moosajee *et al.*, 2016). The disorder was first reported in 1938 by Wolfram and Wagener, who described eight siblings, four of whom had juvenile-onset diabetes and optic atrophy (Wolfram and Wagener, 1938). Wolfram syndrome is considered a rare disease and has an estimated prevalence of 1 in 770,000 in the UK, with a carrier prevalence of 1 in 354 (Barrett *et al.*, 1995a). Other prevalence estimates include 1 in 100,000 in a North American population and 1 in 710,000 in the Japanese population (Fraser and Gunn, 1977; Matsunaga *et al.*, 2014). The prognosis is poor and most patients die prematurely, usually due to respiratory failure and the median age of death is 27±11.4 years (de Heredia *et al.*, 2013). There are currently no treatments to halt or reverse the progression of Wolfram syndrome and care is purely supportive (Urano, 2016). Wolfram syndrome presents as two known clinical subtypes caused by mutations in two unrelated genes: Wolfram syndrome 1 (WFS1) and Wolfram syndrome 2 (WFS2) (Moosajee *et al.*, 2016).

1.12 Wolfram syndrome 1

WFS1 is characterised by diabetes insipidus, diabetes mellitus, optic atrophy and deafness (DIDMOAD). More than half of WFS1 patients will show the full 'DIDMOAD' phenotype and patients may also present with additional clinical features (**Table 1.2**) (de Heredia *et al.*, 2013; Urano, 2016). WFS1 is primarily caused by recessive mutations in the *WFS1* gene located on chromosome 4p16.1 (Inoue *et al.*, 1998; Strom *et al.*, 1998). Numerous mutations distributed throughout the entire *WFS1* gene have been reported including point mutations (missense, nonsense, splice site), deletions, insertions and duplications (de Heredia *et al.*, 2013). Recessive *WFS1* mutations are predominantly deleterious for protein expression (Hofmann *et al.*, 2003; Hofmann and Bauer, 2006). In addition, dominant *WFS1* mutations are increasingly being recognised and cause a Wolfram-like syndrome characterised by optic atrophy and sensorineural hearing loss (SNHL). The pathogenic mechanisms of dominant *WFS1* mutations remain unknown, although a dominant negative effect has been proposed (Hogewind *et al.*, 2010; Rendtorff *et al.*, 2011).

Major symptoms	Common symptoms
Diabetes mellitus Optic nerve atrophy Diabetes insipidus Deafness Ataxia Urinary Tract Problems • Neurogenic bladder • Bladder Incontinence • Urinary tract infections	General • Fatigue • Hypersomnolence Neurological • Apnea • Dysphagia • Headaches Psychiatric • Anxiety • Panic attacks • Depression • Mood swings Endocrine • Hypogonadism • Hyponatremia

Table 1.2 Common clinical manifestations of Wolfram syndrome (Reproduced from Urano, 2016)**.**

1.12.1 Functions of the Wolframin protein

The *WFS1* gene encodes an 890 amino acid transmembrane protein localised to the ER called Wolframin (Strom *et al.*, 1998; Takeda *et al.*, 2001). No significant homologies have been identified indicating that Wolframin is a member of a novel protein family (Takeda *et al.*, 2001). The protein has nine predicted transmembrane domains and long hydrophilic stretches on the N- and the C-terminals, with the C-terminal extending into the ER lumen and the N-terminal extending into the cytoplasm (Hofmann *et al.*, 2003; Yamaguchi *et al.*, 2004). Wolframin assembles into higher weight molecular complexes (~400 kDa) that are likely homo-oligomers of Wolframin monomers (100 kDa), although the contribution of other proteins to these complexes has not been excluded (Hofmann *et al.*, 2003). The only post-translational modification of Wolframin appears to be asparagine (N)-linked glycosylation, which is essential for protein stability. The protein harbours 5 consensus sites for N glycosylation (NXS/T) at N28, N335, N500, N661 and N746, however only the N661

and N746 sites are located within luminal domains (Hofmann *et al.*, 2003). Wolframin is ubiquitously expressed in all tissue types though at different levels; it is highly expressed in the brain, pancreas, heart, muscle, lung and placenta (Inoue *et al.*, 1998; Hofmann *et al.*, 2003). Wolframin is expressed in human RGCs and the protein is predominantly localised in the soma and the initial portion of the axon (Schmidt-Kastner *et al.*, 2009). The function of Wolframin is not fully characterised, studies have shown that the protein participates in the maintenance of ER homeostasis including a role in protein folding/maturation, in the response to ER stress termed the UPR and in the regulation of cellular Ca^{2+} homeostasis (Ishihara *et al.*, 2004; Fonseca *et al.*, 2005; Gharanei *et al.*, 2013; Cagalinec *et al.*, 2016).

The loss of *WFS1* function in pancreatic β-cells is associated with increased ER stress, activation of all three UPR pathways and an enhanced susceptibility to ER stress induced apoptosis, indicating that Wolframin is required for the maintenance of ER homeostasis in these cells (Ishihara *et al.*, 2004; Fonseca *et al.*, 2005; Yamada *et al.*, 2006). ER stress has further been observed in *WFS1* depleted human neuroblastoma SK-N-AS cells, *Wfs1* deficient mouse retinas and *WFS1* deficient neurones (Gharanei *et al.*, 2013; Bonnet Wersinger *et al.*, 2014; Cagalinec *et al.*, 2016). Wolframin is functionally linked to the ER stress response and increased expression of *WFS1* mRNA and the Wolframin protein was found in response to the artificial induction of ER stress (Yamaguchi *et al.*, 2004). Wolframin appears to be under the regulation of the IRE1α, PERK and ATF6β signalling pathways of the UPR (Fonseca *et al.*, 2005; Odisho *et al.*, 2015). A well conserved ER stress response element (ERSE)-like sequence in the *WFS1* promoter region is suggested to be critical for X-box binding protein 1 (XBP1) dependent upregulation of the *WFS1* gene. Notably, *WFS1* was the most upregulated gene following transfection of a XBP1 expressing vector in SH-SY5Y cells (Kakiuchi *et al.*, 2006).

Wolframin in turn is directly involved in the regulation of the UPR and negatively regulates the transcription factor ATF6α by promoting ubiquitination through the E3 ubiquitin protein ligase HRD1, which leads to proteasomal degradation. Under ER stress conditions, ATF6α is released from Wolframin regulation in order to activate its branch of the UPR. Loss of *WFS1* function is linked with dysregulation of ATF6α turnover and hyperactivation of its downstream target genes (Fonseca *et al.*, 2010). Two genes specifically induced by ATF6β are *WFS1*

and *HRD1*, suggesting that a Wolframin-dependent feedback mechanism exists to control ATF6α expression during prolonged ER stress (Odisho *et al.*, 2015). However, it is likely that ER stress and activation of the UPR secondary to *WFS1* loss of function are primarily due to the requirement of Wolframin for maintenance of ER homeostasis, upstream of the UPR signalling pathways, rather than dysregulation of any single UPR pathway (Fonseca *et al.*, 2010). The exact requirement of Wolframin for ER homeostasis is unclear; Wolframin has been shown to interact with the sodium (Na^+)-potassium (K^+) ATPase β1 subunit supporting a role in protein maturation and several lines of evidence indicate Wolframin is essential for ER Ca^{2+} homeostasis (Osman *et al.*, 2003; Zatyka *et al.*, 2008).

Reconstitution of Wolframin into lipid bilayers induced a cation-selective ion channel; however, it was not shown directly that Wolframin-dependent channels conducted Ca^{2+}. Wolframin may therefore be a novel ER Ca^{2+} channel or function to regulate an existing ER channel involved in Ca^{2+} homeostasis (Osman *et al.*, 2003). In agreement with a regulatory role, Wolframin has been shown to negatively regulate the expression of the SERCA, likely via proteasome-mediated degradation. SERCA is released from Wolframin regulation upon the onset of ER stress resulting in increased SERCA expression, a mechanism which is suggested to ensure ER Ca^{2+} homeostasis is maintained or restored (Zatyka *et al.*, 2015). Wolframin has also been shown to interact with calmodulin (CaM), a protein which binds Ca^{2+} and coordinates a variety of downstream processes. CaM binds Wolframin at the cytoplasmic N-terminal domain in a Ca^{2+}-dependent manner, indicating that CaM could regulate Wolframin function through a novel Ca^{2+} signalling pathway (Yurimoto *et al.*, 2009). This pathway is likely important for regulating the role of Wolframin in ER Ca^{2+} homeostasis as Wolframin lacks Ca^{2+} or ATP binding domains (Osman *et al.*, 2003; Yurimoto *et al.*, 2009). At the ER, Wolframin appears to be involved in the positive regulation of the ER Ca^{2+} store; ER [Ca^{2+}] was found to be decreased in *WFS1* knockdown human embryonic kidney 293 (HEK293) cells compared to controls (Takei *et al.*, 2006). Knockdown of *WFS1* in a pancreatic β-cell line and ectopic expression of a dominant Wolframin mutant in HEK293 cells have also been shown to cause depletion of ER Ca^{2+} levels (Hara *et al.*, 2014). In contrast, no defect in ER Ca^{2+} homeostasis, including basal levels and maximal ER Ca^{2+} uptake capacity, was observed in *WFS1* deficient neurones (Cagalinec *et al.*, 2016). The link

between Wolframin and ER Ca^{2+} channels remains unresolved. The IP_3R was shown to be dysfunctional in *WFS1* deficient neurones, however, whether this was related to ER stress or through disturbed Wolframin-mediated IP_3R regulation is unknown (Cagalinec *et al.*, 2016).

1.13 Wolfram syndrome 2

WFS2 was first described in 3 consanguineous Jordanian families with 14 Wolfram syndrome patients. Affected individuals presented with diabetes mellitus, optic atrophy and high frequency SNHL, as well as features not previously described in WFS1 including peptic ulcer disease and bleeding tendencies secondary to defective platelet aggregation (El-Shanti *et al.*, 2000). WFS2 is caused by autosomal recessive mutations in the *CISD2* gene (CDGSH Iron Sulfur Domain 2, synonyms: *MINER1*, *ZCD2*, *ERIS*, *NAF1*) located on chromosome 4q24 (Amr *et al.*, 2007). To date, five families have been described and reported mutations include a homozygous missense mutation (c.109 G>C, p. Glu37Gln) in Jordanian families, an intragenic exon 2 homozygous deletion in a European Caucasian female and a probable homozygous mutation (c.103+1 G>A) within a donor splice site in two sisters from an Italian family (Amr *et al.*, 2007; Mozzillo *et al.*, 2014; Rondinelli *et al.*, 2015). The missense mutation, c.109 G>C, was found to disrupt mRNA splicing and eliminate the second exon, this results in a frameshift leading to a premature stop codon, which truncates 75% of the protein (Amr *et al.*, 2007). The clinical features of the reported WFS2 patients are broadly similar and there is considerable overlap with the clinical features of WFS1 (**Table 1.3**); the presence of peptic ulcers and bleeding tendencies without diabetes insipidus can be considered diagnostic criteria for WFS2 (Mozzillo *et al.*, 2014).

	WFS1	***WFS2*** (El-Shanti *et al*., 2000)	***WFS2*** (Mozzilla *et al*., 2014)	***WFS2*** (Rondinelli et al., 2015)
Diabetes mellitus	Yes	Yes	Yes	Yes
Diabetes Insipidus	Yes	No	No	Suspected
Optic Atrophy	Yes	Yes	Yes	Yes
Hearing loss	Yes	Yes	Yes	Yes
Peptic Ulcer	No	Yes	Yes	Yes
Platelet aggregation defects	No	Yes	Yes	N/A
Bladder dysfunction	Yes	Yes	Yes	Yes
Psychiatric problems	Yes	Yes	No	Yes

Table 1.3 Comparison of the phenotypes of WFS1 and WFS2

1.13.1 Function of the CISD2 protein

The *CISD2* gene implicated in WFS2 encodes a 135 amino acid protein called CDGSH iron-sulfur domain containing protein 2 (CISD2). CISD2 is a member of a small family of three proteins that are defined by a unique CDGSH domain with the consensus sequence C-X-C-X_2-(S/T)-X_2-P-X-**C**-**D**-**G**-(**S**/A/T)-**H** (Wiley *et al.*, 2007a). The CDGSH domain binds a redox-active [2Fe-2S] cluster coordinated by a rare Cys_3-His arrangement (Wiley *et al.*, 2007b). CISD2 contains a single CDGSH domain, an N-terminal transmembrane domain and an atypical ER localisation sequence (Conlan *et al.*, 2009). Numerous studies have confirmed that CISD2 localises to the ER and that the protein is also enriched at the MAM (Amr *et al.*, 2007; Wiley *et al.*, 2007a; Wiley *et al.*, 2013; Wang *et al.*, 2014). One study in mouse has suggested that CISD2 is located at the OMM (Chen *et al.*, 2009). Nevertheless, CISD2 is most likely an integral ER transmembrane protein and the CDGSH domain is oriented towards the cytosol (Wiley *et al.*, 2013). Crystallographic studies of the soluble CISD2 form revealed that it exists as a homodimer, harbouring two labile and redox-active [2Fe-2S] clusters, one on each protomer (Conlan *et al.*, 2009).

One likely role for CISD2 is [2Fe-2S] cluster assembly and/or transfer. The rare Cys_3-His [2Fe-2S] cluster coordination of the CDGSH domain has been found in other [Fe-S] cluster transfer proteins and it has been demonstrated that CISD2 can donate an [2Fe-2S] cluster to apo-ferredoxin, the standard protein used for Fe-S cluster transfer experiments (Qi and Cowan, 2011; Zuris *et al.*, 2011). The significance of CISD2 [2Fe-2S] cluster transfer *in vivo* is not entirely clear and the physical recipients of [2Fe-2S] clusters are not well characterised. CISD2 could participate in both Fe/S cluster protein repair and in the biogenesis of cytosolic and nuclear Fe/S cluster proteins (Tamir *et al.*, 2013; Lipper *et al.*, 2015). It is possible that CISD2 acts as [2Fe-2S] cluster reservoir, providing [2Fe-2S] clusters when in an oxidised state, for example when the cell is stressed (Tamir *et al.*, 2013). CISD2 may also be involved in the biogenesis of cytosolic and nuclear Fe/S proteins and link the mitochondrial iron-sulfur cluster (ISC) assembly machinery with the cytosolic Fe/S protein assembly (CIA) apparatus (Lipper *et al.*, 2015).

In addition to its function as a Fe/S cluster protein, CISD2 is also implicated in the regulation of macroautophagy (hereafter referred to as ‘autophagy’), and cellular Ca^{2+} homeostasis via protein-protein interactions with Bcl-2 and the IP_3R (Chang *et*

al., 2010). Autophagy is an essential cellular process responsible for the turnover of cellular macromolecules and dysfunctional organelles. Basal levels of autophagy maintain cellular homeostasis, whereas, upregulated autophagy in response to various physiological stresses serves as a cell survival mechanism (Decuypere *et al.*, 2012). CISD2 was shown to be required for the negative regulation of autophagy by Bcl-2 in response to nutrient depletion in H1299 epithelial cells by contributing to the interaction of Bcl-2 with Beclin 1, a key member of an autophagy initiating complex (Chang *et al.*, 2010).

The generation and characterisation of two *Cisd2* deficient mouse models (hereafter referred to as 'ageing *Cisd*2-/- mice' and 'skeletal *Cisd*2-/- mice') also support a role for Cisd2 in autophagy regulation (Chen *et al.*, 2009; Chang *et al.*, 2012). Ageing *Cisd*2-/- mice are characterised by a premature ageing phenotype, with neuronal and muscle degeneration and clinical manifestations of WFS2 including optic nerve degeneration and impaired glucose tolerance. This phenotype was associated with mitochondrial abnormalities and increased autophagy was detected in cardiac and skeletal muscle (Chen *et al.*, 2009). Skeletal *Cisd2* -/- mice are characterised by the early degeneration of skeletal muscle. Autophagy markers were increased in skeletal, diaphragm and tibialis anterior muscle of skeletal *Cisd2* -/- mice. Moreover, increased autophagic flux was found in primary myoblasts isolated from the diaphragm of the skeletal *Cisd* -/- mice. In contrast to the ageing *Cisd2* -/- mouse model there was no evidence of mitochondrial dysfunction, rather mitochondria appeared enlarged and elongated with dense cristae in the skeletal *Cisd* -/- mice, which is likely an adaptive response to stress (Chang *et al.*, 2012). Despite differences in phenotype both *Cisd*-/- mouse models suggest that Cisd2 has a role in autophagy regulation. Interestingly, there was no evidence of apoptosis in either mouse model suggesting that neuronal and muscle degeneration secondary to *Cisd2* loss of function could be linked to autophagic cell death (Chen *et al.*, 2009; Chang *et al.*, 2012).

Finally, CISD2 has been shown to interact with the IP_3R, suggesting that CISD2 is involved in the regulation of Ca^{2+} homeostasis. The function of this interaction is thought to be coupled to Bcl-2 and CISD2 was shown to be required for Bcl-2 mediated depression of ER Ca^{2+} stores upon overexpression of ER targeted Bcl-2 (Chang *et al.*, 2010). However, the regulation of ER Ca^{2+} homeostasis by Bcl-2

is complex and conflicting evidence exists. It is suggested that ER localised Bcl-2 acts to decrease ER [Ca^{2+}]. Although, other studies have suggested that Bcl-2 does not decrease ER Ca^{2+} levels, instead it is proposed that Bcl-2 regulates IP_3R mediate Ca^{2+} flux by inhibiting high amplitude Ca^{2+} transients that lead to cell death and stimulating low amplitude Ca^{2+} transients that promote cell survival (Distelhorst and Bootman, 2011). The role of CISD2 in cellular Ca^{2+} homeostasis remains unclear; it is uncertain if CISD2 modulates IP_3R activity and/or ER [Ca^{2+}] under basal conditions, whether CISD2 has functions relating to Ca^{2+} homeostasis that are independent of Bcl-2 and there are differing reports on how *CISD2* deficiency disturbs ER Ca^{2+} homeostasis (Chang *et al.*, 2010; Chang *et al.*, 2012; Wiley *et al.*, 2013; Wang *et al.*, 2014). Direct measurement of ER [Ca^{2+}] levels with ER targeted aequorin (ER-Aeq) in two different *CISD2*-deficient cell lines (H1299 epithelial cells and MEFS) suggests that ER [Ca^{2+}] is not disturbed under basal conditions (Chang *et al.*, 2012; Wang *et al.*, 2014). However, analysis of cytosolic Ca^{2+} following modulation of ER Ca^{2+} stores with thapsigargin in a lymphoblastoid cell line established from a WFS2 patient, with the homozygous missense mutation c.109 G>C, suggested ER [Ca^{2+}] was increased secondary to *CISD2* mutations (Amr *et al.*, 2007).

1.14 Mitochondrial dysfunction and the pathophysiology of Wolfram syndrome

Wolfram syndrome was initially suspected to be a mitochondrial disease because the multisystemic clinical features were similar to the phenotypes associated with classical mitochondrial disease and the organs affected had a high metabolic demand (Bu and Rotter, 1993). However, this hypothesis was challenged by the identification of the *WFS1* and *CISD2* genes and the subsequent localisation of the respective proteins to the ER (Inoue *et al.*, 1998; Strom *et al.*, 1998; Amr *et al.*, 2007; Wiley *et al.*, 2013). Furthermore, no evidence for marked respiratory chain dysfunction was found in Wolfram syndrome patient muscle biopsies and numerous studies have demonstrated that *WFS1* or *CIDS2* deficiency perturbs ER homeostasis, indicating that Wolfram syndrome is an ER-related disease (Jackson *et al.*, 1994; Barrett *et al.*, 1995b; Barrett *et al.*, 2000; Fonseca *et al.*, 2005; Wiley *et al.*, 2013; Bonnet Wersinger *et al.*, 2014). ER dysfunction is a distinct disease mechanism underlying RGC loss, which is otherwise predominantly associated with mitochondrial dysfunction (Maresca *et al.*, 2013). However, recent studies have

provided evidence that mitochondrial dysfunction likely participates in the pathophysiology of Wolfram syndrome, raising the possibility that Wolfram syndrome is a disease caused by primary ER dysfunction and secondary mitochondrial impairment (Ross-Cisneros *et al.*, 2013; Cagalinec *et al.*, 2016).

The phenotype caused by dominant *WFS1* mutations is intriguingly similar to the phenotype described in patients with specific pathogenic *OPA1* mutations who presented with optic atrophy and deafness (Amati-Bonneau *et al.*, 2005; Hogewind *et al.*, 2010). These *OPA1* mutations were associated with mitochondrial network fragmentation, loss of mitochondrial membrane potential and impaired ATP synthesis in patient derived fibroblasts (Amati-Bonneau *et al.*, 2005). The association of optic atrophy and deafness without other clinical features is rare and appears to only be attributable to mutations in the *OPA1* and *WFS1* genes (Amati-Bonneau *et al.*, 2005; Rendtorff *et al.*, 2011). In addition, the pattern of optic nerve degeneration observed in WFS1 primarily involving the papillomacular bundle, is similar to the pattern of RGC loss in LHON and other mitochondrial optic neuropathies (Ross-Cisneros *et al.*, 2013). Furthermore, the localisation of Wolframin in RGCs, with high expression in the prelaminar region of the optic nerve corresponds with the distribution of mitochondria in RGCs (Schmidt-Kastner *et al.*, 2009; Ross-Cisneros *et al.*, 2013). Together, these observations suggest that mitochondrial dysfunction, which is a common theme underlying RGC loss in inherited optic neuropathies, extends to Wolfram syndrome.

Mitochondrial dysfunction has been found in models of *WFS1* and *CISD2* deficiency. A recent study has demonstrated that dynamic mitochondrial processes including fusion, fission, transport and turnover were disturbedl in *WFS1* deficient neurones (Cagalinec *et al.*, 2016). In these neurones there was a decreased rate of the fusion and fission, which was associated with decreased average mitochondrial length indicative of mitochondrial network fragmentation. Further observations included decreased mitochondrial axonal and decreased mitochondrial density in the axons of the *WFS1* deficient neurones. These mitochondrial dynamic defects were accompanied by decreased mitochondrial membrane potential and reduced ATP levels. Importantly, the mitochondrial dysfunction in *WFS1* deficient neurones was shown to be secondary to disturbed ER homeostasis, IP_3R dysregulation and increased cytosolic [Ca^{2+}] (Cagalinec *et al.*, 2016). In ageing *Cisd*2-/- mice,

mitochondrial degeneration, characterised by breakdown of the OMM and disturbance of the cristae, was observed by TEM in numerous tissues. Furthermore, mitochondria isolated from skeletal muscle of the ageing *Cisd*2-/- mice, displayed decreased oxygen consumption (substrates: glutamate, malate and ADP) and decreased electron transport activity between complexes (Chen *et al.*, 2009).

Overall, these observations indicate that *WFS1* or *CISD2* deficiency can disturb mitochondrial function and support the view that mitochondrial dysfunction is involved in the pathophysiology of Wolfram syndrome.

Chapter 2. Aims

This project was undertaken to further explore the genetic and molecular basis of inherited optic neuropathies, in particular the disease mechanisms associated with Wolfram syndrome. The specific aims were:

1. To screen a well-characterised cohort of patients with suspected inherited optic atrophy, who do not harbour pathogenic mutations in the *OPA1* or *OPA3* genes, for possible pathogenic mutations in the *WFS1*, *RTN4IP1* and *C12orf65* genes.
2. To study and compare the pathological consequences of dominant and recessive *WFS1* mutations in patient-derived mutant primary fibroblast cell lines.
3. To investigate the disease mechanisms associated with a novel homozygous *CISD2* mutation in a patient with Wolfram syndrome 2.
4. To optimise an *in vivo* technique for visualising and quantifying mitochondrial axonal transport in a zebrafish model.

Chapter 3. Materials and Methods

3.1 Polymerase chain reaction

Polymerase chain reactions (PCRs) were carried out on a 96 well Veriti Thermal Cycler (ThermoFisher, Loughborough, UK). DNA samples were amplified in a 25 µl reaction mix: 2.5 µl ImmoBuffer (10x; Bioline, London, UK), 2.5 µl dNTP mix (2 mM each dNTP) (Bioline), 0.2 µl Immolase DNA polymerase (Bioline), 0.63 µl forward primer (10 µM), 0.63 µl reverse primer (10 µM), 2 µl $MgCl_2$ (50 mM; Bioline), 15.54 µl dH_2O and 1 µl sample DNA. The reaction conditions were: initial activation at 95 °C for 7 minutes, followed by 30 cycles of denaturation at 95 °C for 1 minute, annealing at 65 °C and extension at 72 °C for 1 minutes, then a final extension step at 72 °C for 10 minutes. Six annealing temperatures ranging from 55 °C to 65 °C at 2 °C intervals were tested for each primer set to determine the optimal conditions. Betaine (Sigma-Aldrich, Dorset, UK) was used to enhance PCR for primer sets that had poor specificity or yield under standard conditions.

3.2 Agarose gel electrophoresis

Agarose (1 g) was dissolved in TAE buffer (100 ml; TAE, Tris-acetate-EDTA) by heating in a microwave for two minutes. After cooling, 40 µl ethidium bromide (1 mg/ml; Sigma-Aldrich) was added and the solution was poured into a casting tray, a gel comb was inserted and the gel was allowed to set. Gel electrophoresis was carried out in a horizontal gel unit (Scie-Plas, Cambridge, UK) in TAE buffer and run at 65 V for 45 minutes. Gels were imaged using a GelDoc-It imaging system (UVP, California, USA). For PCR analysis by agarose gel electrophoresis, 6 µl of PCR product was mixed with 6 µl of Orange G loading buffer (0.1% w/v Orange G powder; Sigma-Aldrich) and 10 µl was loaded onto the gel. 5 µl of Hyperladder IV (100bp to 1013bp, Bioline) was used as a molecular weight marker.

3.3 Sequencing

3.3.1 Exo I/Fast AP DNA purification

Prior to sequencing, PCR products were purified with an Exo I/FastAP mixture (ThermoFisher) consisting of 0.5 µl Exo I and 1 µl FastAP added to 3 to 5 µl of PCR product on ice. The mixture was incubated for 15 minutes at 37 °C followed by 15 minutes at 85 °C in a Veriti Thermal Cycler.

3.3.2 BigDye terminator cycle sequencing

Following Exo I/FastAP purification, terminator cycle sequencing was performed using the BigDye Terminator v3.1 Cycle Sequencing Kit (ThermoFisher). The reaction mix consists of 1 µl Big Dye, 2 µl BigDye Terminator Sequencing Buffer, 1 µl forward or reverse primer (10 µM) and 11 µl dH_2O. The reaction mix was added to 3-5 µl purified PCR product. The sequencing reaction conditions were: initial denaturation at 96 °C for 1 minute, followed by 25 cycles of 96 °C for 10 seconds, 50 °C for 5 seconds and 60 °C for 4 minutes.

3.3.3 Ethanol Precipitation

The terminator cycle sequencing product was purified by ethanol precipitation to remove excess salt and unincorporated dye terminators. 2 µl sodium acetate (3 M, Sigma-Aldrich), 2 µl EDTA (125 nM; Sigma-Aldrich) and 70 µl 100 % ethanol was added to product. The solution was mixed, incubated at room temperature for 15 minutes and then centrifuged at 2000 x g for 30 minutes. Following centrifugation the supernatant was removed, 70 µl of 70 % ethanol was added and the sample was centrifuged at 1650 x g for a further 12 minutes. The supernatant was removed and the precipitated product was allowed to air dry in the dark.

3.3.4 Sequencing

The precipitated product was resuspended in 10 µl Hi-Dye (ThermoFisher) and denatured at 95 °C for 2 minutes. Sequencing was performed by capillary electrophoresis on a 3130 Genetic Analyser (ThermoFisher). Gene sequences were analysed using SeqScape Software V2.6 (ThermoFisher) by alignment with the corresponding GenBank gene reference sequence.

3.4 Fibroblast Cell Culture

3.4.1 Fibroblast cell maintenance

Human skin fibroblasts were cultured in low glucose minimum essential media (MEM; ThermoFisher) supplement with fetal bovine serum (FBS, 10 % v/v; Sigma-Aldrich), 50 units/ml penicillin (ThermoFisher), 50 µg/ml streptomycin (ThermoFisher), MEM vitamin solution (1 % v/v; ThermoFisher), non-essential amino acids (1 % v/v; ThermoFisher), sodium pyruvate (1 mM; ThermoFisher) and L-glutamine (2 mM; ThermoFisher). Fibroblasts were grown in standard cell culture flasks (VWR, Lutterworth, UK) at 37 °C in a humidified cell culture incubator (Heracell 150i, ThermoFisher) containing 5 % CO_2. Fibroblasts were monitored with an inverted microscope. Media was changed as required, ~3-4 days.

3.4.2 Subculture of fibroblasts

Once fibroblasts reached 90% confluency, they were passaged. To subculture fibroblasts, the media was aspirated and the cells were washed once with phosphate buffered saline (PBS; ThermoFisher) and treated with Trypsin-EDTA (ThermoFisher) for 5 minutes at 37 °C in a humidified cell culture incubator to detach the cells from the flask. Fresh media was added and the cells were pelleted at 1300 x g for 5 minutes in a bench centrifuge (Heraeus Megafuge 16; ThermoFisher). Following centrifugation, the supernatant was aspirated and the cell pellet was resuspended in fresh media. The cell suspension was split 1 in 3 into fresh cell culture flasks. All experiments were performed on fibroblasts with similar passage numbers, ranging from 4 to 12.

3.4.3 Cell counting and seeding

Cell counting was performed using a haemocytometer (AC1000 Improved Neubauer; Hawksley, Lancing, UK). Cells were harvested as described in Section 3.4.2. Following cell resuspension, 10 µl of the cell suspension was mixed with 10 µl of Trypan blue (Sigma-Aldrich), a vital stain used to assess cell viability. Then 10 µl of the stained cell suspension was applied to the haemocytometer chamber and covered with a glass coverslip. Using an inverted microscope, the viable cells (unstained) in the four large corner squares of the haemocytometer chamber were counted. The average cell count from the four squares was multiplied by two to

correct for the Trypan blue dilution, and then multiplied by 10^4 to obtain the number of cells per ml.

3.4.4 Cryopreservation

For long-term storage, cells were frozen and stored in liquid nitrogen. Cells were harvested as described in Section 3.4.2. The pelleted cells were resuspended in freezing medium: FBS and 5% (v/v) dimethyl sulfoxide (DMSO; Sigma-Aldrich), filtered sterilized through a 0.22 µm PES filter (PALL, Portsmouth, UK). The cell suspension was transferred to a cryovial. The cryovial was placed in a Mr Frosty (Nalgene, Matlock, UK) filled with isopropanol (Sigma-Aldrich), which ensures a gradual freezing process, and the Mr Frosty was placed at -80 °C. After 24 hours, the cryovial was removed and transferred to liquid nitrogen.

To recover cells from liquid nitrogen, cells were rapidly thawed and transferred to a 15 ml conical centrifuge tube containing 5 ml media. The cells were pelleted at 1300 x g for 5 minutes in a bench centrifuge. The supernatant was aspirated and the cell pellet was resuspended in fresh media. The cell suspension was transferred to a standard cell culture flask and maintained as described in Section 3.4.1.

3.5 Protein extraction from fibroblasts

Cells were harvested as described in Section 3.4.2. On ice, the cell pellet was washed twice with PBS and resuspended in 50 µl lysis buffer (50 mM Tris-HCl pH 7.5, 130 mM NaCl, 2 mM $MgCl_2$, 0.1% Triton X and a protease inhibitor cocktail tablet EDTA-free (Roche, West Sussex, UK)). The cell suspension was vortexed for 30 seconds every 5 minutes for 15 minutes. Following lysis, the cell suspension was centrifuged at 2600 x g for 2 minutes at 4 °C. The supernatant was collected and the cell debris was discarded.

3.6 Bradford assay

The Bradford assay was used to determine the total protein concentration of cell lysates (Bradford, 1976). Bovine serum album (BSA; Sigma-Aldrich) was used to create a standard curve of known protein concentrations: 0, 0.05, 0.1, 0.2, 0.3, 0.4 and 0.5 mg/ml. On a 96 well microplate (ThermoFisher), 10 µl of each standard and each sample was measured in triplicate; 190 µl of diluted Bradford reagent (Bio-Rad Laboratories, Hertfordshire, UK) was added to each well and absorbance was

measured at 595 nm on a Multiskan ascent (ThermoFisher). Sample protein concentrations were calculated based on the standard curve.

3.7 Western blotting

3.7.1 Lithium dodecyl sulfate-polyacrylamide gel electrophoresis (LDS-PAGE)

Cell lysates containing 40 µg of protein (prepared in NuPage LDS Sample Buffer and NuPage Sample Reducing Agent (ThermoFisher)) were loaded onto pre-cast NuPAGE 4-12% Bis-Tris gels (ThermoFisher) in an XCell SureLock electrophoresis system (ThermoFisher). Electrophoresis was carried out in NuPage MES running buffer (ThermoFisher) with 435 µl NuPage Antioxidant added to the upper buffer chamber (ThermoFisher) at 200 V for ~40 minutes. Two molecular markers were run in parallel to visualise protein molecular weight: SeeBluePlus2 (ThermoFisher) and a biotinylated protein ladder (Cell Signalling, Boston, USA). For high molecular weight (HMW) proteins a Precision Plus Protein Dual Color Standards (Bio-Rad) molecular marker was used and electrophoresis duration was extended as required.

3.7.2 Protein transfer to PVDF membrane and antibody incubation

Following LDS-PAGE, proteins were transferred to a polyvinylidene difluoride (PVDF) membrane using iBlot 2 Transfer Stacks (ThermoFisher) and an iBlot 2 Dry Blotting System (ThermoFisher). The iBlot transfer stack was assembled according to the manufacturer's instructions: bottom stack-membrane-gel-top stack. The assembled stack was placed into the iBlot system and a pre-programmed method was used for the transfer of proteins: 20 V for 1 minute, 23 V for 4 minutes and 25 V for 2 minutes. For HMW proteins a custom method was used: 25 V for 10 minutes. Following transfer, the membrane was removed from the stack and blocked in 5 % (w/v) milk in Tris buffer saline (Santa Cruz, Dallas, USA) with 1 % (v/v) Tween 20 (TBST; Sigma-Aldrich) for 1 hour at room temperature. After blocking, the membrane was incubated in the primary antibody (**Table 3.1**) overnight at 4 °C. The membrane was washed 3 times for ten minutes with TBST and incubated in the appropriate secondary antibody (**Table 3.1**) and an anti-biotin antibody (**Table 3.1**) (Cell signalling) for 1 hour at room temperature. The membrane was washed 4 times for 5 minutes with TBST prior to being developed.

Antibody	Manufacturer	Dilutions
anti-Wolframin	Proteintech, Manchester, UK (1158-1-AP)	1:500
anti-GRP94	Cell Signaling (#2104)	1:4000
anti-Bip	Abnova, Cambridge, UK (PAB2462)	1:1000
anti-IP_3R	Santa Cruz (SC-377518)	1:100
anti-SERCA	Santa Cruz (SC-376235)	1:500
anti-VDAC	Abcam, Cambridge (ab14734)	1:500
anti-MCU	Sigma-Aldrich (HP016480)	1:500
anti-pPDH	Abcam (ab168379)	1:2000
anti-total-PDH	Abcam (ab177461)	1:500
anti-Caspase 3	Cell Signaling (#9662)	1:1000
anti-PARP	Cell Signaling (#9542)	1:1000
anti-Tubulin	Abcam (ab59680)	1:2000
Rabbit anti-mouse	Dako, Cambridge, UK (P0260)	1:1000
Swine anti-rabbit	Dako (P0399)	1:1000
anti-Biotin	Cell Signaling (#7727)	1:2000

Table 3.1 Antibodies

3.7.3 Chemiluminescent Detection and Densitometry

Signals were visualised using Clarity Western ECL substrate (Bio-Rad) and imaged with an Amersham Imager 600 (GE Healthcare, Amersham, London, UK. Densitometry was performed using ImageQuant TL 8.1 software (GE Healthcare). Tubulin was used for signal normalisation.

3.8 Cloning

3.8.1 Plasmids

The following plasmids were used: pcDNA-D1ER (Addgene #36325, a gift from Amy Palmer and Roger Tsien), pAC-GFPC1-Sec61beta (Addgene #15108, a gift from Tom Rapoport), neuroD:GFP (a gift from Tamily A. Weismann) and neuroD:mito-RFP (a gift from Tamily A. Weismann).

3.8.2 Transformation

Transformations were performed using JM109 high efficiency competent cells (Promega, Southampton, UK). 2X Yeast Tryptone (2YT) broth and 2YT agar plates were used as growth medium. 2YT broth and 2YT agar were autoclaved and allowed to cool before the addition of the appropriate antibiotics. Agar plates were prepared under aseptic conditions, allowed to solidify at room temperature, dried at 37 °C and stored at 4 °C for up to one month. On ice, plasmid DNA was added to pre-aliquoted competent cells (25 µl), gently mixed and incubated for 20 minutes. The cells were heat-shocked for 45 seconds at 42 °C, and returned to ice for 2 minutes. Then 475 µl of 2YT broth was added and the mixture was incubated at 37 °C for 1 hour with shaking. Under ascetic conditions, 100 µl of each transformation culture was spread onto an agar plate. Plates were inverted and incubated overnight at 37 °C.

3.8.3 Plasmid purification

Growth medium was inoculated with a single colony carrying the plasmid and incubated overnight at 37 °C with shaking. On the following day, the cell suspension was centrifuged at 6000 x g for 15 minutes at 4 °C. Plasmid purification was performed using a Qiagen Plasmid Kit (Qiagen, Manchester, UK); a Mini or Maxi prep was performed as appropriate according to the manufacturer's instructions. Plasmid DNA was resuspended in 500 µl dH_20. Plasmids were analyzed by agarose gel electrophoresis by comparison to a molecular weight marker as described in Section 3.2. The concentration of DNA was determined using a NanoDrop 2000 UV-Vis spectrophotometer (ThermoFisher).

3.9 Live Cell Confocal Microscopy

3.9.1 ER Ca^{2+} measurement

The ER targeted fluorescence resonance energy transfer (FRET) based probe D1ER was used to measure ER Ca^{2+} levels. D1ER consists of a Ca^{2+} binding calmodulin domain between two fluorescent proteins: enhanced cyan fluorescent protein (CFP) and citrine fluorescent protein (YFP). A calreticulin targeting sequence and a KDEL ER retention sequence ensure D1ER is localised to the ER. When calmodulin binds Ca^{2+} an intramolecular rearrangement occurs bringing the CFP and YFP into close proximity, which leads to FRET from the CFP to YFP. The FRET signal enables the ratiometric assessment of free ER Ca^{2+} using the FRET to CFP ratio (**Figure 3.1**).

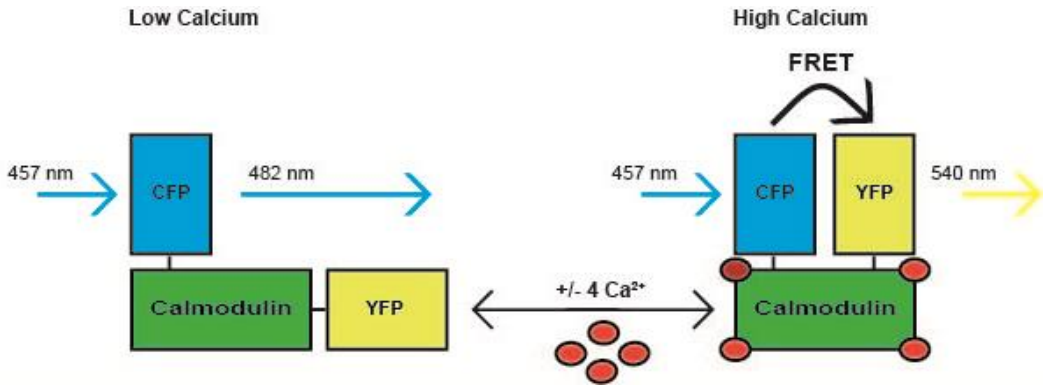

Figure 3.1 Schematic of the D1ER probe. Showing the CFP, calmodulin domain and YFP under low and high Ca^{2+} conditions, when the calmodulin domain binds Ca^{2+} the CFP and YFP are brought into close proximity resulting in increased FRET signal.

Fibroblast cell lines were seeded at 100,000 cells/dish on glass bottom dishes (Willco, Amsterdam, Netherlands) 3 days before the experiment. Cells were transiently transfected with D1ER 2 days before imaging in opti-MEM (ThermoFisher) with GeneJuice Transfection Reagent (Merck Millipore, Watford, UK) and 2 µg of plasmid DNA. Cells were washed twice with PBS and imaged in Hank's balanced salt solution (HBSS) without phenol red or Ca^{2+} (ThermoFisher) and supplemented with 5 mM glucose (Sigma-Aldrich) and 25 mM HEPES (Sigma-Aldrich) at pH 7.4. Live cell imaging was performed at room temperature with a Nikon A1R inverted confocal microscope equipped with a x60, 1.40 NA oil objective (Nikon, Surrey, UK). The filters used were a 457 nm excitation filter and two emission filters: 482 nm for CFP

and 540 nm for YFP. The FRET to CFP ratio was calculated by ratioing the emission at 540 nm and 482 nm. To calibrate the D1ER probe, cells were permeabilized with 600 nM digitonin and ER Ca^{2+} was depleted with 9 mM EGTA or ER Ca^{2+} was increased with 30 mM $CaCl_2$ (Sigma-Aldrich), 3 mM ATP (Sigma-Aldrich) and 3 mM $MgCl_2$ (Sigma-Aldrich).

3.9.2 ER Ca^{2+} flux analysis

Fibroblast cell lines were seeded at 100,000 cells/dish on glass bottom dishes and allowed to adhere overnight. Fluo-4-am (ThermoFisher) and Rhod-2-am (ThermoFisher) were used to evaluate cytosolic and mitochondrial Ca^{2+}, respectively. Fluo-4 (4 µM) was loaded at 37 °C for 15 minutes or Rhod-2 (8 µM) was loaded at room temperature for 30 minutes. Cells were washed twice with PBS and incubated in tyrodes solution (137 mM NaCl, 2.7 mM KCl, 1 mM $MgCl_2$, 0.2 mM Na_2HPO_4, 12 mM $NaHCO_3$, 2 mM $CaCl_2$, 10 mM Glucose, pH 7 (All Sigma-Aldrich)) for 15 minutes. Dynamic measurements of cytosolic and mitochondrial Ca^{2+} were performed at room temperature with a Nikon A1R inverted confocal microscope equipped with a x60, 1.40 NA oil objective in resonant scanning mode at 3.7fps for 5 minutes. After one minute (providing basal fluorescence) histamine (100 µM; Sigma-Aldrich) was added to evoke IP_3R dependent ER Ca^{2+} release and the Ca^{2+} transient was monitored. Image analysis was performed in Fiji, the background was subtracted and Ca^{2+} levels were calculated as $(F-F_o)/F_o$ where F indicates fluorescence and F_o indicates basal fluorescence.

3.9.3 Mitochondrial-ER colocalisation and morphology analysis

Fibroblast cell lines were seeded at 100,000 cells/dish on glass bottom dishes three days before the experiment. GFP-Sec61β was transiently transfected to detect the ER. Cells were transfected ~48 hours before imaging in opti-MEM with GeneJuice Transfection Reagent and 1 µg of plasmid DNA. Mitotracker red (75 nM, ThermoFisher) was loaded at 37°C for 30 minutes to detect mitochondria immediately before imaging. Cells were washed twice with PBS and imaged in MEM without phenol red (ThermoFisher) supplemented with 25 mM HEPES. Live cells were imaged at room temperature with a Nikon A1R inverted confocal microscope equipped with a x60, 1.40 NA oil objective. Sixty nine Z-stacks were acquired across the cell at 0.11 µm increments using a high speed piezo Z stage. All image analysis

was performed in Huygens Essential Software (SVI, Hilversum, Netherlands). Images were deconvolved and 3D-reconstructed. Colocalisation of the ER and mitochondria signals was quantified using the Manders' coefficient. M1 indicates the fraction of ER that colocalises with mitochondria and M2 indicates the fraction of mitochondria that colocalises with ER.

Analysis of the mitochondrial network and ER volume was performed individually using Huygens Essentials software. The Huygens Object Analyser was used to calculate the length and volume of each mitochondrial fragment or the total volume of the ER in a 3D-reconstructed image. The following parameters were analyzed for mitochondria in each cell line: (i) the average length of mitochondrial fragments, (ii) the average volume of mitochondrial fragments, (iii) the total length of the mitochondrial network, (iv) the total volume of the mitochondrial network and (v) the total number of mitochondrial fragments. The distribution of the length and volume of mitochondrial fragments within the mitochondrial network was calculated. Individual mitochondrial fragments were sorted into bins based on their length and volume. For length, the mitochondrial fragments were sorted into bins of: <2 µm, 2 to 5 µm, 5 to 10 µm and >10 µm. For volume, the mitochondrial fragments were sorted into bins of: <0.5 μm^3, 0.5 to 1 μm^3, 1 to 5 μm^3, 5 to 10 μm^3 and 10 μm^3.

3.9.4 Analysis of mitochondrial membrane potential

Fibroblast cell lines were seeded at 100,000 cells/dish on glass bottom dishes and allowed to adhere overnight. Mitochondrial membrane potential was assessed with tetramethylrhodamine, methyl ester (TMRM; ThermoFisher) a cell-permeant, cationic fluorescent dye that is sequestered by active mitochondria. TMRM (10 nM) was loaded at 37 °C for 40 minutes. Cells were washed twice with PBS and incubated in tyrodes solution. Imaging was performed at room temperature with a Nikon A1R inverted confocal microscope equipped with a x60, 1.40 NA oil objective. After one minute, carbonylcyanide-p-trifluoromethoxyphenylhydrazone (FCCP, 10 µM; Sigma-Aldrich) was added to dissipate the membrane potential. Image analysis was performed in Fiji. Basal TMRM signal was normalised to the remaining signal following FCCP application and presented as (F/F_o) where F is basal fluorescence and Fo is fluorescence after FCCP application.

3.10 Cytosolic Ca^{2+} measurement

Cytosolic [Ca^{2+}] was determined using the ratiometric Ca^{2+} sensitive fluorescent dye Fura-2-am at basal levels and after thapsigargin induced ER Ca^{2+} depletion. Fura-2-AM shows dual excitation; Ca^{2+}-bound Fura-2-am has a peak excitation wavelength of 340 nm and Ca^{2+}-free Fura-2-AM has a peak excitation wavelength of 380 nm. Free cytosolic [Ca^{2+}] is therefore proportional to the ratio of 340/380 emission intensities detected at 510 nm. Fibroblast cell lines were seeded at 40,000 cells/well on black 96 well optical bottom microplates (ThermoFisher) the day before the experiment. Cells were loaded with 5µM Fura-2 (ThermoFisher) at 37°C for 1 hour 30 minutes, then washed twice with PBS and incubated for a further 30 minutes. Fluorescence was monitored on a Varioskan™ LUX multimode microplate reader (ThermoFisher) at emission wavelength 510 nm following alternate excitations at 340 nm and 380 nm. ER Ca^{2+} depletion was triggered by addition of 1 µM thapsigargin. To calibrate the Fura-2 probe, R_{min} was determined by addition of 2 µM ionomycin (ThermoFisher) and 3 mM EGTA (Sigma), and R_{max} was determined by addition of 2 µM ionomycin (ThermoFisher) and 10 mM $CaCl_2$ (Sigma). The standard equation was used to calculate cytosolic [Ca^{2+}]: $[Ca^{2+}] = K_d \times Q \times [(R-R_{min})/R_{max}-R]$, where R is the 340/380 ratio, R_{min} is the 340/380 ratio under Ca^{2+} free conditions, R_{max} is the 340/380 ratio under Ca^{2+} saturating conditions, Q is the ratio of emission intensity at 380 nm for Ca^{2+} free and Ca^{2+} saturated Fura-2 and Kd was assumed to be 225 nM.

3.11 Mitochondrial OXPHOS analysis

3.11.1 Seahorse XF^e Extracellular Flux Analyzer

The Seahorse XF^e Extracellular Flux Analyzer (Agilent Technologies, California, USA) was used to measure oxygen consumption rate (OCR) as a measure of mitochondrial respiratory function in whole cells. Fibroblast cell lines were seeded at 40,000 cells/well on XF96 cell culture microplates (Agilent Technologies) and allowed to adhere overnight. Prior to analysis the medium was exchanged to unbuffered DMEM supplemented with 5 mM glucose (Sigma-Aldrich), 1 mM sodium pyruvate (Sigma-Aldrich) and 2 mM L-glutamine (ThermoFisher) and cells were incubated at 37 °C in a non-CO_2 incubator for 1 hour. OCR was measured on a Seahorse XF^e Extracellular Flux Analyzer under basal conditions and following the sequential addition of oligomycin (1µM; Sigma-Aldrich) to inhibit complex V, the uncoupled

FCCP (0.5 µM) to measure maximal uncoupler stimulated OCR and rotenone (1µM; Sigma-Aldrich) together with antimycin A (1µM; Sigma-Aldrich) to inhibit complexes I and III and measure non-mitochondrial OCR. OCR was normalized to mg of protein using the Bradford assay. Four parameters of mitochondrial respiratory function were calculated: (i) basal respiration, (ii) ATP-linked respiration, (iii) proton leak and (iv) maximal respiration. Basal respiration was determined as the difference between OCR under basal conditions and non-mitochondrial OCR. ATP-linked respiration was determined as the difference between OCR under basal conditions and OCR following oligomycin treatment. Proton leak was determined as the difference between OCR following oligomycin injection and non-mitochondrial OCR. Maximal respiration was determined as the difference between OCR following FCCP stimulation and non-mitochondrial respiration.

3.11.2 Oxygraph respirometer

Respiration was measured in permeabilized fibroblasts at 37 °C in a high-resolution Oxygraph-2K respirometer (Oroboros, Innsbruck, Austria) in 2 ml glass chambers. Stirrer speed was set to 750 rpm and data was recorded in DatLab software (Oroboros, Innsbruck, Austria) at 2 second intervals. Fibroblasts were grown to ~70-80% confluency, harvested as described in Section 3.4.2 and resuspended in respiratory buffer (0.5 mM EGTA, 3 mM MgCl2.6H2O, 60 mM Lactobionate, 20 mM Taurine, 10 mM KH_2PO_4, 20 mM HEPES, 110 mM sucrose and 1mg/ml BSA at pH7.1(All Sigma-Aldrich)). The fibroblasts were transferred to the Oxygraph chamber and digitonin (4 µg/million cells; Sigma-Aldrich) was added to selectively permeabilize the plasma membrane whilst leaving intracellular organelle membranes and the ER-mitochondria interaction intact. Following the loss of plasma membrane integrity the cytosol and all solutes leak from the cell and the composition of the intracellular space completely equilibrates with the incubation medium. Accordingly, the stepwise addition of substrates or inhibitors facilitates the site-specific analysis of mitochondrial respiratory chain function in a mostly intact cellular environment. Respiration was started with complex I-dependent substrates by addition of pyruvate (5 mM; Sigma-Aldrich) and malate (5 mM; Sigma-Aldrich). Complex I-coupled respiration was determined by addition of NAD+ (0.5 mM; Sigma-Aldrich) and ADP (1.5 mM; Merck Millipore). Succinate (10 mM; Sigma-Aldrich) was added to reach maximal coupled respiration, and then rotenone (1µM) was added to determine

complex II-dependent respiration. Antimycin A (2.5 µM) was added to determine non-mitochondrial respiration. The results were expressed as flux control ratios; complex I (CI)-dependent respiration and complex II (CII)-dependent respiration were both normalised to the maximal respiratory rate by complexes I and II (CI+CII), determined as indicated in figure 6.3A.

3.11.3 CellTiter-Glo ATP Assay

ATP levels were measured using the CellTiter-Glo Luminescent Assay (Promega, Southampton, UK) according to the manufacturer's instructions. Fibroblast cell lines were seeded at 40,000 cells/well on 96 well white microplates (ThermoFisher) and allowed to adhere overnight. The cells were incubated for 1 hour 30 minutes at 37 °C in either (i) glucose (5 mM) to measure ATP under basal conditions; (ii) 2-deoxy-D-glucose (2-DG; 5 mM, Sigma-Aldrich), which inhibits glycolysis and activates mitochondrial OXPHOS, to measure ATP due to OXPHOS; (iii) oligomycin (2.5 µg/ml), a complex V inhibitor, to measure ATP due to glycolysis and (iv) 2-DG (5 mM) and oligomycin (2.5 µg/ml) as a positive control. Following incubation, 90 µl of buffer was removed and 100 µl of CellTiter-glo reagent was added to each well. Following 25 minutes incubation in the dark with 10 minutes shaking, luminescence was measured on a Luminoskan Ascent (ThermoFisher) with a 1000 ms integration time. Luminescence signal was normalized to mg of protein using the Bradford assay.

3.12 Measurement of ROS

The fluorescent probe 2', 7'-dichlorodihydrofluorescein diacetate (H_2DCFDA; ThermoFisher) was used to measure ROS levels. Fibroblast cell lines were seeded at a 25,000 cells/well on black 96 well optical bottom microplates and allowed to adhere overnight. Cells were washed with PBS and incubated with H_2DCFDA (20 µM) in 100 µl PBS or H_2DCFDA (20 µM) and hydrogen peroxide (H_20_2) (80 µM; Sigma-Aldrich) in 100 µl PBS for 30 minutes at 37°C. Following incubation, cells were washed twice with PBS and fluorescence was measured on a Fluoroskan Ascent (ThermoFisher) at emission wavelength 535 nm following excitation at 485 nm. Fluorescence signal was normalized to mg of protein using the Bradford assay.

3.13 Real-time quantitative PCR

3.13.1 DNA extraction from fibroblasts

Total DNA was extracted from cell pellets using a DNeasy Blood and Tissue Kit (Qiagen) according to the manufacturer's instructions; all buffers were provided by the kit and the centrifuge steps were performed at room temperature. The concentration of eluted DNA was determined using a NanoDrop 2000 UV-Vis spectrophotometer.

3.13.2 mtDNA Copy Number

Real-time quantitative PCR (RT-qPCR) is a reliable method to measure the quantity of DNA product being amplified in 'real-time' during the PCR reaction. The quantification of the relative mtDNA copy number was performed using a duplex qPCR assay with primers specific to the mitochondrial-encoded *MTND1* gene and the nuclear-encoded *B2M* gene. Target specific probes were designed within the target specific primers, which are covalently attached to a fluorescent reporter dye on the 5' end and a non-fluorescent quencher dye on the 3' end. During the PCR reaction when the amplicon extends, the fluorescent reporter dye is cleaved from the probe by Taq polymerase endonuclease activity and the emission spectra of the reporter can be measured. Primer and probe details are given in **Table 3.2**. Reactions were performed using the iQ5 thermocycler (Bio-Rad) in 96 well plates in 25 µl reactions containing: 0.75 µl of each primer, 0.5 µl of each probe, 12.5 µl iTaq SuperMix (Bio-Rad), 7.5 µl dH2O and 1 µl sample DNA. The reaction conditions were: initial denaturation at 95 °C for 3 minutes, followed by 40 cycles of denaturation at 95 °C for 10 seconds, and annealing/extension at 62.5 °C for 1 minute. Fluorescent levels were measured during each annealing and extension phase and mtDNA copy number was calculated with the comparative threshold method.

For each target, a standard curve was used to assess amplification efficiency. Templates for each gene were amplified using standard PCR (Section 3.1), and separated by agarose gel electrophoresis (Section 3.2). The fragments were extracted and purified from the agarose gel using a QIAquick Gel Extraction Kit (Qiagen) according to the manufacturer's instructions. Templates were serially diluted with dH_2O to generate a standard curve ranging from 10^9 to 10^2 copies and included on each reaction plate.

Target	Forward Primer	Reverse primer	Dye	Probe
B2M	CACTGAAAAAGATGAGTATGCC	AACATTCCCTGACAATCCC	FAM	CCGTGTGAACCATGTGACTTTGTC
MTND1	ACGCCATAAAACTCTTCACCAAAG	GGGTTCATAGTAGAAGAGCGATGG	HEX	ACCCGCCACATCTACCATCACCCTC

Table 3.2 RT-qPCR probes and primers for quantification of mtDNA copy number

3.14 Cell viability Analysis

3.14.1 Drugs

The following cellular stressors were used to assess fibroblast sensitivity to stress: staurosporine (STS; Merck Millipore), tert-Butyl hydroperoxide solution (t-BH; Sigma-Aldrich), thapsigargin (Sigma-Aldrich).

3.14.2 MTT assay

Fibroblast cell lines were seeded at 40,000 cells/well on 96 well microplates and allowed to adhere overnight. Cell viability was determined after exposure to STS (1 µM), t-BH (200 µM) or thapsigargin (4 µM) at 0, 2, 5 and 8 hours with the MTT assay (3-[4,5-dimethylthiazol-2-yl]-2,5 diphenyl tetrazolium bromide (MTT); Sigma-Aldrich). At the selected time point, MTT (0.5 mg/ml final concentration) was added to each well and plates were incubated at 37 °C for 1 hour. Following incubation, the media was carefully removed from each well, 100 µl DMSO (Sigma-Aldrich) was added to solubilise the formazan crystals and absorbance was measured at 570 nm on a Multiskan ascent. MTT absorbance at 0 hours was considered 100 % cell viability and signals at 2, 5 and 8 hours were presented as percentage of the signal at 0 hours.

3.14.3 Caspase 3 activity assay

Fibroblast cell lines were seeded at 40,000 cells/well on black 96 well optical bottom microplates and allowed to adhere overnight. Caspase 3 activity was assessed following treatment with cellular stressors with the fluorescent substrate, N-Acetyl-Asp-Glu-Val-Asp-7-amido-4-Trifluoromethylcoumarin (AC-DEVD-AFC; Cayman Chemical, Michigan, USA). Caspase 3 selectivity cleaves the DEVD sequence releasing the fluoregenic AFC and caspase activity is expressed as ΔF/min/mg of protein. Cells were incubated with STS (1 µM), t-BH (200 µM) or thapsigargin (4 µM) for 5 hours. Following treatment, the media was removed, the cells were washed with PBS and 20 µl of lysis buffer (50 mM HEPES, 0.1% CHAPS pH 7.4) was added, the cells were lysed by shaking at 1000 rpm for 30 minutes at 4°C. Once the cells were lysed, an equal volume of assay buffer (40 mM HEPES, 0.2% CHAPS, 4 mM EDTA pH 7.4) with 200 µM Ac-DECD-AFC was added. Following 30 minutes incubation at 37°C, fluorescence was monitored at emission wavelength 505 nm following

excitation at 400 nm on Tecan Infinite 200 microplate reader (Tecan, Männedorf, Switzerland).

3.15 Statistical Analysis

Statistical analysis was performed in GraphPad Prism 5 (GraphPad Software, La Jolla, USA) using a two-tailed unpaired t test. Comparisons were considered non-significant (NS) if the P value was greater than 0.05 and significant if the P value was less than 0.05.

Chapter 4. Optic Neuropathy Gene Screening

4.1 Introduction

Inherited optic neuropathies are a genetically heterogeneous group of disorders characterised by irreversible RGC loss, optic atrophy and progressive visual impairment. Mutations in a number of genes have been identified (**Table 1.1**), some of which are relatively rare, and the mode of inheritance is traditionally classified as maternal (mitochondrial), autosomal dominant, autosomal recessive or X-linked (Yu-Wai-Man *et al.*, 2011a).

The referral of patients with unexplained visual failure or suspected inherited optic neuropathies to the neuro-ophthalmology and neurogenetics services in Newcastle upon Tyne has led to the establishment of a comprehensively phenotyped cohort of patients with a likely genetic basis for their optic atrophy. LHON and DOA are the two most common inherited optic neuropathies seen in clinical practice, and with current genetic testing protocols a confirmed molecular diagnosis can be achieved in ~50% of patients (Ferre *et al.*, 2009; Yu-Wai-Man *et al.*, 2011b; Chen *et al.*, 2014). Optic atrophy is also common in hereditary neurodegenerative disorders as part of a complex spectrum of clinical features caused by underlying mitochondrial dysfunction (Yu-Wai-Man *et al.*, 2011a). Novel genes associated with optic atrophy continue to be identified and the phenotypic spectrum and mode of inheritance of known optic atrophy genes, such as *OPA1* and *WFS1*, are being revised as more patients are identified and genetic testing becomes more widely available (Angebault *et al.*, 2015; Charif *et al.*, 2015; Grenier *et al.*, 2016; Spiegel *et al.*, 2016). Reaching a confirmed molecular diagnosis can be challenging and the genetic defect responsible for the development of optic atrophy and visual failure remains unresolved in a significant proportion of patients.

Genetic testing has important benefits for patients and their families by enabling informed genetic counselling and assessment of the likely disease progression and severity (Yu-Wai-Man *et al.*, 2011a). Patients can be advised on the avoidance of risk factors associated with increased risk of visual failure, such as smoking and alcohol for LHON carriers (Kirkman *et al.*, 2009). Importantly, prenatal testing can be offered to women of childbearing age and individuals who are eligible for recruitment into clinical trials can be identified (Yu-Wai-Man *et al.*, 2011a).

4.1.1 WFS1

The *WFS1* gene (4p16.1) consists of 8 exons, 7 of which encode Wolframin, a transmembrane protein that localizes to the ER (Inoue *et al.*, 1998; Strom *et al.*, 1998). Mutations in the *WFS1* gene are associated with WFS1 and related disorders, in which optic atrophy is a constant and central feature (Moosajee *et al.*, 2016).

4.1.2 RTN4IP1

The *RTN4IP1* gene (6q21) encodes for a mitochondrial protein that was identified in a yeast two-hybrid screen using reticulon 4 (RTN4) as bait. The *RTN4IP1* gene comprises of 9 protein-coding exons and the resulting protein has a putative N-terminal mitochondrial targeting sequence. The function of RTN4IP1 remains unknown, although it has been confirmed to localise to mitochondria (Hu *et al.*, 2002). Mutations in *RTN4IP1* have recently been associated with inherited optic neuropathy. A homozygous mutation, c.308G>A (p.Arg103His), was identified as the cause of early-onset recessive optic neuropathy in two siblings from a consanguineous Moroccan family. This variant modifies an evolutionary conserved amino acid, which was predicted to be pathogenic by *in silico* analysis, and the variant segregated with the disease in the family. Four additional subjects harbouring *RTN4IP1* mutations were identified by Sanger sequencing in 240 European inherited optic neuropathy probands with no previous genetic diagnosis, implying that this gene is likely to be a rare recessive cause of inherited optic neuropathy. Two subjects were homozygous for the same c.308G>A mutation and two subjects harboured compound heterozygous mutations, including the c.308G>A mutation and a nonsense mutation c.601A>T, (p.Lys201*) (Angebault *et al.*, 2015).

4.1.3 C12orf65

The *C12orf65* gene (12q24.31) encodes for a mitochondrial matrix protein that is part of the mitochondrial translation system. C12orf65 belongs to a family of mitochondrial class 1 peptide release factors characterized by a peptidyl-hydrolase domain containing a conserved glycine-glycine-glutamine (GGQ) motif. Peptide release factors recognize when a stop codon on translated mRNA enters the mitoribosome and terminate translation through hydrolysis of the ester bond connecting the nascent polypeptide to the peptidyl-tRNA, thus releasing the newly synthesized protein (Antonicka *et al.*, 2010; Duarte *et al.*, 2012). The C12orf65 protein contains a release

factor-1 (RF-1) domain (amino acids 53-146) containing the GGQ motif (amino acids 71-73), but its precise function remains unclear (Antonicka *et al.*, 2010). C12orf65 does not exhibit peptidyl-tRNA hydrolase activity or coprecipitate with the mitoribosome and it is instead hypothesized to participate in the recycling of abortive peptidyl-tRNAs released from the ribosome (Antonicka *et al.*, 2010; Duarte *et al.*, 2012).

The *C12orf65* gene consists of three exons and 501bp from exons two and three comprise its protein-coding region. Mutations in *C12orf65* were first described in three patients from two unrelated families presenting with optic atrophy, opthalmoplegia and progressive encephalomyopathy (Antonicka *et al.*, 2010). Subsequently, at least nine recessive *C12orf65* mutations have been reported associated with a range of clinical features including optic atrophy, peripheral neuropathy and spastic paraplegia (Antonicka *et al.*, 2010; Shimazaki *et al.*, 2012; Buchert *et al.*, 2013; Heidary *et al.*, 2014; Pyle *et al.*, 2014; Spiegel *et al.*, 2014; Tucci *et al.*, 2014; Imagawa *et al.*, 2016). All reported *C12orf65* mutations led to truncation of the C12orf65 protein and a genotype-phenotype relationship has been established where N-terminal mutations that disrupt the RF-1 domain are associated with a severe phenotype and C-terminal mutations that do not affect the RF-1 domain are associated with a milder phenotype (**Figure 4.1**) (Spiegel *et al.*, 2014; Imagawa *et al.*, 2016).

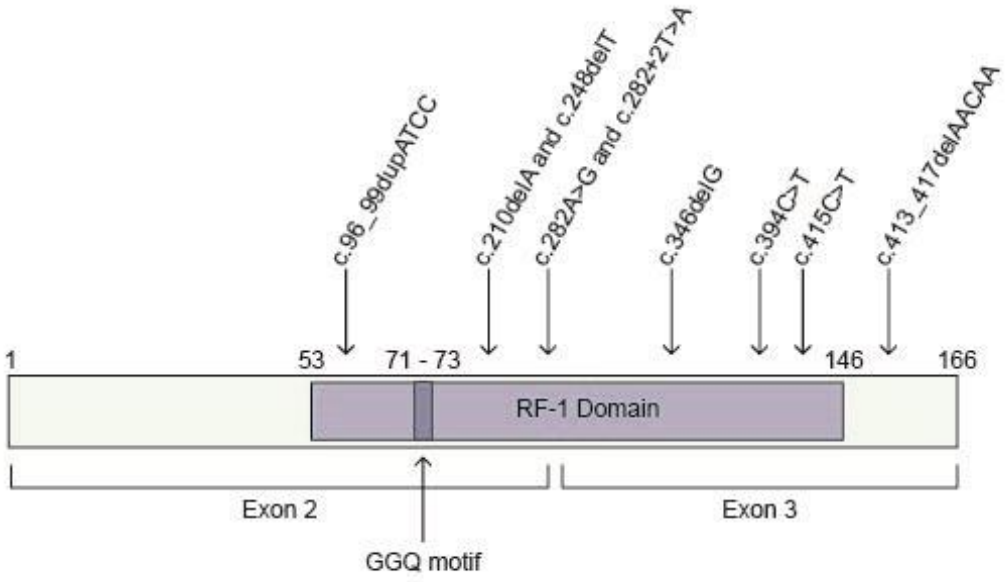

Figure 4.1 Schematic of C12orf65 structure. The protein structure and previously reported *C12orf65* mutations, arrows indicate the resulting protein truncation.

Due to the previous association of the *WFS1*, *RTN4IP1* and *C12orf65* genes with inherited optic atrophy phenotypes (Inoue *et al.*, 1998; Strom *et al.*, 1998; Antonicka *et al.*, 2010; Angebault *et al.*, 2015), the purpose of this study was to screen these genes for potential pathogenic mutations in a selected group of patients from the Newcastle optic atrophy cohort.

4.2 Materials and Methods

4.2.1 Patient Cohort

The Newcastle optic atrophy cohort consisted of 30 patients who had previously been diagnosed with likely inherited optic atrophy, but who do not harbour pathogenic mutations in the *OPA1* or *OPA3* gene (**Table 4.1**). Genomic DNA was available for each patient.

Patient	Clinical features
1	Optic atrophy, diabetes, ataxia and stoke-like episodes
2	Optic atrophy and deafness
3	Optic atrophy plus
4	Optic atrophy plus, ataxia and peripheral neuropathy
5	Optic atrophy
6	Optic atrophy, CPEO and peripheral neuropathy
7	CAPOS
8	CAPOS
9	CAPOS
10	Optic atrophy and diabetes mellitus
11	Optic atrophy plus, ataxia and peripheral neuropathy
12	Optic atrophy plus, CPEO, spastic paraplegia and ataxia
13	Optic atrophy plus
14	Optic atrophy plus
15	Optic atrophy and peripheral neuropathy
16	Optic atrophy plus, CPEO and proximal myopathy
17	Optic atrophy
18	Optic atrophy plus, CPEO and ataxia
19	Optic atrophy and deafness
20	Optic atrophy and deafness
21	Optic atrophy and ataxia
22	Optic atrophy
23	Optic atrophy
24	Optic atrophy
25	Optic atrophy
26	Optic atrophy
27	Optic atrophy and nystagmus
28	Optic atrophy
29	Optic atrophy and deafness
30	Optic atrophy and raised 3-methylglutaconic acid

Table 4.1 The Newcastle optic atrophy cohort. The clinical features of each patient. CAPOS, cerebellar ataxia, areflexia, pes cavus, optic atrophy and sensorineural hearing loss; CPEO, chronic progressive external ophthalmoplegia.

4.2.2 Sequencing

Primer sets for *WFS1* (**Table 4.2**), *RTN4IP1* (**Table 4.3**) and *C12orf65* (**Table 4.4**) were designed with Primer3 and primer specificity was confirmed using Primer-Blast (Untergasser *et al.*, 2012; Ye *et al.*, 2012). The entire coding regions and exon-intron boundaries of the *WFS1*, *RTN4IP1 C12orf65* genes were amplified by PCR and PCR products were Sanger sequenced as described in Sections 3.1-3.3.

4.2.3 Sequencing Analysis

Sequencing results were analyzed as described in Section 3.3.4. The following GenBank reference sequences were used: *WFS1* (NG_011700.1), *RTN4IP1* (NG_047205.1) and *C12orf65* (NG_027517.1). Identified variants were described according to the Human Genome Variation Society nomenclature (den Dunnen *et al.*, 2016). All variants were checked against the literature, mutation databases where appropriate (https://lovd.euro-wabb.org, accessed on 9 October 2016) and the National Centre for Biotechnology Information (NCBI) Single Nucleotide Polymorphism Database (dbSNP) (Sherry *et al.*, 2001). As required, the likelihood of a non-synonymous variant being pathogenic was determined with PolyPhen2. This tool predicts the impact of an amino acid substitution and scores a variant from 0.0 (tolerated) to 1.0 (deleterious) (http://genetics.bwh.harvard.edu/pph2/, accessed on 9 October).

Exon	Amplicon size (bp)	Forward primer	Reverse primer
1	366	CGGAGATGTGGAGTGATTGG	ACAGTGCCTCAGGGCTCTT
2	491	TCAGCGAGATCCTGTATGGA	AGCTGCACAATGCTGAACTG
3	499	TTCCCTGTCTGTGTCTGTGTCT	GAGGTGATGCCCAAGATGAG
4	926	AAGCCCTTTTATGGGCTCTC	AATTTCCCAACAGCATCACC
5	495	CCCTGGTAACCAAGTCCTGA	GCACGGTCTCTACAGGAAGG
6	395	ATGATCCCCAGAACGTAGGA	ACCGCCTGAGATCCTAGCAG
7	684	GTCACCCGTGCTGTGAGAA	GGCACGGCTGTAAGACACTC
8a	497	GTCAGAGGGAGGCGTGAGAT	GGGATGCAGTCCTTGCTG
8b	540	CAACCTGGATGTGGAGCAG	TCCATCGGCTACTTCCTCTT
8c	482	TTTCAAGGGCACCTACTGCT	CCATGTTGGTCTCCTTCCAG
8d	384	GGTCAAGCTCATCCTGGTGT	CTCTGTCGCCTTAAGCTGCT
8e	599	ACATGCTCCCGTTCTTCATC	CACTGGTGCATGCCTGTC

Table 4.2 *WFS1* primer sets

Exon	Amplicon size (bp)	Forward primer	Reverse primer
1a	567	GCGCAGCCATCTTTAATTGT	TGAACTGCGTGCTCAAATTC
1	649	GCGAAGAGCGGAATAACAGT	AGAAGGATTCCCTGGCCATT
2	465	CCATGTCTTTGCTGTTGTGAA	CAGATTCAGGGAGCAGAAGC
3	475	GGATATGCTGGCATCTGCTT	GCAGGCAGTGTTACTGAATGG
4	495	GGTTTTGCTGGTCTCAGAGG	CTGAGAATCCACAGAATGAAGC
5	336	CTGCAGTTTCTTGGTGAACCT	CCAGACCTACCTTTCTCTCAGC
6	455	TCTCTGACAGATGGCTTCCT	GCCAACCTAAGTAACTTCTAGT GACA
7	486	CCTTCCATCTCCATCAAAGC	GTGACTGCAGAGTCCATGCT
8	366	AGTCATTGTGCCAAGGTGCT	AAGGTCAGGTGAGCAGGCTA
9	397	ACCTGGGTCCACTGGAGAG	ACTGGCCAAAATGGTGTGTT

Table 4.3 *RTN4IP1* primer sets

Exon	Amplicon size (bp)	Forward primer	Reverse primer
2	486	TACCCTGCACTGCTTTCCTT	CAGGACTGTTTTCACCATTGTAG
3	397	GCAACCAACAAAACCAGCAA	CAGGACTGTTTTCACCATTGTAG

Table 4.4 *C12orf65* primer sets

4.3 Results

4.3.1 WFS1 genetic screen

The *WSF1* gene was sequenced in 14 patients. In total, 13 exonic *WFS1* variants were identified, including three non-synonymous variants (**Table 4.5**). All 13 *WFS1* variants have previously been reported in healthy controls on dbSNP.

Location	DNA	Protein	dbSNP	Heterozygous	Homozygous
Exon 5	c.612C>T	p.(Val204=)	Yes	1	0
Exon 6	c.684C>G	p.(Arg228=)	Yes	6	6
Exon 8	c.997G>A	p.(Ile333Val)	Yes	5	4
Exon 8	c.1023C>T	p.(Phe341=)	Yes	2	0
Exon 8	c.1185C>T	p.(Val395=)	Yes	9	4
Exon 8	c.1367G>A	p.(Arg456His)	Yes	2	0
Exon 8	c.1500C>T	p.(Asn500=)	Yes	8	4
Exon 8	c.1725C>T	p.(Ala575=)	Yes	2	0
Exon 8	c.1832G>A	p.(Arg611His)	Yes	9	3
Exon 8	c.2322G>A	p.(Lys774=)	Yes	9	4
Exon 8	c.2424C>T	p.(Ser808=)	Yes	1	0
Exon 8	c.2433G>A	p.(Lys811=)	Yes	9	4
Exon 8	c.2565 A>G	p.(Ser855=)	Yes	7	6

Table 4.5 *WFS1* variants identified

4.3.2 RTN4IP1 genetic screen

The *RTN4IP1* gene was sequenced in 11 patients. Overall, three synonymous variants were identified, all of which have previously been reported in healthy controls on dbSNP (**Table 4.6**).

Location	DNA	Protein	dbSNP	Heterozygous	Homozygous
Exon 1b	c.114 T>A	p.(Pro38=)	Yes	5	0
Exon 2	c.201 C>T	p.(IleI67=)	Yes	1	0
Exon 9	c.1182 C>T	p.(Asn394=)	Yes	1	0

Table 4.6 *RTN4IP1* variants identified

4.3.3 C12orf65 genetic screen

The *C12orf65* gene was sequenced in 29 patients and two variants were identified. One variant was synonymous and one was non-synonymous; both have previously been reported in healthy controls on dbSNP (**Table 4.7**). In addition, the non-synonymous variant scored 0.179 on PolyPhen2, indicating the variant is likely benign (http://genetics.bwh.harvard.edu/pph2/, accessed on 9 October).

Location	DNA	Protein	dbSNP	Heterozygous	Homozygous
Exon 2	c.44G>A	p.(Arg15Gly)	Yes	2	0
Exon 2	c.273C>T	p.(Ile91=)	Yes	1	0

Table 4.7 *C12orf65* variants identified

4.4 Discussion

Inherited optic neuropathies are genetically heterogeneous and the underlying genetically defect remains unknown in ~40-60 % of patients referred to tertiary centres for further investigation (Ferre *et al.*, 2009; Yu-Wai-Man *et al.*, 2011b). In this study, a well-characterised cohort of patients with likely inherited optic atrophy, but no molecular diagnosis, was screened for possible pathogenic mutations in the *WFS1*, *RTN4IP1* and *C12orf65* genes (Inoue *et al.*, 1998; Strom *et al.*, 1998; Antonicka *et al.*, 2010; Angebault *et al.*, 2015).

The *WFS1* gene was sequenced in 14 patients and 13 exonic variants were identified, including three non-synonymous variants. All variants had previously been reported on dbSNP and are likely non-pathogenic. Wolfram syndrome has an estimated prevalence of 1 in 770,000 in the UK (Barrett *et al.*, 1995a), and at least 281 unique *WFS1* mutations have been reported to date (https://lovd.euro-wabb.org, accessed on 9 October 2016). It is not entirely unexpected that no *WFS1* mutations were identified in the patient cohort. Most patients did not fit the minimal diagnostic criteria for Wolfram syndrome, which is the co-occurrence of diabetes mellitus and optic atrophy typically with juvenile onset and approximately 85 % of patients will have both clinical features by the second decade (Rigoli *et al.*, 2011; de Heredia *et al.*, 2013). Nevertheless, dominant mutations in the *WFS1* gene are associated with optic atrophy and SNHL, also referred to as Wolfram-like syndrome (Hogewind *et al.*, 2010; Rendtorff *et al.*, 2011), and recently, recessive *WFS1* mutations have been reported in the context of isolated optic atrophy (Chaussenot *et al.*, 2015; Grenier *et al.*, 2016). Therefore, although no pathogenic mutations were identified, the systematic analysis of the *WFS1* gene is warranted in patients with suspected inherited optic neuropathy.

The *RTN4IP1* gene was sequenced in 11 patients and three synonymous variants were identified. All variants have previously been reported and are likely non-pathogenic. To date, *RTN4IP1* mutations have been identified in six subjects from four families associated with both isolated and syndromic optic neuropathy (Angebault *et al.*, 2015). The fact that no pathogenic *RTN4IP1* mutations were identified in the Newcastle optic atrophy cohort further suggests that mutations in the *RTN4IP1* gene are likely a rare cause of inherited optic atrophy.

The *C12orf65* gene was sequenced in 29 patients and two variants were identified. One variant was synonymous and has previously been reported on dbSNP. A non-synonymous variant (c.273C>T, p.Arg15Gly) was also identified. The variant is likely non-pathogenic as it has previously been reported on dbSNP, although the submission has not been validated, and it was predicted to be benign by *in silico* analysis on PolyPhen-2. Furthermore, the variant is a missense mutation in a heterozygous state, which does not affect the RF-1 domain, whereas previous *C12orf65* mutations have primarily been nonsense truncating mutations with a recessive mode of inheritance (Imagawa *et al.*, 2016).

One limitation of this study is that deep intronic mutations or large-scale deletions/duplications cannot be excluded. However, the relevance of these mutational subtypes in the context of *RTN4IP1* and *C12orf65* remains unclear. In rare cases, large deletions of the *WFS1* gene have been described in Wolfram syndrome (Chaussenot *et al.*, 2015).

In summary, no pathogenic mutations in the *WFS1*, *RTN4IP1* or *C12orf65* genes have been identified in a well-characterised cohort of 30 patients with suspected inherited optic neuropathy. Further investigations are underway to ascertain the cause of optic atrophy in these patients with next-generation whole exome and genome sequencing.

.

Chapter 5. Ca^{2+} Homeostasis at the Mitochondria Associated Membrane in Wolfram Syndrome 1

5.1 Introduction

Wolfram syndrome is a multisystemic neurodegenerative disease characterised by diabetes insipidus, diabetes mellitus, optic atrophy and deafness (DIDMOAD) (Wolfram and Wagener, 1938). This disorder is primarily caused by recessive mutations in the *WFS1* gene (4p16.1), although dominant mutations associated with Wolfram-like syndrome are increasingly being reported (Inoue *et al.*, 1998; Strom *et al.*, 1998; Hogewind *et al.*, 2010; Rendtorff *et al.*, 2011). The *WFS1* gene encodes a transmembrane ER protein termed Wolframin, which is involved in ER maintenance and the regulation of cellular Ca^{2+} homeostasis (Takeda *et al.*, 2001; Takei *et al.*, 2006; Hara *et al.*, 2014). Numerous studies have reported that *WFS1* deficiency induces ER stress and disturbs cellular Ca^{2+} homeostasis (Hara *et al.*, 2014; Lu *et al.*, 2014; Cagalinec *et al.*, 2016).

Historically, Wolfram syndrome was initially suspected to be a mitochondrial disease because the multisystemic clinical manifestations were reminiscent of the complex phenotypes observed in classical mitochondrial disease and the organ systems affected had a high metabolic demand (Bu and Rotter, 1993). However, the identification of the *WFS1* gene and the observation that Wolframin deficiency led to ER dysfunction put this hypothesis into question and suggested that Wolfram syndrome was instead an ER-related disease (Fonseca *et al.*, 2005; Yamada *et al.*, 2006). Nevertheless, the disease mechanisms underlying Wolfram syndrome have not been fully resolved and there is mounting evidence that *WFS1* mutations cause mitochondrial dysfunction (Ross-Cisneros *et al.*, 2013; Cagalinec *et al.*, 2016). The histopathological investigation of optic nerve degeneration in post-mortem retinal tissue from a WFS1 patient revealed a pattern of RGC loss that is characteristic of mitochondrial optic neuropathies (Ross-Cisneros *et al.*, 2013). Furthermore, a recent investigation of mitochondrial function in *WFS1* deficient neurones revealed mitochondrial defects including disturbed mitochondrial dynamics and impaired OXPHOS function. Notably, mitochondrial dysfunction was shown to be secondary to ER stress and perturbed cytosolic Ca^{2+} homeostasis (Cagalinec *et al.*, 2016).

It is possible that primary ER dysfunction in Wolfram syndrome may cause mitochondrial impairment through disturbed ER-mitochondria interactions. The ER

and mitochondria interact physically and functionally at interfaces termed MAMs, and it is now becoming apparent that dysfunction in either organelle can have a negative impact on the other (Paillusson *et al.*, 2016). The MAM is enriched in proteins associated with cellular Ca^{2+} signalling and a key function is the efficient transfer of Ca^{2+} from the ER to mitochondria, which serves to regulate cellular Ca^{2+} homeostasis, mitochondrial bioenergetics and apoptosis (van Vliet *et al.*, 2014). Compelling evidence exists for a link between MAM dysfunction, disturbed Ca^{2+} homeostasis and neurodegenerative diseases such as AD, PD and ALS (Paillusson *et al.*, 2016). Perhaps the strongest evidence for MAM dysfunction in disease exists for ALS and several proteins enriched at the MAM have been implicated in familial ALS, including VAPB and Sigma1R (Al-Saif *et al.*, 2011; De Vos *et al.*, 2012). Established concepts include tightening of the VAPB-PTP5IP1 MAM protein tether and enhanced ER-mitochondrial Ca^{2+} flux secondary to mutations in the gene encoding VAPB (De Vos *et al.*, 2012), and altered ER ultrastructure, loss of ER-mitochondrial contact and disturbed cellular Ca^{2+} homeostasis as a consequence of Sigma1R deficiency (Hayashi and Su, 2007; Al-Saif *et al.*, 2011). Interestingly, Wolframin was identified in three different proteomic studies of the MAM. This indicates that Wolframin is enriched at the MAM and likely has functions within this domain, possibility related to regulation of Ca^{2+} homeostasis. Importantly, these observations suggest that *WFS1* mutations could disturb the function of the MAM (Zhang *et al.*, 2011; Poston *et al.*, 2013; Horner *et al.*, 2015)

To further clarify the deleterious consequences of *WFS1* mutations, the present study used a cell culture model consisting of fibroblasts derived from Wolfram syndrome patients harbouring recessive or dominant *WFS1* mutations to explore cellular Ca^{2+} homeostasis and the ER-mitochondrial axis.

5.2 Methods

5.2.1 Patient Cohort

Primary fibroblast cell lines were established from five probands (W1-W5) with a clinical diagnosis of Wolfram syndrome or Wolfram-like syndrome and with confirmed pathogenic *WFS1* mutations (**Table 5.1**; hereafter referred to as *WFS1* fibroblasts). All five patients have optic atrophy associated with marked thinning of the RGC layer on optical coherence tomography (OCT) imaging. The mode of inheritance was autosomal recessive for three patients (W1-W3) and autosomal dominant for two patients (W4-W5). Three control fibroblast cell lines (C1-C3) were included for comparison (**Table 5.2**).

The project underwent appropriate ethical review before commencement. Ethical approval was obtained from the National Research Ethics Service; now part of the Health Research Authority. The project was then reviewed, ethically assessed, and approved by Newcastle University.

Proband	Age (years)	Sex	OA onset (years)	Clinical features	Visual acuity RE	Visual acuity LE	Nucleotide change	Protein change
W1	33	Female	4	Optic atrophy, deafness and progressive ataxia	CF	CF	c.409_424dup16 c.2262_2263del2	p.V142GfsX110 p.C755SfsX3
W2	26	Male	12	DIDMOAD	6/60	6/60	c.1433G>A c.2648_2651del4	p.W478X p.F883SfsX68
W3	49	Male	24	Optic atrophy, deafness and diabetes mellitus	CF	CF	c.1558C>T c.1372G>A	p.Q520X p.A458T
W4	49	Female	6	Optic atrophy and deafness	CF	CF	c.2161A>T	p.N721Y
W5	65	Male	52	Optic atrophy and deafness	6/36	6/36	c.2051 C>T	p.A684V

Table 5.1 Clinical features and *WFS1* mutations of the Wolfram syndrome patient cohort. OA, optic atrophy; CF, counting fingers; RE, right eye; LE, left eye.

Control	Age (years)	Sex
C1	45	Female
C2	51	Male
C3	-	-

Table 5.2 Details of the control fibroblast cell lines.

5.3 Results

5.3.1 Wolframin protein expression in WFS1 fibroblasts

Wolframin protein expression was assessed in *WFS1* and control fibroblasts by western blot analysis. Recessive *WFS1* mutations (W1-W3) caused complete loss of Wolframin signal (**Figure 5.1**). In contrast, the steady-state levels of Wolframin, when normalized to tubulin, did not appear to be affected in fibroblasts with dominant *WFS1* mutations (**Figure 5.1**). As recessive *WFS1* mutations caused complete loss of the Wolframin protein, fibroblasts carrying recessive *WFS1* mutations were merged into one group termed *WFS1* rec for further analysis.

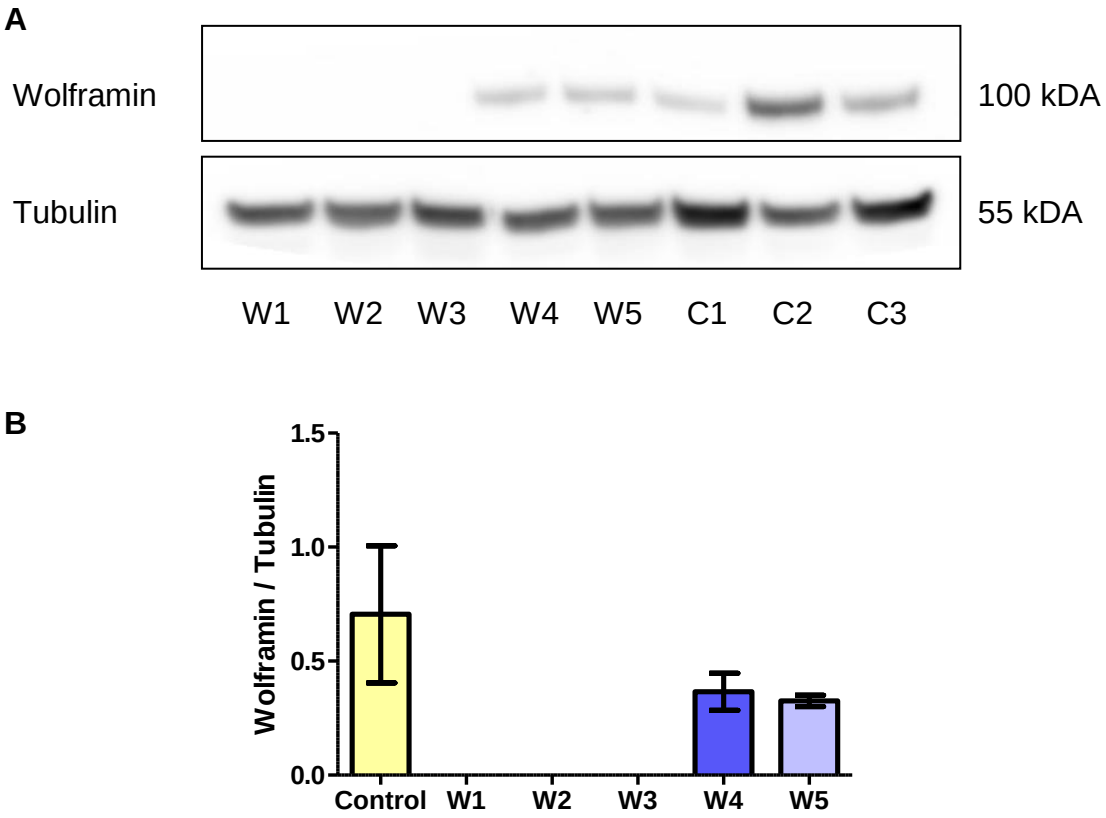

Figure 5.1 Western blot analysis of Wolframin in *WFS1* fibroblasts.
(A) Representative western blot of Wolframin in *WFS1* (W1-W5) and control (C1-C3) fibroblasts. (B) Densitometric analysis of Wolframin levels normalized against tubulin. Data are mean ± SEM. n = 3. No results were significantly different when compared to controls, two-tailed unpaired t test.

5.3.2 Expression of ER stress markers in WFS1 fibroblasts

To evaluate ER homeostasis in *WFS1* fibroblasts the protein levels of two ER chaperones, glucose regulated protein 94 (GRP94) and binding immunoglobulin protein (Bip), were assessed by western blot analysis. There was no significant difference observed in GRP94 or Bip levels in *WFS1* fibroblasts when compared with controls (**Figure 5.2**).

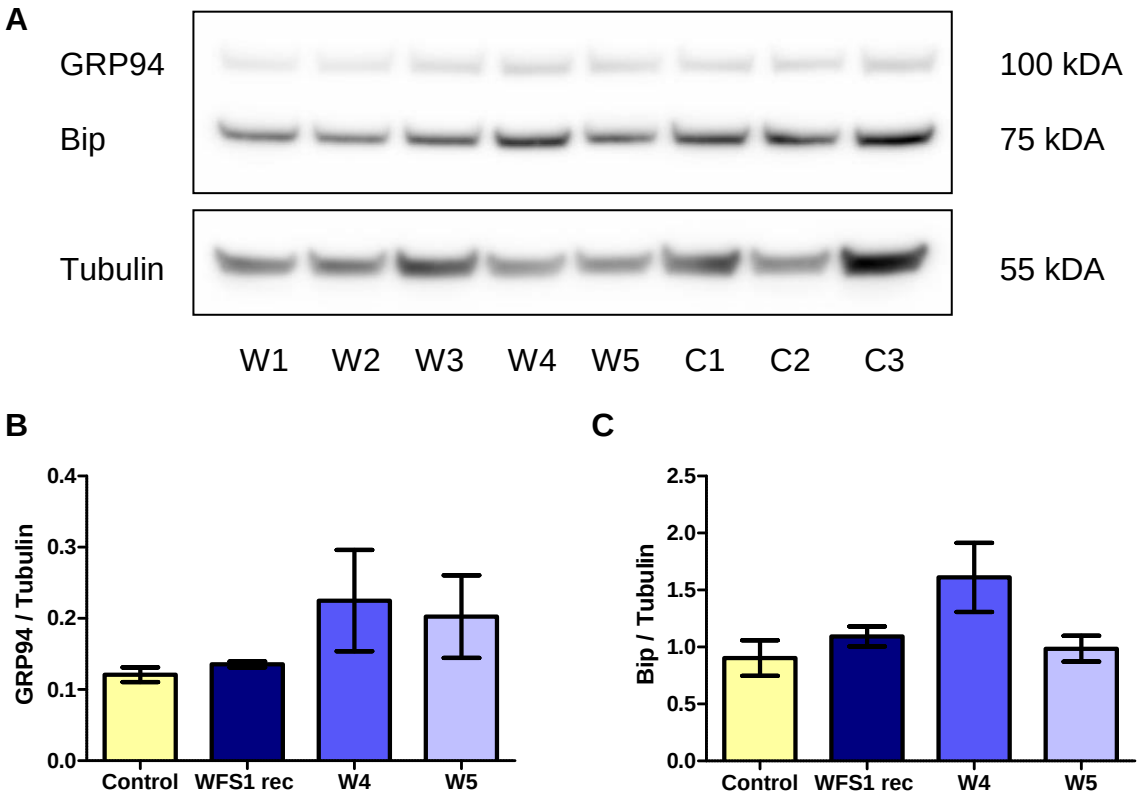

Figure 5.2 Western blot analyses of ER stress markers in *WFS1* fibroblasts. (A) Representative western blots of GRP94 and Bip in *WFS1* and control fibroblasts. (B, C) Densitometric analysis of (B) GRP94 and (C) Bip levels normalized against tubulin. Data are mean ± SEM. n = ≥ 3. No results were significantly different when compared to controls, two-tailed unpaired t test.

5.3.3 Analysis of ER Ca^{2+} levels with the D1ER probe in WFS1 fibroblasts

The ER-targeted cameleon D1ER was used to assess ER Ca^{2+} levels in *WFS1* and control fibroblasts. To confirm the D1ER probe was functioning correctly it was expressed in control cells (**Figure 5.3**). FRET/CFP ratios were then assessed in digitonin permeabilized cells following treatment with either the Ca^{2+} chelator EGTA to decrease ER [Ca^{2+}] or with a combination of Ca^{2+}, $MgCl_2$ and ATP to increase ER [Ca^{2+}]. As expected treatment with EGTA decreased the FRET/CFP ratio and treatment with Ca^{2+}, $MgCl_2$ and ATP increased the FRET/CFP ratio (**Figure 5.4**).

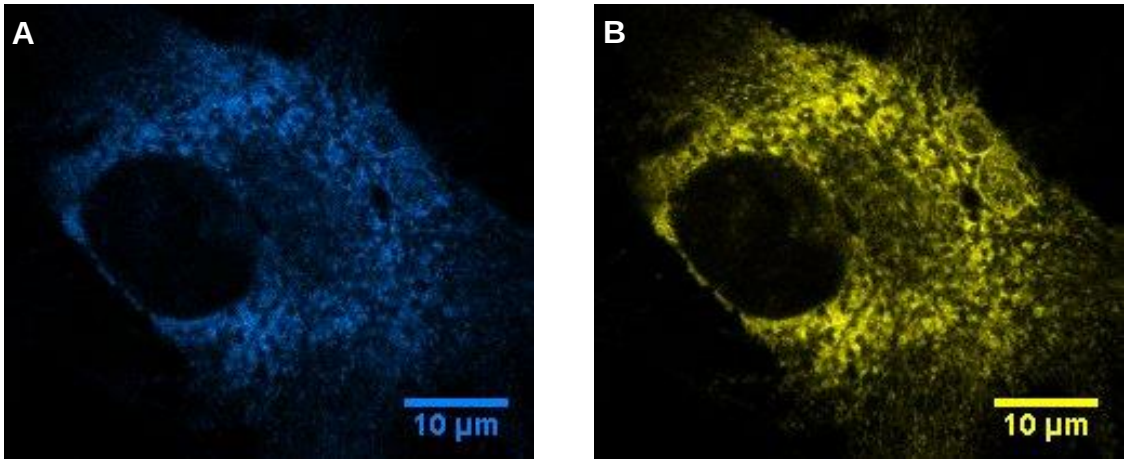

Figure 5.3 Imaging of the D1ER probe. (A, B) Representative confocal images of control fibroblasts expressing D1ER: (A) the CFP signal and (B) the YFP signal. The reticular pattern is indicative of ER localisation. Regions of interest were analysed using Fiji.

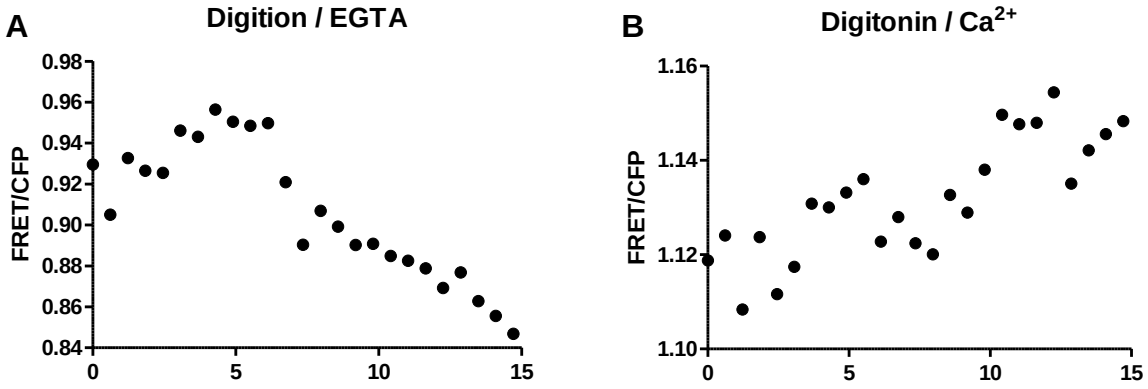

Figure 5.4 Optimization of the D1ER probe. (A, B) Control cells were permeabilized with digitonin and treated with (A) EGTA to deplete ER Ca^{2+} or (B) Ca^{2+}, $MgCl_2$ and ATP to increase ER Ca^{2+} and monitored for 15 minutes. FRET/CFP ratios were calculated using Fiji.

Once validated the D1ER probe was used to assess ER Ca^{2+} levels in *WFS1* and control fibroblasts. No significant difference was observed in the average FRET/CFP ratios of *WFS1* fibroblasts in comparison with controls, indicating that ER Ca^{2+} levels are not disturbed in *WFS1* fibroblasts (**Figure 5.5**).

.

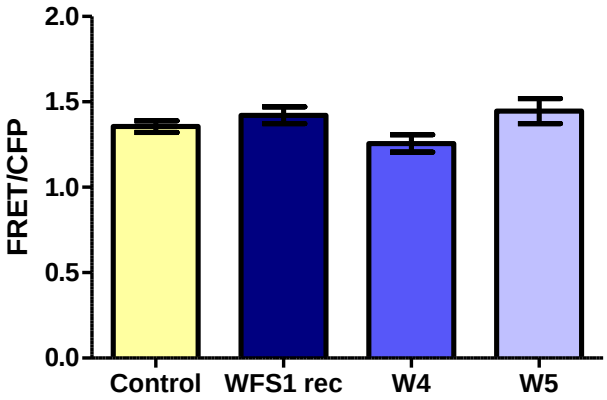

Figure 5.5 Analysis of ER Ca^{2+} levels in *WFS1* fibroblasts. The average FRET/CFP ratios of *WFS1* and control fibroblasts. Data are mean ± SEM. n = ≥ 15. No results were significantly different when compared to controls, two-tailed unpaired t test.

5.3.4 Cytosolic Ca^{2+} levels are not disturbed in WFS1 fibroblasts

The ratiometric Ca^{2+} sensitive fluorescent dye Fura-2-am was used to measure cytosolic [Ca^{2+}] at basal levels and following thapsigargin induced ER Ca^{2+} depletion in *WFS1* and control fibroblasts.

Two thapsigargin concentrations (1 µM and 10 µM) were tested on a Fura-2-AM loaded control cell line to determine the optimal thapsigargin concentration to inhibit SERCA and induce ER Ca^{2+} depletion in fibroblasts. Both 1 µM and 10 µM thapsigargin significantly increased cytosolic [Ca^{2+}] in comparison to basal cytosolic [Ca^{2+}]. There was no significant difference in peak cytosolic [Ca^{2+}] levels induced by 1 µM and 10 µM thapsigargin, therefore 1 µM thapsigargin was chosen for the ER Ca^{2+} depletion experiments (**Figure 5.6**).

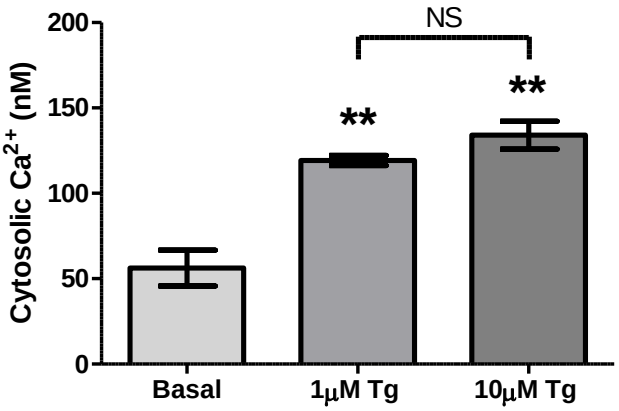

Figure 5.6 Optimization of thapsigargin induced ER Ca^{2+} depletion in fibroblasts. Comparison of cytosolic [Ca^{2+}] in control fibroblasts at basal and following treatment with two thapsigargin (Tg) concentrations: 1 µM and 10 µM. Data are mean ± SEM. n = 3 (triplicate of a single experiment). ** p = ≤ 0.01, when compared to basal, two-tailed unpaired t test. NS - when 1 µM Tg and 10 µM Tg were compared, two-tailed unpaired t test.

The optimized Fura-2-AM assay was used to assess cytosolic Ca^{2+} homeostasis in *WFS1* fibroblasts. There was no significant difference observed in basal cytosolic [Ca^{2+}] in *WFS1* fibroblasts when compared to controls (**Figure 5.7**). Likewise, both peak cytosolic [Ca^{2+}] measured following thapsigargin treatment and thapsigargin sensitive Ca^{2+} stores, defined as the difference between peak cytosolic [Ca^{2+}] and basal cytosolic [Ca^{2+}], were similar between *WFS1* and control fibroblasts (**Figure 5.8**)

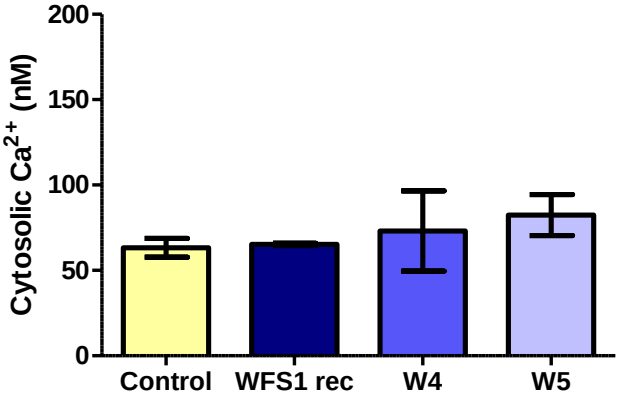

Figure 5.7 Analysis of basal cytosolic [Ca^{2+}] in *WFS1* fibroblasts. Data are mean ± SEM. n = 3. No results were significantly different when compared to controls, two-tailed unpaired t test.

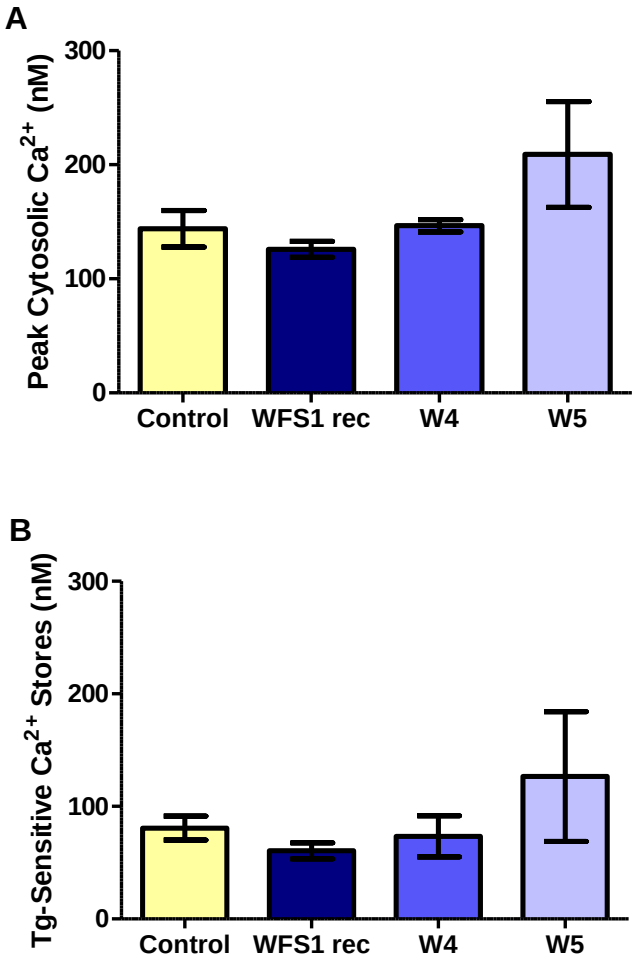

Figure 5.8 Analysis of thapsigargin induced ER Ca^{2+} depletion in *WFS1* fibroblasts. (A, B) Analysis of (A) peak cytosolic [Ca^{2+}] following thapsigargin treatment and (B) thapsigargin (Tg) sensitive Ca^{2+} stores in *WFS1* and control fibroblasts. Data are mean ± SEM. n = 3. No results were significantly different when compared to controls, two-tailed unpaired t test.

5.3.5 ER to mitochondrial Ca^{2+} flux is decreased in WFS1 fibroblasts

To assess ER-mitochondrial Ca^{2+} flux in *WFS1* and control fibroblasts, histamine (100 µM) was used to induce IP_3R dependent ER Ca^{2+} release and the following Ca^{2+} transient was monitored by high speed confocal microscopy in the mitochondria and cytosol with the Ca^{2+} sensitive fluorescent dyes Rhod-2-AM and Fluo-4-AM, respectively (**Figure 5.9**). Representative traces of mitochondrial and cytosolic Ca^{2+} transients are shown in **figure 5.10 B, D**.

Histamine stimulated peak mitochondrial Ca^{2+} levels were significantly reduced in *WFS1* rec and W4 fibroblasts when compared to controls. No significant difference was observed in peak cytosolic Ca^{2+} levels in these cell lines in comparison to controls (**Figure 5.10 A, C**). Conversely, in W5 fibroblasts peak mitochondrial Ca^{2+} levels were normal and peak cytosolic Ca^{2+} levels were significantly reduced in comparison to controls (**Figure 5.10 A, C**).

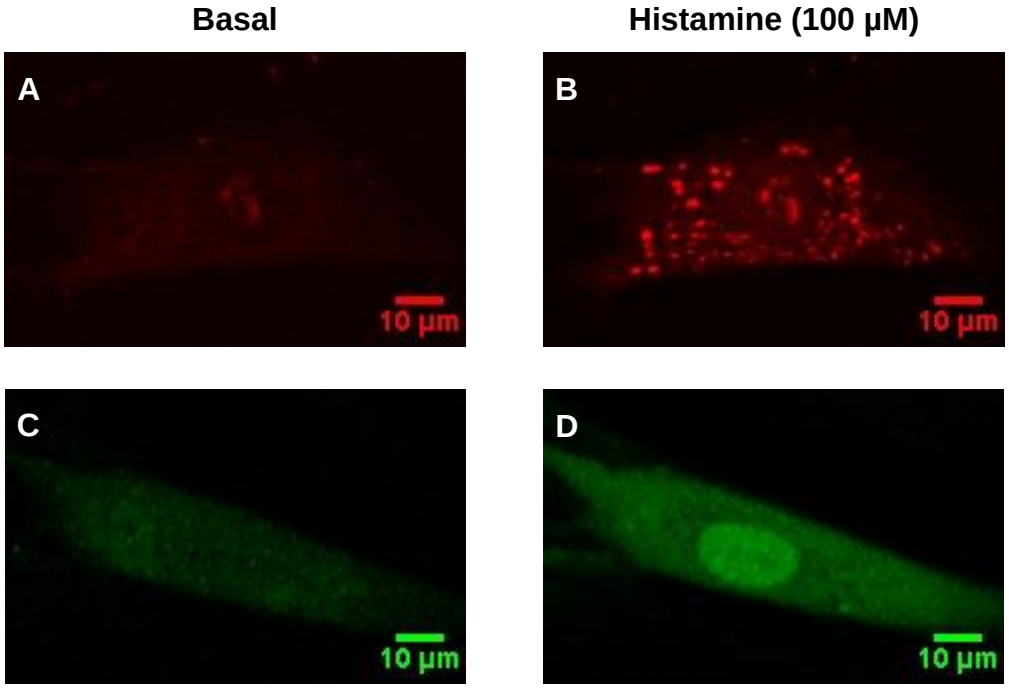

Figure 5.9 Imaging of cellular Ca^{2+} transients with Ca^{2+} sensitive fluorescent dyes. (A-D) Representative images demonstrating analysis of (A, B) mitochondrial Ca^{2+} with Rhod-2-AM (red) and (C, D) cytosolic Ca^{2+} with Fluo-4-AM (green) before and after histamine application. Regions of interest were analysed using Fiji.

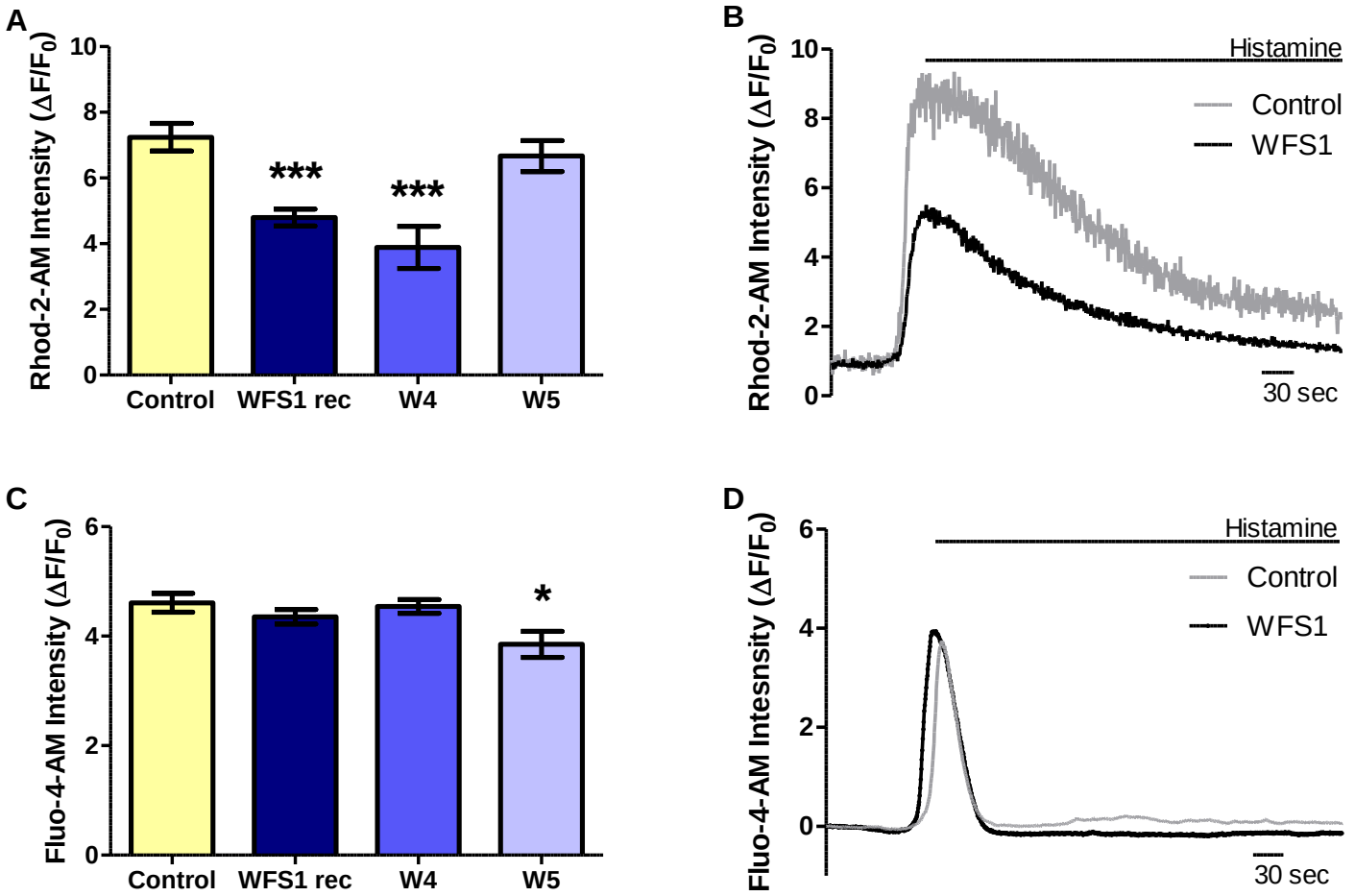

Figure 5.10 Disturbed Ca^{2+} flux in *WFS1* fibroblasts. (A, C) Analysis of average peak (A) mitochondrial and (C) cytosolic Ca^{2+} levels following histamine induced ER Ca^{2+} release in *WFS1* and control fibroblasts. Data are mean ± SEM. n = ≥ 8. *** p = ≤ 0.001, * p = ≤ 0.05, two-tailed unpaired t test. (B, D) Representative traces of (B) mitochondrial and (D) cytosolic Ca^{2+} transients in *WFS1* and control fibroblasts. Where indicated the cells were stimulated with histamine.

5.3.6 *ER-mitochondrial contact is not disturbed in WFS1 fibroblasts with reduced mitochondrial Ca^{2+} uptake*

The interaction between the ER and mitochondria was assessed in *WFS1* and control fibroblasts. Fibroblasts were transfected with GFP Sec61β to detect ER and loaded with MitoTracker Red to stain mitochondria (**Figure 5.11A**). Sixty nine Z-stacks were acquired across the cell at 0.11 µm increments with live cell confocal microscopy. After image deconvolution and 3D reconstruction of Z-axis stacks, colocalization of the two signals was quantified using the Manders' coefficient, M1 and M2, in Huygens Object Analyser (**Figure 5.11B**). M1 indicates the fraction of ER that colocalises with mitochondria and M2 indicates the fraction of mitochondria that colocalises with ER.

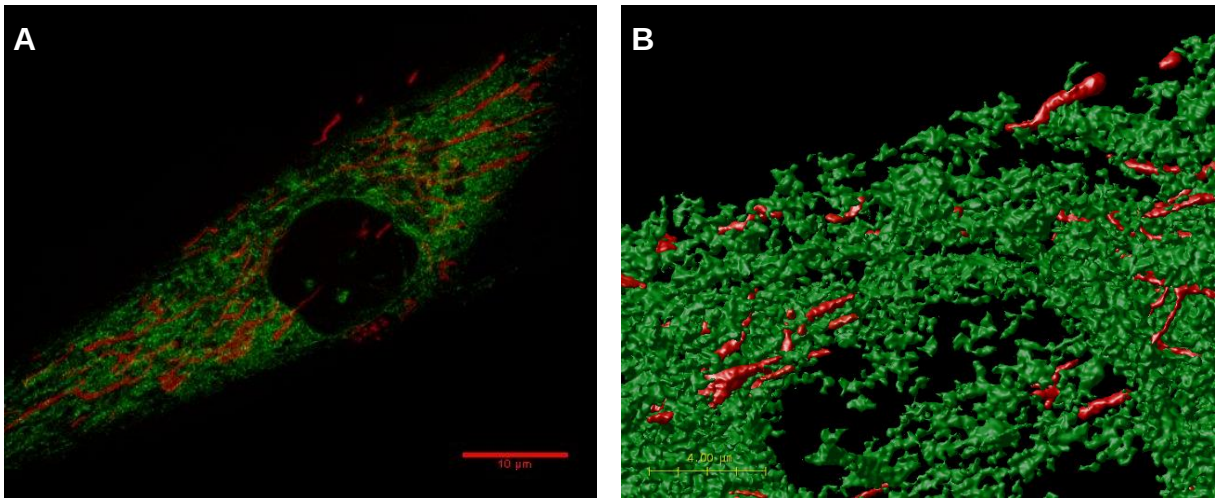

Figure 5.11 Representative images demonstrating analysis of ER-mitochondrial contact. (A) GFP Sec61β labelled ER (green) and MitoTracker Red labelled mitochondria (red) in a control cell line (B) Zoomed 3D-reconstruction of the ER (green) and mitochondrial network (red) in a control cell line created in Huygens Object Analyzer.

There was no significant difference observed in the Manders' coefficient M1 or M2 in *WFS1* rec and W4 fibroblasts when compared to the corresponding Manders' coefficient in controls. In contrast, in W5 fibroblasts Manders' coefficient M2 was significantly increased in comparison to controls and Manders' coefficient M1 was normal; indicating that mitochondria are more closely associated with the ER in this cell line (**Figure 5.12**).

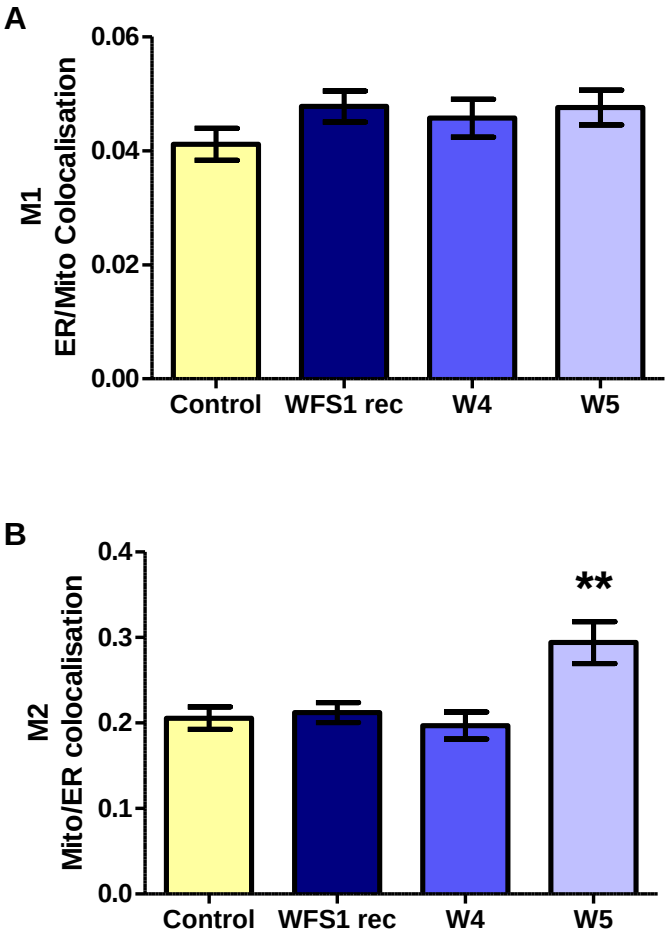

Figure 5.12 Analysis of ER-mitochondrial contact in *WFS1* fibroblasts. (A-B) Analysis of (A) Manders' coefficient M1 ER/Mitochondrial (Mito) colocalisation and (B) Manders' coefficient M2 Mito/ER colocalisation in *WFS1* and control fibroblasts. Data are mean ± SEM. n = ≥ 16. ** p = ≤ 0.01, two-tailed unpaired t test.

5.3.7 Analysis of mitochondrial membrane potential in WFS1 fibroblasts

Mitochondrial membrane potential was assessed in *WFS1* and control fibroblasts using confocal microscopy and the cell permeant dye TMRM which accumulates within mitochondria as a function of membrane potential (**Figure 5.13A**). TMRM signal was normalised to the remaining TMRM signal following dissipation of the membrane potential with FCCP (10 µM). There was no significant difference in TMRM intensity in *WFS1* fibroblasts compared to controls suggesting that mitochondrial membrane potential is normal in *WFS1* fibroblasts (**Figure 5.13B**).

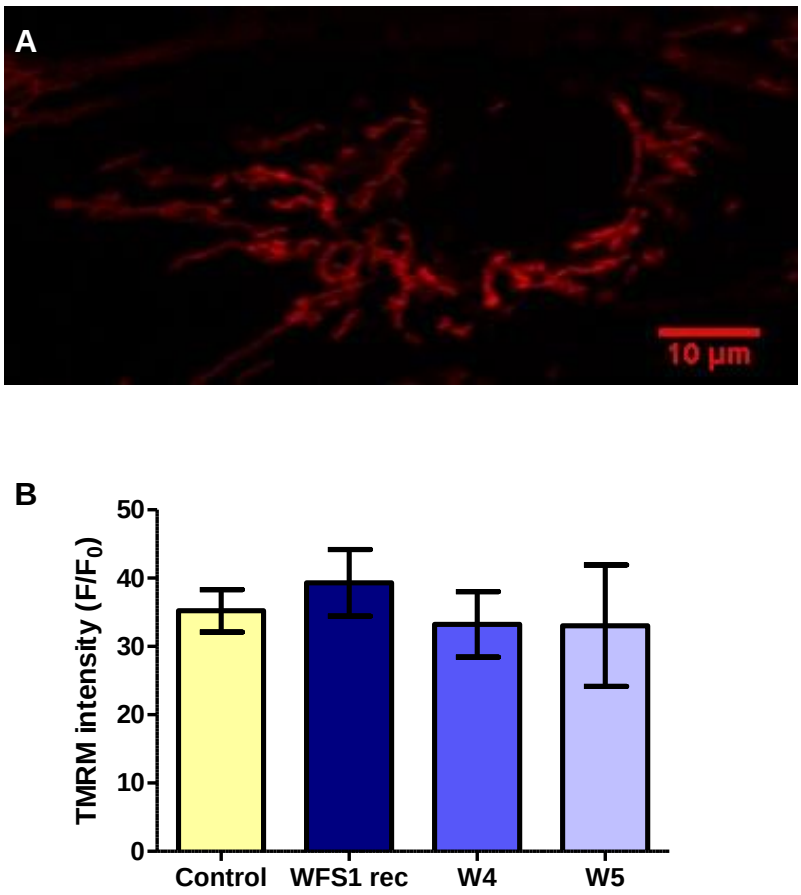

Figure 5.13 Mitochondrial membrane potential assessed by TMRM in *WFS1* fibroblasts. (A) Representative image of a TMRM loaded control fibroblast. Regions of interest were analyzed using Fiji. (B) Analysis of the average TMRM intensity of *WFS1* and control fibroblasts. Data are mean ± SEM. n = ≥ 5. No results were significantly different when compared to controls, two-tailed unpaired t test.

5.3.8 Expression of key Ca^{2+} channels and pumps in WFS1 fibroblasts

Expression of the IP_3R, SERCA, VDAC and MCU were assessed by western blot analysis in *WFS1* and control fibroblasts. There was no significant difference observed in IP_3R levels between *WFS1* and control fibroblasts (**Figure 5.14A, B**). SERCA levels were significantly increased in *WFS1* rec and W4 fibroblasts when compared to controls. SERCA levels were increased in W5 fibroblasts in comparison to controls, although the increase was not statistically significant (**Figure 5.14A, C**). VDAC levels were not significantly different between *WFS1* fibroblasts and controls (**Figure 5.14A, D**). No significant difference was observed in MCU levels in *WFS1* rec and W4 fibroblasts compared to controls, whereas, expression of the MCU was significantly increased in W5 fibroblasts compared with controls (**Figure 5.14A, E**).

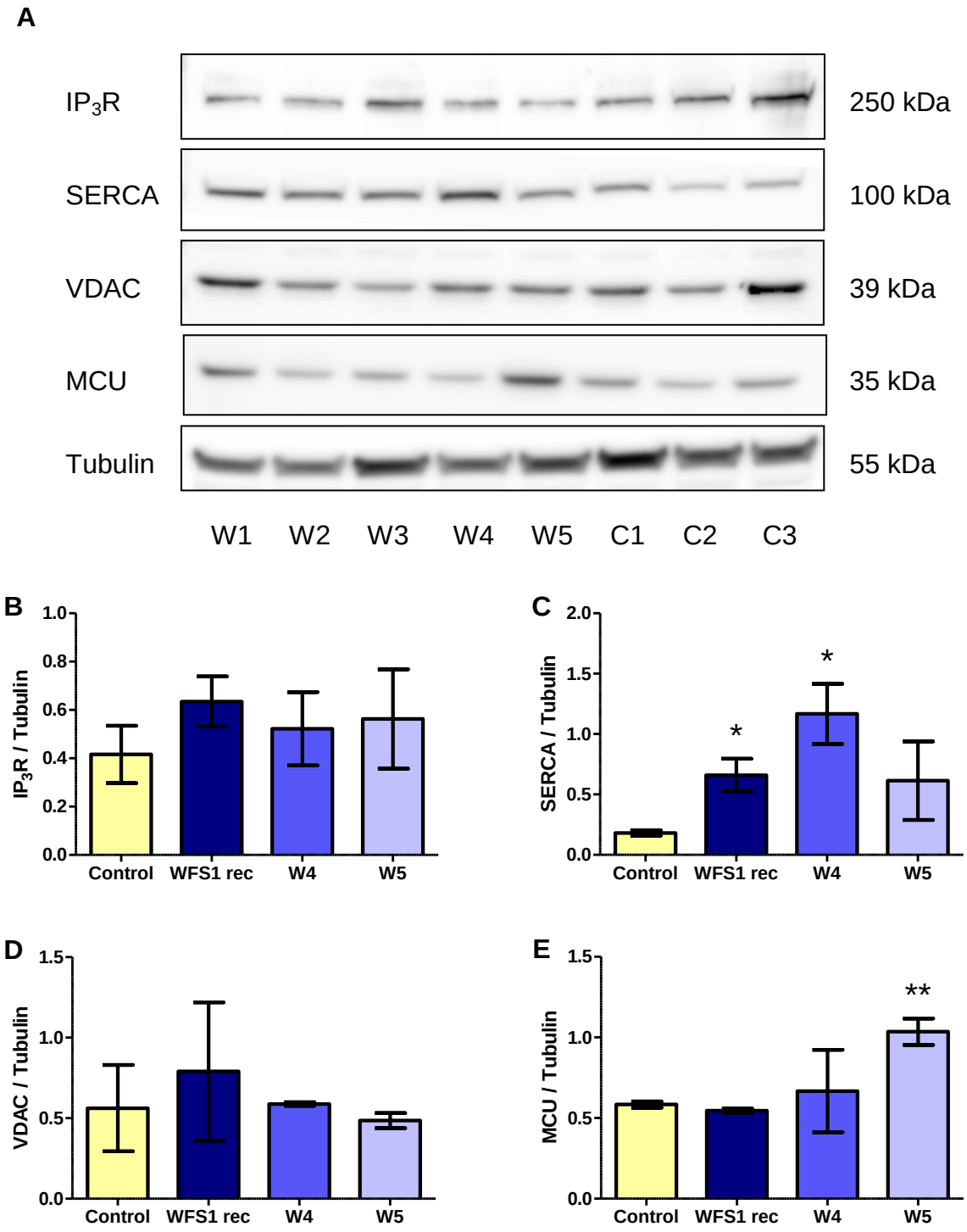

Figure 5.14 Western blot analyses of key Ca^{2+} channels and pumps in *WFS1* fibroblasts. (A) Representative western blots of the IP_3R, SERCA, VDAC and MCU in *WFS1* and control fibroblasts. (B-E) Densitometric analysis of the (B) IP_3R, (C) SERCA, (D) VDAC and (E) MCU levels normalized against tubulin. Data are mean ± SEM. n = ≥ 2. * p = ≤ 0.05, ** p = ≤ 0.01, two-tailed unpaired t test.

5.4 Discussion

This study demonstrates that *WFS1* mutations impair ER-mitochondrial Ca^{2+} flux at the MAM. A number of potential mechanisms underlying reduced Ca^{2+} flux were explored, but the exact nature of reduced mitochondrial Ca^{2+} uptake needs to be further clarified. Interestingly, one cell line carrying a dominant *WFS1* mutation (W5) showed normal ER-mitochondrial Ca^{2+} flux and this was associated with increased mitochondrial-ER contact and upregulation of MCU expression. Although speculative, the latter could represent a secondary compensatory mechanism that partially alleviates the deleterious impact of this specific *WFS1* mutation.

Five primary fibroblast cell lines established from Wolfram syndrome patients were included in this study (**Table 5.1**). In agreement with previous studies, recessive *WFS1* mutations caused complete loss of the Wolframin protein. Nonsense and frameshift mutations in the *WFS1* gene have been shown to cause protein loss due to unstable *WFS1* mRNA and subsequent nonsense mediated mRNA decay (Hofmann *et al.*, 2003). Missense mutations in the *WFS1* gene are suggested to cause Wolframin loss due to protein instability and rapid proteasomal degradation (Hofmann and Bauer, 2006). These mechanisms likely contribute to Wolframin loss in the fibroblasts harbouring recessive *WFS1* mutations. In contrast, dominant missense mutations in *WFS1* did not appear to affect the steady-state levels of Wolframin. However, there was variability in Wolframin expression across the control cell lines, including one control cell line showing notably increased Wolframin levels in comparison with the two other control cell lines. The pathogenic mechanisms of dominant *WFS1* mutations still remain to be defined, although a dominant negative effect has been proposed (Hogewind *et al.*, 2010; Rendtorff *et al.*, 2011).

No evidence of ER stress was observed in *WFS1* fibroblasts by western blot analysis of the ER chaperones GRP94 or Bip suggesting that *WFS1* mutations do not induce ER stress in primary fibroblast cell lines. Consistent with this observation, it has previously been demonstrated that Wolfram syndrome patient and control fibroblasts were not sensitive to treatment with a range of ER stress inducers including brefeldin A, thapsigargin, ionophore 2957, bradykinin and lactocysteine (Philbrook *et al.*, 2005). ER stress induction in *Wfs1* deficient mice was also found specifically in pancreatic β-cells and not in heart, skeletal muscle or brown adipose tissue (Yamada *et al.*, 2006). Together, these results suggest that ER stress

induction due to *WFS1* mutations is likely to be cell type specific. The induction of ER stress by *WFS1* deficiency in pancreatic β-cells has been explained by the heavy demands placed on the ER in β-cells during insulin biosynthesis, which sensitizes β-cells to disturbances in ER homeostasis (Fonseca *et al.*, 2010). ER stress has also been described in *WFS1* deficient neurones and in the retina of *Wfs1* deficient mice (Gharanei *et al.*, 2013; Bonnet Wersinger *et al.*, 2014; Cagalinec *et al.*, 2016). In order to conclusively confirm the absence of ER stress in *WFS1* fibroblasts more sensitive methods such as qRT-PCR analysis of the UPR signalling pathways or luciferase based promoter assays that reflect UPR activation should be considered in addition to western blot analysis (Oslowski and Urano, 2011).

Disturbed cellular Ca^{2+} homeostasis is emerging as a key pathogenic mechanism in Wolfram syndrome. Previous studies have primarily focused on the impact of *WFS1* deficiency on Ca^{2+} homeostasis in the ER and cytosolic compartments. The transfer of Ca^{2+} from the ER to mitochondria is an important mechanism by which the ER and mitochondria communicate to maintain cellular homeostasis and was therefore assessed in *WFS1* fibroblasts. Importantly, following IP_3R dependent ER Ca^{2+} release, significantly reduced peak mitochondrial Ca^{2+} levels were observed in *WFS1* rec and W4 fibroblasts, demonstrating that *WFS1* mutations had a deleterious impact on Ca^{2+} flux between the ER and mitochondria. Interestingly, normal ER-mitochondrial Ca^{2+} flux was found in W5 fibroblasts. Only one study has previously assessed mitochondrial Ca^{2+} homeostasis secondary to *WFS1* deficiency using *WFS1* knockdown HEK293 cells (Takei *et al.*, 2006). In this particular experimental model, peak mitochondrial [Ca^{2+}] was significantly reduced upon Ca^{2+} readdition following ER Ca^{2+} depletion induced by cyclopiazonic acid (CPA; SERCA inhibitor) (Takei *et al.*, 2006). This previous study is not entirely comparable with the present analysis of ER-mitochondrial Ca^{2+} flux in *WFS1* fibroblasts as two different methods of ER Ca^{2+} modulation were used. Nevertheless, both studies suggest that mitochondrial Ca^{2+} uptake is disturbed by *WFS1* deficiency. MAM dysfunction is increasingly being implicated in other neurodegenerative disorders, establishing disturbed ER-mitochondria interactions as an important disease mechanism (Area-Gomez *et al.*, 2012; Guardia-Laguarta *et al.*, 2014). The reduced ER-mitochondrial Ca^{2+} flux found in *WFS1* fibroblasts provides a potential mechanism by which *WFS1* mutations could impact mitochondrial function.

No disturbance was observed in ER or cytosolic Ca^{2+} homeostasis in *WFS1* fibroblasts, which is in contrast with previous studies showing disturbed ER and cytosolic Ca^{2+} homeostasis in *WFS1* deficient cells (Takei *et al.*, 2006; Hara *et al.*, 2014; Lu *et al.*, 2014; Cagalinec *et al.*, 2016). Although, the results of this study are consistent with the normal ER Ca^{2+} homeostasis reported in *WFS1* deficient neurones and the normal basal cytosolic [Ca^{2+}] observed in a *WFS1* depleted MIN6 insulinoma cell line (Zatyka *et al.*, 2015; Cagalinec *et al.*, 2016). Contrasting results have been reported in the different *WFS1* deficient models that have been characterised, including pancreatic β-cell lines, neuronal cell lines, HEK293 cells, and the Wolfram syndrome fibroblasts used in this study. The effect of *WFS1* deficiency on cellular Ca^{2+} homeostasis therefore appears to be cell type dependent. One limitation of this study is that fibroblasts may not be fully representative of the neuropathology of Wolfram syndrome and it would preferable to study the neuronal populations that are affected in this disorder, including RGCs. Fibroblasts have been shown to be resistant against most stressors and it is likely that fibroblasts are less susceptible to *WFS1* deficiency than pancreatic β or neuronal cell lines, which are anatomically and functionally more complex cell types (Philbrook *et al.*, 2005; Auburger *et al.*, 2012).

A number of potential molecular mechanisms underlying reduced ER-mitochondrial Ca^{2+} flux in *WFS1* fibroblasts were investigated including ER-mitochondrial interactions, mitochondrial membrane potential and protein expression of Ca^{2+} channels. However, *WFS1* fibroblasts that previously showed reduced ER-mitochondrial Ca^{2+} flux showed no significant disturbance in any of these parameters. Additionally, measurement of ER Ca^{2+} demonstrated that reduced ER-mitochondrial Ca^{2+} flux was not due to depletion of the ER Ca^{2+} store. In contrast, W5 fibroblasts, showed significantly increased mitochondrial-ER association and upregulation of MCU expression. Increased ER-mitochondrial areas of contact are known to correlate with increased mitochondria Ca^{2+} uptake following ER Ca^{2+} release (Csordas *et al.*, 2006). Moreover, MCU overexpression has been shown to increase mitochondrial Ca^{2+} buffering following agonist-induced IP_3R-dependent ER Ca^{2+} release, which in turn decreased cytosolic Ca^{2+} transients (De Stefani *et al.*, 2011). The increased ER-mitochondrial apposition and the greater MCU expression in W5 fibroblasts could therefore represent a compensatory mechanism to maintain

mitochondrial Ca^{2+} uptake. These observations can explain the normal mitochondrial transients and significantly reduced peak of cytosolic Ca^{2+} transients observed in W5 fibroblasts. It is unclear why W5 fibroblasts have a different cellular phenotype to the *WFS1* rec and W4 fibroblasts. The p.A684V mutation in W5 fibroblasts has previously been reported in six families with Wolfram syndrome so there can be no doubt about its pathogenicity (Rendtorff *et al.*, 2011). Further studies are required to investigate the apparent compensatory mechanisms that are active in W5 fibroblasts as these could help inform possible therapeutic strategies.

The observations in W5 fibroblasts confirm that the assays used to measure ER-mitochondrial apposition and Ca^{2+} channel expression are sensitive enough to identify any disturbance in the *WFS1* fibroblasts with reduced ER-mitochondria Ca^{2+} flux. Nevertheless, there are limitations to the ER-mitochondria imaging analysis used for this study on *WFS1* fibroblasts, including the spatial resolution limits of confocal microscopy. Furthermore, western blot analysis does not exclude a functional defect in the Ca^{2+} signalling apparatus at the MAM. A recent study has demonstrated that IP_3R mediated Ca^{2+} release is reduced in *WFS1* deficient neurones (Cagalinec *et al.*, 2016). It is possible that a similar mechanism is active in *WFS1* fibroblasts and is responsible for the reduced mitochondrial Ca^{2+} uptake following IP_3R-dependent ER Ca^{2+} release. Future investigations should determine whether Wolframin directly interacts with and regulates the IP_3R. Moreover, investigation of the MAM domain with higher resolution imaging modalities such as electron microscopy and quantification of the IP_3R and VDAC interaction would further clarify the nature of mitochondrial Ca^{2+} defect in *WFS1* fibroblasts (Tubbs *et al.*, 2014). These investigations may also further elucidate the molecular mechanism underlying the compensatory response in W5 fibroblasts.

Finally, SERCA expression was assessed in *WFS1* fibroblasts. It has previously been demonstrated that Wolframin is involved in the regulation of SERCA and that SERCA levels are increased in *WFS1* depleted cells (Zatyka *et al.*, 2015). In agreement with this previous study, SERCA levels were significantly increased in all the *WFS1* fibroblasts, except for W5 fibroblasts. Increased SERCA expression did not correlate with any disturbance in basal ER Ca^{2+} levels or peak cytosolic [Ca^{2+}] following SERCA inhibition in *WFS1* fibroblasts. Further investigations are required to determine the impact of increased SERCA expression in *WFS1* fibroblasts.

In summary, this study demonstrates a functional defect in the ER-mitochondrial interaction in fibroblasts harbouring recessive or dominant *WFS1* mutations, thus, providing a powerful mechanism by which *WFS1* mutations can disturb mitochondrial function (**Figure 5.15**). The reduced ER-mitochondrial Ca^{2+} flux could impact on a host of mitochondrial functions regulated by Ca^{2+} uptake such as OXPHOS and mitochondrial-mediated apoptosis. These pathological mechanisms are likely to be relevant to the underlying neuropathology of Wolfram syndrome, and these results support mitochondrial dysfunction as a key player that could potentially be modulated to slow or halt disease progression for patients with progressive and disabling visual loss and neurological deficits.

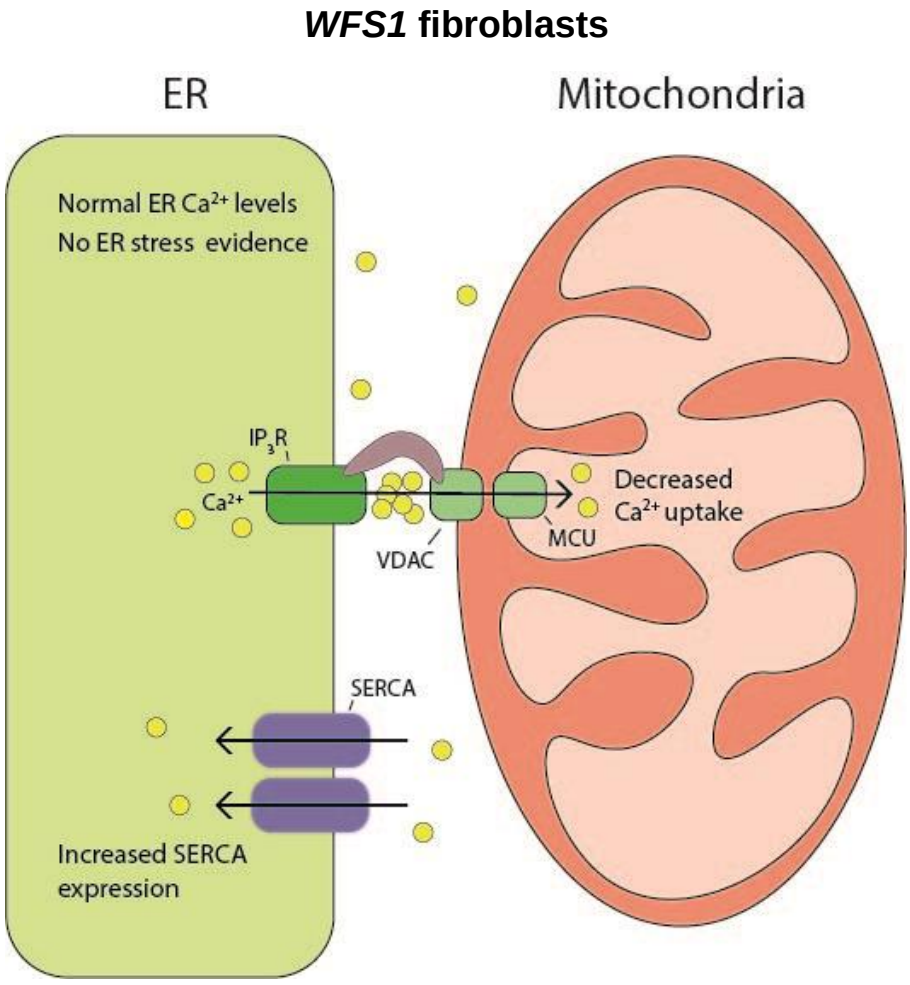

Figure 5.15 Schematic model highlighting the proposed dysfunction in *WFS1* fibroblasts. *WFS1* mutations had a deleterious impact on ER-mitochondrial Ca^{2+} flux. No difference was found in ER Ca^{2+} levels, ER-mitochondrial apposition or expression level of key Ca^{2+} channels, although, SERCA levels were increased.

Chapter 6. Mitochondrial Function in Wolfram Syndrome 1

6.1 Introduction

The functional interaction between the ER and mitochondria at the MAM is critical for cellular homeostasis and MAM dysfunction is increasingly being recognised as an important contributor to both monogenic and complex neurodegenerative diseases (Paillusson *et al.*, 2016). As described in Chapter 5, fibroblasts established from patients with Wolfram syndrome harbouring dominant or recessive *WFS1* mutations showed evidence of disturbed ER-mitochondrial interactions. An important observation was that *WFS1* mutations had a deleterious impact on ER-mitochondrial Ca^{2+} transfer.

The transfer of Ca^{2+} from the ER to the mitochondria is an essential function of the MAM and regulates cellular Ca^{2+} homeostasis, mitochondrial bioenergetics and mitochondrial-mediated apoptosis (van Vliet *et al.*, 2014). Under basal conditions, ER-mitochondrial Ca^{2+} transfer is necessary to stimulate OXPHOS and maintain ATP synthesis (Cardenas *et al.*, 2010). A rise in mitochondrial matrix Ca^{2+} promotes respiration and ATP production by stimulating the Ca^{2+}-dependent dehydrogenases of the TCA cycle, increasing the production of reducing equivalents which drive the respiratory chain, and by activating complex V (Glancy and Balaban, 2012). Conversely, excessive mitochondrial Ca^{2+} uptake is associated with the induction of cell death and factors that decrease or increase ER-mitochondrial Ca^{2+} flux have been shown to reduce or enhance the susceptibility of cells to apoptosis induction, respectively (Bononi *et al.*, 2013).

To determine the consequences of disturbed ER-mitochondrial interactions on mitochondrial function in Wolfram syndrome, mitochondrial bioenergetics and cell viability were characterised in *WFS1* fibroblasts (**Table 5.1**). OXPHOS function was determined by measuring mitochondrial respiration, cellular ATP content and ROS levels. Cell viability was assessed under basal conditions and following the treatment with selected cellular stressors including STS, a non-specific kinase inhibitor that induces apoptosis; t-BH, an oxidative stressor that has also been suggested to mobilise Ca^{2+} from the ER to the mitochondria (Bononi *et al.*, 2013); and thapsigargin, an inhibitor of the SERCA that induces ER stress through ER Ca^{2} depletion (Zatyka *et al.*, 2015).

6.2 Results

6.2.1 Analysis of mitochondrial respiration in WFS1 fibroblasts

To investigate mitochondrial respiratory function, OCR was measured in intact *WFS1* and control fibroblasts using the Seahorse XF^{e} Extracellular Flux Analyzer. OCR was measured at basal and following the sequential addition of: (i) oligomycin to inhibit complex V, (ii) FCCP to measure maximal uncoupler stimulated OCR and (iii) rotenone together with antimycin A to inhibit mitochondrial respiration and measure non-mitochondrial OCR (**Figure 6.1**).

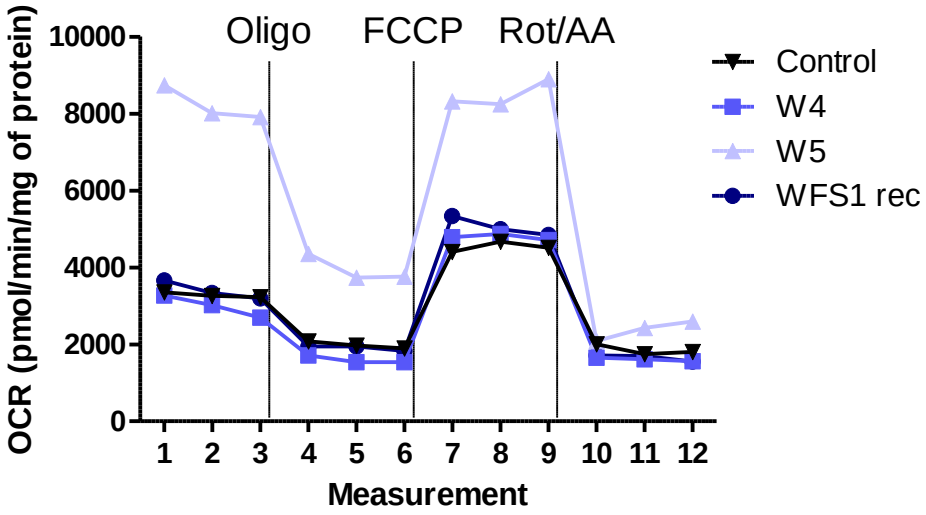

Figure 6.1 Representative Seahorse measurement of OCR in *WFS1* fibroblasts. Example OCR traces for *WFS1* rec (dark blue), W4 (blue), W5 (light blue) and control (black) fibroblasts. Oligomycin (Oligo), FCCP and rotenone/antimycin A (Rot/AA) were added where indicated.

Four parameters of mitochondrial respiratory function were calculated as described in Section 3.11.1: (i) basal respiration, (ii) ATP-linked respiration, (iii) proton leak and (iv) maximal respiration. A disturbance in one or more of these parameters would be indicative of disturbed respiratory function. However, no significant difference was observed in all four parameters in *WFS1* rec and W4 fibroblasts compared to controls (**Figure 6.2**). Surprisingly, W5 fibroblasts showed significantly increased OCR in all four parameters when compared to controls (**Figure 6.2**).

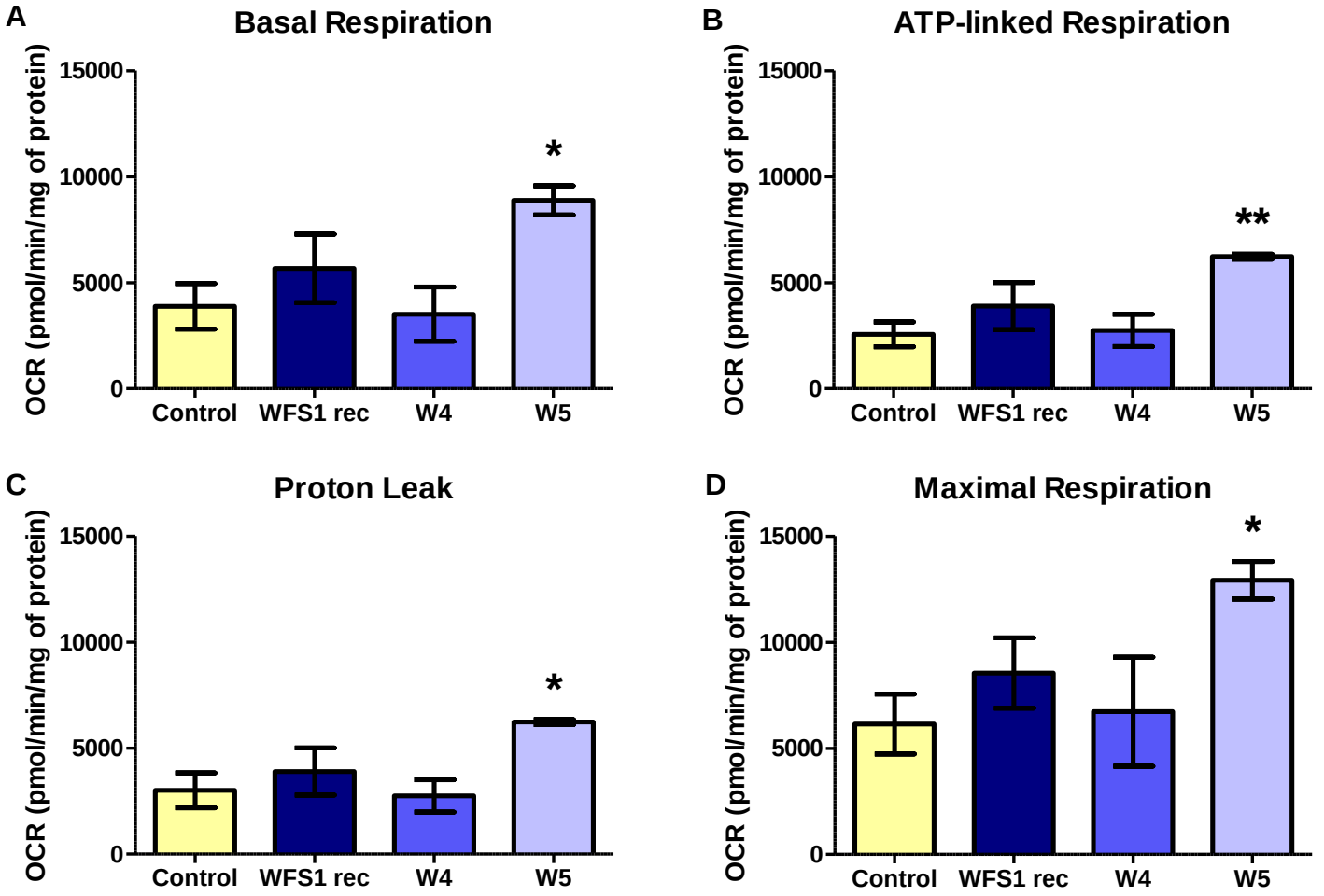

Figure 6.2 Parameters of mitochondrial respiratory function in *WFS1* fibroblasts determined by Seahorse analysis. (A) Basal respiration. (B) ATP-linked respiration. (C) Proton Leak. (D) Maximal Respiration. Data are mean ± SEM. n = 3. * p = ≤ 0.05, ** p = ≤ 0.01, two-tailed unpaired t test.

6.2.2 Complex I-dependent respiration is reduced in WFS1 fibroblasts

To assess the absence of a respiratory defect in *WFS1* fibroblasts with reduced mitochondrial Ca^{2+} uptake, complex I-dependent respiration and complex II-dependent respiration were assessed in permeabilized *WFS1* and control fibroblasts with the Oxygraph respirometer (**Figure 6.3A**). The results were expressed as flux control ratios.

The CI/(CI+CII) ratio which indicates complex I-dependent respiration was significantly reduced compared to controls in *WFS1* rec and W4 fibroblasts. In contrast, the CI/(CI+CII) ratio was not significantly different between controls and W5 fibroblasts (**Figure 6.3B**). No significant difference was observed in the CII/(CI+CII) ratios between *WFS1* and control fibroblasts (**Figure 6.3C**), indicating complex II-dependent respiration is normal in *WFS1* fibroblasts.

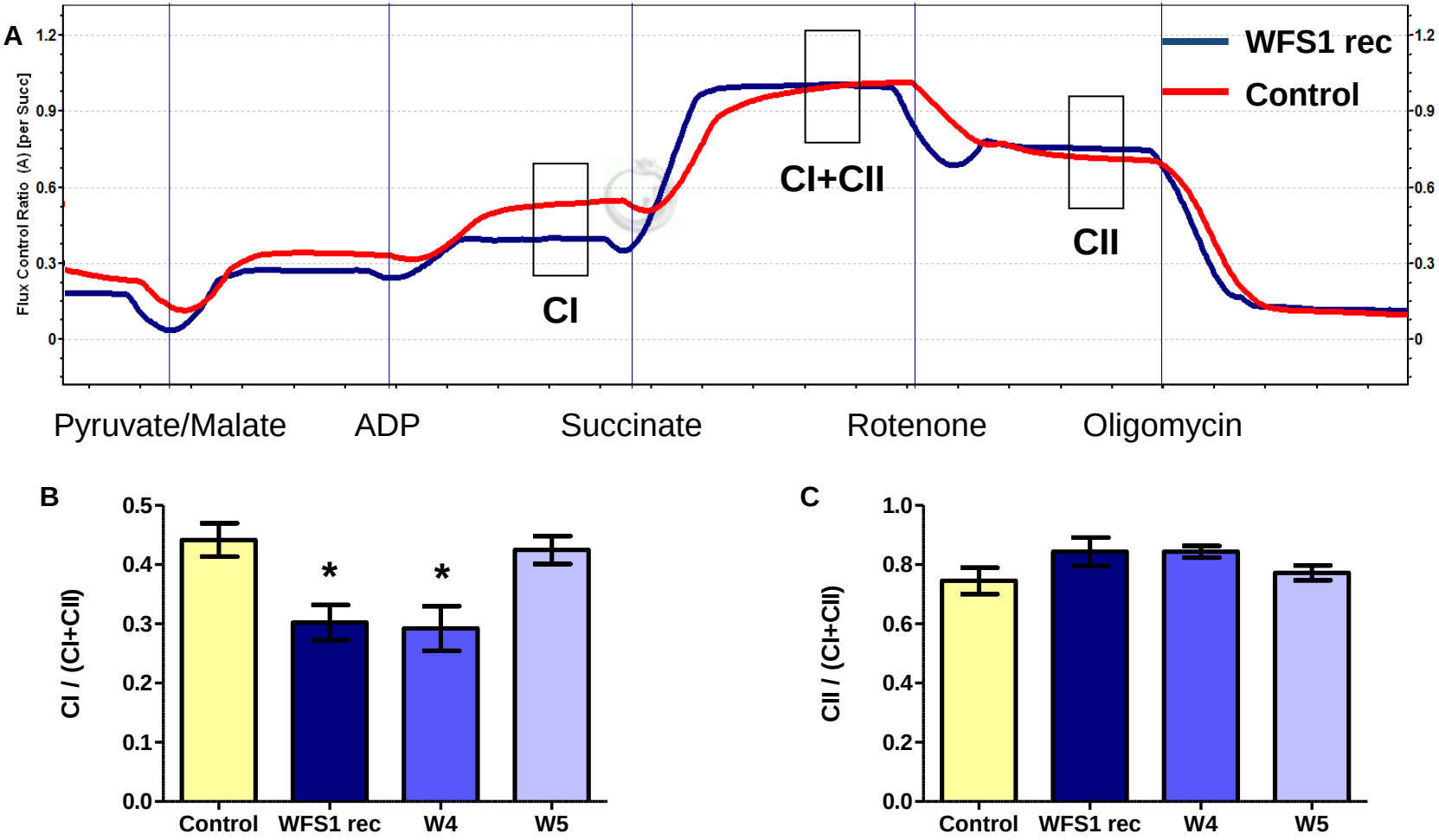

Figure 6.3 Complex I-dependent respiration is reduced in *WFS1* fibroblasts. (A) Example Oxygraph traces of permeabilized *WFS1* (blue) and control (red) fibroblasts. Substrates and inhibitors were added where indicated. CI, CII and CI+CII respiration were determined as shown. (B, C) Analysis of (B) CI/(CI+CII) and (C) CII/(CI+CII) ratios in permeabilized *WFS1* and control fibroblasts. Data are mean ± SEM. n = ≥ 3. * p = ≤ 0.05, two-tailed unpaired t test.

6.2.3 Pyruvate dehydrogenase regulation in WFS1 fibroblast

To further investigate the reduced complex I-dependent respiration observed in *WFS1* fibroblasts the phosphorylation status of the PDH (pPDH) at serine 293 was assessed by western blot analysis. However, no significant difference was observed in PDH phosphorylation between *WFS1* and control fibroblasts (**Figure 6.4**). Suggesting that substrate flux through the PDH is not disturbed in *WFS1* fibroblasts under basal conditions.

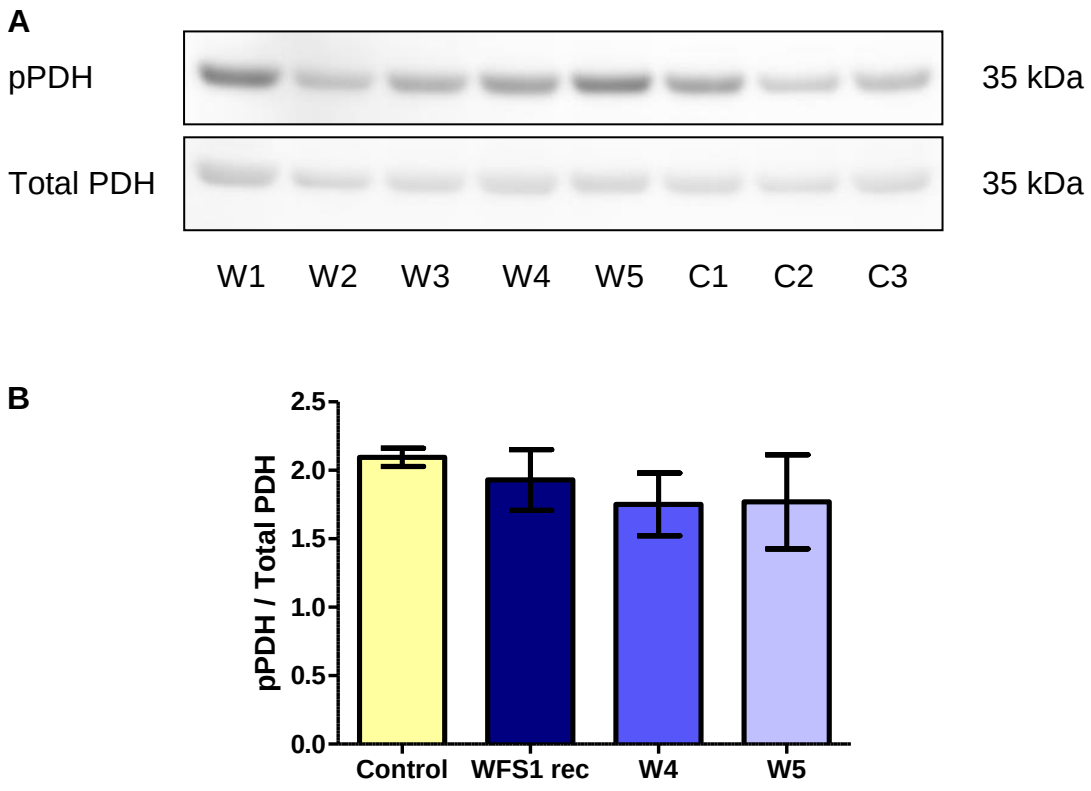

Figure 6.4 PDH regulation in *WFS1* fibroblast. (A) Representative western blots of pPDH and total PDH in *WFS1* and control fibroblasts. (B) Densitometric analysis of pPDH levels normalized against total PDH. Data are mean ± SEM. n = 3. No results were significantly different when compared to controls, two-tailed unpaired t test.

6.2.4 Analysis of ATP content in WFS1 fibroblasts

To conclude the OXPHOS analysis, ATP content was determined in *WFS1* and control fibroblasts with the CellTiter-Glo ATP assay, in which luminescence signal is proportional to ATP content. For a thorough analysis, ATP content was determined under four conditions: (i) glucose, (ii) 2-DG, (iii) oligomycin and (iv) 2-DG and oligomycin, as described in Section 3.11.3. ATP content was depleted under 2-DG and oligomycin in all cell lines, confirming the assay functioned as expected (**Figure 6.5**).

ATP content was normal in *WFS1* rec and W4 fibroblasts under all four assay conditions, confirming the lack of a severe OXPHOS defect in these fibroblasts (**Figure 6.5**). In contrast, ATP content was increased under glucose and significantly increased under 2-DG conditions in W5 fibroblasts compared to controls (**Figure 6.5**). Notably, 2-DG treatment resulted in decreased ATP content in comparison to glucose in all cell lines except W5 fibroblasts where ATP content was mostly maintained. Moreover, no significant difference was observed between W5 fibroblasts and controls under oligomycin conditions, where fibroblasts are reliant on glycolysis for ATP, further suggesting that the increased ATP content in W5 fibroblasts is directly related to OXPHOS function (**Figure 6.5**).

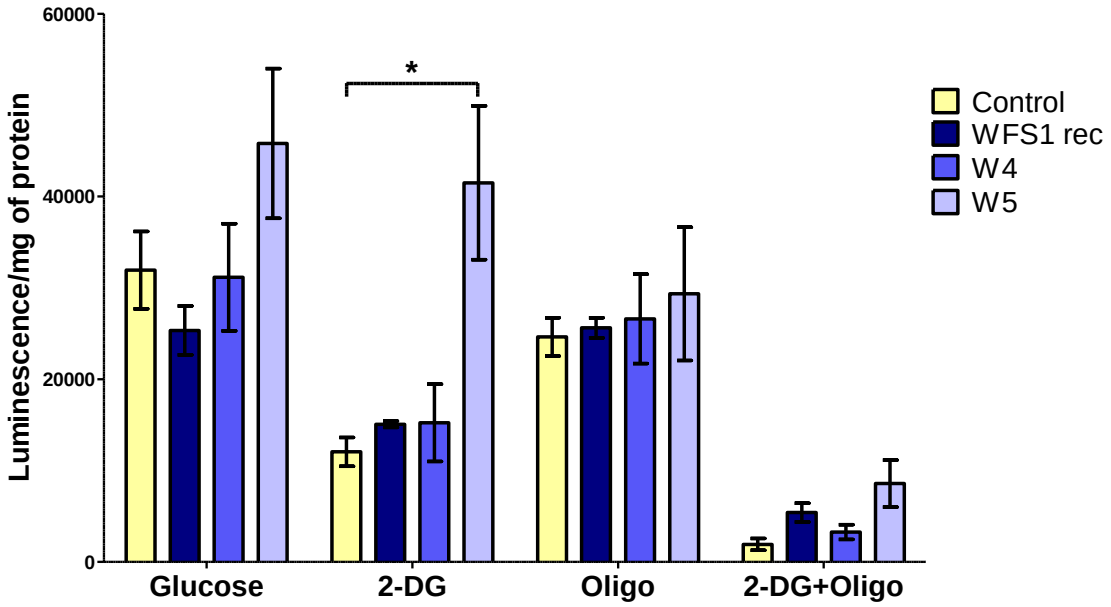

Figure 6.5 ATP content in *WFS1* fibroblasts. ATP content was assessed in *WFS1* and control fibroblasts under four conditions: glucose, 2-DG, oligomycin (oligo) and 2-DG+oligo. Data are mean ± SEM. n = 4. * p = ≤ 0.05, two-tailed unpaired t test

6.2.5 Determination of ROS levels in WFS1 fibroblasts

ROS levels were assessed in *WFS1* and control fibroblasts using H_2DCFDA, an indicator of generalised oxidative stress that fluoresces upon oxidation. ROS levels were determined under basal conditions and following H_20_2 treatment as a positive control. As expected, H_20_2 treatment increased ROS levels compared to basal conditions. No significant difference was observed in ROS levels between *WFS1* and control fibroblasts under either condition.

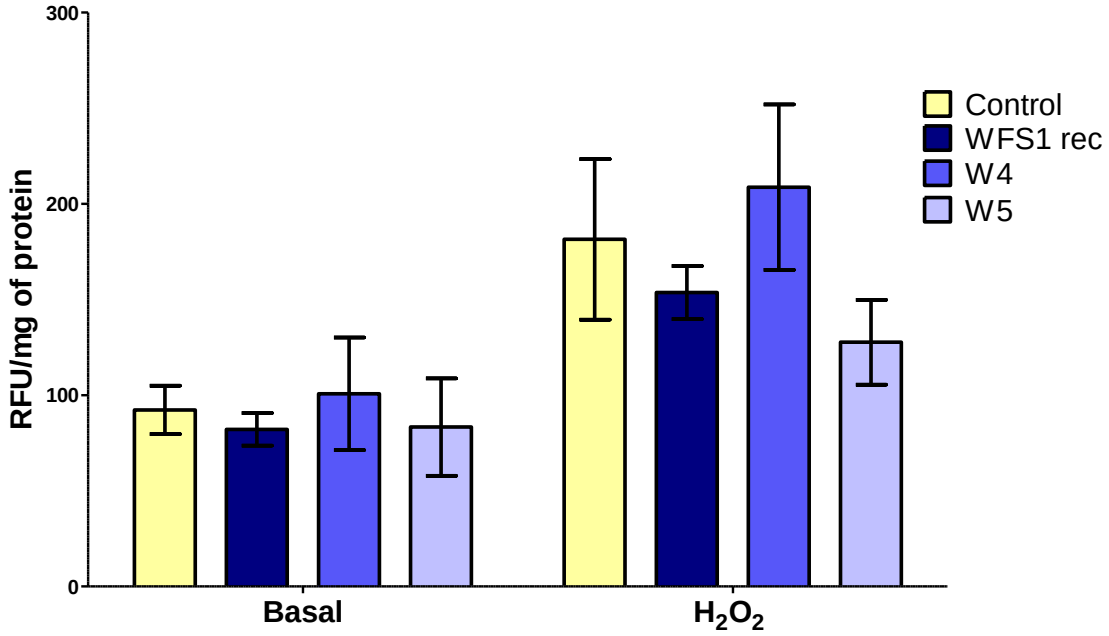

Figure 6.6 Assessment of ROS levels in *WFS1* fibroblasts using H_2DCFDA. ROS levels at basal and following H_20_2 treatment. Data are mean ± SEM. n = 3. No results were significantly different when compared to controls, two-tailed unpaired t test.

6.2.6 mtDNA Copy Number Analysis in WFS1 fibroblasts

The copy number of mtDNA was measured via RT-qPCR in *WFS1* and control fibroblasts. Amplification of the mtDNA gene ND1 was compared to the nuclear-encoded gene B2M. No significant difference was observed in mtDNA copy number between *WFS1* and control fibroblasts (**Figure 6.7**).

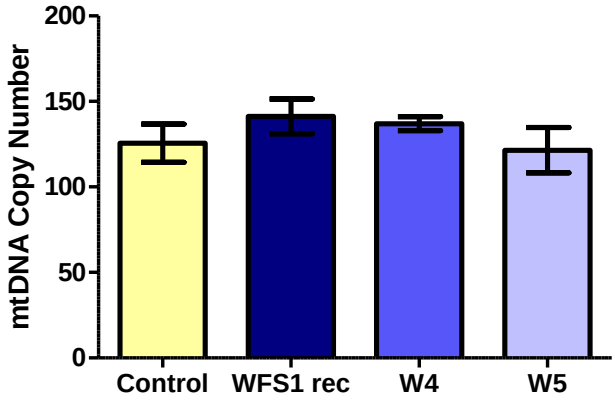

Figure 6.7 mtDNA Copy Number in *WFS1* fibroblasts. Data are mean ± SEM. n = 3. No results were significantly different when compared to controls, two-tailed unpaired t test.

6.2.7 Sensitivity of WFS1 fibroblasts to cell stressors

Cell viability was determined in *WFS1* and control fibroblasts following treatment with STS (1 µM), t-BH (200 µM) or thapsigargin (4 µM) at 2, 5 and 8 hours with the MTT assay. No significant difference was observed in cell viability between *WFS1* and control fibroblasts following treatment with STS or t-BH at all-time points (**Figure 6.8 A, B**). Unexpectedly, following treatment with thapsigargin, cell viability was significantly increased in *WFS1* rec and W4 fibroblasts compared with controls. In contrast, thapsigargin treatment seemed to reduce cell viability in W5 fibroblasts compared with controls, although this decrease was not statistically significant at any time point (**Figure 6.8C**).

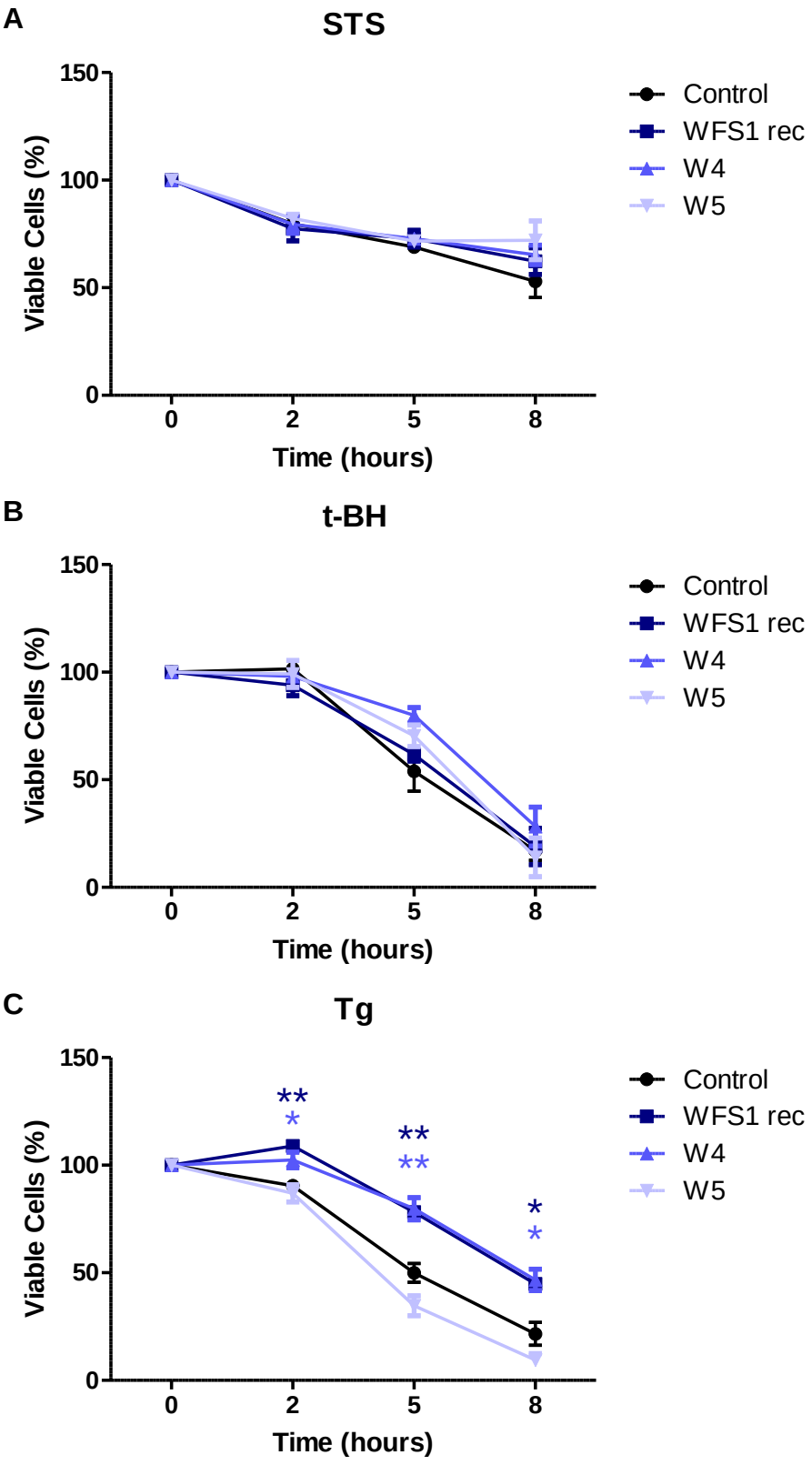

Figure 6.8 *Viability* of *WFS1* following treatment with cell stressors.
(A-C) Cell viability was determined in *WFS1* and control fibroblasts following treatment with (A) STS (B) t-BH or (C) thapsigargin (Tg) at 2, 5 and 8 hours with the MTT assay. Data are mean ± SEM. n = ≥ 3. * p = ≤ 0.05, ** p = ≤ 0.01, two-tailed unpaired t test.

6.2.8 Caspase 3 Activity

Apoptosis induction is usually associated with caspase activation; therefore, measurement of caspase 3 activity determines whether cells are committed to irreversible apoptosis. Caspase 3 activity was assessed in *WFS1* and control fibroblasts at basal condition and following treatment with STS (1 µM), t-BH (200 µM) or thapsigargin (4 µM) for 5 hours by measurement of Ac-DEVD-AFC substrate processing. Caspase 3 activity was not significantly different between *WFS1* and control fibroblasts for all conditions (**Figure 6.9**). STS treatment induced increased levels of caspase 3 activity in all cell lines compared to basal conditions, suggesting the assay functioned as expected.

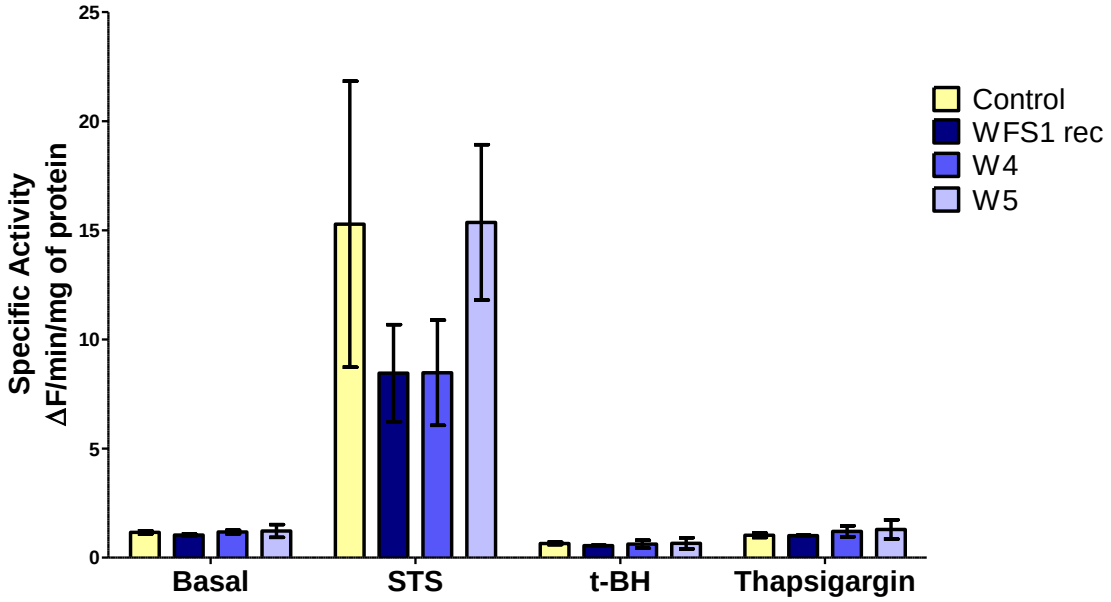

Figure 6.9 Caspase 3 activities in *WFS1* fibroblasts following treatment with cell stressors. Caspase 3 activity was determined in *WFS1* and control fibroblasts using Ac-DEVD-AFC substrate processing under basal conditions and following treatment with STS, t-BH or thapsigargin for 5 hours. Data are mean ± SEM. n = 3. No results were significantly different when compared to controls, two-tailed unpaired t test.

6.3 Discussion

This study investigated the downstream consequences of disturbed ER-mitochondrial interactions in fibroblasts established from Wolfram syndrome patients with *WFS1* mutations by characterising mitochondrial bioenergetics and cell viability. No severe OXPHOS defect was observed in *WFS1* rec or W4 fibroblasts, which previously showed reduced ER-mitochondrial Ca^{2+} flux. However, these fibroblasts did have a selective decrease in complex I-dependent respiration, which has previously been reported in cell lines harbouring pathogenic *OPA1* mutations or the primary LHON mtDNA mutations (Baracca *et al.*, 2005; Chevrollier *et al.*, 2008; Zanna *et al.*, 2008). In contrast, OXPHOS was significantly enhanced in W5 fibroblasts, which had normal mitochondrial Ca^{2+} uptake. Interestingly, *WFS1* rec and W4 fibroblasts were less sensitive to treatment with the ER stressor thapsigargin. This observation contrasts with the enhanced susceptibility to ER stress induced cell death found in *WFS1* deficient β-cells (Ishihara *et al.*, 2004; Fonseca *et al.*, 2005; Yamada *et al.*, 2006).

Despite the reduced ER-mitochondrial Ca^{2+} transfer, no severe OXPHOS defect was found in intact *WFS1* rec or W4 fibroblasts. In particular, basal respiration, FCCP stimulated maximal respiration and ATP content under 'forced OXPHOS' (2-DG) conditions were comparable to controls. These results are consistent with previous investigations of muscle biopsies from patients with Wolfram syndrome that did not reveal any evidence of marked respiratory chain dysfunction (Jackson *et al.*, 1994; Barrett *et al.*, 1995b). In contrast, *WFS1* deficient neurones showed decreased mitochondrial membrane potential together with lower cytosolic ATP levels and a *WFS1* depleted MIN6 insulinoma cell line presented with decreased total ATP content and an impaired ATP rise in response to high glucose (Zatyka *et al.*, 2015; Cagalinec *et al.*, 2016). Only low level Ca^{2+} transfer was found necessary to maintain OXPHOS in lymphocyte cells and it is possible that the observed decrease in mitochondrial Ca^{2+} uptake is not sufficient to adversely affect mitochondrial bioenergetics in *WFS1* fibroblasts (Cardenas *et al.*, 2010). Furthermore, *WFS1* mutations in fibroblasts, unlike the situation in neuronal population including RGCs, may not stress mitochondria to the point where relevant disease-associated changes are evident. It is likely that *WFS1* deficient neuronal or pancreatic β cells are less tolerant of disturbed Ca^{2+} homeostasis and are more likely to show mitochondrial dysfunction (Wiley *et al.*, 2013).

Interestingly, W5 fibroblasts showed significantly enhanced OXPHOS activity, highlighted by increased ATP-linked respiration and increased ATP content under 'forced OXPHOS' conditions. Increased OXPHOS has previously been described in lymphoblastoid cell lines established from *OPA1*-linked DOA patients that maintained visual function, indicating that increased OXPHOS is likely a compensatory response to pathogenic mutations (Van Bergen *et al.*, 2011). The enhanced OXPHOS observed in W5 fibroblasts is therefore likely part of the compensatory response to *WFS1* mutation that appears to be active in this cell line. It remains to be determined how enhanced OXPHOS is related to the remodelling of the ER-mitochondrial axis observed in W5 fibroblasts. No difference was observed in mitochondrial mass or mtDNA copy number in W5 fibroblasts suggesting that increased mitochondrial biogenesis does not underlie the compensatory mechanism in W5 fibroblasts. Further investigations are required to determine the molecular mechanisms underlying this compensatory response.

Although no severe OXPHOS defect was found in intact *WFS1* fibroblasts, reduced complex I-dependent respiration was observed in *WFS1* rec and W4 fibroblasts upon site-specific analysis of the mitochondrial respiratory chain. This defect was not found in W5 fibroblasts suggesting that it is specifically related to disturbed ER-mitochondrial Ca^{2+} flux. Isolated complex I-deficiency is the most frequently observed defect of mitochondrial bioenergetics (Distelmaier *et al.*, 2009). Importantly, complex I-deficiency is a common feature of mitochondrial optic neuropathies and has been previously described in studies of LHON and DOA (Baracca *et al.*, 2005; Chevrollier *et al.*, 2008; Zanna *et al.*, 2008). This suggests that a common biochemical is shared by Wolfram syndrome, LHON and DOA. Similar to fibroblasts established from LHON or DOA patients, *WFS1* fibroblasts appear to compensate for the reduced complex I-dependent respiration as no difference was observed in respiratory capacity or ATP content in intact *WFS1* fibroblasts (Baracca *et al.*, 2005; Zanna *et al.*, 2008). It is possible that the complex I-deficiency is only apparent when the substrates available for respiration are controlled, in this case pyruvate and malate, and the defect might not be due to primary respiratory chain dysfunction, but rather decreased PDH activity, which is activated by a Ca^{2+}-dependent pyruvate dehydrogenase phosphatase (Denton, 2009). PDH activity could therefore be perturbed secondary to the reduced mitochondrial Ca^{2+} uptake in

WFS1 fibroblasts. However, no difference was observed in the phosphorylation status of the PDH at serine 293 suggesting that PDH regulation, at least in the basal state, is not disturbed in *WFS1* fibroblasts. Further investigations are required to determine the nature of the complex I defect in *WFS1* fibroblasts. Analysis of complex I-dependent respiration with different substrates, such as glutamate and malate, and blue native electrophoresis followed by in-gel catalytic activity assays would clarify how the OXPHOS system is perturbed in WFS1 fibroblasts (Wittig *et al.*, 2007). Further investigation of the PDH in *WFS1* fibroblasts should include analysis of the three PDH phosphorylation sites, PDH enzyme activity and the cellular NAD/NADH ratio at basal and under galactose conditions (to shift ATP production to OXPHOS) (Rardin *et al.*, 2009; Wiley *et al.*, 2013).

ROS homeostasis is critical for cellular function and excessive ROS levels have been reported in many neurodegenerative diseases, including LHON and DOA (Yarosh *et al.*, 2008; Tang *et al.*, 2009; Lin *et al.*, 2012). ROS levels, assessed by H_2DCFDA, were normal in WFS1 fibroblasts. However, H_2DCFDA has various limitations and reacts with a broad range of cellular ROS (Kalyanaraman *et al.*, 2012). Further investigations are required to confirm the absence of oxidative stress in *WFS1* fibroblasts.

No difference was observed in cell viability between *WFS1* and control fibroblasts following treatment with STS or t-BH. This suggests that decreased Ca^{2+} flux does not affect Ca^{2+} mediated cell death in *WFS1* fibroblasts. Surprisingly, *WFS1* rec and W4 fibroblasts were less susceptible to thapsigargin treatment than controls, demonstrated by increased viability of these fibroblasts at all time points on the MTT assay. This observation compares with previous investigations of Wolfram syndrome patient fibroblasts, where cell death was not detected following treatment with a range of ER stressors including thapsigargin (Philbrook *et al.*, 2005). In contrast, *WFS1* deficient pancreatic β-cells showed increased susceptibility to ER stress induced apoptosis (Yamada *et al.*, 2006). Overall, these findings imply that increased susceptibility to ER stress-induced cell death is not present in a primary fibroblast model of Wolfram syndrome. Although ER stress sensitivity has been excluded, the reasons why *WFS1* rec and W4 fibroblasts are less susceptible to thapsigargin treatment remain unknown. Increased SERCA expression has previously been described in thapsigargin resistant hamster smooth muscle cells (Rishi *et al.*, 1998).

It is possible that a similar mechanism is active in the *WFS1* fibroblasts as SERCA expression was found to be significantly increased in *WFS1* rec and W4 fibroblasts compared to controls.

One limitation of these conclusions is that measurement of cell viability via the MTT assay indicates metabolic activity rather than cell death. Caspase 3 activity was assessed in *WFS1* fibroblasts following treatment with cellular stressors; however, the assay had limitations including large variation between assay replicates. Following treatment with t-BH or thapsigargin, caspase 3 activity was similar to basal conditions in all cell lines, indicating that caspase 3-dependent apoptosis was not measured under these conditions. Caspase 3 has previously been shown to be involved in t-BH and thapsigargin induced cell death, suggesting that cell death following treatment is unlikely to be caspase 3 independent (Dahmer, 2005; Bononi *et al.*, 2013). It is possible that caspase 3 activity was not increased at the time point measured in the present assay. Further work is required to conclusively confirm the absence of a defect in Ca^{2+}-mediated apoptosis or lack of ER stressor sensitivity in *WFS1* fibroblasts.

In summary, this study has shown that disturbed ER-mitochondrial interactions in *WFS1* fibroblasts results in impairment of complex I-dependent respiration. *WFS1* fibroblasts are able to compensate and maintain OXPHOS function in intact cells. The present data provides clues to the disease mechanisms of Wolfram syndrome and these results further support the hypothesis that mitochondrial dysfunction plays an important role in Wolfram syndrome, providing an attractive target for therapeutic modulation.

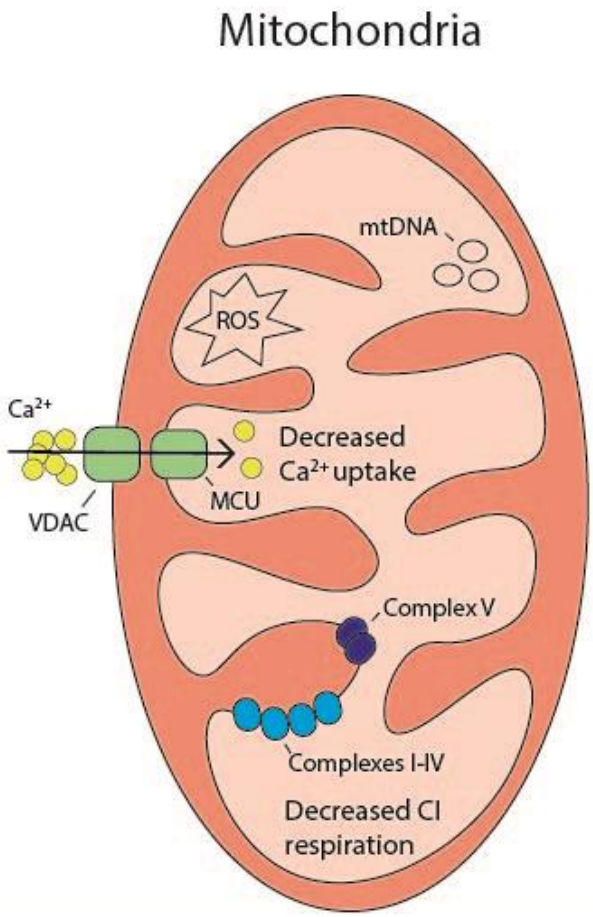

Figure 6.10 Schematic highlighting the mitochondrial parameters investigated in *WFS1* fibroblasts. OXPHOS function, ROS levels and mtDNA copy number was assessed in *WFS1* fibroblasts. No gross OXPHOS defect was found in WFS1 fibroblasts with reduced Ca^{2+} uptake, however, these cells did show a selective decrease in complex I-dependent respiration. There was no disturbance found in ROS levels or mtDNA copy number.

Chapter 7. Investigation of Disease Mechanisms in Wolfram Syndrome 2

7.1 Introduction

WFS2 is a rare disorder caused by recessive mutations in the *CISD2* gene (Amr *et al.*, 2007). Patients with WFS2 manifest the main clinical features of Wolfram syndrome, namely optic atrophy and diabetes, but in addition, they have distinct phenotypic features that include peptic ulcers, bleeding tendencies secondary to defective platelet aggregation and the absence of diabetes insipidus (El-Shanti *et al.*, 2000). To date, WFS2 has been described in 13 patients across six families (Amr *et al.*, 2007; Mozzillo *et al.*, 2014; Rondinelli *et al.*, 2015).

Interestingly, both *WFS1* and *CISD2* encode transmembrane proteins localised to the ER that appear to regulate cellular Ca^{2+} homeostasis. Moreover, deficiencies in both genes are associated with mitochondrial abnormalities that are potentially secondary to disrupted cytosolic Ca^{2+} signalling and/or disturbed ER-mitochondrial interactions at the MAM (Amr *et al.*, 2007; Wiley *et al.*, 2013; Lu *et al.*, 2014; Cagalinec *et al.*, 2016). Wolframin and CISD2 have both been localised to the MAM suggesting they have roles within this domain, a key function of which is the transfer of Ca^{2+} from the ER to mitochondria, which in turn regulates cellular Ca^{2+} signalling, mitochondrial bioenergetics and apoptosis (Wiley *et al.*, 2013; Horner *et al.*, 2015).

However, it is unclear how CISD2 regulates Ca^{2+} homeostasis and there is no consensus on how *CISD2* loss of function disrupts Ca^{2+} homeostasis in the three main cellular Ca^{2+} compartments: the ER, the cytosol and mitochondria (Amr *et al.*, 2007; Chang *et al.*, 2012; Wiley *et al.*, 2013; Wang *et al.*, 2014). In addition, only one study has assessed cellular Ca^{2+} homeostasis secondary to pathogenic *CISD2* mutations and the analysis was restricted to the cytosol (Amr *et al.*, 2007). Further studies are required to understand the disease mechanisms of WFS2, specifically how pathogenic *CISD2* mutations affect cellular Ca^{2+} homeostasis and the MAM domain, and whether WFS1 and WFS2 share overlapping pathological pathways. The present study used a fibroblast cell line established from a patient harbouring a novel homozygous *CISD2* mutation to investigate how cellular Ca^{2+} homeostasis, the mitochondria-ER axis and mitochondrial function are affected in this disorder.

7.2 Methods

7.2.1 Patient Cohort

The patient is a Moroccan male born from consanguineous parents. He developed diabetes mellitus at age 8 and progressive visual impairment first attributed to diabetic retinopathy. At age 45, neurological examination showed cerebellar ataxia, myoclonic tremor, dysarthria, dysexecutive syndrome and pseudobulbar affect. Brain MRI showed supra- and infratentorial brain atrophy. Ophthalmological examination with fundoscopy and OCT revealed bilateral optic atrophy without evidence of diabetic retinopathy. Visual acuity without correction was 1/20 (right eye) and 1/10 (left eye). The patient had a normal audiogram and there was no evidence of diabetes insipidus, haematologic abnormalities, peptic ulcers or urinary tract abnormalities.

Screening of the *WFS1* and *CISD2* genes revealed a novel homozygous *CISD2* mutation (c.215 A>G, p.Asn72Ser). In support of pathogenicity, the mutation segregated with the disease in the family, modified a highly conserved amino acid, was absent from control databases and was predicted to be pathogenic by *in silico* analysis and 3D structural analysis.

Fibroblasts (referred to as *CISD2* fibroblasts) were established from the patient. Western blot analysis revealed no significant difference in the expression level of the CISD2 protein between *CISD2* and control fibroblasts. The patient information, CISD2 western blot analysis and *CISD2* fibroblasts were provided by Dr Cécile Rouzier and Professor Véronique Paquis-Flucklinger (Nice Sophia-Antipolis University) as part of an ongoing collaboration with Dr Patrick Yu-Wai-Man. Three control fibroblast cell lines were included for comparison (**Table 5.2**).

7.3 Results

7.3.1 ER Ca^{2+} levels are not disturbed in CISD2 fibroblasts

FRET experiments using the ER-targeted cameleon probe, D1ER, were performed to assess ER Ca^{2+} levels in *CISD2* fibroblasts. Briefly, the FRET signal produced from CFP to the YFP upon D1ER binding of Ca^{2+} enabled the ratiometric assessment of free ER Ca^{2+} using the FRET to CFP ratio (**Figure 7.1**).

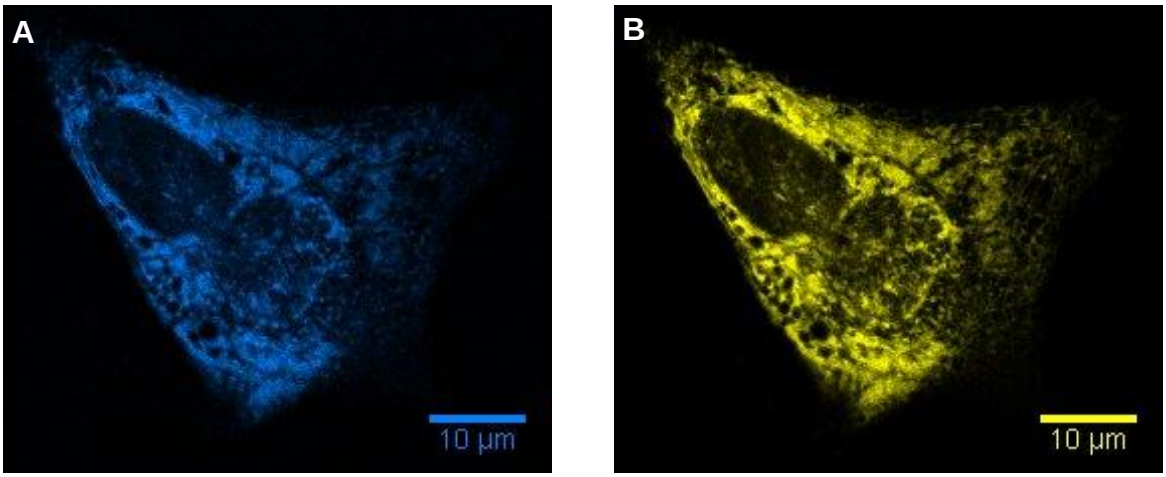

Figure 7.1 Imaging the D1ER probe. (A.B) Representative confocal images of *CISD2* fibroblasts expressing D1ER: (A) the CFP signal and (B) the YFP signal. The reticular pattern is indicative of ER localisation. Regions of interest were analysed using Fiji.

There was a trend for slightly increased FRET/CFP ratios in the *CISD2* fibroblasts (**Figure 7.2**), although there was no statistical significant difference when compared with controls. This suggests that there is no gross variation in basal ER Ca^{2+} levels between *CISD2* and control fibroblasts.

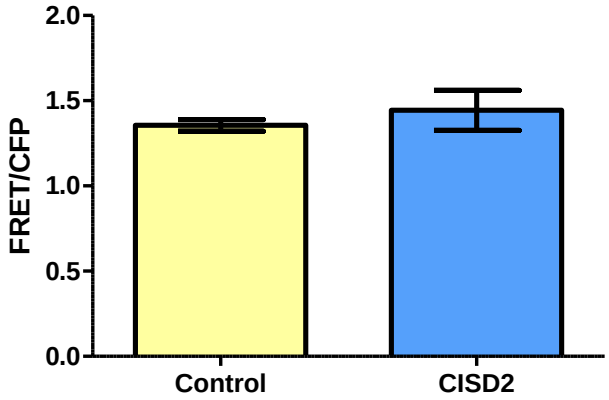

Figure 7.2 Evaluation of ER Ca^{2+} levels with the D1ER probe. Comparison of the average FRET/CFP ratios of *CISD2* and control fibroblasts. Data are mean ± SEM. n = ≥ 16. No significant difference when compared to controls, two-tailed unpaired t test.

7.3.2 CISD2 fibroblasts show increased cytosolic [Ca^{2+}]

The ratiometric Ca^{2+} sensitive fluorescent dye Fura-2-am was used to measure cytosolic [Ca^{2+}] in *CISD2* and control fibroblasts at basal and following thapsigargin induced ER Ca^{2+} depletion. Basal cytosolic [Ca^{2+}] was significantly increased in *CISD2* fibroblasts when compared with controls (**Figure 7.3**).

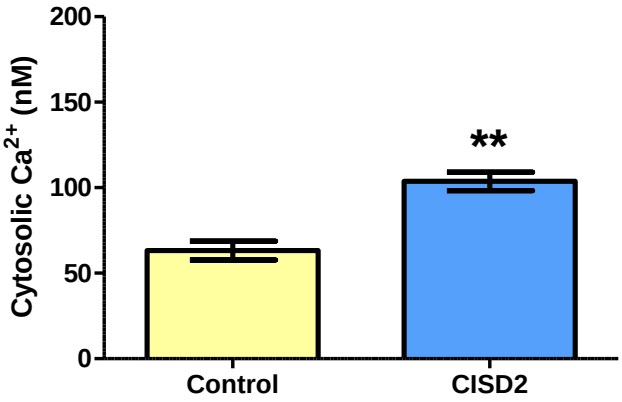

Figure 7.3 Increased cytosolic [Ca^{2+}] in *CISD2* fibroblasts. Comparison of cytosolic [Ca^{2+}] in *CISD2* and control fibroblast. Data are mean ± SEM. n = 3. ** p = ≤0.01, two-tailed unpaired t test.

Peak cytosolic [Ca^{2+}] following thapsigargin treatment was similar between *CISD2* and control fibroblasts (**Figure 7.4A**), whereas, thapsigargin sensitive Ca^{2+} stores, defined as the difference between peak cytosolic [Ca^{2+}] and basal cytosolic [Ca^{2+}], were decreased in *CISD2* fibroblasts in comparison to controls, although this decrease did not quite reach statistical significance (**Figure 7.4B**).

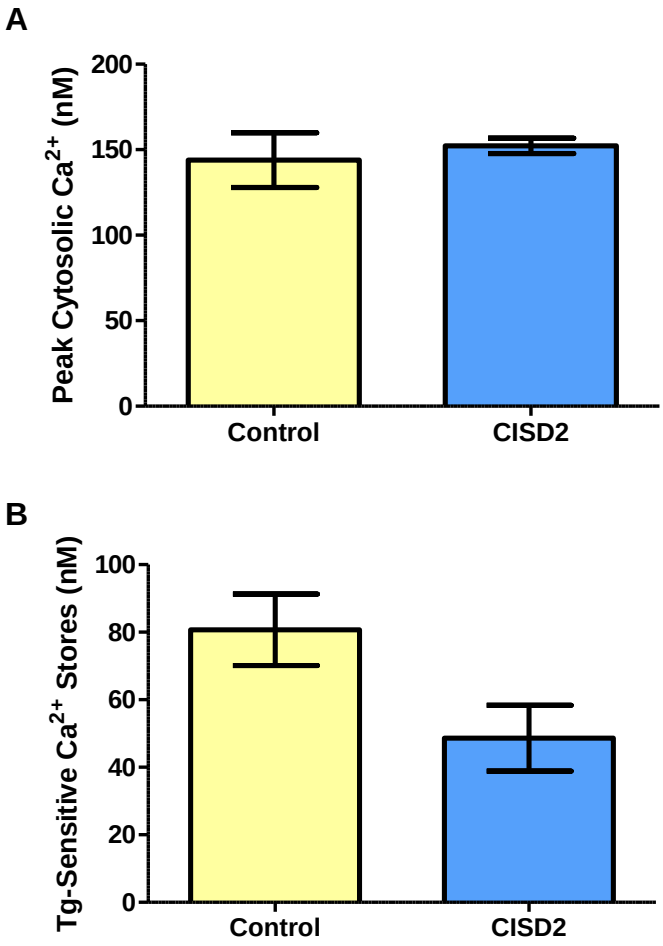

Figure 7.4 Analysis of thapsigargin induced ER Ca^{2+} depletion in *CISD2* fibroblasts. Comparison of (A) peak cytosolic [Ca^{2+}] levels after thapsigargin treatment and (B) thapsigargin (Tg)-sensitive Ca^{2+} stores in *CISD2* and control fibroblasts. Data are mean ± SEM. n = 3. No results were significantly different when compared to controls, two-tailed unpaired t test.

7.3.3 ER to Mitochondrial Ca^{2+} flux is increased in CISD2 fibroblasts

To evaluate Ca^{2+} flux between the ER and mitochondria in *CISD2* fibroblasts, histamine stimulated IP_3R-dependent ER Ca^{2+} transients were monitored in the mitochondria and cytosol with the Ca^{2+} sensitive fluorescent dyes Rhod-2-AM and Fluo-4-AM, respectively (**Figure 7.5**). Peak mitochondrial Ca^{2+} levels following histamine stimulation were significantly increased in *CISD2* fibroblasts compared to controls (**Figure 7.6A**). In contrast, peak cytosolic Ca^{2+} levels were significantly decreased in *CISD2* fibroblasts in comparison to controls (**Figure 7.6C**).

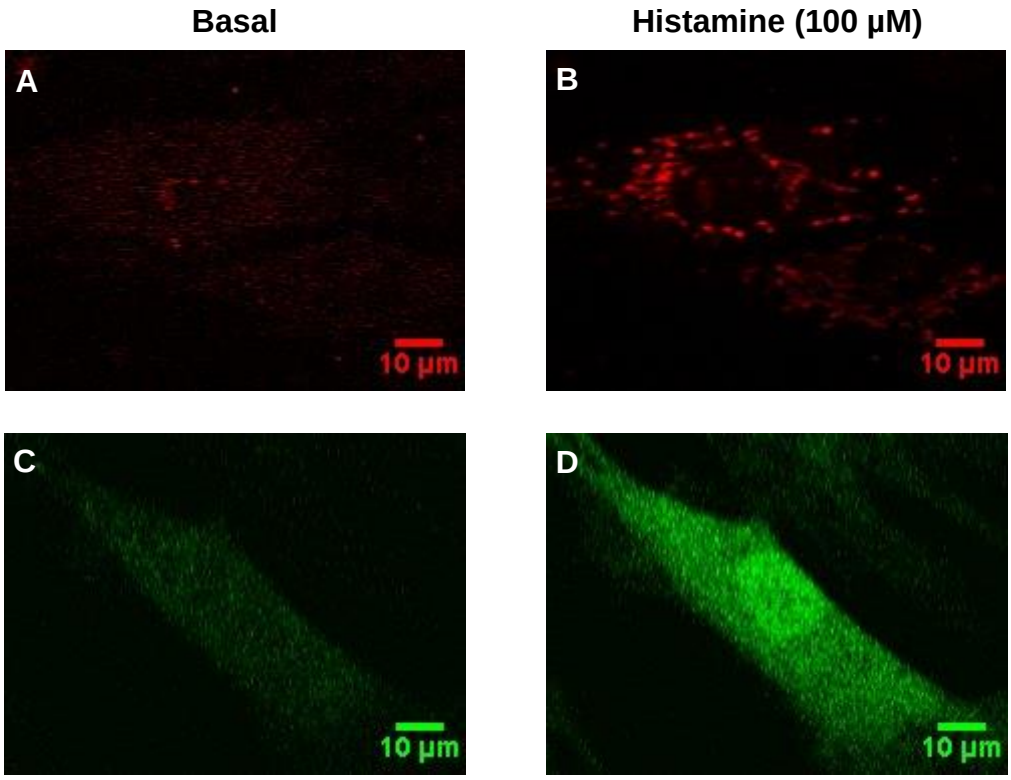

Figure 7.5 Imaging of cellular Ca^{2+} flux with Ca^{2+} sensitive fluorescent dyes. (A-D) Representative images demonstrating analysis of (A, B) mitochondrial Ca^{2+} with Rhod-2-AM (red) and (C, D) cytosolic Ca^{2+} with Fluo-4-AM (green) before and after histamine stimulation. Regions of interest were analysed using Fiji.

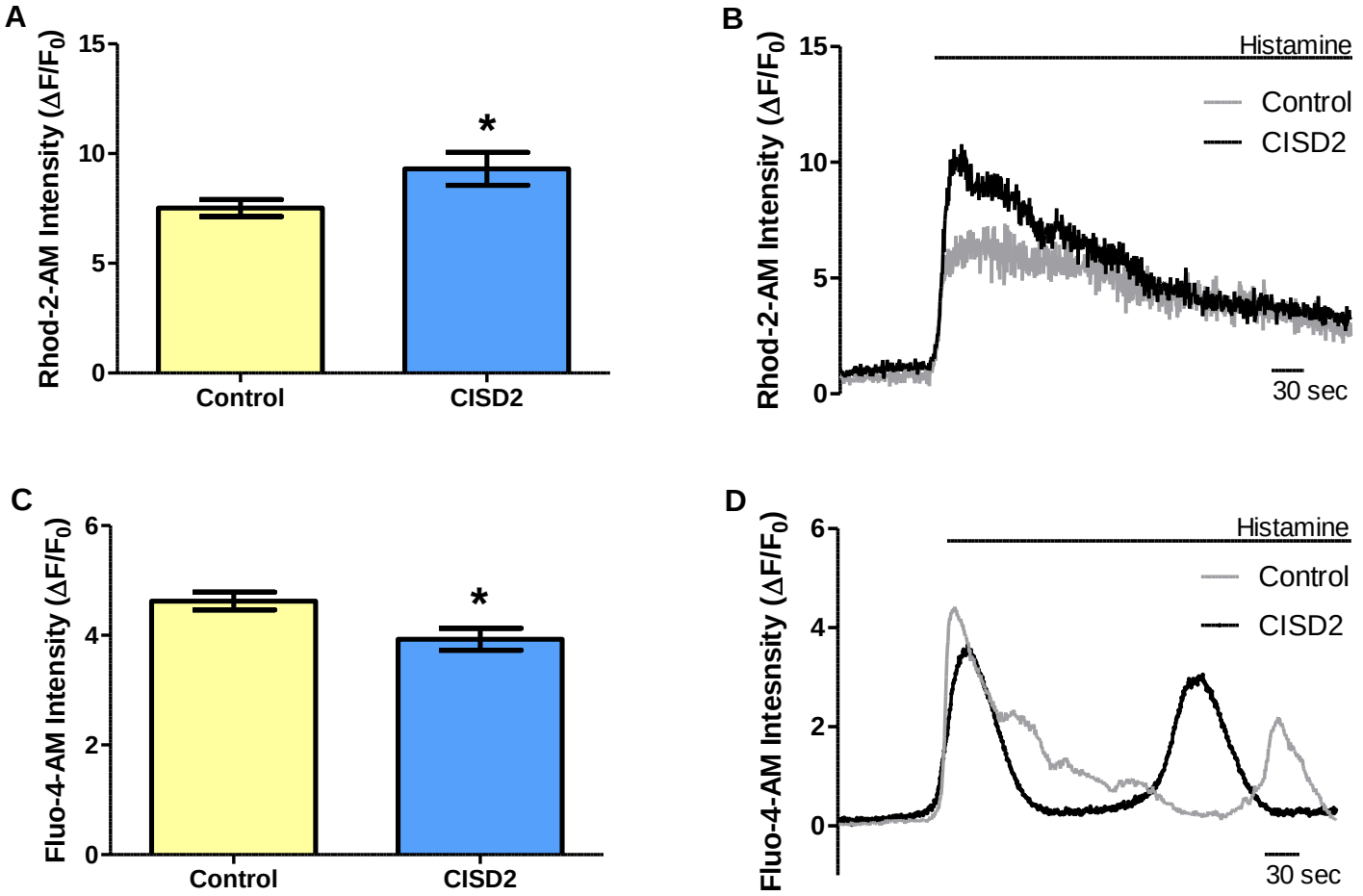

Figure 7.6 Disturbed Ca^{2+} flux in *CISD2* fibroblasts. (A, C) Analysis of average peak (A) mitochondrial and (C) cytosolic Ca^{2+} levels following histamine induced ER Ca^{2+} release in *CISD2* and control fibroblasts. Data are mean ± SEM. n = ≥ 14. * p = ≤ 0.05, two-tailed unpaired t test. (B, D) Representative traces of (B) mitochondrial and (D) cytosolic Ca^{2+} transients in *CISD2* and control fibroblasts. Where indicated the cells were stimulated with histamine.

7.3.4 ER-mitochondrial contact is increased in CISD2 fibroblasts

ER-mitochondrial contact is critical for mitochondrial Ca^{2+} uptake following ER Ca^{2+} release and was therefore assessed in *CISD2* fibroblasts. Briefly, GFP Sec61β was transfected to visualize the ER and MitoTracker Red was loaded to label the mitochondrial network. Z-axis stacks were acquired by confocal microscopy for 3D-reconstruction and colocalisation analysis was performed using the Manders' Coefficient: M1 and M2 in Huygens Object Analyser (**Figure 7.8**). M1 indicates the fraction of ER that colocalises with mitochondria and M2 indicates the fraction of mitochondria that colocalises with ER. Both Manders' coefficient M1 and M2 were significantly increased in *CISD2* fibroblasts compared to controls (**Figure 7.7**).

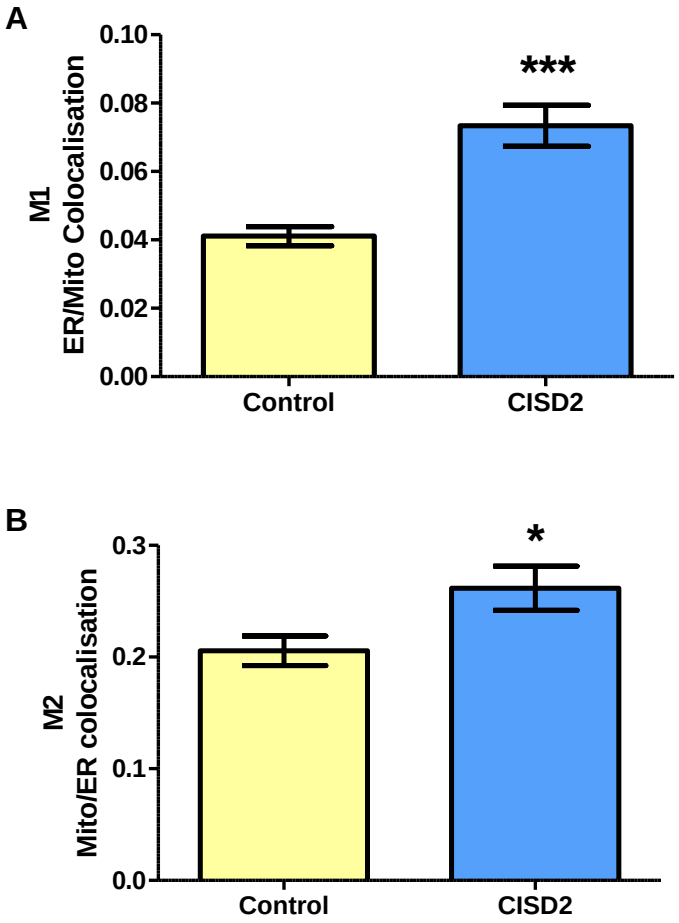

Figure 7.7 Increased ER-mitochondrial contacts in *CISD2* fibroblasts. (A-B) Analysis of (A) Manders' coefficient M1 ER/Mitochondrial (Mito) colocalisation and (B) Manders' coefficient M2 Mito/ER colocalisation in *CISD2* and control fibroblasts. Data are mean ± SEM. n = ≥ 26. *** p ≤0.0001, * p = ≤0.05, two-tailed unpaired t test.

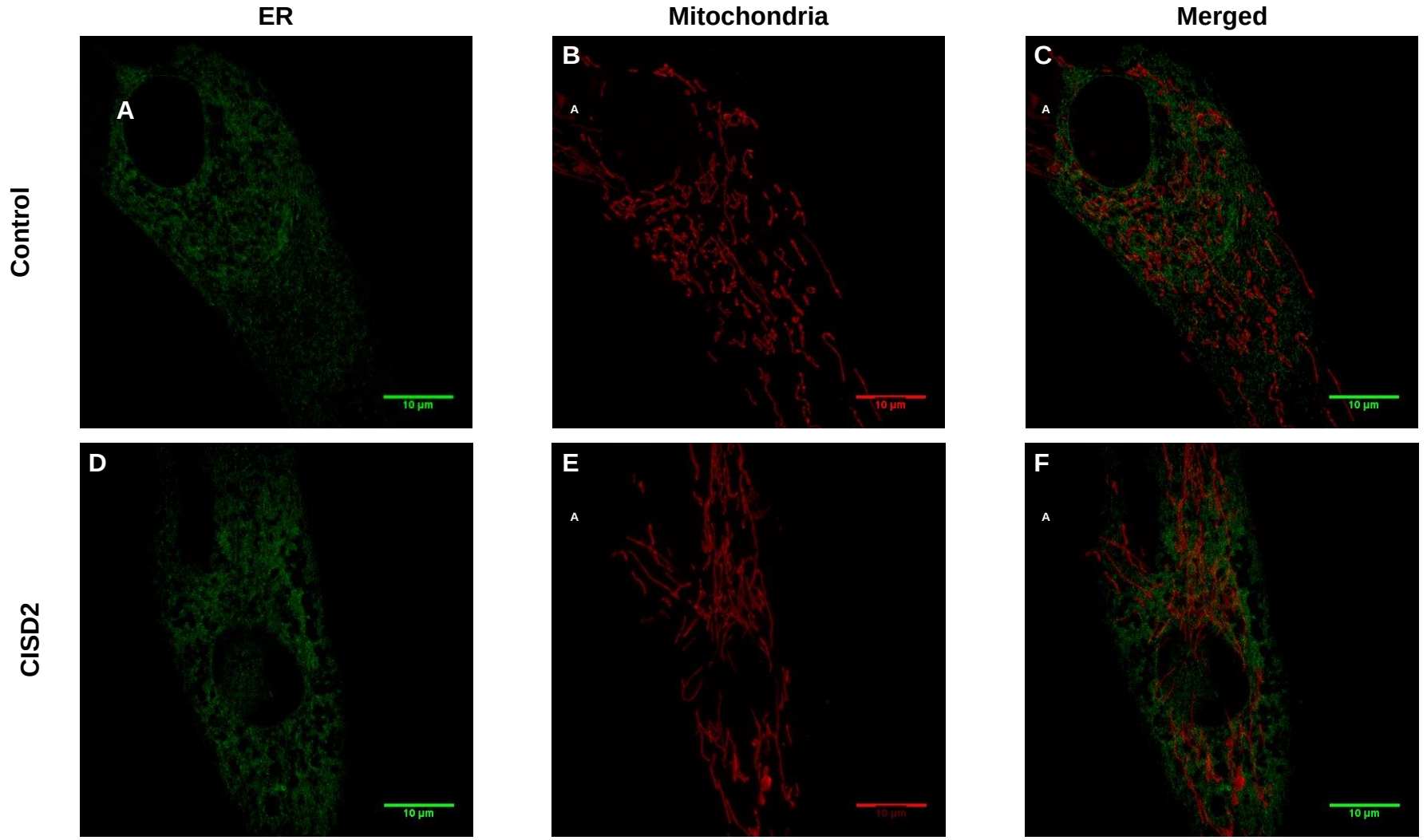

Figure 7.8 Representative images of the ER and mitochondrial network in control and *CISD2* fibroblasts.
(A, D) Fibroblasts were transfected with GFP Sec61β to label ER and (B, E) loaded with MitoTracker Red to label mitochondria, signal acquisition was performed simultaneously. Cell lines are indicated. (C, F) Analysis was performed on merged images.

7.3.5 CISD2 fibroblasts show an elongated mitochondrial network

In parallel with the analysis of ER-mitochondria contacts, mitochondrial network morphology and ER volume were investigated in *CISD2* and control fibroblasts. The mitochondrial network appeared more fused and elongated in *CISD2* fibroblasts in comparison with controls (**Figure 7.8 B, E**). To obtain a robust analysis of the mitochondrial network morphology Huygens Essentials Software was used to measure the length and volume of each mitochondrial fragment within the mitochondrial network in 3D-reconstructions of *CISD2* and control fibroblasts (**Figure 7.9**).

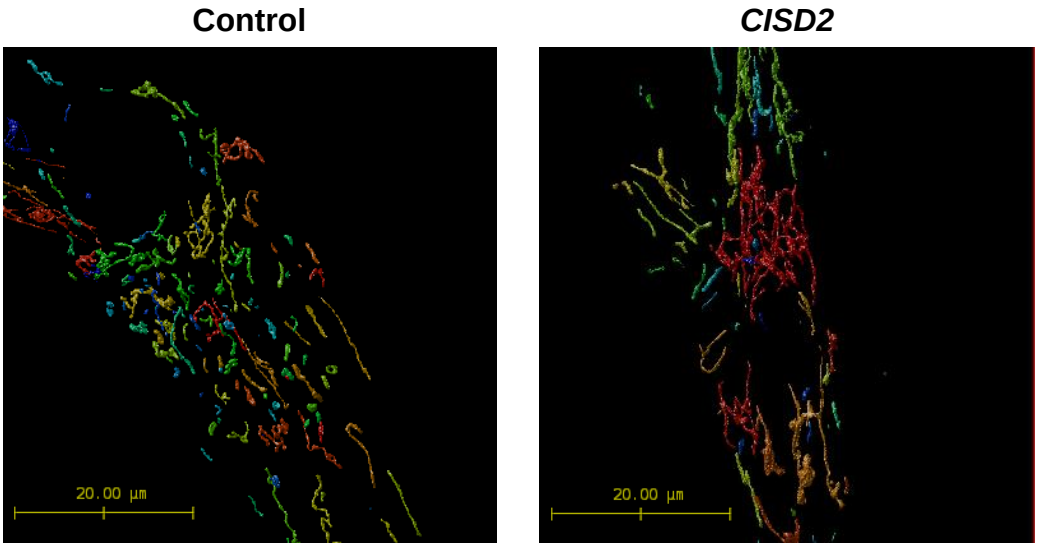

Figure 7.9 Example 3D-reconstructed mitochondrial networks in control and *CISD2* fibroblasts. Huygens Object Analyzer was used to determine the length and volume of each mitochondrial fragment. Cell lines are indicated.

As expected from the gross morphological analysis the average length of mitochondrial fragments was significantly increased in *CISD2* fibroblasts compared with controls (**Figure 7.10A**). Likewise, the average volume of mitochondrial fragments was significantly increased in *CISD2* fibroblasts compared with controls (**Figure 7.10B**). Furthermore, the total number of mitochondrial fragments was significantly decreased in *CISD2* fibroblasts in comparison with controls (**Figure 7.10C**). Taken together, these results suggest that the mitochondrial network is more fused and elongated in *CISD2* fibroblasts than in controls.

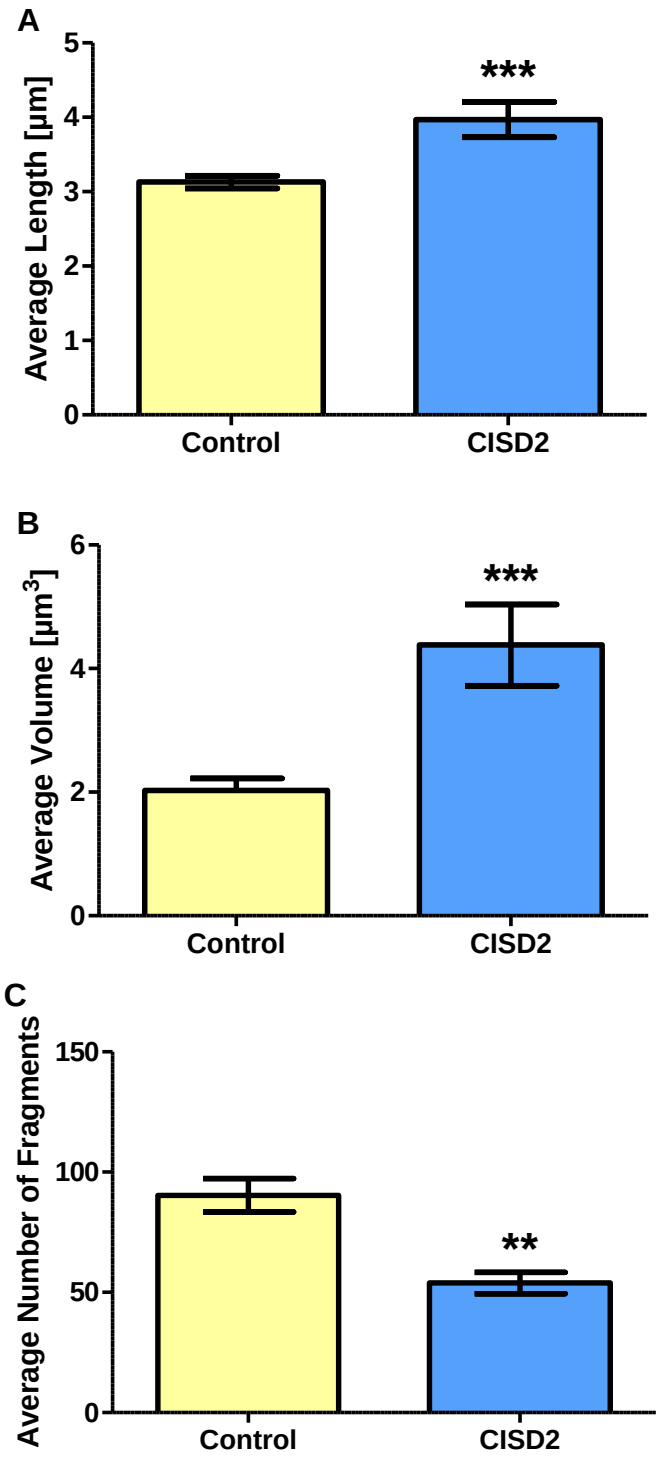

Figure 7.10 Altered mitochondrial fragment morphology in *CISD2* fibroblasts. Analysis of average (A) mitochondrial fragment length, (B) mitochondrial fragment volume and (C) number of mitochondrial fragments in *CISD2* and control fibroblasts. Data are mean ± SEM. n = ≥ 25. *** p = ≤0.0001, ** p = ≤0.01, two-tailed unpaired t test.

The distribution of the length and volume of mitochondrial fragments in *CISD2* fibroblasts and controls were also evaluated, with individual mitochondrial fragments being sorted into bins based on their length and volume. There was a shift in mitochondrial fragment morphology in *CISD2* fibroblasts, with significantly more 'larger fragments' and significantly less 'smaller fragments' for both length and volume in *CISD2* fibroblasts compared to controls (**Figure 7.11**).

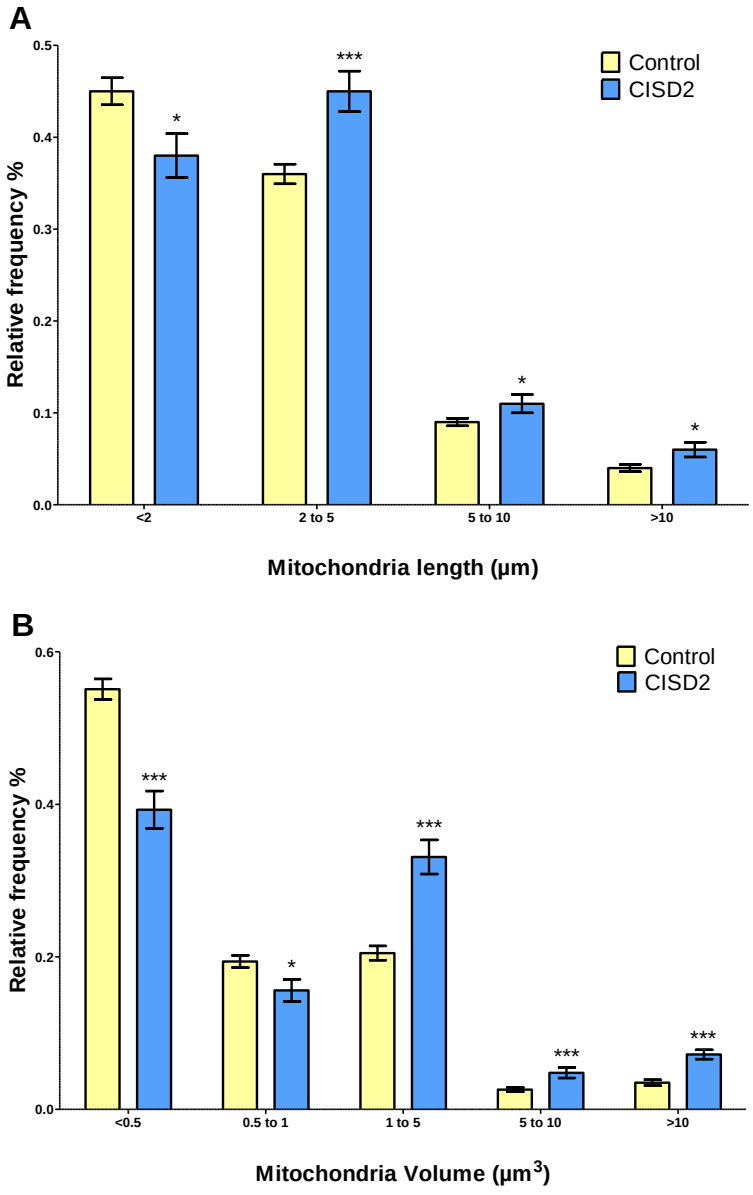

Figure 7.11 Distribution of the length and volume of mitochondrial fragments in *CISD2* fibroblasts. Data are mean ± SEM. n = ≥ 25. *** p = ≤ 0.001, * p = ≤ 0.05, two-tailed unpaired t test.

To conclude the analysis of the mitochondrial network in *CISD2* fibroblasts the total length and volume of the mitochondrial network was compared between *CISD2* and control fibroblasts. Despite an increased average fragment length, the total length of the mitochondrial network was significantly decreased in *CISD2* fibroblasts compared to controls (**Figure 7.12A**). In contrast, the total volume of the mitochondrial network was significantly increased in *CISD2* fibroblasts in comparison to controls (**Figure 7.12B**).

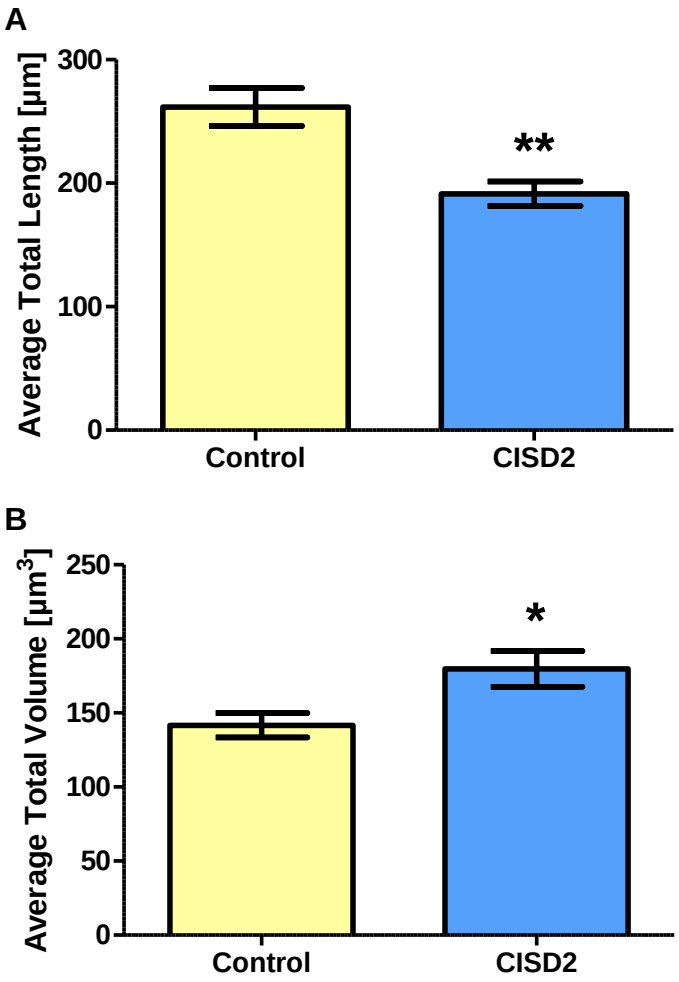

Figure 7.12 Altered mitochondrial network morphology in *CISD2* fibroblasts. Analysis of average (A) total mitochondrial network length and (B) total mitochondrial network volume in *CISD2* and control fibroblasts. Data are mean ± SEM. n = ≥ 25. ** p = ≤0.01, * p = ≤ 0.05, two-tailed unpaired t test.

The ER morphology was compared between *CISD2* and control fibroblasts. Analysis was restricted to total ER volume because the ER was represented by one large continuous compartment. There was no significant difference observed in total ER volume between the *CISD2* and control fibroblasts (**Figure 7.13**).

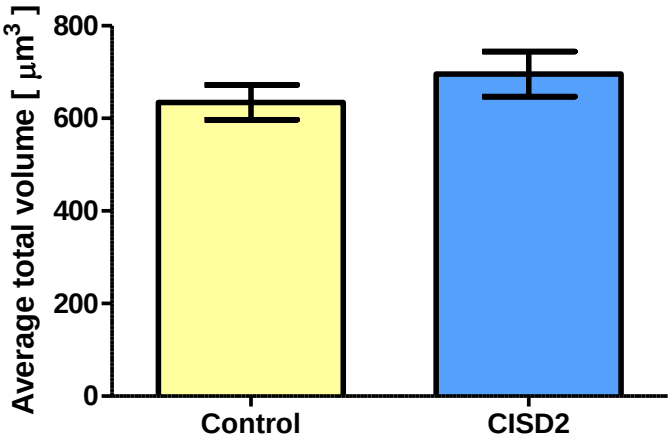

Figure 7.13 The average total ER volume in *CISD2* fibroblasts. Data are mean ± SEM. n = ≥ 25. No significant difference when compared to controls, two-tailed unpaired t test.

7.3.6 ATP content and cell viability of CISD2 fibroblasts

The transfer of Ca^{2+} from the ER to the mitochondria regulates mitochondrial bioenergetics and apoptosis. To investigate OXPHOS function in *CISD2* fibroblasts ATP levels were determined with the CellTiter-Glo ATP assay under four conditions: (i) glucose, (ii) 2-DG, (iii) oligomycin and (iv) 2-DG and oligomycin. There was a trend for decreased ATP levels under all four assay conditions in the *CISD2* fibroblasts compared to controls, however no significant difference was observed under any condition between the two groups (**Figure 7.14**). Apoptosis was assessed in untreated *CISD2* and control fibroblasts by western blot analysis of the apoptosis markers caspase 3 and poly (ADP-ribose) polymerase (PARP); they both undergo proteolytic processing during apoptosis which is detected using western blot as cleaved-caspase 3 (19, 17 kDa) and cleaved-PARP (89 kDa). There was no evidence of proteolytic processing of either marker in *CISD2* or control fibroblasts (**Figure 7.15**).

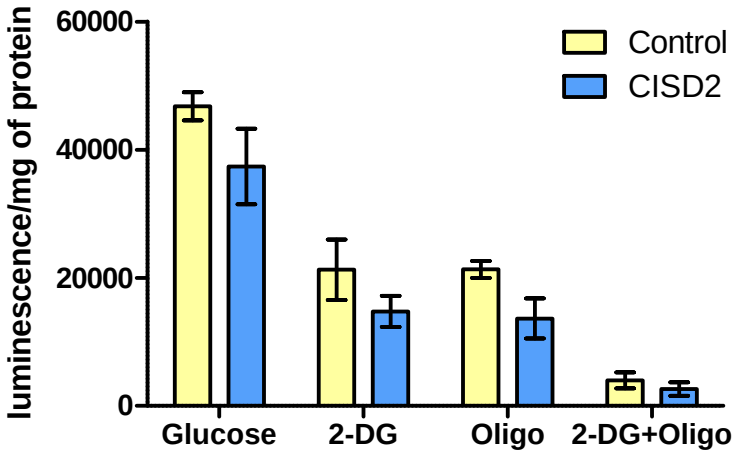

Figure 7.14 ATP content in *CISD2* fibroblasts. ATP content was assessed under four conditions: glucose, 2-DG, oligomycin (oligo) and 2-DG+oligo. Data are mean ± SEM. n = 3. No results were significantly different when compared to controls, two-tailed unpaired t test.

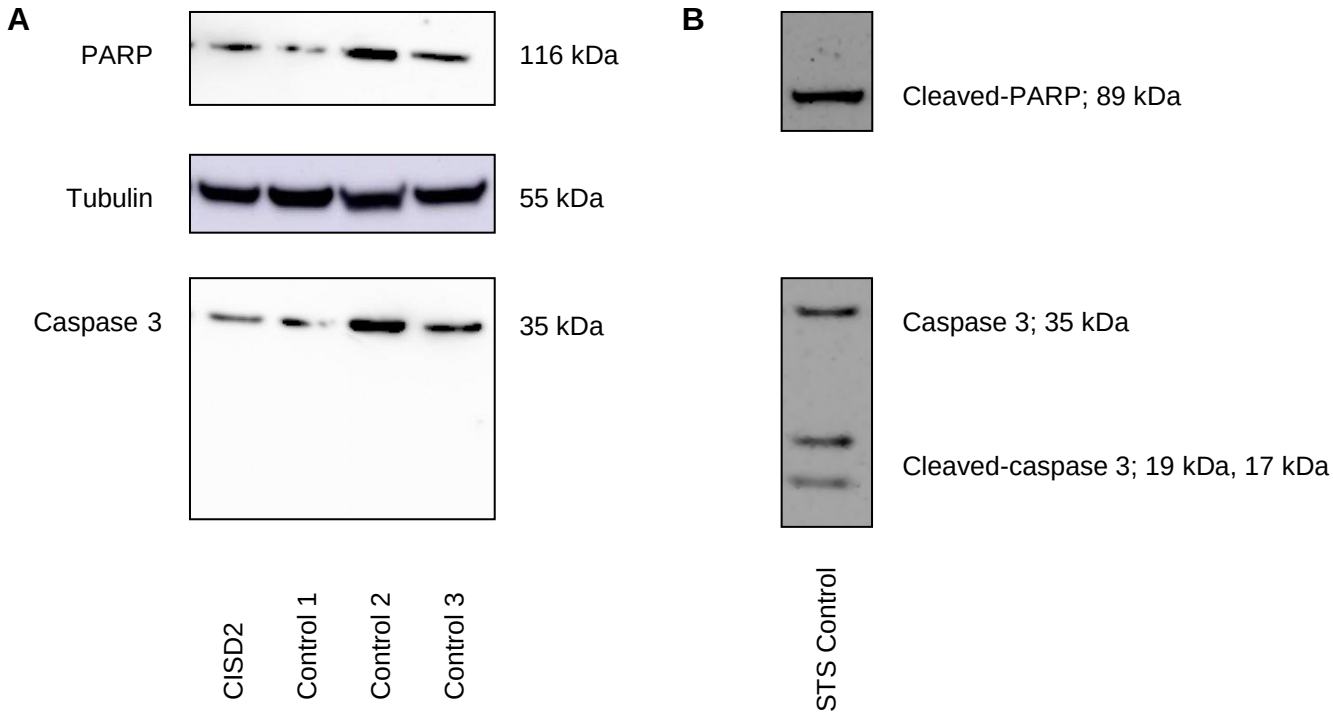

Figure 7.15 Western blot analysis of apoptosis in *CISD2* fibroblasts.
(A) Representative western blots of caspase 3 and PARP in untreated *CISD2* and control fibroblasts. (B) Caspase 3 and PARP antibodies had previously been validated on a STS treated controls.

7.4 Discussion

Wolfram syndrome is genetically heterogeneous with the majority of patients harbouring *WFS1* mutations, but in rare cases, *CISD2* mutations have been reported (Inoue *et al.*, 1998; Strom *et al.*, 1998; Amr *et al.*, 2007). Using a fibroblast cell line established from a patient harbouring a novel homozygous *CISD2* mutation (c.215A>G; p.Asn72Ser), the present study demonstrates that *CISD2* mutation disturbs cellular Ca^{2+} homeostasis comprising enhanced Ca^{2+} flux from the ER to mitochondria and cytosolic Ca^{2+} abnormalities. This Ca^{2+} dysregulation was associated with increased ER-mitochondrial contact and a 'hyperfused' mitochondrial network. There were no obvious downstream effects of disturbed Ca^{2+} homeostasis on cellular bioenergetics and apoptosis. These results provide important insight into the potential disease mechanisms underlying *CISD2* mutations and WFS2.

CISD2 deficiency has previously been shown to disturb basal cytosolic and mitochondrial Ca^{2+} levels, although conflicting results have been reported (Wiley *et al.*, 2013; Wang *et al.*, 2014). No studies have assessed the impact of *CISD2* mutations on IP_3R dependent ER-mitochondria Ca^{2+} flux, which is an important potential mechanism linking ER dysfunction with mitochondrial impairment in Wolfram syndrome. In *CISD2* fibroblasts, Ca^{2+} flux from the ER to mitochondria was enhanced as demonstrated by significantly increased peak mitochondrial Ca^{2+} levels following IP_3R dependent ER Ca^{2+} release. In addition, *CISD2* fibroblasts showed significantly increased basal cytosolic [Ca^{2+}], which was coupled with a significant decrease in the amplitude of cytosolic Ca^{2+} transients following IP_3R dependent ER Ca^{2+} release. In agreement with previous studies, no difference was observed in ER Ca^{2+} levels by direct assessment with the D1ER probe in *CISD2* fibroblasts (Chang *et al.*, 2012; Wang *et al.*, 2014). This suggests that the disturbed Ca^{2+} homeostasis in *CISD2* fibroblasts is not due to alterations in ER Ca^{2+} levels.

The increased ER-mitochondrial Ca^{2+} flux observed in *CISD2* fibroblasts has potential consequences for a number of mitochondrial functions including mitochondrial bioenergetics and mitochondrial-mediated apoptosis (van Vliet *et al.*, 2014). However, under 'forced OXPHOS' conditions with 2-DG supplementation, ATP levels were not significantly different between *CISD2* and control fibroblasts suggesting that OXPHOS function is not adversely affected by the homozygous *CISD2* mutation. In contrast, immortalized *Cisd2*-/- MEFs were found to have

increased mitochondrial Ca^{2+} loading under basal conditions, which was associated with increased mitochondrial respiration and enhanced cellular ATP utilization (Wiley *et al.*, 2013). Given that ER-mitochondrial Ca^{2+} flux was increased, it is expected that the *CISD2* fibroblasts would show increased sensitivity to Ca^{2+} mediated apoptosis induction. Excessive mitochondrial Ca^{2+} accumulation can cause cell death via opening of the mPTP, loss of mitochondrial integrity and release of pro-apoptotic factors (La Rovere *et al.*, 2016). No evidence of apoptosis was found by western blot analysis of caspase 3 and PARP under basal conditions in *CISD2* fibroblasts. However, this represents a restricted analysis to a single cell death pathway under basal conditions. Future investigations to determine the sensitivity of *CISD2* fibroblasts to stressors that mobilise Ca^{2+} from the ER to mitochondria (e.g. t-BH or ceramide) are needed to clarify this potential pathogenic mechanism (Bononi *et al.*, 2013).

There are also potential pathological consequences of the disturbed cytosolic Ca^{2+} homeostasis observed in *CISD2* fibroblasts. To regulate diverse processes, cytosolic Ca^{2+} signals have unique spatiotemporal signatures (Smedler and Uhlen, 2014). Thus, the decreased amplitude of cytosolic Ca^{2+} transients following ER Ca^{2+} release and consistently elevated basal cytosolic [Ca^{2+}] in *CISD2* fibroblasts suggests that *CISD2* mutations disrupts cellular Ca^{2+} signalling. These results agree with two previous studies which have shown increased cytosolic [Ca^{2+}] secondary to *CISD2* deficiency (Chang *et al.*, 2012; Wang *et al.*, 2014), but contrast with previous studies which have shown normal or decreased basal cytosolic [Ca^{2+}] and increased IP_3R dependent cytosolic Ca^{2+} transients (Amr *et al.*, 2007; Wiley *et al.*, 2013). These differences are likely due to factors such as the unique properties of the different cell lines used including primary and immortalised cell lines, the difference between *CISD2* knockout and pathogenic *CISD2* mutations, and the different experimental conditions.

Despite the differences reported in the literature, the overall picture indicates that *CISD2* deficiency disturbs cytosolic Ca^{2+} homeostasis and further studies are required to determine the exact downstream consequences. Consistently elevated basal cytosolic [Ca^{2+}] has been shown to lead to the pathological activation of Ca^{2+} dependent enzymes in other neurodegenerative diseases, for example calpain and calcineurin, which induce apoptosis through various pathways (Vosler *et al.*, 2008;

Mukherjee and Soto, 2011). Increased cytosolic [Ca^{2+}] secondary to *WFS1* deficiency has been shown to cause calpain activation in a neuronal progenitor cells derived from Wolfram syndrome induced pluripotent stem cells (iPSCs) (Lu *et al.*, 2014). Moreover, CISD2 has been shown to negatively regulate calpain-2 by direct protein-protein interactions and *CISD2* deficiency resulted in calpain activation in a neuronal cell line (Lu *et al.*, 2014). It is unclear whether calpains are activated in *CISD2* fibroblasts and these Ca^{2+} signalling pathways deserve further investigation.

Analysis of ER-mitochondrial signal colocalisation in the *CISD2* fibroblasts suggested an increased degree of ER-mitochondria contact, possibly at the MAM. A greater area of physical contact between the ER and mitochondrial compartments has been shown to correlate with increased ER-mitochondria Ca^{2+} flux (Csordas *et al.*, 2006). The increased ER-mitochondria contact observed in *CISD2* fibroblasts could therefore explain the increased Ca^{2+} flux between these two organelles. However, this hypothesis needs to be substantiated by further investigations of the ER-mitochondria interaction through biomaging methods with a significantly higher spatial resolution than is possible with confocal microscopy. Moreover, increased ER-mitochondria signal colocalisation, whilst an important observation, does not necessarily indicate greater functional interactions. For example, it is possible that the increased mitochondrial-ER signal colocalisation is an artefact secondary to the significantly increased total volume of the mitochondrial network observed in *CISD2* fibroblasts and does not represent an increased functional interaction between the two organelles. Further investigation of the MAM domain including electron microscopy analysis, quantification of the IP_3R and VDAC interaction and direct measurement of Ca^{2+} hotspots on the OMM in *CISD2* fibroblasts would clarify the impact of *CISD2* mutations on the MAM domain (Giacomello *et al.*, 2010; Tubbs *et al.*, 2014).

It is intriguing why ER-mitochondrial contacts are increased in *CISD2* fibroblasts. One explanation is that increased ER-mitochondrial contact is due to ER stress, which has been shown to lead to increased MAM apposition, either as an adaptive response or due to apoptosis induction (Chami *et al.*, 2008; Bravo *et al.*, 2011). Both *WFS1* and *CISD2* deficiency have previously been shown to disturb ER homeostasis leading to ER stress and activation of the UPR (Fonseca *et al.*, 2010; Wiley *et al.*, 2013). Whether these cellular mechanisms are relevant to *CISD2*

fibroblasts is unclear and further investigation of the three main UPR signalling pathways and ER chaperone levels is needed to clarify whether *CISD2* fibroblasts are under ER stress.

Alternatively, disturbed Ca^{2+} homeostasis and increased ER-mitochondria interactions in *CISD2* fibroblasts could be caused by dysregulation of the IP_3R. CISD2 has previously been shown to interact with the IP_3R, and evidence suggests that CISD2 is required for Bcl-2 mediated regulation of cellular Ca^{2+} homeostasis (Chang *et al.*, 2010). Bcl-2 is proposed to functionally interact with the IP_3R and inhibit high amplitude Ca^{2+} transients and promote low amplitude Ca^{2+} transients (Chen *et al.*, 2004). The Bcl-2-IP3R interaction also negatively regulates IP_3R dependent Ca^{2+} transfer to mitochondria (Hanson *et al.*, 2008). CISD2 may therefore have a role in the negative regulation of IP_3R dependent Ca^{2+} release. Loss of this function in *CISD2* fibroblasts could account for the observed increased cytosolic $[Ca^{2+}]$ and ER-mitochondrial Ca^{2+} flux. IP_3R dependent ER Ca^{2+} release has also been shown to decrease mitochondrial movement which is suggested to facilitate the formation of stable ER-mitochondrial interactions (Wang *et al.*, 2000; Yi *et al.*, 2004). Therefore, dysregulation of the IP_3R secondary to *CISD2* mutations may also promote undesirable ER-mitochondria interactions. Further investigations are required to clarify IP_3R function secondary to *CISD2* deficiency and address these potential pathogenic mechanisms.

Interestingly, one mitochondrial abnormality observed in *CISD2* fibroblasts was an elongated mitochondrial network, demonstrated by significantly increased average length and volume of mitochondrial fragments in the *CISD2* fibroblast compared with controls. This conclusion was further supported by a detailed analysis of the distribution of the length and volume of mitochondrial fragments in *CISD2* and control fibroblasts. *CISD2* fibroblasts contained significantly more ‘larger’ mitochondrial fragments and less ‘smaller’ mitochondrial fragments than controls. In agreement with these observations, it has previously been reported that mitochondria are significantly enlarged and elongated in diaphragm muscle and myoblasts from skeletal *Cisd*2-/- mice (Chang *et al.*, 2012). On the other hand, transient *CISD2* knockdown (<4 hours) in H1299 epithelial cells had no effect on mitochondrial morphology (Chang *et al.*, 2010). These results suggest that CISD2 is not directly involved in mitochondrial network dynamics, unlike direct mediators such as MFN2

and OPA1, and that the elongated mitochondrial network in *CISD2* fibroblasts is likely a compensatory response to adverse cellular conditions caused by the *CISD2* mutation identified in the patient. Consistent with this concept, mitochondria have been shown to undergo hyperfusion termed 'stress-induced mitochondrial hyperfusion' in response to various cellular stressors (Tondera *et al.*, 2009). Similarly, mitochondria have been shown to fuse and elongate during starvation induced autophagy to protect mitochondria from degradation and maintain ATP production (Gomes *et al.*, 2011; Rambold *et al.*, 2011). Increased autophagy has been observed in two *Cisd2* deficient mouse models and there was no evidence of increased mitophagy (Chen *et al.*, 2009; Chang *et al.*, 2012), this suggests that mitochondrial elongation in *CISD2* fibroblasts could be a compensatory response to cellular stress, possibly dysregulated autophagy. Interestingly, patient cell lines harbouring pathogenic *OPA1* mutations, associated with DOA, have been linked with increased mitophagy, but in this case, the mitochondrial network was fragmented and not elongated as in *CISD2* fibroblasts (Carelli *et al.*, 2015; Yu-Wai-Man *et al.*, 2016). The links between ER dysfunction, mitochondrial dynamics and mitophagy in RGCs clearly deserve further attention.

In summary, the results of this study support a model whereby altered cellular Ca^{2+} homeostasis and disturbed ER-mitochondria interactions caused by *CISD2* mutations (**Figure 7.16)** are likely to be important pathophysiological players that contribute to the progressive neurodegenerative process that underlies Wolfram syndrome.

CISD2 fibroblasts

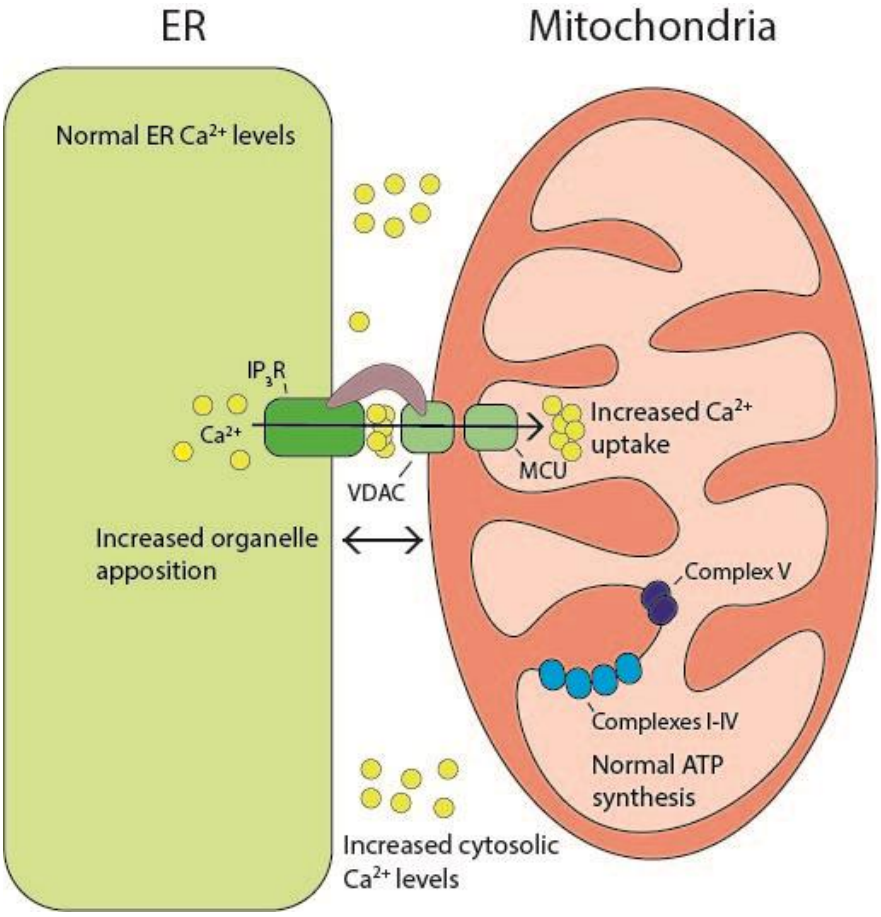

Figure 7.16 Schematic model highlighting the proposed dysfunction in *CISD2* fibroblasts. Mutation of the *CISD2* gene was associated with disturbed Ca^{2+} homeostasis including enhanced ER-mitochondrial Ca^{2+} flux and increased cytosolic [Ca^{2+}]. This was accompanied by increased ER-mitochondrial contact. There was no evidence of disturbed OXPHOS dysfunction.

Chapter 8. Quantifying Mitochondrial Axonal Transport in a Zebrafish Model

8.1 Introduction

RGCs have a long axonal segment that extends from the inner retina to the lateral geniculate nucleus which imposes a number of physical and functional constraints. The lamina cribosa at the optic nerve head divides the prelaminar unmyelinated axonal region from the post-laminar myelinated axonal region. Mitochondria are unevenly distributed in RGC and are concentrated in the prelaminar unmyelinated region due to the higher energy requirements for signal conduction in the absence of myelin insulation and at synapses where ATP demand is high (Barron *et al*., 2004). Consequently, the transport and distribution of mitochondria along RGC axons is critical for normal function (Yu *et al.*, 2013), and the loss of RGCs in inherited optic neuropathies could result from the disturbance of this fundamental process (Lopez Sanchez *et al.*, 2016).

Mitochondrial distribution in neurones is highly regulated by cellular Ca^{2+} signalling (Lin and Sheng, 2015). A direct consequence of the disturbed Ca^{2+} homeostasis observed in Wolfram syndrome models could therefore be the disruption of mitochondrial transport and distribution in neurones (Lin and Sheng, 2015). Consistent with this hypothesis, it has recently been demonstrated that mitochondrial transport was disturbed in *WFS1* shRNA-treated neurones and neurones from *Wfs1* -/- mice comprising a lower density of mitochondria in axons and decreased velocity of both anterograde and retrograde mitochondrial transport (Cagalinec *et al.*, 2016).

Zebrafish (*Danio rerio*) are tropical freshwater fish from the Cyprinidae family and they are frequently used to study biological processes, especially in early development, and to model human disease (Steele *et al.*, 2014). There are several advantageous features of zebrafish that make them a valuable tool for disease modelling. Genetic information and cellular processes are largely conserved between humans and zebrafish. Moreover, zebrafish embryos develop rapidly, high numbers can be obtained and they are readily amenable to experimental manipulation (Pickart and Klee, 2014). Zebrafish embryos are also transparent, a unique advantage, which enables live imaging of cellular processes by microscopy and zebrafish are

increasingly being utilized for the *in vivo* analysis of mitochondrial dynamics in disease (Bergamin *et al.*, 2016; Dukes *et al.*, 2016).

An assay to investigate mitochondrial motility in the lateral line of live zebrafish embryos has recently been described (Marra *et al.*, 2015). The lateral line system is a mechanosensory organ which extends along the whole length of the zebrafish and detects movement and vibration in the surrounding water (Chitnis *et al.*, 2012). The zebrafish lateral line and mitochondria are labelled by a GFP and a mitochondrial targeted-RFP (mito-RFP) tag, respectively. These are injected into one cell stage zebrafish embryos in plasmid form under a neuroD promoter. NeuroD is a transcription factor expressed in differentiating neurones including the lateral line (Marra *et al.*, 2015). Mitochondria in the lateral line can then be directly visualised in live zebrafish by microscopy and the motility patterns of axonal mitochondria can be quantified (Marra *et al.*, 2015).

The aim of this study was to optimise the assay described by *Marra and colleagues* to both visualize and quantify mitochondrial motility along the lateral line of zebrafish embryos. Once established in Dr Yu-Wai-Man's laboratory, this assay could be applied to zebrafish models of Wolfram syndrome and other inherited optic neuropathies to investigate how disturbed mitochondrial axonal transport influences the underlying neuropathology and the extent to which it contributes to RGC loss and visual failure.

8.2 Methods

8.2.1 Zebrafish strain, maintenance and husbandry

The golden zebrafish strain was used and maintained in accordance with standard guidelines. Zebrafish were paired the evening prior to injection. A single male and female zebrafish were paired in a breeding tank with two mesh dividers; one separating the two zebrafish and one separating the two zebrafish from the tank floor. On the morning of injection, the mesh divider separating the zebrafish was removed and the zebrafish coupled. Embryos were collected, washed in 'blue water' (system water containing 0.1% methylene blue (Sigma-Aldrich)) and raised at 28.5 °C in blue water.

8.2.2 Plasmids and zebrafish embryo microinjection

The neuroD:GFP and neuroD:mito-RFP plasmids were a kind gift from Assistant Professor Tamily A. Weismann (Lewis & Clark, USA). To co-label the zebrafish lateral line system and mitochondria, the neuroD:GFP and neuroD:mito-RFP plasmids were microinjected into one cell stage zebrafish embryos. Embryos were injected with 1.5 ng/µl (~3 pg total) of each plasmid in Danieau buffer (58 mM NaCl, 0.7 mM KCL, 0.4 mM $MgSO_4$, 0.6 mM $Ca(NO_3)_2$, and 0.5 mM HEPES, pH 7.6 (All Sigma-Aldrich)) with 0.05 % phenol red (Sigma-Aldrich). Microinjection was performed using a FemtoJet Microinjector (Eppendorf, Hamburg, Germany) and a glass needle (made by pulling a filamented glass capillary (Hilgenberg, Malsfeld, Germany) on a P-97 Flaming/Brown Micropipette puller (Sutter Instrument Co, California, USA)). A micrometer was used to calibrate the injection droplet to approximately 2 nl by changing the injection pressure (140-160 psi) and time (1-4 seconds) on the microinjector. Embryos were viewed down a Leica MZ9.5 stereomicroscope (Leica, Milton Keynes, UK) defective embryos were removed and the injection was performed into the yolk.

8.2.3 Nocodazole treatment

Zebrafish embryos were transferred into nocodazole (200 nM; Sigma-Aldrich) dissolved in blue water containing DMSO (0.1 %; Sigma-Aldrich) at 24 hours post fertilization (hpf) and maintained in this solution until imaging at 48 hpf. Control

zebrafish were maintained in blue water containing DMSO (0.1 %) without nocodazole.

8.2.4 Zebrafish imaging

Following plasmid injection (Section 8.2.2), zebrafish were screened at 48hpf for GFP expression using a Leica MZ9.5 stereomicroscope with an attached fluorescence illuminator. Selected zebrafish were mounted in low melt agarose (1 % v/v; Sigma-Aldrich) on glass bottom dishes and covered with E3 medium (5 mM NaCl, 0.17 mM KCl, 0.33 mM $CaCl_2$, 0.33 mM $MgSO_4$ (All Sigma-Aldrich)) to maintain an aqueous environment. Time-lapse images of the GFP and mito-RFP signal were acquired at 5 second intervals for 5 minutes with a Nikon A1R inverted confocal microscope equipped with a x60, 1.40 NA oil objective. Imaging was performed at room temperature.

8.2.5 Analysis of mitochondrial movement

Time-lapse image series were analyzed using Fiji. A segmented line was drawn along the ROI and a kymograph was generated to quantify mitochondrial movement using the multiple kymograph plugin (Fiji). A kymograph displays the fluorescent intensity along the segmented line from each frame as a horizontal line. The total kymograph, with a horizontal line for each frame of the time series stacked along the y axis shows a dynamic process in single image. The x axis represents distance and the y axis represents time (**Figure 8.2**). Mitochondrial velocity is calculated by converting the change in x into µm and the change in y into seconds; mitochondrial velocity is expressed as µm/s.

.

8.3 Results

8.3.1 Measuring mitochondrial motility in the zebrafish lateral line

The zebrafish lateral line and the mitochondria were labelled with a GFP and a mitochondrial targeted RFP tag, respectively. Zebrafish embryo transparency enabled direct imaging of the lateral line and mitochondria by confocal microscopy. Time-lapse imaging of mitochondrial motility was performed in live 48 hpf zebrafish embryos; both stationary and motile mitochondria were readily identifiable (**Figure 8.1**).

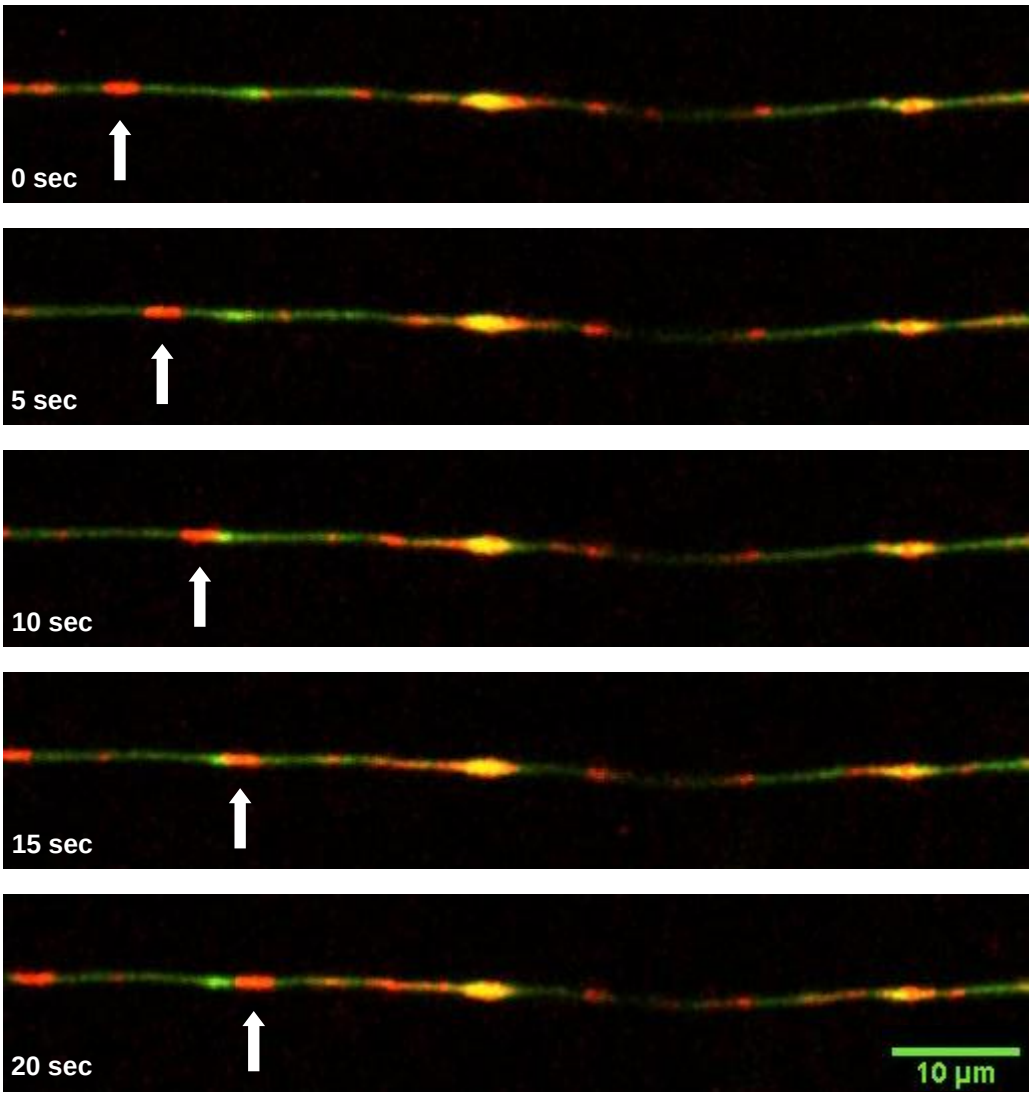

Figure 8.1 Time-lapse images showing mitochondrial motility in the zebrafish lateral line. Sequential images of the neuroD:GFP labelled zebrafish lateral line (green) and neuroD:mito-RFP labelled mitochondria (red) at 5 second (sec) intervals. The white arrow tracks a motile mitochondrion.

A kymograph was generated to quantify mitochondrial motility. Diagonal white lines depict anterograde and retrograde mitochondrial movement, and vertical white lines depict stationary mitochondria (**Figure 8.2A**). Mitochondrial velocity is calculated based on the slope of the white line. In the example provided, the yellow line equates to a mitochondrial velocity of 0.61 µm/s. Mitochondria with a velocity ≥0.01 µm/s are considered motile and ~42 % of mitochondria in the present kymograph were motile (**Figure 8.2B**). The mean mitochondrial velocities for anterograde and retrograde mitochondrial movement in the example kymograph can also be derived (**Figure 8.2C**).

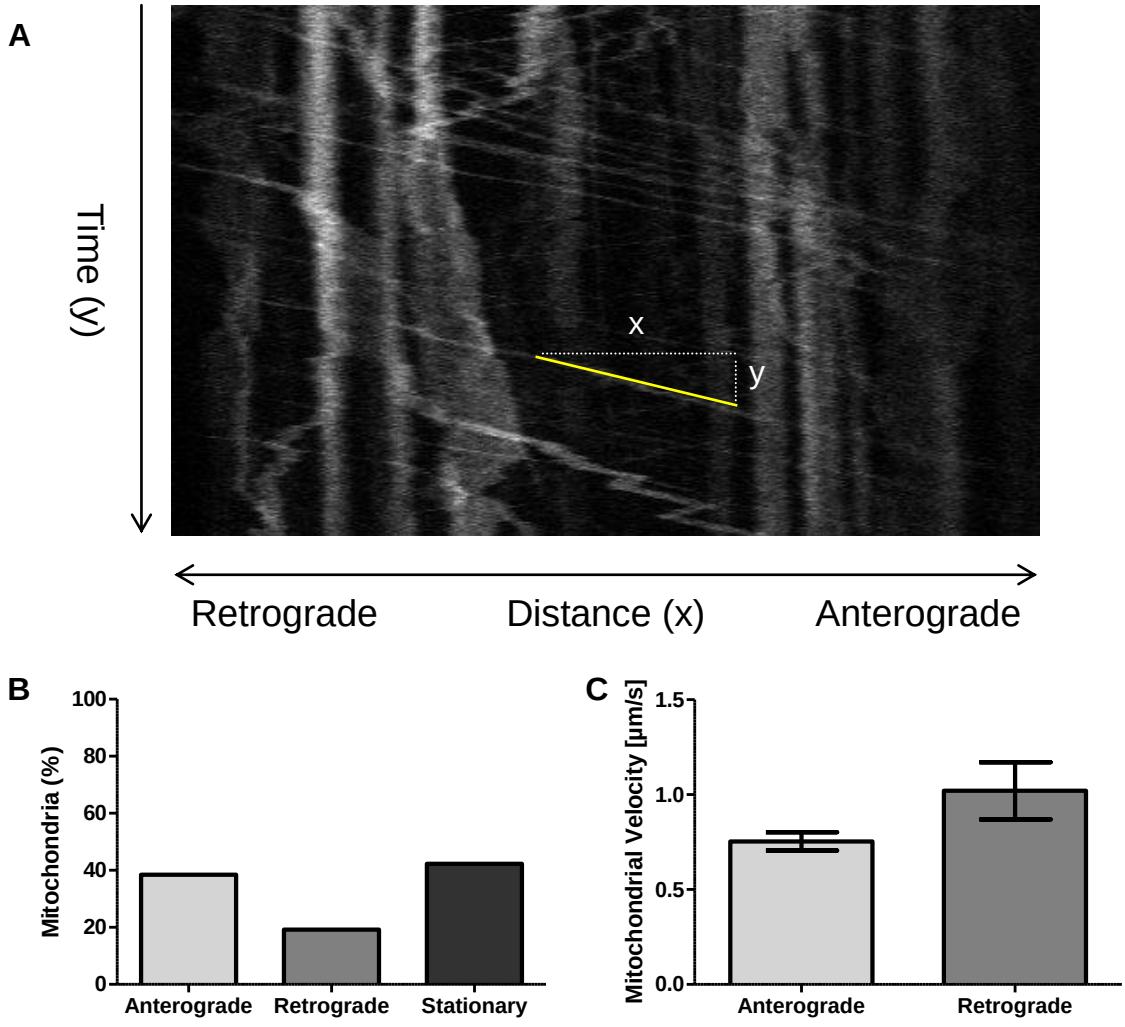

Figure 8.2 Analysis of mitochondrial motility in the zebrafish lateral line. (A) Representative kymograph, white lines represent the spatial location of mitochondria over time. The yellow line highlights the analysis of mitochondrial velocity; change in x and y are converted into µm and seconds, respectively. Mitochondrial velocity is expressed as µm/s. (B) Patterns of mitochondrial motility quantified from the kymograph. (C) Mean mitochondrial velocity for anterograde and retrograde mitochondrial transport quantified from the kymograph.

8.3.2 Nocodazole inhibits mitochondrial motility in the zebrafish lateral line

To confirm that disturbances in mitochondrial motility could be measured, zebrafish were treated with nocodazole, which interferes with microtubule polymerization, and mitochondrial motility was analyzed. As expected, nocodazole treatment arrested mitochondrial movement in the zebrafish lateral line. Kymograph analysis showed no actively moving mitochondria as observed under basal conditions; the mitochondria present have been depicted as vertical lines, indicating that mitochondria were mostly stationary in the lateral line of nocodazole treated zebrafish (**Figure 8.3**).

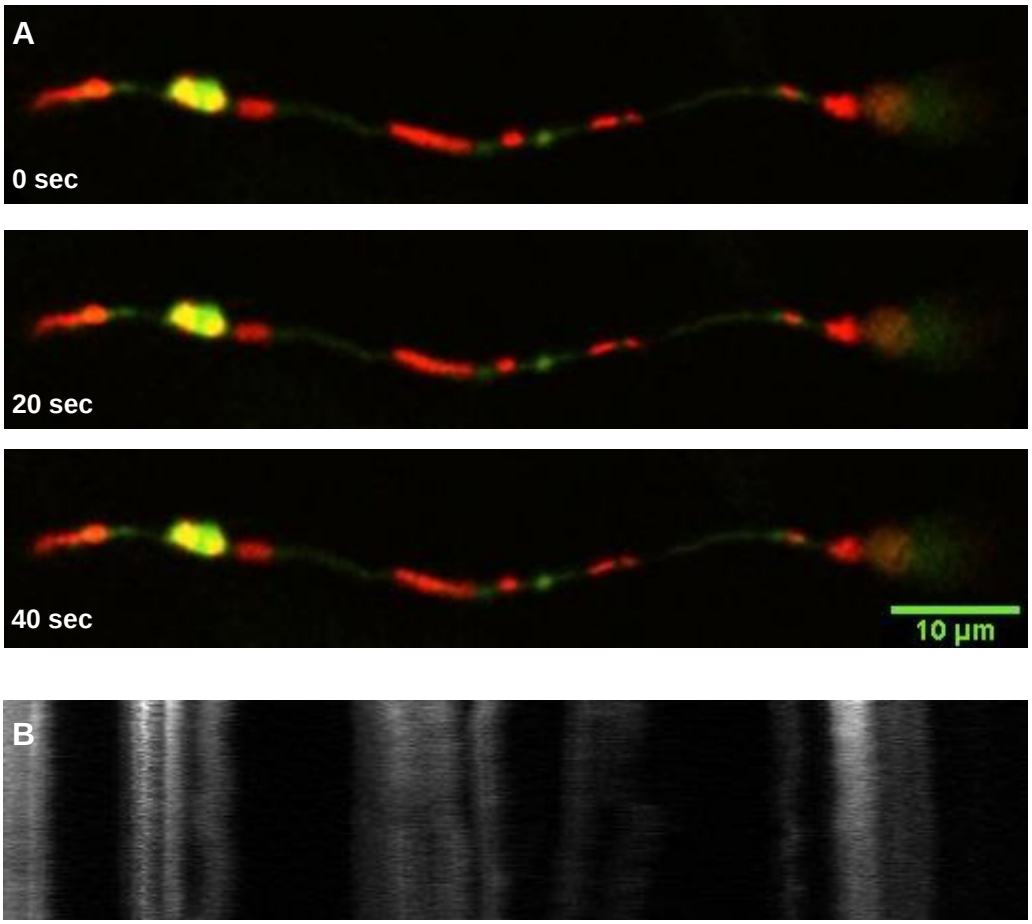

Figure 8.3 Analysis of mitochondrial motility in nocodazole treated zebrafish. (A) Sequential images of the neuroD:GFP labelled lateral line (green) and neuroD:mito-RFP labelled mitochondria (red) at 20 second (sec) intervals in nocodazole treated zebrafish. (B) Kymograph analysis of mitochondria in the lateral line of nocodazole treated zebrafish. Vertical lines indicate that mitochondria were mostly stationary.

8.4 Discussion

This chapter describes the setting up of an experimental assay to analyze mitochondrial motility in the zebrafish lateral line (Marra *et al.*, 2015). The expected patterns of mitochondrial movement in neuronal axons were observed in the zebrafish lateral line, including bi-directional movement, stop-start movement, changes in direction and also stationary mitochondria (Lin and Sheng, 2015). Moreover, the mitochondrial velocities that were quantified were within physiological ranges. The velocity of mitochondrial movement in neurones is somewhat variable and velocities ranging from 0.2 to 1.5 µm/s have previously been reported (MacAskill and Kittler, 2010; Bergamin *et al.*, 2016). To investigate whether disturbances in mitochondrial motility could be detected by the assay zebrafish were treated with nocodazole. Nocodazole binds to tubulin and prevents the formation of interchain linkages, thus inhibiting the dynamic assembly of microtubules. As mitochondria are dependent on microtubule based motors for long-range transport in neurones, nocodazole treatment is known to disturbed mitochondrial transport (Friedman *et al.*, 2010). As expected, nocodazole treatment severely impaired mitochondrial movement in the zebrafish lateral line, thus confirming that the assay can detect changes in mitochondrial dynamics (Plucinska *et al.*, 2012).

Previous studies investigating mitochondrial dynamics in zebrafish have primarily used transgenic zebrafish expressing a mitochondrial targeted fluorescent protein. In zebrafish, mitochondrial transport has been studied in at least Rohon-Beard sensory neurones, the lateral line system, motor neurones, dopaminergic neurones and RGCs (Plucinska *et al.*, 2012; Auer *et al.*, 2015; Bergamin *et al.*, 2016; Dukes *et al.*, 2016). An advantage of the present assay is the simplicity of labelling the mitochondria and neurones with injectable plasmids and the ease of imaging the zebrafish lateral line. The present assay is readily applicable to the study of mitochondrial dynamics in an antisense morpholino based or transgenic zebrafish model of Wolfram syndrome. Quantification of mitochondrial motility in an *in vivo* model would provide important insight into the disease mechanisms underlying Wolfram syndrome. Importantly, if mitochondrial dynamics are disturbed in a zebrafish model of not only Wolfram syndrome, but also other inherited optic neuropathies such as DOA *(Cagalinec et al., 2016; Yu-Wai-Man et al., 2016),* this

assay could also facilitate the screening of candidate drug molecules to rescue the pathological cellular phenotype.

The fact remains that mitochondrial dynamics are not being assessed directly in zebrafish RGCs, which is the specific cell type that contributes to optic nerve neurodegeneration and visual failure. One study has investigated mitochondrial dynamics in zebrafish RGCs (Auer *et al.*, 2015). This study showed that disruption of a kinesin motor that mediates anterograde transport of mitochondria was associated with depletion of mitochondria from RGC axon terminals and impaired RGC synaptic transmission (Auer *et al.*, 2015). However, imaging deeply located RGCs in an intact zebrafish embryo is technically more challenging than imaging the superficially located lateral line system (Auer *et al.*, 2015). Still, the neuroD transcription factor is likely expressed in the RGCs of zebrafish, suggesting that this assay could be extended to investigate mitochondrial dynamics in RGCs of zebrafish (Ochocinska and Hitchcock, 2009).

In summary, a reliable method has been established for imaging and quantifying mitochondrial axonal transport in an *in vivo* zebrafish model. This assay will be applied in future work aimed at further dissecting the disease mechanisms in Wolfram syndrome caused by *WFS1* mutations and in therapeutic drug screening.

Chapter 9. General Discussion

The research described within this thesis was undertaken to further explore the genetic and molecular basis of inherited optic neuropathies. The principle focus was on the disease mechanisms that contribute to the progressive neurodegenerative process seen in patients with Wolfram syndrome harbouring pathogenic *WFS1* mutations (Inoue *et al.*, 1998; Strom *et al.*, 1998).

9.1 Genetic screening for WFS1, RTN4IP1 and C12orf65 mutations in patients with suspected inherited optic neuropathies

The most common inherited optic neuropathies seen in clinical practice are LHON and DOA secondary to pathogenic *OPA1* mutations. However, with the advent of next-generation sequencing, the list of genes known to cause optic atrophy has increased significantly (**Table 1.1**) and this genetic heterogeneity can pose considerable diagnostic challenges. The underlying molecular defect still remains unknown in ~40-60 % of patients with a likely genetic basis for their optic atrophy (Ferre *et al.*, 2009; Yu-Wai-Man *et al.*, 2011b). Genetic screening of the *WFS1*, *RTN4IP1* and *C12orf65* genes in selected patients from a well-characterised cohort of 30 patients with suspected inherited optic neuropathy revealed no pathogenic mutations (**Chapter 4**). Reaching a confirmed genetic diagnosis has important implications for patients and their families, and further investigations are underway to determine the causative genes in this patient cohort with a combination of whole exome and whole genome sequencing. It is likely that the optic atrophy genes that still remain to be found are relatively rare and multicentre collaborations will be essential to identify a sufficient number of families and unequivocally confirm pathogenicity.

9.2 Mitochondrial dysfunction and the pathophysiology of Wolfram syndrome

Two clinical subtypes of Wolfram syndrome have been described that share overlapping clinical features. WFS1 and related disorders are secondary to recessive or dominant mutations in the *WFS1* gene, whereas, WFS2 is caused by recessive mutations in the *CISD2* gene (Moosajee *et al.*, 2016). The proteins encoded by *WFS1* and *CISD2* both localise to the ER, and although they have been proposed to have different cellular functions, one common role appears to be the regulation of

cellular Ca^{2+} homeostasis (Osman *et al.*, 2003; Chang *et al.*, 2010; Cagalinec *et al.*, 2016). In addition, the function of both proteins is essential for ER homeostasis as demonstrated by the onset of ER stress upon their deficiency (Fonseca *et al.*, 2005; Wiley *et al.*, 2013). It is now well established that mitochondrial dysfunction contributes to RGC loss in inherited optic neuropathies such as LHON and DOA (Yu-Wai-Man *et al.*, 2016). In contrast, the role of mitochondrial dysfunction in the pathophysiology of Wolfram syndrome is controversial and following the discovery of the *WFS1* gene, the literature has primarily focused on the concept of Wolfram syndrome being an ER-related disease (Ishihara *et al.*, 2004; Fonseca *et al.*, 2005; Yamada *et al.*, 2006). There are currently no treatments available for patients with Wolfram syndrome and further studies are required to clarify the disease mechanisms and identify therapeutic targets.

These studies were conducted in fibroblasts harbouring *WFS1* and *CISD2* mutations as it is relatively straightforward to obtain a skin biopsy and establish primary cell cultures. However, there are inherent limitations to using fibroblasts when trying to extrapolate the results obtained to a complex neuronal cell such as a RGC, which have a long axonal segment that extend from the inner retina to the lateral geniculate nucleus. Notwithstanding these limitations, fibroblasts established from Wolfram syndrome patients harbouring confirmed pathogenic *WFS1* and *CISD2* mutations are a valid *in vitro* model and they can help elucidate relevant disease mechanisms that deserve further study and that could be manipulated as therapeutic targets.

In fibroblasts, *WFS1* mutations decreased ER-mitochondrial Ca^{2+} flux, which was associated with a selective impairment of complex I-dependent respiration (**Chapter 5 and 6**). Interestingly, *CISD2* fibroblasts showed a contrasting phenotype characterised by enhanced ER-mitochondrial Ca^{2+} flux, which is likely the result of increased ER-mitochondrial apposition at the MAM (**Chapter 7**). The reasons for these differences are unclear; the functions of the Wolframin and CISD2 proteins appear to converge on regulation of the IP_3R (Chang *et al.*, 2010; Cagalinec *et al.*, 2016), and it will therefore be very interesting to further investigate IP_3R function and how this is modulated by pathogenic *WFS1* and *CISD2* mutations. Taken in the context of the wider literature, these studies clearly demonstrate that mutations in genes that encode ER proteins with putative roles at the MAM can affect

mitochondrial function by disturbing the structure and function of ER-mitochondrial interactions. The observation that primary ER dysfunction can cause secondary mitochondrial impairment is mechanistically highly relevant and it represents an obvious pathological pathway that could be targeted for the development of therapeutic strategies for patients with Wolfram syndrome.

As mentioned previously, a limitation of these studies is the use of fibroblasts as an *in vitro* disease model, which will not entirely reflect the neuropathology of Wolfram syndrome (Philbrook *et al.*, 2005; Auburger *et al.*, 2012). To address the need to study a neuronal model and replicate the findings obtained in mutant fibroblasts, four of the fibroblast cell lines harbouring *WFS1* mutations (W1-W4) have been reprogrammed to derive iPSCs. The differentiation of these patient-specific iPSCs into RGCs or neuronal cell types will provide an extremely valuable model to investigate the disease mechanisms of Wolfram syndrome in disease-relevant cells. In addition, these iPSC-derived neuronal cells can be used to address questions that cannot be answered using *WFS1* fibroblasts. In particular, it will be fascinating to determine the extent to which *WFS1* mutations disturb the transport and distribution of mitochondria from the soma and along the long axonal segment towards the terminal synapses. The physical constraints imposed by long neurones can also be dissected further in the context of cellular Ca^{2+} homeostasis, neuronal cell death and mitophagy.

The conclusions concerning the deleterious consequences of *CISD2* mutations are based on one cell line from a patient harbouring a novel homozygous mutation (c.215 A>G, p.Asn72Ser). Acknowledging the fact that WFS2 is relatively rare compared with WFS1, the phenotype of this specific *CISD2* cell line was in part comparable to that observed in one cell line carrying a dominant *WFS1* mutation (W5), which exhibited an apparent compensatory response with preserved complex I activity and no major disturbance in Ca^{2+} flux between the ER and mitochondrial compartments. The observations of increased MAM activity and elongated mitochondrial network in the *CISD2* fibroblasts could therefore represent a compensatory response to the *CISD2* mutation, rather than the disease mechanisms of WFS2. Further investigations are required to clarify mitochondrial function in the *CISD2* fibroblasts, including the assays applied to the *WFS1* fibroblasts such as Oxygraph respirometer analysis of mitochondrial respiratory chain function. Although

somewhat limited by the relatively rarity of WFS2 in the population, the characterisation of additional cell lines established from patients carrying different pathogenic *CISD2* mutations are required to fully establish the pathological consequences of *CISD2* mutations and whether there are common patterns across different genotypes and phenotypes.

9.3 Quantifying mitochondrial motility in the zebrafish lateral line

As described in Chapter 8, an assay to analyze mitochondrial motility in the zebrafish lateral line using targeted fluorescent proteins and confocal microscopy was optimized (Marra *et al.*, 2015). The assay enabled the quantification of dynamic mitochondrial processes and provided parameters, such as the velocity and direction of mitochondrial transport. This *in vivo* assay will now be used for the study of two transgenic zebrafish lines carrying pathogenic nonsense *Wfs1* mutations.

As previously discussed, the alterations in cellular Ca^{2+} homeostasis observed in *WFS1* and *CISD2* fibroblasts suggest that disturbed mitochondrial dynamics could underlie RGC loss in Wolfram syndrome. This disease mechanism has recently been investigated in *WFS1* deficient neurones and rather strikingly, *WFS1* deficiency disturbed neuronal mitochondrial transport and decreased axonal mitochondrial density (Cagalinec *et al.*, 2016). However, these observations could be strengthened further by the use of an *in vivo* animal model, which enables the study of mitochondrial dynamics in neurones that still retain their physiological connectivity and synaptic activity (Dukes *et al.*, 2016). Application of the present assay to investigate mitochondrial motility therefore represents a powerful method to study mitochondrial dynamics in disease not only for Wolfram syndrome, but also for other inherited optic neuropathies such as *OPA1*-related DOA.

The zebrafish is an attractive *in vivo* disease model for a number of practical reasons, including cost and ease of genetic manipulation. One advantage of assessing mitochondrial dynamics in the zebrafish lateral line is that other physiological processes are readily investigable in this system. The zebrafish lateral line is amenable to the investigation of cellular Ca^{2+} homeostasis with genetically-encoded calcium indicator (GECI) proteins targeted to the cytosol, mitochondria and ER. Conveniently, ER-mitochondrial Ca^{2+} flux can be assessed using these probes following IP_3R stimulation with adenophostin A (Esterberg *et al.*, 2014). In addition,

mitochondrial function in the zebrafish lateral line can be determined by assessing mitochondrial membrane potential with TMRM followed by treatment with the ATP synthase inhibitor oligomycin and the uncoupler FCCP (Esterberg *et al.*, 2014). Application of these methods to a zebrafish model of Wolfram syndrome, which is currently being developed, would determine whether the model resembles the phenotype observed in *WFS1* fibroblasts. Importantly, assessment of mitochondrial dynamics and function could be put into the context of cellular Ca^{2+} homeostasis.

One limitation of the mitochondrial motility assay is that due to constraints of confocal microscopy, imaging is limited to a single focal plane. Nevertheless, these images can be used to assess the density of mitochondria in axons by calculating mitochondrial volume under the assumption that mitochondria are cylindrical in shape (Plucinska *et al.*, 2012). To circumvent these technical limitations, the assay could be significantly improved by using advanced imaging techniques such as light-sheet microscopy, where a plane or 'sheet of light' is used to illuminate the sample rather than the point-scanning approach of confocal microscopy (Ahrens *et al.*, 2013). This technique would enable the high-speed acquisition of a time-series in three dimensions of mitochondrial dynamics in the zebrafish lateral line. Analysis of these images would provide a thorough assessment of mitochondrial transport and morphology in an *in vivo* zebrafish model (Ahrens *et al.*, 2013).

9.4 Therapeutic strategies

There are currently limited treatment options for patients with inherited optic neuropathies and progressive blindness imposes a significant social, economic and psychological burden on affected patients. Hopefully the body of work presented in this thesis will contribute to a better understanding of mitochondrial dysfunction in the pathophysiology of Wolfram syndrome and highlight potential options for rescuing or halting neuronal loss in this disorder. Future work involving the use of neuronal cell types differentiated from mutation-specific iPSCs and a zebrafish model of Wolfram syndrome will provide validation of the disease mechanisms found in *WFS1* mutant fibroblasts. These models also represent powerful tools for prospective drug screening.

Some candidate drug molecules include idebenone and EPI-743, which are shorter-chain analogues of ubiquinone that can act as electron carriers in the ETC, in

addition to being potent antioxidants (Yu-Wai-Man *et al.*, 2016). These two compounds have shown promise in the treatment of LHON and DOA (Klopstock *et al.*, 2011; Sadun *et al.*, 2012; Smith *et al.*, 2016), and should be tested in these *in vitro* and *in vivo* models to gather preclinical data on their possible efficacy in the context of pathogenic *WFS1* mutations. Other therapeutic strategies for optic neuropathies that could be assessed in Wolfram syndrome models include drugs that stimulate mitochondrial biogenesis and ATP synthesis such as bezafibrate, 5-aminoimidazole-4-carboxamide ribonucleoside (AICAR) and acetyl-L-carnitine (ALCAR) (Yu-Wai-Man *et al.*, 2016).

Another important therapeutic strategy is to target ER dysfunction in patients with Wolfram syndrome. The proposed options include the chemical chaperones 4-phenylbutyric acid (PBA) and tauroursodeoxycholic acid (TUDCA), which function to enhance protein folding and processing in the ER, and have been shown to alleviate ER stress in *WFS1* deficient β-cells (Shang *et al.*, 2014; Urano, 2016). Sodium valproate is another potential therapeutic option; this drug is proposed to activate the *WFS1* promoter and increase Wolframin expression, and to increase the production of the cell cycle regulator $p21^{cip}$, expression of which correlated with protection against cell death in *WFS1* depleted human neuroblastoma SK-N-AS cells (Kakiuchi *et al.*, 2009; Gharanei *et al.*, 2013).

9.5 Concluding remarks

In summary, the findings outlined in this thesis indicate that pathogenic *WFS1* and *CISD2* mutations impact negatively on mitochondrial function, which is a common thread uniting all inherited optic neuropathies. Disturbed interactions between the ER and mitochondria are increasingly being recognised in the context of human disease and the complex interplay between these two dynamic cellular compartments is only beginning the be unravelled. Ultimately, the hope is that the mechanistic insights gained from the study of Wolfram syndrome will lead to the development of effective treatments for patients suffering from progressive blindness and neurological decline.

Chapter 10. Appendices

10.1 Appendix A

Appendix A contains the data from the assays described in Chapter 5. Tables are named for the corresponding figure. Statistical analysis was performed using GraphPad with a two-tailed unpaired t test.

Cell line	Wolframin/Tubulin	SEM	N	P value vs. control
Controls	0.7050	0.3000	3	-
W1	-	-	3	-
W2	-	-	3	-
W3	-	-	3	-
W4	0.3656	0.0817	3	0.3364
W5	0.3261	0.0250	3	0.2767

Table 10.1 Western blot analysis of Wolframin in *WFS1* fibroblasts

	GRP98/Tubulin				BIP/Tubulin			
Cell line	**Mean**	**SEM**	**N**	**P value vs. control**	**Mean**	**SEM**	**N**	**P value vs. control**
Controls	0.1209	0.0119	4	-	0.9033	0.1810	4	-
W1	01426	0.0280	4	0.4945	1.2963	0.2355	4	0.2141
W2	0.1370	0.0276	4	0.6029	0.9844	0.0433	4	0.6354
W3	0.1264	0.0240	4	0.8385	0.9985	0.1378	4	0.6642
WFS1 rec	0.1354	0.0005	3	0.2387	1.0931	0.1017	3	0.3317
W4	0.2250	0.0712	4	0.1984	1.6109	0.3032	4	0.0835
W5	0.2025	0.0580	4	0.2152	0.9851	0.1138	4	0.6873

Table 10.2 Western blot analyses of ER stress markers in *WFS1* fibroblasts

Cell line	FRET/CFP	SEM	N	P value vs. control
Controls	1.3556	0.0340	45	-
W1	1.4325	0.1028	15	0.3590
W2	1.4620	0.0619	15	0.1277
W3	1.3705	0.0882	15	0.8481
WFS1 rec	1.4216	0.0488	45	0.1368
W4	1.4460	0.0736	15	0.2173
W5	1.4435	0.1180	15	0.2701

Table 10.3 Analysis of ER Ca^{2+} levels in *WFS1* fibroblasts.

Cell line	Cytosolic Ca^{2+} (nM)	SEM	N	P value vs. control
Controls	65.2402	5.4824	3	-
W1	63.98511	0.5370	3	0.8940
W2	66.05383	11.6062	3	0.8351
W3	65.6816	10.3400	3	0.8427
WFS1 rec	63.2033	0.6367	3	0.7308
W4	73.1005	23.4728	3	0.7024
W5	82.4458	12.01878	3	0.2189

Table 10.4 Analysis of basal cytosolic [Ca^{2+}] in *WFS1* fibroblasts.

	Peak Cytosolic Ca^{2+} (nM)				Tg sensitive Ca^{2+} stores (nM)			
Cell line	**Mean**	**SEM**	**N**	**P value vs. control**	**Mean**	**SEM**	**N**	**P value vs. control**
Controls	143.8811	15.9811	3	-	80.6778	10.5952	3	-
W1	124.4730	32.0574	3	0.6167	60.4879	32.5927	3	0.2491
W2	114.3270	3.4469	3	0.1449	48.2732	11.2282	3	0.1038
W3	138.6637	28.6149	3	0.8812	72.9822	29.7147	3	0.8193
WFS1 rec	125.8212	7.0577	3	0.3597	60.5811	7.1330	3	0.1907
W4	146.5606	5.3848	3	0.8815	73.4600	18.2237	3	0.7493
W5	209.0087	46.3315	3	0.2546	126.5629	57.6378	3	0.4774

Table 10.5 Analysis of thapsigargin induced ER Ca^{2+} depletion in *WFS1* fibroblasts.

	Rhod-2-AM Intensity ($\Delta F/F_o$)				Fluo-4-AM Intensity ($\Delta F/F_o$)			
Cell line	**Mean**	**SEM**	**N**	**P value vs. control**	**Mean**	**SEM**	**N**	**P value vs. control**
Controls	7.2403	0.2582	36	-	4.609	0.1721	24	-
W1	4.5534	0.2876	14	0.0003 ***	4.734	0.1935	10	0.6743
W2	4.8517	0.4418	14	0.0018 **	4.249	0.2376	10	0.2516
W3	5.1061	0.6181	8	0.0268 *	4.157	0.2356	12	0.1355
WFS1 rec	4.7922	0.4191	35	<0.0001***	4.353	0.1231	32	0.8356
W4	3.8855	0.6420	9	0.0005 ***	5.544	0.1259	8	0.0229 *
W5	6.6667	0.4730	12	0.4604	3.850	0.2362	9	0.2361

Table 10.6 Disturbed Ca^{2+} flux in *WFS1* fibroblasts.

	M1 ER/mito colocalisation				M2 mito/ER colocalisation			
Cell line	**Mean**	**SEM**	**N**	**P value vs. control**	**Mean**	**SEM**	**N**	**P value vs. control**
Controls	0.0411	0.0028	56	-	0.2056	0.1321	56	-
W1	0.0443	0.0047	20	0.5514	0.2029	0.0178	20	0.9115
W2	0.0408	0.0028	23	0.9528	0.2008	0.0157	23	0.8362
W3	0.0532	0.0065	16	0.0568	0.2404	0.0295	16	0.2387
WFS1 rec	0.0477	0.0027	59	0.0909	0.2122	0.0117	59	0.7067
W4	0.0457	0.0033	21	0.3619	0.1969	0.0159	21	0.7151
W5	0.0476	0.0031	19	0.2127	0.2941	0.0245	19	0.0015 **

Table 10.7 Analysis of ER-mitochondrial contact in *WFS1* fibroblasts.

Cell line	TMRM intensity (F/F_o)	SEM	N	P value vs. control
Controls	35.22	3.105	19	-
W1	27.19	5.201	6	0.2125
W2	60.20	6.6167	6	0.0008 ***
W3	28.78	4.597	5	0.3353
WFS1 rec	39.31	4.865	17	0.4737
W4	33.23	4.800	5	0.7694
W5	33.04	8.911	7	0.7694

Table 10.8 Mitochondrial membrane potential assessed by TMRM in *WFS1* and control fibroblasts.

	IP3R/Tubulin				SERCA/Tubulin				VDAC/Tubulin				MCU/Tubulin			
Cell line	**Mean**	**SEM**	**N**	**P value vs. control**	**Mean**	**SEM**	**N**	**P value vs. control**	**Mean**	**SEM**	**N**	**P value vs. control**	**Mean**	**SEM**	**N**	**P value vs. control**
Controls	0.4158	0.1187	3	-	0.1808	0.0217	3	-	0.5624	0.2684	2	-	0.5843	0.01928	3	-
W1	0.4276	0.04753	3	0.9310	0.8650	0.0889	3	0.0017 **	1.438	0.5824	2	0.3053	0.5715	0.0530	3	0.8329
W2	0.7407	0.1217	3	0.1286	0.7124	0.0944	3	0.0054 **	0.6966	0.0596	2	0.6737	0.5413	0.1639	3	0.8075
W3	0.7365	0.3009	3	0.3776	0.3999	0.3999	3	0.2240	0.2353	0.0134	2	0.3477	0.5258	0.1918	3	0.7770
WFS1 rec	0.6350	0.1037	3	0.2368	0.6591	0.1369	3	0.0260 **	0.7901	0.4292	2	0.9322	0.5462	0.0134	3	0.1809
W4	0.5218	0.1515	3	0.6111	1.1670	0.2497	3	0.0170 *	0.5882	0.0107	2	0.9322	0.6674	0.2560	3	0.7623
W5	0.5626	0.2057	3	0.5700	0.6147	0.1369	3	0.2534	0.4851	0.0468	2	0.8033	1.0350	0.0821	3	0.0059 **

Table 10.9 Western blot analyses of key Ca^{2+} channels and pumps in *WFS1* fibroblasts.

10.2 Appendix B

Appendix B contains the data from the assays described in Chapter 6. Tables are named for the corresponding figure. Statistical analysis was performed using GraphPad with a two-tailed unpaired t test.

	Basal respiration OCR (pmol/min/mg of protein)				ATP-linked respiration OCR (pmol/min/mg of protein)				Proton Leak OCR (pmol/min/mg of protein)				Maximal Respiration OCR (pmol/min/mg of protein)			
Cell line	**Mean**	**SEM**	**N**	**P value vs. control**	**Mean**	**SEM**	**N**	**P value vs. control**	**Mean**	**SEM**	**N**	**P value vs. control**	**Mean**	**SEM**	**N**	**P value vs. control**
Controls	3209	675	3	-	2555	590	3	-	693	164	3	-	4869	974	3	-
W1	2819	1088	3	0.7762	1867	723	3	0.5021	952	366	3	0.5584	5256	2165	3	0.8785
W2	5799	1182	3	0.1299	4120	713	3	0.1664	1776	389	3	0.0626	9871	2624	3	0.1485
W3	8390	3995	3	0.2701	5702	1872	3	0.1842	2708	2119	3	0.3970	10511	2810	3	0.1307
WFS1 rec	5669	1610	3	0.2314	3897	1113	3	0.3470	1812	507	3	0.1040	8546	1655	3	0.1281
W4	3511	1285	3	0.8454	2740	762	3	0.8573	1228	181	3	0.0944	6729	2568	3	0.5355
W5	8884	686	3	0.0041 **	6228	119	3	0.0037 **	2645	642	3	0.0423 *	12921	877	3	0.0036 **

Table 10.10 Parameters of mitochondrial respiratory function in *WFS1* fibroblasts determined by Seahorse analysis.

	CI/(CI+CII)				CII/(CI+CII)			
Cell line	**Mean**	**SEM**	**N**	**P value vs. control**	**Mean**	**SEM**	**N**	**P value vs. control**
Controls	0.4416	0.0282	3	-	0.7451	0.0449	3	-
W1	0.2372	0.0226	5	0.0014 **	0.9337	0.0134	5	0.0023 **
W2	0.3098	0.0306	5	0.0279 *	0.8273	0.0022	5	0.1084
W3	0.3596	0.0153	5	0.0301 *	0.7698	0.0221	5	0.5954
WFS1 rec	0.3022	0.0296	3	0.0271 *	0.8436	0.0480	3	0.2083
W4	0.4246	0.0378	5	0.6662	0.8434	0.0196	5	0.0573
W5	0.4246	0.0235	5	0.6662	0.7721	0.0248	5	0.5825

Table 10.11 Complex I-dependent respiration is reduced in *WFS1* fibroblasts.

Cell line	pPDH/Total PDH	SEM	N	P value vs. control
Controls	2.094	0.0667	3	-
W1	1.882	0.1110	3	0.1755
W2	1.572	0.1708	3	0.0464 *
W3	2.336	0.3256	3	0.5077
WFS1 rec	1.930	0.2219	3	0.5165
W4	1.750	0.2294	3	0.2232
W5	1.769	0.3437	3	0.4057

Table 10.12 PDH regulation in WFS1 fibroblast.

	Glucose Luminescence/mg of protein				2-DG Luminescence/mg of protein				Oligomycin Luminescence/mg of protein				2-DG+Oligomycin Luminescence/mg of protein			
Cell line	**Mean**	**SEM**	**N**	**P value vs. control**	**Mean**	**SEM**	**N**	**P value vs. control**	**Mean**	**SEM**	**N**	**P value vs. control**	**Mean**	**SEM**	**N**	**P value vs. control**
Controls	31930	4332	3	-	12054	1577	3	-	24630	2095	3	-	1924	646	3	-
W1	19976	3325	4	0.0735	14527	2252	4	0.4434	27293	2659	4	0.4928	7442	2914	4	0.1747
W2	27857	2609	4	0.4256	14988	2519	4	0.4093	23562	2058	4	0.7365	4594	1223	4	0.1445
W3	28181	2096	4	0.4255	15707	2456	4	0.3043	26041	3133	4	0.7449	4167	1030	4	0.1533
WFS1 rec	25338	2683	3	0.2587	15074	343	3	0.1347	25632	1096	3	0.6936	5401	1028	3	0.0458 *
W4	31146	5864	4	0.9237	15233	4236	4	0.5664	26596	4889	4	0.7582	3268	798	4	0.2720
W5	45805	8184	4	0.2587	41493	8419	4	0.0326 *	29346	7291	4	0.6151	8575	2568	4	0.0837

Table 10.13 ATP content in *WFS1* and control fibroblasts.

	Basal RFU/mg of protein				H_2O_2 RFU/mg of protein			
Cell line	**Mean**	**SEM**	**N**	**P value vs. control**	**Mean**	**SEM**	**N**	**P value vs. control**
Controls	92.30	12.68	3	-	181.4	42.01	3	-
W1	67.67	17.36	3	0.3159	83.98	19.05	3	0.1021
W2	84.34	28.74	3	0.8125	145.3	52.08	3	0.6174
W3	94.41	39.38	3	0.9618	231.7	47.52	3	0.4728
WFS1 rec	82.14	8.53	3	0.8052	153.6	13.86	3	0.4669
W4	100.70	29.40	3	0.7682	208.7	43.23	3	0.6741
W5	83.33	25.46	3	0.5143	127.7	22.17	3	0.3209

Table 10.14 Assessment of ROS levels in *WFS1* fibroblasts using H_2DCFDA.

Cell line	mtDNA Copy Number	SEM	N	P value vs. control
Controls	125.6	11.11	3	-
W1	142.7	6.007	3	0.2462
W2	122.8	12.28	3	0.8753
W3	158.2	12.28	3	0.1206
WFS1 rec	141.2	10.22	3	0.3901
W4	137	4.121	3	0.8241
W5	121.5	13.18	3	0.3585

Table 10.15 mtDNA Copy Number in *WFS1* and control fibroblasts.

	STS 2 hours Cell viability (%)				STS 5 hours Cell viability (%)				STS 8 hours Cell viability (%)			
Cell line	**Mean**	**SEM**	**N**	**P value vs. control**	**Mean**	**SEM**	**N**	**P value vs. control**	**Mean**	**SEM**	**N**	**P value vs. control**
Controls	82.48	3.929	3	-	67.90	3.80	3	-	46.15	13.29	3	-
W1	68.45	5.743	4	0.0903	66.18	2.420	4	0.7155	50.03	7.000	4	0.8048
W2	76.13	3.371	4	0.2659	72.50	2.399	4	0.3459	68.49	7.500	4	0.1937
W3	79.67	3.737	4	0.6229	68.94	1.353	4	0.8061	52.96	7.547	4	0.6714
WFS1 rec	77.46	5.625	3	0.4820	72.80	3.911	3	0.4188	62.35	61.61	3	0.3726
W4	79.48	4.156	4	0.6185	72.84	2.405	4	0.3145	65.28	4.500	4	0.2218
W5	82.20	2.782	4	0.9544	71.69	2.120	4	0.4181	72.03	9.000	4	0.1581

Table 10.16 *Viability* of *WFS1* and control fibroblasts following treatment with cell stressors

	t-BH 2 hours Cell viability (%)				t-BH 5 hours Cell viability (%)				t-BH 8 hours Cell viability (%)			
Cell line	**Mean**	**SEM**	**N**	**P value vs. control**	**Mean**	**SEM**	**N**	**P value vs. control**	**Mean**	**SEM**	**N**	**P value vs. control**
Controls	101.6	1.1862	3	-	53.91	9.265	3	-	16.92	4.395	3	-
W1	84.24	6.082	4	0.0341 *	60.11	3.058	4	0.5482	34.11	7.363	4	0.0919
W2	97.92	4.511	4	0.4788	67.36	3.644	4	0.2254	17.95	5.902	4	0.8942
W3	99.66	3.816	4	0.6631	57.47	14.15	4	0.8402	4.933	0.4571	4	0.0350 *
WFS1 rec	93.94	4.878	3	0.1592	61.65	2.956	3	0.5217	19.00	8.438	3	0.8226
W4	98.03	1.511	4	0.1859	79.92	3.650	4	0.0400	28.25	9.085	4	03046
W5	99.19	5.430	4	0.6886	70.42	4.981	4	0.1676	13.89	9.001	4	0.7723

Table 10.17 *Viability* of *WFS1* and control fibroblasts following treatment with cell stressors

	Tg 2 hours Cell viability (%)				Tg 5 hours Cell viability (%)				Tg 8 hours Cell viability (%)			
Cell line	**Mean**	**SEM**	**N**	**P value vs. control**	**Mean**	**SEM**	**N**	**P value vs. control**	**Mean**	**SEM**	**N**	**P value vs. control**
Controls	90.38	2.037	3	-	49.92	4.387	3	-	21.59	5.311	3	-
W1	103.5	4.838	4	0.0462 *	76.00	3.768	4	0.0041 **	50.20	4.408	4	0.0060 **
W2	111.2	5.201	4	0.0098 **	75.69	3.366	4	0.0035 **	40.92	2.074	4	0.0147 *
W3	112.1	6.029	4	0.0144 *	82.75	3.142	4	0.0009 ***	43.34	6.802	4	0.0453 *
WFS1 rec	108.9	2.709	3	0.0025 **	78.15	2.303	3	0.0038 **	44.82	2.780	3	0.0179 *
W4	102.5	3.618	4	0.0268 **	79.77	5.163	4	0.0045 **	46.68	4.964	4	0.0136 *
W5	86.91	4.023	4	0.4709	34.70	4.611	4	0.0539	9.486	2.780	4	0.0935

Table 10.18 *Viability* of *WFS1* and control fibroblasts following treatment with cell stressors

	Basal Specific Activity				STS Specific Activity				t-BH Specific Activity				Thapsigargin Specific Activity			
Cell line	**Mean**	**SEM**	**N**	**P value vs. control**	**Mean**	**SEM**	**N**	**P value vs. control**	**Mean**	**SEM**	**N**	**P value vs. control**	**Mean**	**SEM**	**N**	**P value vs. control**
Controls	1.163	0.06979	3	-	15.29	6.553	3	-	0.6502	0.05773	3	-	1.026	0.1020	3	-
W1	1.062	0.4452	3	0.8337	9.557	3.005	3	0.4714	0.5372	0.1691	3	0.5618	0.9905	0.1001	3	0.8181
W2	1.094	0.01992	3	0.3908	11.63	4.377	3	0.6673	0.5873	0.1796	3	0.7558	1.045	0.0312	3	0.8655
W3	0.9608	0.1145	3	0.2053	4.162	1.292	3	0.1712	0.5422	0.1507	3	0.5403	1.005	0.0355	3	0.8591
WFS1 rec	1.039	0.0401	3	0.1970	8.451	2.227	3	0.3794	0.5556	0.0160	3	0.1895	1.013	0.0121	3	0.9124
W4	1.175	0.0859	3	0.9247	8.477	2.410	3	0.3847	0.6211	0.1812	3	0.8861	1.208	0.2484	3	0.5340
W5	1.223	0.2893	3	0.8503	15.37	3.562	3	0.9918	0.6557	0.5556	3	0.9842	1.291	0.4383	3	0.5866

Table 10.19 Caspase 3 activities in *WFS1* and control fibroblasts following treatment with cell stressors.

10.3 Appendix C

Appendix C contains the data from the assays described in Chapter 7. Tables are named for the corresponding figure. Statistical analysis was performed using GraphPad with a two-tailed unpaired t test.

Cell line	FRET/CFP	SEM	N	P value vs. control
Controls	1.356	0.0340	45	-
CISD2	1.444	0.1180	15	0.3293

Table 10.20 Evaluation of ER Ca^{2+} levels with the D1ER probe.

Cell line	Cytosolic Ca^{2+} (nM)	SEM	N	P value vs. control
Controls	63.20	5.485	3	-
CISD2	103.7	5.415	3	0.0063 **

Table 10.21 Increased cytosolic [Ca^{2+}] in *CISD2* fibroblasts.

	Peak Cytosolic Ca^{2+} (nM)				Tg sensitive Ca^{2+} stores (nM)			
Cell line	**Mean**	**SEM**	**N**	**P value vs. control**	**Mean**	**SEM**	**N**	**P value vs. control**
Controls	143.9	15.98	3	-	80.68	10.59	3	-
CISD2	152.3	4.492	3	0.6383	48.60	9.751	3	0.0898

Table 10.22 Analysis of thapsigargin induced ER Ca^{2+} depletion in *CISD2* fibroblasts

	Rhod-2-AM Intensity ($\Delta F/F_o$)				Fluo-4-AM Intensity ($\Delta F/F_o$)			
Cell line	**Mean**	**SEM**	**N**	**P value vs. control**	**Mean**	**SEM**	**N**	**P value vs. control**
Controls	7.515	0.3878	35	-	4.624	0.1612	25	-
CISD2	9.304	0.7504	15	0.0240 *	3.929	0.1990	14	0.0117 *

Table 10.23 Disturbed Ca^{2+} flux in *CISD2* fibroblasts.

	M1 ER/mito colocalisation				M2 mito/ER colocalisation			
Cell line	**Mean**	**SEM**	**N**	**P value vs. control**	**Mean**	**SEM**	**N**	**P value vs. control**
Controls	0.0411	0.0028	56	-	0.2056	0.0132	56	-
CISD2	0.0734	0.0060	26	<0.0001 ***	0.2616	0.0197	26	0.0199 *

Table 10.24 Increased ER-mitochondrial contacts in *CISD2* fibroblasts.

	Average length (μm)				Average volume (μm^3)				Average number of fragments			
Cell line	**Mean**	**SEM**	**N**	**P value vs. control**	**Mean**	**SEM**	**N**	**P value vs. control**	**Mean**	**SEM**	**N**	**P value vs. control**
Controls	3.130	0.08419	56	-	2.030	0.1911	56	-	90.34	6.961	56	-
CISD2	3.970	0.2380	25	<0.0001 ***	4.380	0.6600	25	<0.0001 ***	53.88	4.466	25	0.0012 **

Table 10.25 Altered mitochondrial fragment morphology in *CISD2* fibroblasts.

	Control (Relative frequency %)			CISD2 (Relative frequency %)			
Mitochondrial length (µm)	**Mean**	**SEM**	**N**	**Mean**	**SEM**	**N**	**P value vs. control**
<2	0.4500	0.0147	56	0.3800	0.0240	25	0.0120 *
2 to 5	0.3600	0.0106	56	0.4500	0.0220	25	<0.0001 ***
5 to 10	0.0900	0.0900	56	0.1100	0.0100	25	0.0284 *
>10	0.0400	0.0040	56	0.0600	0.0008	25	0.0148 *

Table 10.26 Distribution of the length of mitochondrial fragments in *CISD2* fibroblasts.

	Control (Relative frequency %)			CISD2 (Relative frequency %)			
Mitochondrial volume (μm^3)	**Mean**	**SEM**	**N**	**Mean**	**SEM**	**N**	**P value vs. control**
<0.5	0.5510	0.0134	56	0.3930	0.0244	25	<0.0001 ***
0.5 to 1	0.1940	0.0079	56	0.1560	0.0145	25	0.0149 *
1 to 5	0.2050	0.0094	56	0.3310	0.0223	25	<0.0001 ***
5 to 10	0.0260	0.0028	56	0.0480	0.0068	25	0.0006 ***
>10	0.0350	0.0039	56	0.0720	0.0061	25	<0.0001 ***

Table 10.27 Distribution of the volume of mitochondrial fragments in *CISD2* fibroblasts.

	Average total length (μm)				Average total volume (μm^3)			
Cell line	**Mean**	**SEM**	**N**	**P value vs. control**	**Mean**	**SEM**	**N**	**P value vs. control**
Controls	261.7	15.28	56	-	141.7	8.157	56	-
CISD2	191.4	9.910	25	0.0042 **	179.7	12.09	25	0.0113 *

Table 10.28 Altered mitochondrial network morphology in *CISD2* fibroblasts

Cell line	Average total volume (μm^3)	SEM	N	P value vs. control
Controls	634.7	37.48	51	-
CISD2	965.8	48.74	25	0.3353

Table 10.29 The average total ER volume in *CISD2* fibroblasts.

	Glucose Luminescence/mg of protein				2-DG Luminescence/mg of protein				Oligomycin Luminescence/mg of protein				2-DG+Oligomycin Luminescence/mg of protein			
Cell line	**Mean**	**SEM**	**N**	**P value vs. control**	**Mean**	**SEM**	**N**	**P value vs. control**	**Mean**	**SEM**	**N**	**P value vs. control**	**Mean**	**SEM**	**N**	**P value vs. control**
Controls	47761	2203	3	-	21250	4747	3	-	21304	1321	3	-	3971	1238	3	-
CISD2	37382	5883	3	0.2098	14750	2425	3	0.2896	13637	3128	3	0.0869	2633	1044	3	0.4549

Table 10.30 ATP content in *CISD2* fibroblasts.

10.4 Appendix D

Appendix D contains the data from the assays described in Chapter 8. Tables are named for the corresponding figure.

Cell line	Mitochondria (%)	SEM	N
Anterograde	38.46	-	1
Retrograde	19.23	-	1
Stationary	42.31	-	1

Table 10.31 Analysis of mitochondrial motility in the zebrafish lateral line.

Cell line	Mitochondria (%)	SEM	N
Anterograde	0.753	0.048	10
Retrograde	1.021	0.151	5

Table 10.32 Analysis of mitochondrial motility in the zebrafish lateral line.

Chapter 11. References

Ahrens, M.B., Orger, M.B., Robson, D.N., Li, J.M. and Keller, P.J. (2013) 'Whole-brain functional imaging at cellular resolution using light-sheet microscopy', *Nat Methods*, 10(5), pp. 413-20.

Al-Saif, A., Al-Mohanna, F. and Bohlega, S. (2011) 'A mutation in sigma-1 receptor causes juvenile amyotrophic lateral sclerosis', *Ann Neurol*, 70(6), pp. 913-9.

Alavi, M.V., Bette, S., Schimpf, S., Schuettauf, F., Schraermeyer, U., Wehrl, H.F., Ruttiger, L., Beck, S.C., Tonagel, F., Pichler, B.J., Knipper, M., Peters, T., Laufs, J. and Wissinger, B. (2007) 'A splice site mutation in the murine Opa1 gene features pathology of autosomal dominant optic atrophy', *Brain*, 130(Pt 4), pp. 1029-42.

Amati-Bonneau, P., Guichet, A., Olichon, A., Chevrollier, A., Viala, F., Miot, S., Ayuso, C., Odent, S., Arrouet, C., Verny, C., Calmels, M.N., Simard, G., Belenguer, P., Wang, J., Puel, J.L., Hamel, C., Malthiery, Y., Bonneau, D., Lenaers, G. and Reynier, P. (2005) 'OPA1 R445H mutation in optic atrophy associated with sensorineural deafness', *Ann Neurol*, 58(6), pp. 958-63.

Amati-Bonneau, P., Valentino, M.L., Reynier, P., Gallardo, M.E., Bornstein, B., Boissiere, A., Campos, Y., Rivera, H., de la Aleja, J.G., Carroccia, R., Iommarini, L., Labauge, P., Figarella-Branger, D., Marcorelles, P., Furby, A., Beauvais, K., Letournel, F., Liguori, R., La Morgia, C., Montagna, P., Liguori, M., Zanna, C., Rugolo, M., Cossarizza, A., Wissinger, B., Verny, C., Schwarzenbacher, R., Martin, M.A., Arenas, J., Ayuso, C., Garesse, R., Lenaers, G., Bonneau, D. and Carelli, V. (2008) 'OPA1 mutations induce mitochondrial DNA instability and optic atrophy 'plus' phenotypes', *Brain*, 131(Pt 2), pp. 338-51.

Amr, S., Heisey, C., Zhang, M., Xia, X.J., Shows, K.H., Ajlouni, K., Pandya, A., Satin, L.S., El-Shanti, H. and Shiang, R. (2007) 'A homozygous mutation in a novel zinc-finger protein, ERIS, is responsible for Wolfram syndrome 2', *Am J Hum Genet*, 81(4), pp. 673-83.

Anand, R., Wai, T., Baker, M.J., Kladt, N., Schauss, A.C., Rugarli, E. and Langer, T. (2014) 'The i-AAA protease YME1L and OMA1 cleave OPA1 to balance mitochondrial fusion and fission', *J Cell Biol*, 204(6), pp. 919-29.

Andrews, R.M., Griffiths, P.G., Johnson, M.A. and Turnbull, D.M. (1999a) 'Histochemical localisation of mitochondrial enzyme activity in human optic nerve and retina', *Br J Ophthalmol*, 83(2), pp. 231-5.

Andrews, R.M., Kubacka, I., Chinnery, P.F., Lightowlers, R.N., Turnbull, D.M. and Howell, N. (1999b) 'Reanalysis and revision of the Cambridge reference sequence for human mitochondrial DNA', *Nat Genet*, 23(2), p. 147.

Angebault, C., Guichet, P.O., Talmat-Amar, Y., Charif, M., Gerber, S., Fares-Taie, L., Gueguen, N., Halloy, F., Moore, D., Amati-Bonneau, P., Manes, G., Hebrard, M., Bocquet, B., Quiles, M., Piro-Megy, C., Teigell, M., Delettre, C., Rossel, M., Meunier, I., Preising, M., Lorenz, B., Carelli, V., Chinnery, P.F., Yu-Wai-Man, P., Kaplan, J., Roubertie, A., Barakat, A., Bonneau, D., Reynier, P., Rozet, J.M., Bomont, P., Hamel, C.P. and Lenaers, G. (2015) 'Recessive Mutations in RTN4IP1 Cause Isolated and Syndromic Optic Neuropathies', *Am J Hum Genet*, 97(5), pp. 754-60.

Antonicka, H., Ostergaard, E., Sasarman, F., Weraarpachai, W., Wibrand, F., Pedersen, A.M., Rodenburg, R.J., van der Knaap, M.S., Smeitink, J.A., Chrzanowska-Lightowlers, Z.M. and Shoubridge, E.A. (2010) 'Mutations in C12orf65 in patients with encephalomyopathy and a mitochondrial translation defect', *Am J Hum Genet*, 87(1), pp. 115-22.

Area-Gomez, E., de Groof, A.J., Boldogh, I., Bird, T.D., Gibson, G.E., Koehler, C.M., Yu, W.H., Duff, K.E., Yaffe, M.P., Pon, L.A. and Schon, E.A. (2009) 'Presenilins are enriched in endoplasmic reticulum membranes associated with mitochondria', *Am J Pathol*, 175(5), pp. 1810-6.

Area-Gomez, E., Del Carmen Lara Castillo, M., Tambini, M.D., Guardia-Laguarta, C., de Groof, A.J., Madra, M., Ikenouchi, J., Umeda, M., Bird, T.D., Sturley, S.L. and Schon, E.A. (2012) 'Upregulated function of mitochondria-associated ER membranes in Alzheimer disease', *EMBO J*, 31(21), pp. 4106-23.

Area-Gomez, E. and Schon, E.A. (2016) 'Mitochondria-associated ER membranes and Alzheimer disease', *Curr Opin Genet Dev*, 38, pp. 90-96.

Auburger, G., Klinkenberg, M., Drost, J., Marcus, K., Morales-Gordo, B., Kunz, W.S., Brandt, U., Broccoli, V., Reichmann, H., Gispert, S. and Jendrach, M. (2012) 'Primary skin fibroblasts as a model of Parkinson's disease', *Mol Neurobiol*, 46(1), pp. 20-7.

Auer, T.O., Xiao, T., Bercier, V., Gebhardt, C., Duroure, K., Concordet, J.P., Wyart, C., Suster, M., Kawakami, K., Wittbrodt, J., Baier, H. and Del Bene, F. (2015) 'Deletion of a kinesin I motor unmasks a mechanism of homeostatic branching control by neurotrophin-3', *Elife*, 4.

Baracca, A., Solaini, G., Sgarbi, G., Lenaz, G., Baruzzi, A., Schapira, A.H., Martinuzzi, A. and Carelli, V. (2005) 'Severe impairment of complex I-driven adenosine triphosphate synthesis in leber hereditary optic neuropathy cybrids', *Arch Neurol*, 62(5), pp. 730-6.

Barrett, T.G., Bundey, S.E. and Macleod, A.F. (1995a) 'Neurodegeneration and diabetes: UK nationwide study of Wolfram (DIDMOAD) syndrome', *Lancet*, 346(8988), pp. 1458-63.

Barrett, T.G., Poulton, K. and Bundey, S. (1995b) 'DIDMOAD syndrome; further studies and muscle biochemistry', *J Inherit Metab Dis*, 18(2), pp. 218-20.

Barrett, T.G., Scott-Brown, M., Seller, A., Bednarz, A., Poulton, K. and Poulton, J. (2000) 'The mitochondrial genome in Wolfram syndrome', *J Med Genet*, 37(6), pp. 463-6.

Baughman, J.M., Perocchi, F., Girgis, H.S., Plovanich, M., Belcher-Timme, C.A., Sancak, Y., Bao, X.R., Strittmatter, L., Goldberger, O., Bogorad, R.L., Koteliansky, V. and Mootha, V.K. (2011) 'Integrative genomics identifies MCU as an essential component of the mitochondrial calcium uniporter', *Nature*, 476(7360), pp. 341-5.

Benit, P., Lebon, S. and Rustin, P. (2009) 'Respiratory-chain diseases related to complex III deficiency', *Biochim Biophys Acta*, 1793(1), pp. 181-5.

Bergamin, G., Cieri, D., Vazza, G., Argenton, F. and Mostacciuolo, M.L. (2016) 'Zebrafish Tg(hb9:MTS-Kaede): a new in vivo tool for studying the axonal movement of mitochondria', *Biochim Biophys Acta*, 1860(6), pp. 1247-55.

Bernard-Marissal, N., Medard, J.J., Azzedine, H. and Chrast, R. (2015) 'Dysfunction in endoplasmic reticulum-mitochondria crosstalk underlies SIGMAR1 loss of function mediated motor neuron degeneration', *Brain*, 138(Pt 4), pp. 875-90.

Bertholet, A.M., Millet, A.M., Guillermin, O., Daloyau, M., Davezac, N., Miquel, M.C. and Belenguer, P. (2013) 'OPA1 loss of function affects in vitro neuronal maturation', *Brain*, 136(Pt 5), pp. 1518-33.

Bogenhagen, D.F. (2012) 'Mitochondrial DNA nucleoid structure', *Biochim Biophys Acta*, 1819(9-10), pp. 914-20.

Bonnet Wersinger, D., Benkafadar, N., Jagodzinska, J., Hamel, C., Tanizawa, Y., Lenaers, G. and Delettre, C. (2014) 'Impairment of visual function and retinal ER stress activation in Wfs1-deficient mice', *PLoS One*, 9(5), p. e97222.

Bononi, A., Bonora, M., Marchi, S., Missiroli, S., Poletti, F., Giorgi, C., Pandolfi, P.P. and Pinton, P. (2013) 'Identification of PTEN at the ER and MAMs and its regulation of Ca(2+) signaling and apoptosis in a protein phosphatase-dependent manner', *Cell Death Differ*, 20(12), pp. 1631-43.

Bononi, A., Missiroli, S., Poletti, F., Suski, J.M., Agnoletto, C., Bonora, M., De Marchi, E., Giorgi, C., Marchi, S., Patergnani, S., Rimessi, A., Wieckowski, M.R. and Pinton, P. (2012) 'Mitochondria-associated membranes (MAMs) as hotspot Ca(2+) signaling units', *Adv Exp Med Biol*, 740, pp. 411-37.

Bradford, M.M. (1976) 'A rapid and sensitive method for the quantitation of microgram quantities of protein utilizing the principle of protein-dye binding', *Anal Biochem*, 72, pp. 248-54.

Brand, M.D. and Nicholls, D.G. (2011) 'Assessing mitochondrial dysfunction in cells', *Biochem J*, 435(2), pp. 297-312.

Bravo-Sagua, R., Rodriguez, A.E., Kuzmicic, J., Gutierrez, T., Lopez-Crisosto, C., Quiroga, C., Diaz-Elizondo, J., Chiong, M., Gillette, T.G., Rothermel, B.A. and Lavandero, S. (2013) 'Cell death and survival through the endoplasmic reticulum-mitochondrial axis', *Curr Mol Med*, 13(2), pp. 317-29.

Bravo, R., Vicencio, J.M., Parra, V., Troncoso, R., Munoz, J.P., Bui, M., Quiroga, C., Rodriguez, A.E., Verdejo, H.E., Ferreira, J., Iglewski, M., Chiong, M., Simmen, T., Zorzano, A., Hill, J.A., Rothermel, B.A., Szabadkai, G. and Lavandero, S. (2011) 'Increased ER-mitochondrial coupling promotes mitochondrial respiration and bioenergetics during early phases of ER stress', *J Cell Sci*, 124(Pt 13), pp. 2143-52.

Bristow, E.A., Griffiths, P.G., Andrews, R.M., Johnson, M.A. and Turnbull, D.M. (2002) 'The distribution of mitochondrial activity in relation to optic nerve structure', *Arch Ophthalmol*, 120(6), pp. 791-6.

Bu, X. and Rotter, J.I. (1993) 'Wolfram syndrome: a mitochondrial-mediated disorder?', *Lancet*, 342(8871), pp. 598-600.

Buchert, R., Uebe, S., Radwan, F., Tawamie, H., Issa, S., Shimazaki, H., Henneke, M., Ekici, A.B., Reis, A. and Abou Jamra, R. (2013) 'Mutations in the mitochondrial gene C12ORF65 lead to syndromic autosomal recessive intellectual disability and show genotype phenotype correlation', *Eur J Med Genet*, 56(11), pp. 599-602.

Cagalinec, M., Liiv, M., Hodurova, Z., Hickey, M.A., Vaarmann, A., Mandel, M., Zeb, A., Choubey, V., Kuum, M., Safiulina, D., Vasar, E., Veksler, V. and Kaasik, A. (2016) 'Role of Mitochondrial Dynamics in Neuronal Development: Mechanism for Wolfram Syndrome', *PLoS Biol*, 14(7), p. e1002511.

Cali, T., Ottolini, D., Negro, A. and Brini, M. (2012) 'alpha-Synuclein controls mitochondrial calcium homeostasis by enhancing endoplasmic reticulum-mitochondria interactions', *J Biol Chem*, 287(22), pp. 17914-29.

Cali, T., Ottolini, D., Negro, A. and Brini, M. (2013) 'Enhanced parkin levels favor ER-mitochondria crosstalk and guarantee Ca(2+) transfer to sustain cell bioenergetics', *Biochim Biophys Acta*, 1832(4), pp. 495-508.

Calvo, S.E., Clauser, K.R. and Mootha, V.K. (2016) 'MitoCarta2.0: an updated inventory of mammalian mitochondrial proteins', *Nucleic Acids Res*, 44(D1), pp. D1251-7.

Cardenas, C., Miller, R.A., Smith, I., Bui, T., Molgo, J., Muller, M., Vais, H., Cheung, K.H., Yang, J., Parker, I., Thompson, C.B., Birnbaum, M.J., Hallows, K.R. and Foskett, J.K. (2010) 'Essential regulation of cell bioenergetics by constitutive InsP3 receptor Ca2+ transfer to mitochondria', *Cell*, 142(2), pp. 270-83.

Carelli, V., Musumeci, O., Caporali, L., Zanna, C., La Morgia, C., Del Dotto, V., Porcelli, A.M., Rugolo, M., Valentino, M.L., Iommarini, L., Maresca, A., Barboni, P., Carbonelli, M., Trombetta, C., Valente, E.M., Patergnani, S., Giorgi, C., Pinton, P., Rizzo, G., Tonon, C., Lodi, R., Avoni, P., Liguori, R., Baruzzi, A., Toscano, A. and Zeviani, M. (2015) 'Syndromic parkinsonism and dementia associated with OPA1 missense mutations', *Ann Neurol*, 78(1), pp. 21-38.

Carelli, V., Ross-Cisneros, F.N. and Sadun, A.A. (2004) 'Mitochondrial dysfunction as a cause of optic neuropathies', *Prog Retin Eye Res*, 23(1), pp. 53-89.

Chami, M., Oules, B., Szabadkai, G., Tacine, R., Rizzuto, R. and Paterlini-Brechot, P. (2008) 'Role of SERCA1 truncated isoform in the proapoptotic calcium transfer from ER to mitochondria during ER stress', *Mol Cell*, 32(5), pp. 641-51.

Chang, C.R. and Blackstone, C. (2010) 'Dynamic regulation of mitochondrial fission through modification of the dynamin-related protein Drp1', *Ann N Y Acad Sci*, 1201, pp. 34-9.

Chang, N.C., Nguyen, M., Bourdon, J., Risse, P.A., Martin, J., Danialou, G., Rizzuto, R., Petrof, B.J. and Shore, G.C. (2012) 'Bcl-2-associated autophagy regulator Naf-1 required for maintenance of skeletal muscle', *Hum Mol Genet*, 21(10), pp. 2277-87.

Chang, N.C., Nguyen, M., Germain, M. and Shore, G.C. (2010) 'Antagonism of Beclin 1-dependent autophagy by BCL-2 at the endoplasmic reticulum requires NAF-1', *EMBO J*, 29(3), pp. 606-18.

Charif, M., Roubertie, A., Salime, S., Mamouni, S., Goizet, C., Hamel, C.P. and Lenaers, G. (2015) 'A novel mutation of AFG3L2 might cause dominant optic atrophy in patients with mild intellectual disability', *Front Genet*, 6, p. 311.

Chaussenot, A., Rouzier, C., Quere, M., Plutino, M., Ait-El-Mkadem, S., Bannwarth, S., Barth, M., Dollfus, H., Charles, P., Nicolino, M., Chabrol, B., Vialettes, B. and Paquis-Flucklinger, V. (2015) 'Mutation update and uncommon phenotypes in a French cohort of 96 patients with WFS1-related disorders', *Clin Genet*, 87(5), pp. 430-9.

Chen, H., Detmer, S.A., Ewald, A.J., Griffin, E.E., Fraser, S.E. and Chan, D.C. (2003) 'Mitofusins Mfn1 and Mfn2 coordinately regulate mitochondrial fusion and are essential for embryonic development', *J Cell Biol*, 160(2), pp. 189-200.

Chen, H., Vermulst, M., Wang, Y.E., Chomyn, A., Prolla, T.A., McCaffery, J.M. and Chan, D.C. (2010) 'Mitochondrial fusion is required for mtDNA stability in skeletal muscle and tolerance of mtDNA mutations', *Cell*, 141(2), pp. 280-9.

Chen, J., Xu, K., Zhang, X., Jiang, F., Liu, L., Dong, B., Ren, Y. and Li, Y. (2014) 'Mutation screening of mitochondrial DNA as well as OPA1 and OPA3 in a Chinese cohort with suspected hereditary optic atrophy', *Invest Ophthalmol Vis Sci*, 55(10), pp. 6987-95.

Chen, R., Valencia, I., Zhong, F., McColl, K.S., Roderick, H.L., Bootman, M.D., Berridge, M.J., Conway, S.J., Holmes, A.B., Mignery, G.A., Velez, P. and Distelhorst, C.W. (2004) 'Bcl-2 functionally interacts with inositol 1,4,5-trisphosphate receptors to regulate calcium

release from the ER in response to inositol 1,4,5-trisphosphate', *J Cell Biol*, 166(2), pp. 193-203.

Chen, Y.F., Kao, C.H., Chen, Y.T., Wang, C.H., Wu, C.Y., Tsai, C.Y., Liu, F.C., Yang, C.W., Wei, Y.H., Hsu, M.T., Tsai, S.F. and Tsai, T.F. (2009) 'Cisd2 deficiency drives premature aging and causes mitochondria-mediated defects in mice', *Genes Dev*, 23(10), pp. 1183-94.

Chevrollier, A., Guillet, V., Loiseau, D., Gueguen, N., de Crescenzo, M.A., Verny, C., Ferre, M., Dollfus, H., Odent, S., Milea, D., Goizet, C., Amati-Bonneau, P., Procaccio, V., Bonneau, D. and Reynier, P. (2008) 'Hereditary optic neuropathies share a common mitochondrial coupling defect', *Ann Neurol*, 63(6), pp. 794-8.

Chinnery, P.F. and Hudson, G. (2013) 'Mitochondrial genetics', *Br Med Bull*, 106, pp. 135-59.

Chitnis, A.B., Nogare, D.D. and Matsuda, M. (2012) 'Building the posterior lateral line system in zebrafish', *Dev Neurobiol*, 72(3), pp. 234-55.

Cogliati, S., Enriquez, J.A. and Scorrano, L. (2016) 'Mitochondrial Cristae: Where Beauty Meets Functionality', *Trends Biochem Sci*, 41(3), pp. 261-73.

Conlan, A.R., Axelrod, H.L., Cohen, A.E., Abresch, E.C., Zuris, J., Yee, D., Nechushtai, R., Jennings, P.A. and Paddock, M.L. (2009) 'Crystal structure of Miner1: The redox-active 2Fe-2S protein causative in Wolfram Syndrome 2', *J Mol Biol*, 392(1), pp. 143-53.

Cosson, P., Marchetti, A., Ravazzola, M. and Orci, L. (2012) 'Mitofusin-2 independent juxtaposition of endoplasmic reticulum and mitochondria: an ultrastructural study', *PLoS One*, 7(9), p. e46293.

Crawford, E.D. and Wells, J.A. (2011) 'Caspase substrates and cellular remodeling', *Annu Rev Biochem*, 80, pp. 1055-87.

Cruz-Bermudez, A., Vicente-Blanco, R.J., Hernandez-Sierra, R., Montero, M., Alvarez, J., Gonzalez Manrique, M., Blazquez, A., Martin, M.A., Ayuso, C., Garesse, R. and Fernandez-Moreno, M.A. (2016) 'Functional Characterization of Three Concomitant MtDNA LHON Mutations Shows No Synergistic Effect on Mitochondrial Activity', *PLoS One*, 11(1), p. e0146816.

Csordas, G., Renken, C., Varnai, P., Walter, L., Weaver, D., Buttle, K.F., Balla, T., Mannella, C.A. and Hajnoczky, G. (2006) 'Structural and functional features and significance of the physical linkage between ER and mitochondria', *J Cell Biol*, 174(7), pp. 915-21.

Dahmer, M.K. (2005) 'Caspases-2, -3, and -7 are involved in thapsigargin-induced apoptosis of SH-SY5Y neuroblastoma cells', *J Neurosci Res*, 80(4), pp. 576-83.

Davies, V.J., Hollins, A.J., Piechota, M.J., Yip, W., Davies, J.R., White, K.E., Nicols, P.P., Boulton, M.E. and Votruba, M. (2007) 'Opa1 deficiency in a mouse model of autosomal dominant optic atrophy impairs mitochondrial morphology, optic nerve structure and visual function', *Hum Mol Genet*, 16(11), pp. 1307-18.

Dayanithi, G., Chen-Kuo-Chang, M., Viero, C., Hamel, C., Muller, A. and Lenaers, G. (2010) 'Characterization of Ca2+ signalling in postnatal mouse retinal ganglion cells: involvement of OPA1 in Ca2+ clearance', *Ophthalmic Genet*, 31(2), pp. 53-65.

de Brito, O.M. and Scorrano, L. (2008) 'Mitofusin 2 tethers endoplasmic reticulum to mitochondria', *Nature*, 456(7222), pp. 605-10.

de Heredia, M.L., Cleries, R. and Nunes, V. (2013) 'Genotypic classification of patients with Wolfram syndrome: insights into the natural history of the disease and correlation with phenotype', *Genet Med*, 15(7), pp. 497-506.

De Stefani, D., Raffaello, A., Teardo, E., Szabo, I. and Rizzuto, R. (2011) 'A forty-kilodalton protein of the inner membrane is the mitochondrial calcium uniporter', *Nature*, 476(7360), pp. 336-40.

De Vos, K.J., Morotz, G.M., Stoica, R., Tudor, E.L., Lau, K.F., Ackerley, S., Warley, A., Shaw, C.E. and Miller, C.C. (2012) 'VAPB interacts with the mitochondrial protein PTPIP51 to regulate calcium homeostasis', *Hum Mol Genet*, 21(6), pp. 1299-311.

Decuypere, J.P., Parys, J.B. and Bultynck, G. (2012) 'Regulation of the autophagic bcl-2/beclin 1 interaction', *Cells*, 1(3), pp. 284-312.

den Dunnen, J.T., Dalgleish, R., Maglott, D.R., Hart, R.K., Greenblatt, M.S., McGowan-Jordan, J., Roux, A.F., Smith, T., Antonarakis, S.E. and Taschner, P.E. (2016) 'HGVS Recommendations for the Description of Sequence Variants: 2016 Update', *Hum Mutat*, 37(6), pp. 564-9.

Deniaud, A., Sharaf el dein, O., Maillier, E., Poncet, D., Kroemer, G., Lemaire, C. and Brenner, C. (2008) 'Endoplasmic reticulum stress induces calcium-dependent permeability transition, mitochondrial outer membrane permeabilization and apoptosis', *Oncogene*, 27(3), pp. 285-99.

Denton, R.M. (2009) 'Regulation of mitochondrial dehydrogenases by calcium ions', *Biochim Biophys Acta*, 1787(11), pp. 1309-16.

Distelhorst, C.W. and Bootman, M.D. (2011) 'Bcl-2 interaction with the inositol 1,4,5-trisphosphate receptor: role in Ca(2+) signaling and disease', *Cell Calcium*, 50(3), pp. 234-41.

Distelmaier, F., Koopman, W.J., van den Heuvel, L.P., Rodenburg, R.J., Mayatepek, E., Willems, P.H. and Smeitink, J.A. (2009) 'Mitochondrial complex I deficiency: from organelle dysfunction to clinical disease', *Brain*, 132(Pt 4), pp. 833-42.

Duarte, I., Nabuurs, S.B., Magno, R. and Huynen, M. (2012) 'Evolution and diversification of the organellar release factor family', *Mol Biol Evol*, 29(11), pp. 3497-512.

Dukanovic, J. and Rapaport, D. (2011) 'Multiple pathways in the integration of proteins into the mitochondrial outer membrane', *Biochim Biophys Acta*, 1808(3), pp. 971-80.

Dukes, A.A., Bai, Q., Van Laar, V.S., Zhou, Y., Ilin, V., David, C.N., Agim, Z.S., Bonkowsky, J.L., Cannon, J.R., Watkins, S.C., Croix, C.M., Burton, E.A. and Berman, S.B. (2016) 'Live imaging of mitochondrial dynamics in CNS dopaminergic neurons in vivo demonstrates early reversal of mitochondrial transport following MPP(+) exposure', *Neurobiol Dis*, 95, pp. 238-49.

El-Shanti, H., Lidral, A.C., Jarrah, N., Druhan, L. and Ajlouni, K. (2000) 'Homozygosity mapping identifies an additional locus for Wolfram syndrome on chromosome 4q', *Am J Hum Genet*, 66(4), pp. 1229-36.

Esterberg, R., Hailey, D.W., Rubel, E.W. and Raible, D.W. (2014) 'ER-mitochondrial calcium flow underlies vulnerability of mechanosensory hair cells to damage', *J Neurosci*, 34(29), pp. 9703-19.

Eura, Y., Ishihara, N., Yokota, S. and Mihara, K. (2003) 'Two mitofusin proteins, mammalian homologues of FZO, with distinct functions are both required for mitochondrial fusion', *J Biochem*, 134(3), pp. 333-44.

Fernandez-Vizarra, E., Tiranti, V. and Zeviani, M. (2009) 'Assembly of the oxidative phosphorylation system in humans: what we have learned by studying its defects', *Biochim Biophys Acta*, 1793(1), pp. 200-11.

Ferre, M., Bonneau, D., Milea, D., Chevrollier, A., Verny, C., Dollfus, H., Ayuso, C., Defoort, S., Vignal, C., Zanlonghi, X., Charlin, J.F., Kaplan, J., Odent, S., Hamel, C.P., Procaccio, V., Reynier, P. and Amati-Bonneau, P. (2009) 'Molecular screening of 980 cases of suspected hereditary optic neuropathy with a report on 77 novel OPA1 mutations', *Hum Mutat*, 30(7), pp. E692-705.

Fiedorczuk, K., Letts, J.A., Degliesposti, G., Kaszuba, K., Skehel, M. and Sazanov, L.A. (2016) 'Atomic structure of the entire mammalian mitochondrial complex I', *Nature*.

Filadi, R., Greotti, E., Turacchio, G., Luini, A., Pozzan, T. and Pizzo, P. (2015) 'Mitofusin 2 ablation increases endoplasmic reticulum-mitochondria coupling', *Proc Natl Acad Sci U S A*, 112(17), pp. E2174-81.

Fonseca, S.G., Fukuma, M., Lipson, K.L., Nguyen, L.X., Allen, J.R., Oka, Y. and Urano, F. (2005) 'WFS1 is a novel component of the unfolded protein response and maintains homeostasis of the endoplasmic reticulum in pancreatic beta-cells', *J Biol Chem*, 280(47), pp. 39609-15.

Fonseca, S.G., Ishigaki, S., Oslowski, C.M., Lu, S., Lipson, K.L., Ghosh, R., Hayashi, E., Ishihara, H., Oka, Y., Permutt, M.A. and Urano, F. (2010) 'Wolfram syndrome 1 gene negatively regulates ER stress signaling in rodent and human cells', *J Clin Invest*, 120(3), pp. 744-55.

Fransson, S., Ruusala, A. and Aspenstrom, P. (2006) 'The atypical Rho GTPases Miro-1 and Miro-2 have essential roles in mitochondrial trafficking', *Biochem Biophys Res Commun*, 344(2), pp. 500-10.

Fraser, F.C. and Gunn, T. (1977) 'Diabetes mellitus, diabetes insipidus, and optic atrophy. An autosomal recessive syndrome?', *J Med Genet*, 14(3), pp. 190-3.

Friedman, J.R., Lackner, L.L., West, M., DiBenedetto, J.R., Nunnari, J. and Voeltz, G.K. (2011) 'ER tubules mark sites of mitochondrial division', *Science*, 334(6054), pp. 358-62.

Friedman, J.R. and Nunnari, J. (2014) 'Mitochondrial form and function', *Nature*, 505(7483), pp. 335-43.

Friedman, J.R., Webster, B.M., Mastronarde, D.N., Verhey, K.J. and Voeltz, G.K. (2010) 'ER sliding dynamics and ER-mitochondrial contacts occur on acetylated microtubules', *J Cell Biol*, 190(3), pp. 363-75.

Fulop, L., Rajki, A., Maka, E., Molnar, M.J. and Spat, A. (2015) 'Mitochondrial Ca2+ uptake correlates with the severity of the symptoms in autosomal dominant optic atrophy', *Cell Calcium*, 57(1), pp. 49-55.

Fulop, L., Szanda, G., Enyedi, B., Varnai, P. and Spat, A. (2011) 'The effect of OPA1 on mitochondrial Ca(2)(+) signaling', *PLoS One*, 6(9), p. e25199.

Galluzzi, L., Kepp, O., Trojel-Hansen, C. and Kroemer, G. (2012) 'Mitochondrial control of cellular life, stress, and death', *Circ Res*, 111(9), pp. 1198-207.

Gharanei, S., Zatyka, M., Astuti, D., Fenton, J., Sik, A., Nagy, Z. and Barrett, T.G. (2013) 'Vacuolar-type H+-ATPase V1A subunit is a molecular partner of Wolfram syndrome 1 (WFS1) protein, which regulates its expression and stability', *Hum Mol Genet*, 22(2), pp. 203-17.

Giacomello, M., Drago, I., Bortolozzi, M., Scorzeto, M., Gianelle, A., Pizzo, P. and Pozzan, T. (2010) 'Ca2+ hot spots on the mitochondrial surface are generated by Ca2+ mobilization

from stores, but not by activation of store-operated Ca2+ channels', *Mol Cell*, 38(2), pp. 280-90.

Giacomello, M. and Pellegrini, L. (2016) 'The coming of age of the mitochondria-ER contact: a matter of thickness', *Cell Death Differ*, 23(9), pp. 1417-27.

Giorgio, V., von Stockum, S., Antoniel, M., Fabbro, A., Fogolari, F., Forte, M., Glick, G.D., Petronilli, V., Zoratti, M., Szabo, I., Lippe, G. and Bernardi, P. (2013) 'Dimers of mitochondrial ATP synthase form the permeability transition pore', *Proc Natl Acad Sci U S A*, 110(15), pp. 5887-92.

Glancy, B. and Balaban, R.S. (2012) 'Role of mitochondrial Ca2+ in the regulation of cellular energetics', *Biochemistry*, 51(14), pp. 2959-73.

Gomes, L.C., Di Benedetto, G. and Scorrano, L. (2011) 'During autophagy mitochondria elongate, are spared from degradation and sustain cell viability', *Nat Cell Biol*, 13(5), pp. 589-98.

Gray, M.W. (2012) 'Mitochondrial evolution', *Cold Spring Harb Perspect Biol*, 4(9), p. a011403.

Grenier, J., Meunier, I., Daien, V., Baudoin, C., Halloy, F., Bocquet, B., Blanchet, C., Delettre, C., Esmenjaud, E., Roubertie, A., Lenaers, G. and Hamel, C.P. (2016) 'WFS1 in Optic Neuropathies: Mutation Findings in Nonsyndromic Optic Atrophy and Assessment of Clinical Severity', *Ophthalmology*, 123(9), pp. 1989-98.

Guardia-Laguarta, C., Area-Gomez, E., Rub, C., Liu, Y., Magrane, J., Becker, D., Voos, W., Schon, E.A. and Przedborski, S. (2014) 'alpha-Synuclein is localized to mitochondria-associated ER membranes', *J Neurosci*, 34(1), pp. 249-59.

Hanson, C.J., Bootman, M.D., Distelhorst, C.W., Wojcikiewicz, R.J. and Roderick, H.L. (2008) 'Bcl-2 suppresses Ca2+ release through inositol 1,4,5-trisphosphate receptors and inhibits Ca2+ uptake by mitochondria without affecting ER calcium store content', *Cell Calcium*, 44(3), pp. 324-38.

Hara, T., Mahadevan, J., Kanekura, K., Hara, M., Lu, S. and Urano, F. (2014) 'Calcium efflux from the endoplasmic reticulum leads to beta-cell death', *Endocrinology*, 155(3), pp. 758-68.

Haroon, M.F., Fatima, A., Scholer, S., Gieseler, A., Horn, T.F., Kirches, E., Wolf, G. and Kreutzmann, P. (2007) 'Minocycline, a possible neuroprotective agent in Leber's hereditary optic neuropathy (LHON): studies of cybrid cells bearing 11,778 mutation', *Neurobiol Dis*, 28(3), pp. 237-50.

Hayashi, G. and Cortopassi, G. (2015) 'Oxidative stress in inherited mitochondrial diseases', *Free Radic Biol Med*, 88(Pt A), pp. 10-7.

Hayashi, T. and Su, T.P. (2007) 'Sigma-1 receptor chaperones at the ER-mitochondrion interface regulate Ca(2+) signaling and cell survival', *Cell*, 131(3), pp. 596-610.

Heidary, G., Calderwood, L., Cox, G.F., Robson, C.D., Teot, L.A., Mullon, J. and Anselm, I. (2014) 'Optic atrophy and a Leigh-like syndrome due to mutations in the c12orf65 gene: report of a novel mutation and review of the literature', *J Neuroophthalmol*, 34(1), pp. 39-43.

Hofmann, S. and Bauer, M.F. (2006) 'Wolfram syndrome-associated mutations lead to instability and proteasomal degradation of wolframin', *FEBS Lett*, 580(16), pp. 4000-4.

Hofmann, S., Philbrook, C., Gerbitz, K.D. and Bauer, M.F. (2003) 'Wolfram syndrome: structural and functional analyses of mutant and wild-type wolframin, the WFS1 gene product', *Hum Mol Genet*, 12(16), pp. 2003-12.

Hogewind, B.F., Pennings, R.J., Hol, F.A., Kunst, H.P., Hoefsloot, E.H., Cruysberg, J.R. and Cremers, C.W. (2010) 'Autosomal dominant optic neuropathy and sensorineual hearing loss associated with a novel mutation of WFS1', *Mol Vis*, 16, pp. 26-35.

Holt, I.J., Harding, A.E. and Morgan-Hughes, J.A. (1988) 'Deletions of muscle mitochondrial DNA in patients with mitochondrial myopathies', *Nature*, 331(6158), pp. 717-9.

Horner, S.M., Wilkins, C., Badil, S., Iskarpatyoti, J. and Gale, M., Jr. (2015) 'Proteomic analysis of mitochondrial-associated ER membranes (MAM) during RNA virus infection reveals dynamic changes in protein and organelle trafficking', *PLoS One*, 10(3), p. e0117963.

Hu, W.H., Hausmann, O.N., Yan, M.S., Walters, W.M., Wong, P.K. and Bethea, J.R. (2002) 'Identification and characterization of a novel Nogo-interacting mitochondrial protein (NIMP)', *J Neurochem*, 81(1), pp. 36-45.

Imagawa, E., Fattal-Valevski, A., Eyal, O., Miyatake, S., Saada, A., Nakashima, M., Tsurusaki, Y., Saitsu, H., Miyake, N. and Matsumoto, N. (2016) 'Homozygous p.V116* mutation in C12orf65 results in Leigh syndrome', *J Neurol Neurosurg Psychiatry*, 87(2), pp. 212-6.

Inoue, H., Tanizawa, Y., Wasson, J., Behn, P., Kalidas, K., Bernal-Mizrachi, E., Mueckler, M., Marshall, H., Donis-Keller, H., Crock, P., Rogers, D., Mikuni, M., Kumashiro, H., Higashi, K., Sobue, G., Oka, Y. and Permutt, M.A. (1998) 'A gene encoding a transmembrane protein is mutated in patients with diabetes mellitus and optic atrophy (Wolfram syndrome)', *Nat Genet*, 20(2), pp. 143-8.

Ishihara, H., Takeda, S., Tamura, A., Takahashi, R., Yamaguchi, S., Takei, D., Yamada, T., Inoue, H., Soga, H., Katagiri, H., Tanizawa, Y. and Oka, Y. (2004) 'Disruption of the WFS1 gene in mice causes progressive beta-cell loss and impaired stimulus-secretion coupling in insulin secretion', *Hum Mol Genet*, 13(11), pp. 1159-70.

Ishihara, N., Fujita, Y., Oka, T. and Mihara, K. (2006) 'Regulation of mitochondrial morphology through proteolytic cleavage of OPA1', *EMBO J*, 25(13), pp. 2966-77.

Jackson, M.J., Bindoff, L.A., Weber, K., Wilson, J.N., Ince, P., Alberti, K.G. and Turnbull, D.M. (1994) 'Biochemical and molecular studies of mitochondrial function in diabetes insipidus, diabetes mellitus, optic atrophy, and deafness', *Diabetes Care*, 17(7), pp. 728-33.

Jonckheere, A.I., Smeitink, J.A. and Rodenburg, R.J. (2012) 'Mitochondrial ATP synthase: architecture, function and pathology', *J Inherit Metab Dis*, 35(2), pp. 211-25.

Kadenbach, B. and Huttemann, M. (2015) 'The subunit composition and function of mammalian cytochrome c oxidase', *Mitochondrion*, 24, pp. 64-76.

Kakiuchi, C., Ishigaki, S., Oslowski, C.M., Fonseca, S.G., Kato, T. and Urano, F. (2009) 'Valproate, a mood stabilizer, induces WFS1 expression and modulates its interaction with ER stress protein GRP94', *PLoS One*, 4(1), p. e4134.

Kakiuchi, C., Ishiwata, M., Hayashi, A. and Kato, T. (2006) 'XBP1 induces WFS1 through an endoplasmic reticulum stress response element-like motif in SH-SY5Y cells', *J Neurochem*, 97(2), pp. 545-55.

Kalyanaraman, B., Darley-Usmar, V., Davies, K.J., Dennery, P.A., Forman, H.J., Grisham, M.B., Mann, G.E., Moore, K., Roberts, L.J., 2nd and Ischiropoulos, H. (2012) 'Measuring reactive oxygen and nitrogen species with fluorescent probes: challenges and limitations', *Free Radic Biol Med*, 52(1), pp. 1-6.

Kaufman, R.J. and Malhotra, J.D. (2014) 'Calcium trafficking integrates endoplasmic reticulum function with mitochondrial bioenergetics', *Biochim Biophys Acta*, 1843(10), pp. 2233-9.

Kirkman, M.A., Yu-Wai-Man, P., Korsten, A., Leonhardt, M., Dimitriadis, K., De Coo, I.F., Klopstock, T. and Chinnery, P.F. (2009) 'Gene-environment interactions in Leber hereditary optic neuropathy', *Brain*, 132(Pt 9), pp. 2317-26.

Kiviluoto, S., Vervliet, T., Ivanova, H., Decuypere, J.P., De Smedt, H., Missiaen, L., Bultynck, G. and Parys, J.B. (2013) 'Regulation of inositol 1,4,5-trisphosphate receptors during endoplasmic reticulum stress', *Biochim Biophys Acta*, 1833(7), pp. 1612-24.

Klopstock, T., Yu-Wai-Man, P., Dimitriadis, K., Rouleau, J., Heck, S., Bailie, M., Atawan, A., Chattopadhyay, S., Schubert, M., Garip, A., Kernt, M., Petraki, D., Rummey, C., Leinonen, M., Metz, G., Griffiths, P.G., Meier, T. and Chinnery, P.F. (2011) 'A randomized placebo-controlled trial of idebenone in Leber's hereditary optic neuropathy', *Brain*, 134(Pt 9), pp. 2677-86.

Koopman, W.J., Distelmaier, F., Smeitink, J.A. and Willems, P.H. (2013) 'OXPHOS mutations and neurodegeneration', *EMBO J*, 32(1), pp. 9-29.

Kopek, B.G., Shtengel, G., Xu, C.S., Clayton, D.A. and Hess, H.F. (2012) 'Correlative 3D superresolution fluorescence and electron microscopy reveal the relationship of mitochondrial nucleoids to membranes', *Proc Natl Acad Sci U S A*, 109(16), pp. 6136-41.

Korobova, F., Ramabhadran, V. and Higgs, H.N. (2013) 'An actin-dependent step in mitochondrial fission mediated by the ER-associated formin INF2', *Science*, 339(6118), pp. 464-7.

Koutsopoulos, O.S., Laine, D., Osellame, L., Chudakov, D.M., Parton, R.G., Frazier, A.E. and Ryan, M.T. (2010) 'Human Miltons associate with mitochondria and induce microtubule-dependent remodeling of mitochondrial networks', *Biochim Biophys Acta*, 1803(5), pp. 564-74.

Krebs, J., Agellon, L.B. and Michalak, M. (2015) 'Ca(2+) homeostasis and endoplasmic reticulum (ER) stress: An integrated view of calcium signaling', *Biochem Biophys Res Commun*, 460(1), pp. 114-21.

Krols, M., van Isterdael, G., Asselbergh, B., Kremer, A., Lippens, S., Timmerman, V. and Janssens, S. (2016) 'Mitochondria-associated membranes as hubs for neurodegeneration', *Acta Neuropathol*, 131(4), pp. 505-23.

Kuhlbrandt, W. (2015) 'Structure and function of mitochondrial membrane protein complexes', *BMC Biol*, 13, p. 89.

Kukat, C., Wurm, C.A., Spahr, H., Falkenberg, M., Larsson, N.G. and Jakobs, S. (2011) 'Super-resolution microscopy reveals that mammalian mitochondrial nucleoids have a uniform size and frequently contain a single copy of mtDNA', *Proc Natl Acad Sci U S A*, 108(33), pp. 13534-9.

Kushnareva, Y.E., Gerencser, A.A., Bossy, B., Ju, W.K., White, A.D., Waggoner, J., Ellisman, M.H., Perkins, G. and Bossy-Wetzel, E. (2013) 'Loss of OPA1 disturbs cellular calcium homeostasis and sensitizes for excitotoxicity', *Cell Death Differ*, 20(2), pp. 353-65.

La Rovere, R.M., Roest, G., Bultynck, G. and Parys, J.B. (2016) 'Intracellular Ca(2+) signaling and Ca(2+) microdomains in the control of cell survival, apoptosis and autophagy', *Cell Calcium*, 60(2), pp. 74-87.

Lange, C. and Hunte, C. (2002) 'Crystal structure of the yeast cytochrome bc1 complex with its bound substrate cytochrome c', *Proc Natl Acad Sci U S A*, 99(5), pp. 2800-5.

Lin, C.S., Sharpley, M.S., Fan, W., Waymire, K.G., Sadun, A.A., Carelli, V., Ross-Cisneros, F.N., Baciu, P., Sung, E., McManus, M.J., Pan, B.X., Gil, D.W., Macgregor, G.R. and Wallace, D.C. (2012) 'Mouse mtDNA mutant model of Leber hereditary optic neuropathy', *Proc Natl Acad Sci U S A*, 109(49), pp. 20065-70.

Lin, M.Y. and Sheng, Z.H. (2015) 'Regulation of mitochondrial transport in neurons', *Exp Cell Res*, 334(1), pp. 35-44.

Lipper, C.H., Paddock, M.L., Onuchic, J.N., Mittler, R., Nechushtai, R. and Jennings, P.A. (2015) 'Cancer-Related NEET Proteins Transfer 2Fe-2S Clusters to Anamorsin, a Protein Required for Cytosolic Iron-Sulfur Cluster Biogenesis', *PLoS One*, 10(10), p. e0139699.

Liu, X., Weaver, D., Shirihai, O. and Hajnoczky, G. (2009) 'Mitochondrial 'kiss-and-run': interplay between mitochondrial motility and fusion-fission dynamics', *EMBO J*, 28(20), pp. 3074-89.

Llorente-Folch, I., Rueda, C.B., Pardo, B., Szabadkai, G., Duchen, M.R. and Satrustegui, J. (2015) 'The regulation of neuronal mitochondrial metabolism by calcium', *J Physiol*, 593(16), pp. 3447-62.

Lopez Sanchez, M.I., Crowston, J.G., Mackey, D.A. and Trounce, I.A. (2016) 'Emerging Mitochondrial Therapeutic Targets in Optic Neuropathies', *Pharmacol Ther*, 165, pp. 132-52.

Loson, O.C., Song, Z., Chen, H. and Chan, D.C. (2013) 'Fis1, Mff, MiD49, and MiD51 mediate Drp1 recruitment in mitochondrial fission', *Mol Biol Cell*, 24(5), pp. 659-67.

Lu, S., Kanekura, K., Hara, T., Mahadevan, J., Spears, L.D., Oslowski, C.M., Martinez, R., Yamazaki-Inoue, M., Toyoda, M., Neilson, A., Blanner, P., Brown, C.M., Semenkovich, C.F., Marshall, B.A., Hershey, T., Umezawa, A., Greer, P.A. and Urano, F. (2014) 'A calcium-dependent protease as a potential therapeutic target for Wolfram syndrome', *Proc Natl Acad Sci U S A*, 111(49), pp. E5292-301.

MacAskill, A.F. and Kittler, J.T. (2010) 'Control of mitochondrial transport and localization in neurons', *Trends Cell Biol*, 20(2), pp. 102-12.

Macaskill, A.F., Rinholm, J.E., Twelvetrees, A.E., Arancibia-Carcamo, I.L., Muir, J., Fransson, A., Aspenstrom, P., Attwell, D. and Kittler, J.T. (2009) 'Miro1 is a calcium sensor for glutamate receptor-dependent localization of mitochondria at synapses', *Neuron*, 61(4), pp. 541-55.

Mannella, C.A. (2008) 'Structural diversity of mitochondria: functional implications', *Ann N Y Acad Sci*, 1147, pp. 171-9.

Mannella, C.A., Lederer, W.J. and Jafri, M.S. (2013) 'The connection between inner membrane topology and mitochondrial function', *J Mol Cell Cardiol*, 62, pp. 51-7.

Maresca, A., la Morgia, C., Caporali, L., Valentino, M.L. and Carelli, V. (2013) 'The optic nerve: a "mito-window" on mitochondrial neurodegeneration', *Mol Cell Neurosci*, 55, pp. 62-76.

Margulis, L. (1971) 'Symbiosis and evolution', *Sci Am*, 225(2), pp. 48-57.

Marra, M.H., Tobias, Z.J., Cohen, H.R., Glover, G. and Weissman, T.A. (2015) 'In Vivo Time-Lapse Imaging in the Zebrafish Lateral Line: A Flexible, Open-Ended Research Project for an Undergraduate Neurobiology Laboratory Course', *J Undergrad Neurosci Educ*, 13(3), pp. A215-24.

Matsunaga, K., Tanabe, K., Inoue, H., Okuya, S., Ohta, Y., Akiyama, M., Taguchi, A., Kora, Y., Okayama, N., Yamada, Y., Wada, Y., Amemiya, S., Sugihara, S., Nakao, Y., Oka, Y. and Tanizawa, Y. (2014) 'Wolfram syndrome in the Japanese population; molecular analysis of WFS1 gene and characterization of clinical features', *PLoS One*, 9(9), p. e106906.

Mears, J.A., Lackner, L.L., Fang, S., Ingerman, E., Nunnari, J. and Hinshaw, J.E. (2011) 'Conformational changes in Dnm1 support a contractile mechanism for mitochondrial fission', *Nat Struct Mol Biol*, 18(1), pp. 20-6.

Mendes, C.C., Gomes, D.A., Thompson, M., Souto, N.C., Goes, T.S., Goes, A.M., Rodrigues, M.A., Gomez, M.V., Nathanson, M.H. and Leite, M.F. (2005) 'The type III inositol 1,4,5-trisphosphate receptor preferentially transmits apoptotic Ca2+ signals into mitochondria', *J Biol Chem*, 280(49), pp. 40892-900.

Millet, A.M., Bertholet, A.M., Daloyau, M., Reynier, P., Galinier, A., Devin, A., Wissinguer, B., Belenguer, P. and Davezac, N. (2016) 'Loss of functional OPA1 unbalances redox state: implications in dominant optic atrophy pathogenesis', *Ann Clin Transl Neurol*, 3(6), pp. 408-21.

Mironov, S.L. (2007) 'ADP regulates movements of mitochondria in neurons', *Biophys J*, 92(8), pp. 2944-52.

Mishra, P. and Chan, D.C. (2016) 'Metabolic regulation of mitochondrial dynamics', *J Cell Biol*, 212(4), pp. 379-87.

Moosajee, M., Yu-Wai-Man, P., Rouzier, C., Bitner-Glindzicz, M. and Bowman, R. (2016) 'Clinical utility gene card for: Wolfram syndrome', *Eur J Hum Genet*.

Mozzillo, E., Delvecchio, M., Carella, M., Grandone, E., Palumbo, P., Salina, A., Aloi, C., Buono, P., Izzo, A., D'Annunzio, G., Vecchione, G., Orrico, A., Genesio, R., Simonelli, F. and Franzese, A. (2014) 'A novel CISD2 intragenic deletion, optic neuropathy and platelet aggregation defect in Wolfram syndrome type 2', *BMC Med Genet*, 15, p. 88.

Mukherjee, A. and Soto, C. (2011) 'Role of calcineurin in neurodegeneration produced by misfolded proteins and endoplasmic reticulum stress', *Curr Opin Cell Biol*, 23(2), pp. 223-30.

Murphy, M.P. (2009) 'How mitochondria produce reactive oxygen species', *Biochem J*, 417(1), pp. 1-13.

Nass, M.M. (1966) 'The circularity of mitochondrial DNA', *Proc Natl Acad Sci U S A*, 56(4), pp. 1215-22.

Nsiah-Sefaa, A. and McKenzie, M. (2016) 'Combined defects in oxidative phosphorylation and fatty acid beta-oxidation in mitochondrial disease', *Biosci Rep*, 36(2).

Ochocinska, M.J. and Hitchcock, P.F. (2009) 'NeuroD regulates proliferation of photoreceptor progenitors in the retina of the zebrafish', *Mech Dev*, 126(3-4), pp. 128-41.

Odisho, T., Zhang, L. and Volchuk, A. (2015) 'ATF6beta regulates the Wfs1 gene and has a cell survival role in the ER stress response in pancreatic beta-cells', *Exp Cell Res*, 330(1), pp. 111-22.

Olichon, A., Emorine, L.J., Descoins, E., Pelloquin, L., Brichese, L., Gas, N., Guillou, E., Delettre, C., Valette, A., Hamel, C.P., Ducommun, B., Lenaers, G. and Belenguer, P. (2002) 'The human dynamin-related protein OPA1 is anchored to the mitochondrial inner membrane facing the inter-membrane space', *FEBS Lett*, 523(1-3), pp. 171-6.

Orrenius, S., Gogvadze, V. and Zhivotovsky, B. (2015) 'Calcium and mitochondria in the regulation of cell death', *Biochem Biophys Res Commun*, 460(1), pp. 72-81.

Oslowski, C.M. and Urano, F. (2011) 'Measuring ER stress and the unfolded protein response using mammalian tissue culture system', *Methods Enzymol*, 490, pp. 71-92.

Osman, A.A., Saito, M., Makepeace, C., Permutt, M.A., Schlesinger, P. and Mueckler, M. (2003) 'Wolframin expression induces novel ion channel activity in endoplasmic reticulum membranes and increases intracellular calcium', *J Biol Chem*, 278(52), pp. 52755-62.

Osman, C., Voelker, D.R. and Langer, T. (2011) 'Making heads or tails of phospholipids in mitochondria', *J Cell Biol*, 192(1), pp. 7-16.

Otera, H., Miyata, N., Kuge, O. and Mihara, K. (2016) 'Drp1-dependent mitochondrial fission via MiD49/51 is essential for apoptotic cristae remodeling', *J Cell Biol*, 212(5), pp. 531-44.

Ottolini, D., Cali, T., Negro, A. and Brini, M. (2013) 'The Parkinson disease-related protein DJ-1 counteracts mitochondrial impairment induced by the tumour suppressor protein p53 by enhancing endoplasmic reticulum-mitochondria tethering', *Hum Mol Genet*, 22(11), pp. 2152-68.

Paillusson, S., Stoica, R., Gomez-Suaga, P., Lau, D.H., Mueller, S., Miller, T. and Miller, C.C. (2016) 'There's Something Wrong with my MAM; the ER-Mitochondria Axis and Neurodegenerative Diseases', *Trends Neurosci*, 39(3), pp. 146-57.

Palade, G.E. (1952) 'The fine structure of mitochondria', *Anat Rec*, 114(3), pp. 427-51.

Park, S.H. and Blackstone, C. (2010) 'Further assembly required: construction and dynamics of the endoplasmic reticulum network', *EMBO Rep*, 11(7), pp. 515-21.

Pernas, L. and Scorrano, L. (2016) 'Mito-Morphosis: Mitochondrial Fusion, Fission, and Cristae Remodeling as Key Mediators of Cellular Function', *Annu Rev Physiol*, 78, pp. 505-31.

Philbrook, C., Fritz, E. and Weiher, H. (2005) 'Expressional and functional studies of Wolframin, the gene function deficient in Wolfram syndrome, in mice and patient cells', *Exp Gerontol*, 40(8-9), pp. 671-8.

Picard, M., McManus, M.J., Csordas, G., Varnai, P., Dorn, G.W., 2nd, Williams, D., Hajnoczky, G. and Wallace, D.C. (2015) 'Trans-mitochondrial coordination of cristae at regulated membrane junctions', *Nat Commun*, 6, p. 6259.

Pickart, M.A. and Klee, E.W. (2014) 'Zebrafish approaches enhance the translational research tackle box', *Transl Res*, 163(2), pp. 65-78.

Pilling, A.D., Horiuchi, D., Lively, C.M. and Saxton, W.M. (2006) 'Kinesin-1 and Dynein are the primary motors for fast transport of mitochondria in Drosophila motor axons', *Mol Biol Cell*, 17(4), pp. 2057-68.

Plucinska, G., Paquet, D., Hruscha, A., Godinho, L., Haass, C., Schmid, B. and Misgeld, T. (2012) 'In vivo imaging of disease-related mitochondrial dynamics in a vertebrate model system', *J Neurosci*, 32(46), pp. 16203-12.

Popovic, D.M. (2013) 'Current advances in research of cytochrome c oxidase', *Amino Acids*, 45(5), pp. 1073-87.

Poston, C.N., Krishnan, S.C. and Bazemore-Walker, C.R. (2013) 'In-depth proteomic analysis of mammalian mitochondria-associated membranes (MAM)', *J Proteomics*, 79, pp. 219-30.

Prins, D. and Michalak, M. (2011) 'Organellar calcium buffers', *Cold Spring Harb Perspect Biol*, 3(3).

Pyle, A., Ramesh, V., Bartsakoulia, M., Boczonadi, V., Gomez-Duran, A., Herczegfalvi, A., Blakely, E.L., Smertenko, T., Duff, J., Eglon, G., Moore, D., Yu-Wai-Man, P., Douroudis, K., Santibanez-Koref, M., Griffin, H., Lochmuller, H., Karcagi, V., Taylor, R.W., Chinnery, P.F. and Horvath, R. (2014) 'Behr's Syndrome is Typically Associated with Disturbed Mitochondrial Translation and Mutations in the C12orf65 Gene', *J Neuromuscul Dis*, 1(1), pp. 55-63.

Qi, W. and Cowan, J.A. (2011) 'Structural, Mechanistic and Coordination Chemistry of Relevance to the Biosynthesis of Iron-Sulfur and Related Iron Cofactors', *Coord Chem Rev*, 255(7-8), pp. 688-699.

Quinlan, C.L., Perevoshchikova, I.V., Hey-Mogensen, M., Orr, A.L. and Brand, M.D. (2013) 'Sites of reactive oxygen species generation by mitochondria oxidizing different substrates', *Redox Biol*, 1, pp. 304-12.

Rambold, A.S., Kostelecky, B., Elia, N. and Lippincott-Schwartz, J. (2011) 'Tubular network formation protects mitochondria from autophagosomal degradation during nutrient starvation', *Proc Natl Acad Sci U S A*, 108(25), pp. 10190-5.

Rangaraju, V., Calloway, N. and Ryan, T.A. (2014) 'Activity-driven local ATP synthesis is required for synaptic function', *Cell*, 156(4), pp. 825-35.

Rardin, M.J., Wiley, S.E., Naviaux, R.K., Murphy, A.N. and Dixon, J.E. (2009) 'Monitoring phosphorylation of the pyruvate dehydrogenase complex', *Anal Biochem*, 389(2), pp. 157-64.

Rendtorff, N.D., Lodahl, M., Boulahbel, H., Johansen, I.R., Pandya, A., Welch, K.O., Norris, V.W., Arnos, K.S., Bitner-Glindzicz, M., Emery, S.B., Mets, M.B., Fagerheim, T., Eriksson, K., Hansen, L., Bruhn, H., Moller, C., Lindholm, S., Ensgaard, S., Lesperance, M.M. and Tranebjaerg, L. (2011) 'Identification of p.A684V missense mutation in the WFS1 gene as a frequent cause of autosomal dominant optic atrophy and hearing impairment', *Am J Med Genet A*, 155A(6), pp. 1298-313.

Rigoli, L., Lombardo, F. and Di Bella, C. (2011) 'Wolfram syndrome and WFS1 gene', *Clin Genet*, 79(2), pp. 103-17.

Rishi, A.K., Yu, M., Tsai-Wu, J.J., Belani, C.P., Fontana, J.A., Baker, D.L., Periasamy, M. and Hussain, A. (1998) 'Gene amplification and transcriptional upregulation of the sarco/endoplasmic reticulum Ca2+ transport ATPase in thapsigargin-resistant hamster smooth muscle cells', *Nucleic Acids Res*, 26(19), pp. 4529-37.

Rizzuto, R., Marchi, S., Bonora, M., Aguiari, P., Bononi, A., De Stefani, D., Giorgi, C., Leo, S., Rimessi, A., Siviero, R., Zecchini, E. and Pinton, P. (2009) 'Ca(2+) transfer from the ER to mitochondria: when, how and why', *Biochim Biophys Acta*, 1787(11), pp. 1342-51.

Rizzuto, R., Pinton, P., Carrington, W., Fay, F.S., Fogarty, K.E., Lifshitz, L.M., Tuft, R.A. and Pozzan, T. (1998) 'Close contacts with the endoplasmic reticulum as determinants of mitochondrial Ca2+ responses', *Science*, 280(5370), pp. 1763-6.

Rondinelli, M., Novara, F., Calcaterra, V., Zuffardi, O. and Genovese, S. (2015) 'Wolfram syndrome 2: a novel CISD2 mutation identified in Italian siblings', *Acta Diabetol*, 52(1), pp. 175-8.

Ross-Cisneros, F.N., Pan, B.X., Silva, R.A., Miller, N.R., Albini, T.A., Tranebjaerg, L., Rendtorff, N.D., Lodahl, M., Moraes-Filho, M.N., Moraes, M.N., Salomao, S.R., Berezovsky, A., Belfort, R., Jr., Carelli, V. and Sadun, A.A. (2013) 'Optic nerve histopathology in a case of Wolfram Syndrome: a mitochondrial pattern of axonal loss', *Mitochondrion*, 13(6), pp. 841-5.

Rowland, A.A. and Voeltz, G.K. (2012) 'Endoplasmic reticulum-mitochondria contacts: function of the junction', *Nat Rev Mol Cell Biol*, 13(10), pp. 607-25.

Roy, M., Reddy, P.H., Iijima, M. and Sesaki, H. (2015) 'Mitochondrial division and fusion in metabolism', *Curr Opin Cell Biol*, 33, pp. 111-8.

Rutter, J., Winge, D.R. and Schiffman, J.D. (2010) 'Succinate dehydrogenase - Assembly, regulation and role in human disease', *Mitochondrion*, 10(4), pp. 393-401.

Sadun, A.A., Chicani, C.F., Ross-Cisneros, F.N., Barboni, P., Thoolen, M., Shrader, W.D., Kubis, K., Carelli, V. and Miller, G. (2012) 'Effect of EPI-743 on the clinical course of the mitochondrial disease Leber hereditary optic neuropathy', *Arch Neurol*, 69(3), pp. 331-8.

Saotome, M., Safiulina, D., Szabadkai, G., Das, S., Fransson, A., Aspenstrom, P., Rizzuto, R. and Hajnoczky, G. (2008) 'Bidirectional Ca2+-dependent control of mitochondrial dynamics by the Miro GTPase', *Proc Natl Acad Sci U S A*, 105(52), pp. 20728-33.

Sazanov, L.A. (2015) 'A giant molecular proton pump: structure and mechanism of respiratory complex I', *Nat Rev Mol Cell Biol*, 16(6), pp. 375-88.

Schmidt-Kastner, R., Kreczmanski, P., Preising, M., Diederen, R., Schmitz, C., Reis, D., Blanks, J. and Dorey, C.K. (2009) 'Expression of the diabetes risk gene wolframin (WFS1) in the human retina', *Exp Eye Res*, 89(4), pp. 568-74.

Schmidt, O., Pfanner, N. and Meisinger, C. (2010) 'Mitochondrial protein import: from proteomics to functional mechanisms', *Nat Rev Mol Cell Biol*, 11(9), pp. 655-67.

Schrepfer, E. and Scorrano, L. (2016) 'Mitofusins, from Mitochondria to Metabolism', *Mol Cell*, 61(5), pp. 683-94.

Schwarz, D.S. and Blower, M.D. (2016) 'The endoplasmic reticulum: structure, function and response to cellular signaling', *Cell Mol Life Sci*, 73(1), pp. 79-94.

Scorrano, L. (2013) 'Keeping mitochondria in shape: a matter of life and death', *Eur J Clin Invest*, 43(8), pp. 886-93.

Shadel, G.S. and Horvath, T.L. (2015) 'Mitochondrial ROS signaling in organismal homeostasis', *Cell*, 163(3), pp. 560-9.

Shang, L., Hua, H., Foo, K., Martinez, H., Watanabe, K., Zimmer, M., Kahler, D.J., Freeby, M., Chung, W., LeDuc, C., Goland, R., Leibel, R.L. and Egli, D. (2014) 'beta-cell dysfunction due to increased ER stress in a stem cell model of Wolfram syndrome', *Diabetes*, 63(3), pp. 923-33.

Sheng, Z.H. and Cai, Q. (2012) 'Mitochondrial transport in neurons: impact on synaptic homeostasis and neurodegeneration', *Nat Rev Neurosci*, 13(2), pp. 77-93.

Sherry, S.T., Ward, M.H., Kholodov, M., Baker, J., Phan, L., Smigielski, E.M. and Sirotkin, K. (2001) 'dbSNP: the NCBI database of genetic variation', *Nucleic Acids Res*, 29(1), pp. 308-11.

Shimazaki, H., Takiyama, Y., Ishiura, H., Sakai, C., Matsushima, Y., Hatakeyama, H., Honda, J., Sakoe, K., Naoi, T., Namekawa, M., Fukuda, Y., Takahashi, Y., Goto, J., Tsuji, S., Goto, Y., Nakano, I. and Japan Spastic Paraplegia Research, C. (2012) 'A homozygous mutation of C12orf65 causes spastic paraplegia with optic atrophy and neuropathy (SPG55)', *J Med Genet*, 49(12), pp. 777-84.

Smedler, E. and Uhlen, P. (2014) 'Frequency decoding of calcium oscillations', *Biochim Biophys Acta*, 1840(3), pp. 964-9.

Smith, T.G., Seto, S., Ganne, P. and Votruba, M. (2016) 'A randomized, placebo-controlled trial of the benzoquinone idebenone in a mouse model of OPA1-related dominant optic atrophy reveals a limited therapeutic effect on retinal ganglion cell dendropathy and visual function', *Neuroscience*, 319, pp. 92-106.

Song, Z., Chen, H., Fiket, M., Alexander, C. and Chan, D.C. (2007) 'OPA1 processing controls mitochondrial fusion and is regulated by mRNA splicing, membrane potential, and Yme1L', *J Cell Biol*, 178(5), pp. 749-55.

Song, Z., Ghochani, M., McCaffery, J.M., Frey, T.G. and Chan, D.C. (2009) 'Mitofusins and OPA1 mediate sequential steps in mitochondrial membrane fusion', *Mol Biol Cell*, 20(15), pp. 3525-32.

Sood, A., Jeyaraju, D.V., Prudent, J., Caron, A., Lemieux, P., McBride, H.M., Laplante, M., Toth, K. and Pellegrini, L. (2014) 'A Mitofusin-2-dependent inactivating cleavage of Opa1 links changes in mitochondria cristae and ER contacts in the postprandial liver', *Proc Natl Acad Sci U S A*, 111(45), pp. 16017-22.

Spiegel, R., Mandel, H., Saada, A., Lerer, I., Burger, A., Shaag, A., Shalev, S.A., Jabaly-Habib, H., Goldsher, D., Gomori, J.M., Lossos, A., Elpeleg, O. and Meiner, V. (2014) 'Delineation of C12orf65-related phenotypes: a genotype-phenotype relationship', *Eur J Hum Genet*, 22(8), pp. 1019-25.

Spiegel, R., Saada, A., Flannery, P.J., Burte, F., Soiferman, D., Khayat, M., Eisner, V., Vladovski, E., Taylor, R.W., Bindoff, L.A., Shaag, A., Mandel, H., Schuler-Furman, O., Shalev, S.A., Elpeleg, O. and Yu-Wai-Man, P. (2016) 'Fatal infantile mitochondrial encephalomyopathy, hypertrophic cardiomyopathy and optic atrophy associated with a homozygous OPA1 mutation', *J Med Genet*, 53(2), pp. 127-31.

Spinazzi, M., Cazzola, S., Bortolozzi, M., Baracca, A., Loro, E., Casarin, A., Solaini, G., Sgarbi, G., Casalena, G., Cenacchi, G., Malena, A., Frezza, C., Carrara, F., Angelini, C., Scorrano, L., Salviati, L. and Vergani, L. (2008) 'A novel deletion in the GTPase domain of OPA1 causes defects in mitochondrial morphology and distribution, but not in function', *Hum Mol Genet*, 17(21), pp. 3291-302.

Steele, S.L., Prykhozhij, S.V. and Berman, J.N. (2014) 'Zebrafish as a model system for mitochondrial biology and diseases', *Transl Res*, 163(2), pp. 79-98.

Stoica, R., De Vos, K.J., Paillusson, S., Mueller, S., Sancho, R.M., Lau, K.F., Vizcay-Barrena, G., Lin, W.L., Xu, Y.F., Lewis, J., Dickson, D.W., Petrucelli, L., Mitchell, J.C., Shaw, C.E. and Miller, C.C. (2014) 'ER-mitochondria associations are regulated by the VAPB-PTPIP51 interaction and are disrupted by ALS/FTD-associated TDP-43', *Nat Commun*, 5, p. 3996.

Stone, S.J. and Vance, J.E. (2000) 'Phosphatidylserine synthase-1 and -2 are localized to mitochondria-associated membranes', *J Biol Chem*, 275(44), pp. 34534-40.

Strom, T.M., Hortnagel, K., Hofmann, S., Gekeler, F., Scharfe, C., Rabl, W., Gerbitz, K.D. and Meitinger, T. (1998) 'Diabetes insipidus, diabetes mellitus, optic atrophy and deafness (DIDMOAD) caused by mutations in a novel gene (wolframin) coding for a predicted transmembrane protein', *Hum Mol Genet*, 7(13), pp. 2021-8.

Sun, F., Huo, X., Zhai, Y., Wang, A., Xu, J., Su, D., Bartlam, M. and Rao, Z. (2005) 'Crystal structure of mitochondrial respiratory membrane protein complex II', *Cell*, 121(7), pp. 1043-57.

Szabadkai, G., Bianchi, K., Varnai, P., De Stefani, D., Wieckowski, M.R., Cavagna, D., Nagy, A.I., Balla, T. and Rizzuto, R. (2006) 'Chaperone-mediated coupling of endoplasmic reticulum and mitochondrial Ca2+ channels', *J Cell Biol*, 175(6), pp. 901-11.

Taguchi, N., Ishihara, N., Jofuku, A., Oka, T. and Mihara, K. (2007) 'Mitotic phosphorylation of dynamin-related GTPase Drp1 participates in mitochondrial fission', *J Biol Chem*, 282(15), pp. 11521-9.

Tait, S.W. and Green, D.R. (2010) 'Mitochondria and cell death: outer membrane permeabilization and beyond', *Nat Rev Mol Cell Biol*, 11(9), pp. 621-32.

Takeda, K., Inoue, H., Tanizawa, Y., Matsuzaki, Y., Oba, J., Watanabe, Y., Shinoda, K. and Oka, Y. (2001) 'WFS1 (Wolfram syndrome 1) gene product: predominant subcellular localization to endoplasmic reticulum in cultured cells and neuronal expression in rat brain', *Hum Mol Genet*, 10(5), pp. 477-84.

Takei, D., Ishihara, H., Yamaguchi, S., Yamada, T., Tamura, A., Katagiri, H., Maruyama, Y. and Oka, Y. (2006) 'WFS1 protein modulates the free Ca(2+) concentration in the endoplasmic reticulum', *FEBS Lett*, 580(24), pp. 5635-40.

Tamir, S., Zuris, J.A., Agranat, L., Lipper, C.H., Conlan, A.R., Michaeli, D., Harir, Y., Paddock, M.L., Mittler, R., Cabantchik, Z.I., Jennings, P.A. and Nechushtai, R. (2013) 'Nutrient-deprivation autophagy factor-1 (NAF-1): biochemical properties of a novel cellular target for anti-diabetic drugs', *PLoS One*, 8(5), p. e61202.

Tang, S., Le, P.K., Tse, S., Wallace, D.C. and Huang, T. (2009) 'Heterozygous mutation of Opa1 in Drosophila shortens lifespan mediated through increased reactive oxygen species production', *PLoS One*, 4(2), p. e4492.

Tondera, D., Grandemange, S., Jourdain, A., Karbowski, M., Mattenberger, Y., Herzig, S., Da Cruz, S., Clerc, P., Raschke, I., Merkwirth, C., Ehses, S., Krause, F., Chan, D.C., Alexander, C., Bauer, C., Youle, R., Langer, T. and Martinou, J.C. (2009) 'SLP-2 is required for stress-induced mitochondrial hyperfusion', *EMBO J*, 28(11), pp. 1589-600.

Tubbs, E., Theurey, P., Vial, G., Bendridi, N., Bravard, A., Chauvin, M.A., Ji-Cao, J., Zoulim, F., Bartosch, B., Ovize, M., Vidal, H. and Rieusset, J. (2014) 'Mitochondria-associated endoplasmic reticulum membrane (MAM) integrity is required for insulin signaling and is implicated in hepatic insulin resistance', *Diabetes*, 63(10), pp. 3279-94.

Tucci, A., Liu, Y.T., Preza, E., Pitceathly, R.D., Chalasani, A., Plagnol, V., Land, J.M., Trabzuni, D., Ryten, M., Ukbec, Jaunmuktane, Z., Reilly, M.M., Brandner, S., Hargreaves, I., Hardy, J., Singleton, A.B., Abramov, A.Y. and Houlden, H. (2014) 'Novel C12orf65 mutations in patients with axonal neuropathy and optic atrophy', *J Neurol Neurosurg Psychiatry*, 85(5), pp. 486-92.

Tuppen, H.A., Blakely, E.L., Turnbull, D.M. and Taylor, R.W. (2010) 'Mitochondrial DNA mutations and human disease', *Biochim Biophys Acta*, 1797(2), pp. 113-28.

Twig, G., Elorza, A., Molina, A.J., Mohamed, H., Wikstrom, J.D., Walzer, G., Stiles, L., Haigh, S.E., Katz, S., Las, G., Alroy, J., Wu, M., Py, B.F., Yuan, J., Deeney, J.T., Corkey, B.E. and Shirihai, O.S. (2008) 'Fission and selective fusion govern mitochondrial segregation and elimination by autophagy', *EMBO J*, 27(2), pp. 433-46.

Untergasser, A., Cutcutache, I., Koressaar, T., Ye, J., Faircloth, B.C., Remm, M. and Rozen, S.G. (2012) 'Primer3--new capabilities and interfaces', *Nucleic Acids Res*, 40(15), p. e115.

Urano, F. (2016) 'Wolfram Syndrome: Diagnosis, Management, and Treatment', *Curr Diab Rep*, 16(1), p. 6.

Van Bergen, N.J., Crowston, J.G., Kearns, L.S., Staffieri, S.E., Hewitt, A.W., Cohn, A.C., Mackey, D.A. and Trounce, I.A. (2011) 'Mitochondrial oxidative phosphorylation compensation may preserve vision in patients with OPA1-linked autosomal dominant optic atrophy', *PLoS One*, 6(6), p. e21347.

van Bruggen, E.F., Borst, P., Ruttenberg, G.J., Gruber, M. and Kroon, A.M. (1966) 'Circular mitochondrial DNA', *Biochim Biophys Acta*, 119(2), pp. 437-9.

van Spronsen, M., Mikhaylova, M., Lipka, J., Schlager, M.A., van den Heuvel, D.J., Kuijpers, M., Wulf, P.S., Keijzer, N., Demmers, J., Kapitein, L.C., Jaarsma, D., Gerritsen, H.C., Akhmanova, A. and Hoogenraad, C.C. (2013) 'TRAK/Milton motor-adaptor proteins steer mitochondrial trafficking to axons and dendrites', *Neuron*, 77(3), pp. 485-502.

van Vliet, A.R., Verfaillie, T. and Agostinis, P. (2014) 'New functions of mitochondria associated membranes in cellular signaling', *Biochim Biophys Acta*, 1843(10), pp. 2253-62.

Vance, J.E. (1990) 'Phospholipid synthesis in a membrane fraction associated with mitochondria', *J Biol Chem*, 265(13), pp. 7248-56.

Vinothkumar, K.R., Zhu, J. and Hirst, J. (2014) 'Architecture of mammalian respiratory complex I', *Nature*, 515(7525), pp. 80-4.

Vogel, F., Bornhovd, C., Neupert, W. and Reichert, A.S. (2006) 'Dynamic subcompartmentalization of the mitochondrial inner membrane', *J Cell Biol*, 175(2), pp. 237-47.

Vosler, P.S., Brennan, C.S. and Chen, J. (2008) 'Calpain-mediated signaling mechanisms in neuronal injury and neurodegeneration', *Mol Neurobiol*, 38(1), pp. 78-100.

Wallace, D.C., Singh, G., Lott, M.T., Hodge, J.A., Schurr, T.G., Lezza, A.M., Elsas, L.J., 2nd and Nikoskelainen, E.K. (1988) 'Mitochondrial DNA mutation associated with Leber's hereditary optic neuropathy', *Science*, 242(4884), pp. 1427-30.

Wang, C.H., Chen, Y.F., Wu, C.Y., Wu, P.C., Huang, Y.L., Kao, C.H., Lin, C.H., Kao, L.S., Tsai, T.F. and Wei, Y.H. (2014) 'Cisd2 modulates the differentiation and functioning of adipocytes by regulating intracellular Ca2+ homeostasis', *Hum Mol Genet*, 23(18), pp. 4770-85.

Wang, H.J., Guay, G., Pogan, L., Sauve, R. and Nabi, I.R. (2000) 'Calcium regulates the association between mitochondria and a smooth subdomain of the endoplasmic reticulum', *J Cell Biol*, 150(6), pp. 1489-98.

Wang, X. and Schwarz, T.L. (2009) 'The mechanism of Ca2+ -dependent regulation of kinesin-mediated mitochondrial motility', *Cell*, 136(1), pp. 163-74.

Watt, I.N., Montgomery, M.G., Runswick, M.J., Leslie, A.G. and Walker, J.E. (2010) 'Bioenergetic cost of making an adenosine triphosphate molecule in animal mitochondria', *Proc Natl Acad Sci U S A*, 107(39), pp. 16823-7.

Westermann, B. (2012) 'Bioenergetic role of mitochondrial fusion and fission', *Biochim Biophys Acta*, 1817(10), pp. 1833-8.

Wiley, S.E., Andreyev, A.Y., Divakaruni, A.S., Karisch, R., Perkins, G., Wall, E.A., van der Geer, P., Chen, Y.F., Tsai, T.F., Simon, M.I., Neel, B.G., Dixon, J.E. and Murphy, A.N. (2013) 'Wolfram Syndrome protein, Miner1, regulates sulphydryl redox status, the unfolded protein response, and Ca2+ homeostasis', *EMBO Mol Med*, 5(6), pp. 904-18.

Wiley, S.E., Murphy, A.N., Ross, S.A., van der Geer, P. and Dixon, J.E. (2007a) 'MitoNEET is an iron-containing outer mitochondrial membrane protein that regulates oxidative capacity', *Proc Natl Acad Sci U S A*, 104(13), pp. 5318-23.

Wiley, S.E., Paddock, M.L., Abresch, E.C., Gross, L., van der Geer, P., Nechushtai, R., Murphy, A.N., Jennings, P.A. and Dixon, J.E. (2007b) 'The outer mitochondrial membrane protein mitoNEET contains a novel redox-active 2Fe-2S cluster', *J Biol Chem*, 282(33), pp. 23745-9.

Wilkens, V., Kohl, W. and Busch, K. (2013) 'Restricted diffusion of OXPHOS complexes in dynamic mitochondria delays their exchange between cristae and engenders a transitory mosaic distribution', *J Cell Sci*, 126(Pt 1), pp. 103-16.

Wittig, I., Karas, M. and Schagger, H. (2007) 'High resolution clear native electrophoresis for in-gel functional assays and fluorescence studies of membrane protein complexes', *Mol Cell Proteomics*, 6(7), pp. 1215-25.

Wolfram, D.J. and Wagener, H.P. (1938) 'Diabetes mellitus and simple optic atrophy among siblings: report of four cases', *Mayo Clin Proc*, 13, pp. 715-718.

Yamada, T., Ishihara, H., Tamura, A., Takahashi, R., Yamaguchi, S., Takei, D., Tokita, A., Satake, C., Tashiro, F., Katagiri, H., Aburatani, H., Miyazaki, J. and Oka, Y. (2006) 'WFS1-deficiency increases endoplasmic reticulum stress, impairs cell cycle progression and triggers the apoptotic pathway specifically in pancreatic beta-cells', *Hum Mol Genet*, 15(10), pp. 1600-9.

Yamaguchi, S., Ishihara, H., Tamura, A., Yamada, T., Takahashi, R., Takei, D., Katagiri, H. and Oka, Y. (2004) 'Endoplasmic reticulum stress and N-glycosylation modulate expression of WFS1 protein', *Biochem Biophys Res Commun*, 325(1), pp. 250-6.

Yarosh, W., Monserrate, J., Tong, J.J., Tse, S., Le, P.K., Nguyen, K., Brachmann, C.B., Wallace, D.C. and Huang, T. (2008) 'The molecular mechanisms of OPA1-mediated optic atrophy in Drosophila model and prospects for antioxidant treatment', *PLoS Genet*, 4(1), p. e6.

Ye, J., Coulouris, G., Zaretskaya, I., Cutcutache, I., Rozen, S. and Madden, T.L. (2012) 'Primer-BLAST: a tool to design target-specific primers for polymerase chain reaction', *BMC Bioinformatics*, 13, p. 134.

Yi, M., Weaver, D. and Hajnoczky, G. (2004) 'Control of mitochondrial motility and distribution by the calcium signal: a homeostatic circuit', *J Cell Biol*, 167(4), pp. 661-72.

Yu-Wai-Man, P., Griffiths, P.G. and Chinnery, P.F. (2011a) 'Mitochondrial optic neuropathies - disease mechanisms and therapeutic strategies', *Prog Retin Eye Res*, 30(2), pp. 81-114.

Yu-Wai-Man, P., Shankar, S.P., Biousse, V., Miller, N.R., Bean, L.J., Coffee, B., Hegde, M. and Newman, N.J. (2011b) 'Genetic screening for OPA1 and OPA3 mutations in patients with suspected inherited optic neuropathies', *Ophthalmology*, 118(3), pp. 558-63.

Yu-Wai-Man, P., Votruba, M., Burte, F., La Morgia, C., Barboni, P. and Carelli, V. (2016) 'A neurodegenerative perspective on mitochondrial optic neuropathies', *Acta Neuropathol*.

Yu, D.Y., Cringle, S.J., Balaratnasingam, C., Morgan, W.H., Yu, P.K. and Su, E.N. (2013) 'Retinal ganglion cells: Energetics, compartmentation, axonal transport, cytoskeletons and vulnerability', *Prog Retin Eye Res*, 36, pp. 217-46.

Yurimoto, S., Hatano, N., Tsuchiya, M., Kato, K., Fujimoto, T., Masaki, T., Kobayashi, R. and Tokumitsu, H. (2009) 'Identification and characterization of wolframin, the product of the

wolfram syndrome gene (WFS1), as a novel calmodulin-binding protein', *Biochemistry*, 48(18), pp. 3946-55.

Zampese, E., Fasolato, C., Kipanyula, M.J., Bortolozzi, M., Pozzan, T. and Pizzo, P. (2011) 'Presenilin 2 modulates endoplasmic reticulum (ER)-mitochondria interactions and Ca2+ cross-talk', *Proc Natl Acad Sci U S A*, 108(7), pp. 2777-82.

Zanna, C., Ghelli, A., Porcelli, A.M., Karbowski, M., Youle, R.J., Schimpf, S., Wissinger, B., Pinti, M., Cossarizza, A., Vidoni, S., Valentino, M.L., Rugolo, M. and Carelli, V. (2008) 'OPA1 mutations associated with dominant optic atrophy impair oxidative phosphorylation and mitochondrial fusion', *Brain*, 131(Pt 2), pp. 352-67.

Zatyka, M., Da Silva Xavier, G., Bellomo, E.A., Leadbeater, W., Astuti, D., Smith, J., Michelangeli, F., Rutter, G.A. and Barrett, T.G. (2015) 'Sarco(endo)plasmic reticulum ATPase is a molecular partner of Wolfram syndrome 1 protein, which negatively regulates its expression', *Hum Mol Genet*, 24(3), pp. 814-27.

Zatyka, M., Ricketts, C., da Silva Xavier, G., Minton, J., Fenton, S., Hofmann-Thiel, S., Rutter, G.A. and Barrett, T.G. (2008) 'Sodium-potassium ATPase 1 subunit is a molecular partner of Wolframin, an endoplasmic reticulum protein involved in ER stress', *Hum Mol Genet*, 17(2), pp. 190-200.

Zhang, A., Williamson, C.D., Wong, D.S., Bullough, M.D., Brown, K.J., Hathout, Y. and Colberg-Poley, A.M. (2011) 'Quantitative proteomic analyses of human cytomegalovirus-induced restructuring of endoplasmic reticulum-mitochondrial contacts at late times of infection', *Mol Cell Proteomics*, 10(10), p. M111 009936.

Zuris, J.A., Harir, Y., Conlan, A.R., Shvartsman, M., Michaeli, D., Tamir, S., Paddock, M.L., Onuchic, J.N., Mittler, R., Cabantchik, Z.I., Jennings, P.A. and Nechushtai, R. (2011) 'Facile transfer of [2Fe-2S] clusters from the diabetes drug target mitoNEET to an apo-acceptor protein', *Proc Natl Acad Sci U S A*, 108(32), pp. 13047-52.